



**HAL**  
open science

# Elaboration of functional copolymers absorbing in the near infrared region

Adèle Gapin

► **To cite this version:**

Adèle Gapin. Elaboration of functional copolymers absorbing in the near infrared region. Other. Université de Pau et des Pays de l'Adour, 2020. English. NNT : 2020PAUU3034 . tel-03683832

**HAL Id: tel-03683832**

**<https://theses.hal.science/tel-03683832>**

Submitted on 1 Jun 2022

**HAL** is a multi-disciplinary open access archive for the deposit and dissemination of scientific research documents, whether they are published or not. The documents may come from teaching and research institutions in France or abroad, or from public or private research centers.

L'archive ouverte pluridisciplinaire **HAL**, est destinée au dépôt et à la diffusion de documents scientifiques de niveau recherche, publiés ou non, émanant des établissements d'enseignement et de recherche français ou étrangers, des laboratoires publics ou privés.

# THÈSE

UNIVERSITE DE PAU ET DES PAYS DE L'ADOUR

École doctorale des Sciences Exactes et leurs Applications (ED211)

Présentée et soutenue le 16 Décembre 2020

par **Adèle GAPIN**

pour obtenir le grade de docteur

de l'Université de Pau et des Pays de l'Adour

**Spécialité : Chimie et Physico-Chimie des Polymères**

Elaboration of functional copolymers absorbing in the near  
infrared region

---

Élaboration de copolymères fonctionnels absorbant dans le  
proche infrarouge

## MEMBRES DU JURY

### RAPPORTEURS

- Clément CABANETOS
- Paul D. TOPHAM

Chargé de Recherche CNRS, MOLTECH-Anjou, Université d'Angers  
Professeur, Aston Institute of Materials Research, Aston University

### EXAMINATEURS

- Natalie STINGELIN
- Stéphanie REYNAUD

Professeur, Georgia Institute of Technology  
Directeur de Recherche, CNRS, Université de Pau et des Pays de l'Adour

### DIRECTEUR

- Christine LARTIGAU-DAGRON

Maître de Conférences, HDR, Université de Pau et des Pays de l'Adour

### ENCADRANT

- Antoine BOUSQUET

Maître de Conférences, Université de Pau et des Pays de l'Adour





*To those who left before seeing me complete this thesis work.*

*A ceux partis avant de me voir achever ce travail de thèse.*

## Acknowledgements

I would like to express my special appreciation and thanks to my director Dr. Christine Lartigau-Dagron and my supervisor Dr. Antoine Bousquet for accepting to supervise my thesis work. I deeply thank them for the trust, support and guidance they have given me and which have been of great help in carrying out this work. Without your supervision, advice, and constant help, this dissertation would not have been possible.

I address my sincere thanks to the members of my jury Pr. Natalie Stingelin, Dr. Stéphanie Reynaud, Pr. Paul D. Topham, and Dr. Clément Cabanetos who agreed to evaluate this work.

I would like to thank E2S UPPA, the Doctoral School of Natural Sciences and Applications, and the *Université de Pau et des Pays de l'Adour* for funding my project, my attendance at the 17<sup>th</sup> International Conference on Chemistry and the Environment, and my international doctoral mobility at the Georgia Institute of Technology. I would particularly like to thank Pr. Natalie Stingelin who agreed to build this new collaboration, welcomed me into her laboratory and shared her inspiring advice.

I would like to thank Pr. Bruno Grassl for his advice given during my two thesis monitoring committees, Dr. Elise Deniau for her detailed corrections and especially for the sharing of her passion for research, Dr. Laurent Rubatat for his precious advice on structural characterization, Dr. Sylvain Chambon for having produced electronic devices with synthesized materials and for his corrections and Pr. Corinne Nardin for her many tips throughout my doctorate. This thesis work would not have been the same without the NMR expertise of Dr. Abdel Khoukh, the help of Sylvie Blanc, the recommendations of Virginie Pellerin, the technical support of Anthony Laffore and Francis Erhenfeld, as well as the multiple glassware repairs of Eddy Lasseur.

I would like to express my gratitude to the IR team made up of Dr. Wissem Khelifi, Hisham Idriss, and Alexandre Holmes for their help in the laboratory. Since a laboratory is nothing without them, I would particularly like to express my thanks to the four post-docs who advised, supported and motivated me: Dr. Garbine Aguirre, Dr. Laurence Pessoni, Dr. Hussein Awada, and the one and only Dr. Pierre Marcasuzaa. This doctoral adventure would not have been the same without my precious doctoral colleagues: Dr. Eva Dieuzy and Dr.

Nicolas Benoot who happily shared their office with me; Dr. Eleftheria Batagianni, Sirikorn Chasvised, Dr. Charlène Boussiron, Dr. Laura Garcia-Andujar, Dr. Fatima Sherry, Dr. Ghaya Al Choubassi, Thibault Castagnet, Guillaume Declercq, Dr. Islam Lebouachera, Dr. Fetah Grigha, Dr. Youn Charles-Blin, Dr. Pierre Ranque, Marlène Roch, and so many others. Thank you!

A special thanks goes to my friends who tried to understand my difficulties and offered me their comfort when I needed it: Elodie G., Ahmed, Lorène, Fanny, Aymeric, Elodie S., Inès, Eddy, Lucie, and Alex. I particularly thank my Paulo, for our hours of scientific phone calls.

Finally, my whole gratitude goes to my family for being present at all time when I need them. Last but not least, my deepest thankfulness goes to Arnaud for being a great coach and for the sacrifices that he has made on my behalf. You kept going on while supporting me at every step even in the worst ups and downs.

## List of abbreviations

<b>A</b> Electron-accepting unit	<b>AIBN</b> Azobisisobutyronitrile
<b>ATR</b> Attenuated total reflectance	<b>ATRP</b> Atom transfer radical polymerization
<b>BHJ</b> Bulk heterojunction	<b>BLA</b> Bond length alternation
<b>BrS</b> Bromostyrene	<b>BrV</b> Bromoveratrole
<b>C<sub>60</sub></b> Buckminsterfullerene	<b>CdSe</b> Cadmium selenide
<b>CdTe</b> Cadmium telluride	<b>CHCl<sub>3</sub></b> Chloroform
<b>CNS</b> Colloidal nanosphere	<b>CNT</b> Carbon nanotube
<b>CP</b> Conjugated polymer	<b>CuAAC</b> Copper(I)-catalyzed azide-alkyne cycloaddition
<b>CV</b> Cyclic voltammetry	<b>D</b> Molar mass dispersity
<b>D</b> Electron-donating unit	<b>D-A</b> Donor-acceptor
<b>DMF</b> N,N-dimethylformamide	<b>DNA</b> Deoxyribonucleic acid
<b>DP<sub>n</sub></b> Number average degree of polymerization	<b>DP<sub>w</sub></b> Weight average degree of polymerization
<b>DSC</b> Differential scanning calorimetry	<b>E<sub>g</sub></b> Bandgap energy
<b>EG</b> End-group	<b>EL</b> Electroluminescence
<b>EQE</b> External quantum efficiency $\eta_{\text{ext}}$	<b>FA</b> Fullerene acceptor
<b>FET</b> Field-effect transistor	<b>FF</b> Fill factor
<b>FIR</b> Far-infrared	<b>FRP</b> Free radical polymerization
<b>GO</b> Graphene oxide	<b>GRIM</b> Grignard metathesis polymerization
<b>HOMO</b> Highest occupied molecular orbital	<b>ICT</b> Intramolecular charge transfer
<b>IQE</b> Internal quantum efficiency $\eta_{\text{int}}$	<b>IR</b> Infrared
<b>ITO</b> Indium-tin oxide	<b>J</b> Photocurrent density
<b>J<sub>d</sub></b> Dark current density	<b>J<sub>sc</sub></b> Short circuit current
<b>KCTP</b> Kumada catalyst-transfer polycondensation	<b>LBG</b> Low band-gap
<b>LCD</b> Liquid crystal display	<b>LED</b> Light-emitting diode
<b>LMCT</b> Ligand-to-metal charge transfer	<b>LUMO</b> Lowest occupied molecular orbital
<b>M<sub>0</sub></b> Molar mass of the repeat unit	<b>MALDI-MS</b> Matrix Assisted Laser Desorption Ionization Mass Spectrometry

**MALDI-ToF** Matrix Assisted Laser Desorption Ionization Time-of-Flight

**MLCT** Metal-to-ligand charge transfer

**MOF** Metal-organic framework

**M<sub>w</sub>** Weight-average molar mass

**NIR** Near-infrared

**NMR** Nuclear magnetic resonance

**NP** Nanoparticle

**v** Number of functional groups

**OFET** Organic field-effect transistor

**OPV** Organic photovoltaics

**PA** Photoacoustic

**PD** Photodetector

**PL** Photoluminescence

**PSC** Polymer solar cell

**r** Stoichiometric ratio

**RAFT** Reversible addition-fragmentation chain-transfer

**S<sub>1</sub>** Lowest excited singlet state

**SEC** Size exclusion chromatography

**SPNP** Semiconducting polymer nanoparticle

**T<sub>1</sub>** Lowest excited triplet state

**TGA** Thermogravimetric analysis

**μ<sub>sat</sub>** Saturated charge carrier mobility

**VOA** Variable optical attenuator

**WAXS** Wide-angle X-ray scattering

**ZnO** Zinc oxide

**MIR** Mid-infrared

**M<sub>n</sub>** Number-average molar mass

**MOSFET** Metal-oxide field-effect transistor

**NFA** Nonfullerene acceptor

**NMP** Nitroxide-mediated polymerization

**η<sub>out</sub>** Out-coupling efficiency

**NR** Nanorod

**OPD** Organic photodetector

**OLED** Organic light-emitting diodes

**p** Extent of reaction/conversion

**PCE** Power conversion efficiency

**pH** Potential of hydrogen

**POM** Polarized optical microscopy

**Φ<sub>PL</sub>** Quantum yield or luminescence efficiency

**R** Photoresponsivity

**S<sub>0</sub>** Ground state

**SAXS** Small-angle X-ray scattering

**S<sub>N</sub>2** Nucleophilic substitution 2

**SSA** Specific surface area

**TEM** Transmission electron microscopy

**THF** Tetrahydrofuran

**UV** Ultraviolet

**V<sub>oc</sub>** Open circuit voltage

**XPS** X-ray photoelectron spectroscopy



## Table of contents

General introduction.....	10
Introduction générale.....	13
Chapter 1 .....	16
I. Organic near-infrared materials .....	19
1) Materials .....	20
2) Applications .....	23
II. Low band-gap polymers.....	38
1) Definition and types.....	38
2) Polycondensation .....	43
3) End-functionalization in polycondensation .....	50
III. Hybrid materials.....	58
1) Principle .....	58
2) Grafting methodologies .....	60
IV. Block copolymers involving low band-gap polymers .....	64
1) Synthetic strategies .....	64
2) Rod-rod block copolymers.....	70
3) Rod-coil block copolymers.....	78
V. Conclusion .....	86
VI. References .....	88
Chapter 2 .....	105
I. Introduction .....	108
II. Results and discussion.....	111
1) Synthesis of end-functional low band-gap polymers.....	111
2) Grafting of P(DTS-BT) on the surface of zinc oxide nanoparticles.....	118
3) Photophysics of the hybrid nanoparticles .....	123
4) Elaboration of photovoltaic devices.....	125
III. Conclusion .....	127
IV. References .....	128
Chapter 3 .....	132
I. Introduction .....	134
II. Results and discussion.....	136

1)	Synthesis of the acceptor monomer .....	136
2)	Synthesis of rod-coil block copolymers <i>via</i> the macroinitiator method .....	140
3)	Synthesis of rod-coil block copolymers via the macro end-capper copolymerization method .....	157
4)	Optical, thermal, and structural properties.....	170
III.	Conclusion.....	188
IV.	References .....	190
Chapter 4	.....	196
I.	Introduction .....	198
II.	Results and discussion.....	200
1)	Synthesis of rod-coil block copolymers via the macroinitiator method .....	200
2)	Synthesis of rod-coil block copolymers via the macro end-capper copolymerization method .....	215
3)	Optical and photothermal properties.....	221
4)	Study of the nano-objects in water .....	230
III.	Conclusion .....	236
IV.	References .....	237
General conclusions and outlook	.....	241
Conclusions générales et perspectives	.....	244
Chapter 5: Experimental Part	.....	247
List of publications	.....	262
Abstract.....	.....	263

## General introduction

Research in the field of Near Infra-Red (NIR) technologies is in strong development, driven by technological needs in military and civilian applications, such as imaging, optical communications, energy or sensing.<sup>1</sup> Indeed, since 50 % of the solar energy falls into the infrared (IR) spectral region, photovoltaic materials are under development to increase solar cell efficiency.<sup>2</sup> IR-materials are also synthesized for biosensing and bioimaging because IR light penetrates into tissues, the so-called “biological window”.<sup>3</sup> In robotics, proximity detection of objects or walls at short distance is enabled by integration of NIR optical sensors. NIR photodetector matrices can be used for security applications. The main application is identifying finger or palm prints as well as the blood vessel network.

Owing to their ability to conduct electrons, to absorb or emit light, conjugated polymers (CPs) constitute a class of materials with high potential in a broad range of applications in organic electronics, from photovoltaics to sensors.<sup>4</sup> Organic-based devices promise low costs and interesting properties based on their low density, conformability, flexibility and versatility with a wide range of chemical structures. Organic materials absorbing in the NIR region have been much reported over the last two decades including small molecules and organometallics. They have attracted attention due to their various possible applications, from optoelectronic devices to bioimaging and biomedical therapies. However, low band-gap polymers draw particular attention as they can be employed to elaborate active materials in the NIR region. Their reduced bandgaps determine their optical and electronic properties. Specifically, the synthesis of electron donor–acceptor (D–A) alternating conjugated polymers has demonstrated high potential to decrease the bandgap under 1.5 eV leading to IR-absorbing or emitting materials.<sup>5</sup> Since these polymers can be end-functionalized, they are the subject of considerable interest for incorporating them into rod-coil block copolymers. Indeed, such materials composed of a block absorbing in the NIR region provide a broader light absorption and enhance the performance of optoelectronic devices. In addition, these materials can be applied to various applications, especially in the

---

<sup>1</sup> Rational design of ratiometric near-infrared fluorescent pH probes with various pKa values, based on aminocyanine, T. Myochin, K. Kiyose, K. Hanaoka, H. Kojima, T. Terai, T. Nagano, *JACS* **2011**, 133, 3401

<sup>2</sup> Small-bandgap semiconducting polymers with high near-infrared photoresponse, K. H. Hendriks, W. Li, M. M. Wienk, R. A. J. Janssen, *JACS* **2014**, 136, 12130

<sup>3</sup> Two-Photon-Excited Silica and Organosilica Nanoparticles for Spatiotemporal Cancer Treatment, J. G. Croissant, J. I. Zink, L. Raehm and J.-O. Durand, *Adv Healthcare Mater*, **7**, 1701248

<sup>4</sup> Low-Bandgap Near-IR Conjugated Polymers/Molecules for Organic Electronics, L. Dou, Y. Liu, Z. Hong, G. Li, Y. Yang, *Chem Rev* **2015**, 115, 12633

<sup>5</sup> Low bandgap semiconducting polymers for polymeric photovoltaics, C. Liu, K. Wang, X. Gong, A. J. Heeger, *Chem Soc Rev* **2016**, 45, 4825

biomedical and organic photovoltaic fields, thanks to their self-assembly properties and their better solubility, respectively.

In this context, the research presented in this manuscript focuses on the chemical design and synthesis of novel materials based on low band-gap polymers absorbing in the near infrared region.

In Chapter 1, recent developments in the organic near-infrared materials and their applications in organic photovoltaics (OPV), optoelectronic devices such as organic photodetectors (OPD) or organic light-emitting diodes (OLED), medical imaging such as photoacoustic imaging, and minimal invasive therapies such as photodynamic and photothermal therapies are highlighted. The study is mainly on low band-gap polymers and the two major chemistry design approaches to tune their bandgaps. Polycondensation is presented from theoretical considerations based on Carothers work and practical methodologies are introduced among which Stille polycoupling is one of the most widely used. Moreover, low band-gap polymers can be end-functionalized to broaden the range of their possible applications and we detailed several examples of end-functionalized low band-gap polymers. Hence, new materials can be generated with notably hybrid materials. Different grafting methodologies were briefly reviewed supplemented by some examples of low band-gap polymers attached to surfaces. Finally, different synthetic strategies to synthesize block copolymers involving low band-gap polymers are highlighted. Several examples of rod-rod block copolymers involving two different conjugated blocks and rod-coil block copolymers involving a low band-gap block and a non-conjugated block presenting a coil conformation are developed.

In Chapter 2, the aim is to understand and master the end-functionalization of conjugated polymers with different small molecules. In addition, the influence of the stoichiometry of the end-capper on the length of the chains is studied. Hence, we demonstrated a novel and efficient grafting strategy to anchor a low band-gap polymer poly[(4,4'-bis(2-ethylhexyl)dithieno-[3,2-b:2',3'-d]silole)-2,6-diyl-alt-(2,1,3-benzothiadiazole)-4,7-diyl] P(DTS-BT) onto ZnO nanospheres in a one-step procedure *via* grafting onto technique to create a macromolecular self-assembled monolayer. By reducing the grafting density, patchy particles are obtained in which both polymer and metal oxide surfaces can be reached by electrons and holes.

In Chapter 3, a rod-coil block copolymer based on an IR-absorbing block and a soft

filmogenic block is designed. Such a block copolymer with filmogenic properties can be employed as an additive to improve the film morphology, mechanical properties and processability of the active layer. This material is synthesized *via* two synthetic routes: the macroinitiator method and the macro end-capper copolymerization method. The optical, thermal, and structural properties of the different materials synthesized in this chapter are studied. The incorporation of a coil block improved the solubility of the block copolymers, reduced the formation of aggregates and decreased the  $\pi$ -stacking phenomenon.

In Chapter 4, an amphiphilic rod-coil block copolymer based on an IR- absorbing block able to self-assemble in water is designed. The block copolymers were made of a photothermal hydrophobic block and a biocompatible hydrophilic block. This material is synthesized *via* the macroinitiator synthetic methodology. The optical and photothermal properties of the different materials synthesized in this chapter as well as the morphology of the nano-objects formed in water are studied.

In the experimental part, the synthetic procedures of the different materials developed throughout this manuscript are detailed. In addition, the characterization techniques and their terms of use employed to study the materials are specified.

## Introduction générale

Les recherches dans le domaine des technologies Proche Infra-Rouge (PIR) sont en fort développement, motivées par les besoins technologiques dans des applications militaires et civiles telles que l'imagerie, les communications optiques, l'énergie ou la détection.<sup>6</sup> En effet, comme 50% de l'énergie solaire se trouve dans la région spectrale infrarouge (IR), les matériaux photovoltaïques sont en développement pour augmenter l'efficacité des cellules solaires.<sup>7</sup> Les matériaux IR sont aussi synthétisés pour la détection et l'imagerie biologiques car la lumière infrarouge pénètre dans les tissus, aussi appelée « fenêtre biologique ».<sup>8</sup> En robotique, la proximité de détection des objets ou mur à courte distance est rendue possible par l'intégration de détecteurs optiques PIR. Les photodétecteurs PIR peuvent être utilisés dans le domaine de la sécurité. L'application principale envisagée pourrait consister à identifier l'empreinte du doigt ou de la paume ainsi que le réseau de vaisseaux sanguins.

Grâce à leur capacité à conduire les électrons, à absorber ou émettre la lumière, les polymères conjugués (PCs) constituent une classe de matériaux à fort potentiel dans une large gamme d'applications telles que l'électronique organique, le photovoltaïque ou la détection.<sup>9</sup> Les dispositifs organiques promettent des coûts réduits et des propriétés intéressantes grâce à leur faible densité, leur flexibilité et l'accessibilité à une large gamme de structures chimiques. Les matériaux organiques absorbant dans la région PIR ont été largement rapportés durant ces deux dernières décennies, incluant les petites molécules et les organométalliques. Ils ont attiré l'attention en raison de leurs diverses applications possibles, des dispositifs optoélectroniques à la bioimagerie et aux thérapies biomédicales. Les polymères à faible bande interdite sont très étudiés car leur bande interdite peut être régulé et ainsi conduire à des propriétés optiques et électroniques nouvelles. Récemment, la synthèse de polymères conjugués alternant des donneurs-accepteurs (D-A) d'électrons a démontré un fort potentiel pour réduire la bande interdite en-dessous de 1,5 eV menant à des matériaux absorbants ou émettants dans l'IR.<sup>10</sup> Comme ces polymères peuvent être fonctionnalisés en bout de chaînes, ils sont le sujet d'un intérêt considérable pour les intégrer dans des

<sup>6</sup> Rational design of ratiometric near-infrared fluorescent pH probes with various pKa values, based on aminocyanine, T. Myochin, K. Kiyose, K. Hanaoka, H. Kojima, T. Terai, T. Nagano, *JACS* **2011**, 133, 3401

<sup>7</sup> Small-bandgap semiconducting polymers with high near-infrared photoresponse, K. H. Hendriks, W. Li, M. M. Wienk, R. A. J. Janssen, *JACS* **2014**, 136, 12130

<sup>8</sup> Two-Photon-Excited Silica and Organosilica Nanoparticles for Spatiotemporal Cancer Treatment, J. G. Croissant, J. I. Zink, L. Raehm and J.-O. Durand, *Adv Healthcare Mater*, **7**, 1701248

<sup>9</sup> Low-Bandgap Near-IR Conjugated Polymers/Molecules for Organic Electronics, L. Dou, Y. Liu, Z. Hong, G. Li, Y. Yang, *Chem Rev* **2015**, 115, 12633

<sup>10</sup> Low bandgap semiconducting polymers for polymeric photovoltaics, C. Liu, K. Wang, X. Gong, A. J. Heeger, *Chem Soc Rev* **2016**, 45, 4825

copolymères à blocs rigide-flexible. En effet, de tels matériaux composés d'un bloc absorbant dans le proche infrarouge donnent accès à l'extension de la gamme d'absorption et l'amélioration des performances des dispositifs optoélectroniques. De plus, grâce à leurs propriétés d'auto-assemblage et leur meilleure solubilité, ces matériaux peuvent être utilisés dans de nombreuses applications, notamment dans les domaines biomédical et du photovoltaïque organique.

Dans ce contexte, les recherches présentées dans ce manuscrit se focalisent sur la conception chimique et la synthèse de nouveaux matériaux à base de polymères à faible bande interdite absorbant dans la région du proche infrarouge.

Dans le Chapitre 1, nous avons mis en lumière les développements récents de matériaux proche infrarouge organiques pour leur application en électronique organique comme le photovoltaïque, les photodétecteurs et les diodes électroluminescentes, en imagerie médicale comme l'imagerie photoacoustique et les thérapies à invasion minimale telles que les thérapies photodynamiques et photothermiques. Nous avons concentré notre étude principalement sur les polymères à faible bande interdite et les deux principales approches de conception chimique pour affiner leurs bandes interdites. Nous avons présenté la polycondensation d'un point de vue théorique basée sur le travail de Carothers et les méthodes pratiques parmi lesquelles le polycondensation Stille est l'un des plus utilisés. De plus, les polymères à faible bande interdite peuvent être fonctionnalisés en bout de chaînes pour étendre la gamme de leurs possibles applications et nous avons détaillé plusieurs exemples de polymères à faible bande interdite fonctionnalisés. Ainsi, de nouveaux matériaux peuvent être générés comme notamment les matériaux hybrides. Nous avons brièvement passé en revue les différentes méthodologies de greffage enrichies par quelques exemples de polymères à faible bande interdite attachés à des surfaces. Enfin, nous avons mis en lumière différentes stratégies de synthèse pour obtenir des copolymères à blocs impliquant des polymères à faible bande interdite. Nous avons développé plusieurs exemples de copolymères à blocs dits rigide-rigide impliquant deux blocs conjugués différents et de copolymères à blocs dits rigide-flexible impliquant un bloc à faible bande interdite et un bloc non-conjugué présentant une conformation flexible.

Dans le Chapitre 2, nous nous sommes concentrés à comprendre et maîtriser la fonctionnalisation en bout de chaînes de polymères conjugués avec différentes petites molécules. De plus, nous avons étudié l'influence de la stœchiométrie des monomères et de la

molécule fonctionnalisante sur la longueur des chaînes. Ainsi, nous avons démontré une nouvelle stratégie de greffage efficace pour fixer le polymère à faible bande interdite poly[(4,4'-bis(2-ethylhexyl)dithieno-[3,2-b:2',3'-d]silole)-2,6-diyl-alt-(2,1,3-benzothiadiazole)-4,7-diyl] P(DTS-BT) sur des nanosphères de ZnO *via* la technique de greffage *onto* pour créer une monocouche macromoléculaire auto-assemblée. En réduisant la densité de greffage, nous avons obtenu des particules tachetés (« patchy ») où les surfaces de polymère et d'oxide métallique peuvent être toutes les deux atteintes par des électrons et des trous.

Dans le Chapitre 3, nous avons conçu un copolymère à blocs rigide-flexible constitué d'un bloc absorbant dans l'infrarouge et d'un bloc mou filmogénique. Un tel copolymère à blocs avec des propriétés filmogènes peut être utilisé comme additif pour améliorer la morphologie des films, les propriétés mécaniques et la mise en œuvre de la couche active. Nous avons synthétisé ce matériau *via* deux voies synthétiques : la méthode du macroamorceur et la méthode de copolymérisation avec une macro molécule fonctionnalisante. Nous avons étudié les propriétés optiques, thermiques et structurelles des différents matériaux obtenus dans ce chapitre. L'incorporation d'un bloc flexible a amélioré la solubilité des copolymères à blocs, réduit la formation d'agrégats et le phénomène de  $\pi$ -stacking.

Dans le Chapitre 4, nous avons conçu un copolymère à blocs rigide-flexible amphiphile composé d'un bloc absorbant dans l'infrarouge qui s'auto-assemble dans l'eau. Les copolymères à blocs sont faits d'un bloc hydrophobe présentant des propriétés photothermiques et d'un bloc hydrophile biocompatible. Nous avons synthétisé ce matériau *via* la méthode du macroamorceur. Nous avons étudié les propriétés optiques et photothermiques des différents matériaux obtenus dans ce chapitre ainsi que les morphologies des nano-objets formés dans l'eau.

Dans la partie expérimentale, nous avons détaillé les protocoles de synthèse des différents matériaux développés tout au long de ce manuscrit. De plus, nous avons spécifié les techniques de caractérisations employées pour étudier les matériaux ainsi que leurs conditions d'utilisation.



# Chapter 1

## Table of contents

I. Organic near-infrared materials .....	19
1) Materials.....	20
a. Small molecules and organic dyes.....	20
b. Organometallics.....	21
c. Conjugated polymers .....	22
2) Applications .....	23
a. Organic photovoltaics (OPVs).....	23
b. Organic Photodetectors (OPDs) .....	26
c. Ambipolar Organic Field-Effect Transistors (OFETs).....	29
d. Organic Light-Emitting Diodes (OLEDs) .....	31
e. Variable Optical Attenuators (VOAs) .....	33
f. Photoacoustic imaging.....	33
g. Photodynamic therapy .....	35
h. Photothermal therapy.....	36
II. Low band-gap polymers.....	38
1) Definition and types .....	38
a. Conjugated quinoid type polymers.....	39
b. Donor-acceptor polymers .....	40
2) Polycondensation .....	43
a. Theoretical consideration .....	44
b. Low band-gap polymerization technique .....	47
3) End functionalization in polycondensation .....	50
a. Monofunctional end-capper: a one-step strategy.....	50
b. <i>In situ</i> termination.....	53
c. Post-polymerization modification .....	57
III. Hybrid materials involving low band-gap polymers .....	58
1) Principle .....	58
2) Grafting methodologies.....	60
a. Grafting from.....	60
b. Grafting through .....	61
c. Grafting onto.....	62

IV. Block copolymers involving low band-gap polymers .....	64
1) Synthetic strategies.....	64
a. The macroinitiator method .....	64
b. The macro end-capper copolymerization method .....	66
c. The grafting-to method.....	67
d. Sequential monomer polymerization.....	69
2) Rod-rod block copolymers .....	70
3) Rod-coil block copolymers .....	78
V. Conclusion.....	86
VI. References .....	88

## I. Organic near-infrared materials

Infrared (IR) light is divided into three parts: near-infrared (NIR), mid-infrared (MIR), and far-infrared (FIR). All of them are invisible to human eyes as their wavelengths are longer than those of visible light. NIR technology, located between 780 nm and 3000 nm, is of particular interest as nearly 50% of solar energy takes place in this region. The field of research on organic near-infrared materials has seen much progress in the past few years, driven by both scientific curiosity and technological need particularly in photonics, optical communications, energy, and advanced optoelectronics. Moreover, NIR light penetrates biological tissues making it greatly useful for biophotonics, bioimaging, and sensing applications.<sup>1</sup>

NIR materials, absorbing, emitting, or reflecting NIR light, must present a reduced band-gap, *i.e.* the energy level difference between the lowest unoccupied molecular orbital (LUMO) and the highest occupied molecular orbital (HOMO). Organic materials such as conjugated polymers presenting a band-gap between 1.6 eV and 3 eV absorb visible light whereas a band-gap below 1.6 eV corresponds to NIR light. Indeed, the band-gap energy  $E_g$  (J) is linked to the wavelength of the absorbed photon:

$$E_g = h\nu = \frac{hc}{\lambda} \quad \text{Equation 1.1}$$

Where  $h$  corresponds to the Planck constant ( $6.63 \cdot 10^{-34}$  J.s),  $\nu$  the frequency of the electromagnetic wave associated to the photon ( $s^{-1}$ ),  $\lambda$  the wavelength of the photon (m) and  $c$  the speed of light in vacuum ( $m \cdot s^{-1}$ ). As the Planck constant and the speed of light in vacuum are constants, the previous equation can be simplified as:

$$E_g(eV) = \frac{1240}{\lambda} \quad \text{Equation 1.2}$$

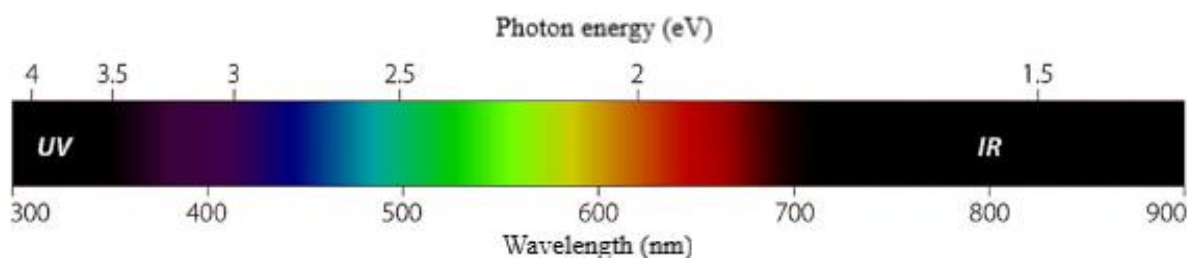


Figure 1: Wavelength range between ultraviolet (UV) and beginning of near-infrared (NIR)

## 1) Materials

## a. Small molecules and organic dyes

Generally used in photoelectric/electric applications, small molecules exhibit interesting advantages such as well-defined molecular structures, high purity, great repeatability, and no end-group contaminants.<sup>2</sup> Actually, contrary to polymers, contaminants and impurities can be identified thanks to mass spectrometry for instance and removed more easily.<sup>3</sup>

Typically, NIR small molecules include ionic dye molecules, large aromatic molecules, quinoid-type molecules, and donor-acceptor (D-A) type molecules. These organic compounds contain chromophores with well-delocalized  $\pi$ -electrons able to absorb or emit in the NIR region. The production of small molecules with band-gaps below 1.6 eV requires the use of donor and acceptor units with strong abilities.

Changing the electron density on the donor and acceptor units is the most effective approach to tune molecular energy levels and band-gaps. One structure frequently used is the D-A-D structure where the absorption and emission maxima can be tuned by changing the donor and the acceptor. However, it has been shown that the acceptor unit plays a more influential role than the donor unit when it comes to band-gap tuning. The most popular acceptor units to build small molecules with low band-gaps (LBG) are the diketopyrrolopyrrole (DPP)<sup>4</sup>, the thienoisindigo (TII)<sup>5,6</sup>, the squaraine<sup>7</sup>, and the boron dipyrromethane (BODIPY)<sup>8</sup> (Figure 2).

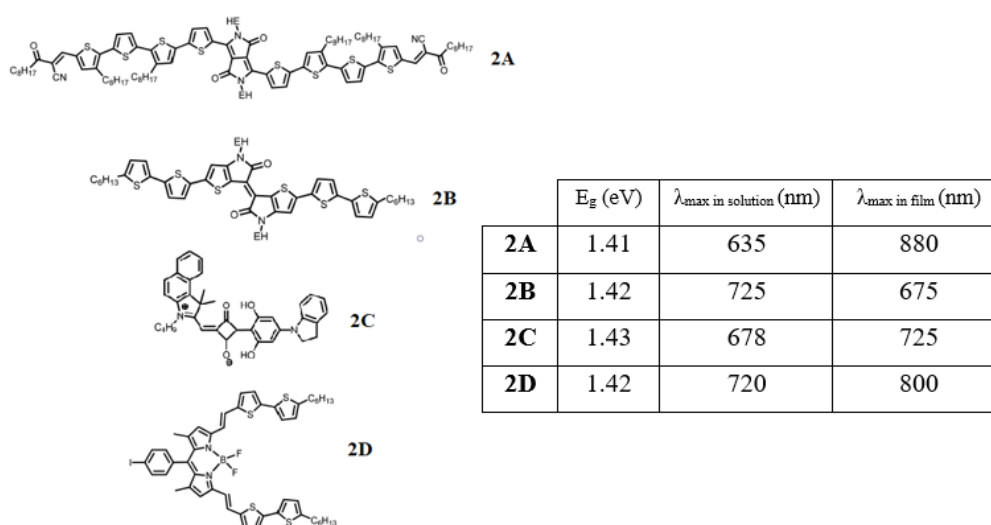


Figure 2: Chemical structures and optical properties of NIR small molecules based on DPP (**2A**)<sup>4</sup>, TII (**2B**)<sup>5,6</sup>, squaraine (**2C**)<sup>7</sup>, and BODIPY (**2D**)<sup>8</sup>

The use of a  $\pi$ -spacer is also crucial as it can extend or break  $\pi$ -conjugation and support or weaken the quinoid structures. Ji *et al.* designed a D-A-D small molecule based on the diketopyrrolopyrrole (DPP) showing low band-gap behavior thanks to the introduction of ethynyl groups as  $\pi$ -linkage.<sup>9</sup> Commonly, the electron-rich thiophene spacer is employed as it promotes the quinoid structure and enhances the coplanarity which is favorable for intramolecular charge transfer (ICT).<sup>10</sup> Some other  $\pi$ -spacers can be applied such as dithienothiophene (DTT), dithienosilole (DTS), cyclopentadithiophene (CPDT), and dithienopyrrole (DTP) (Figure 3).<sup>11</sup>

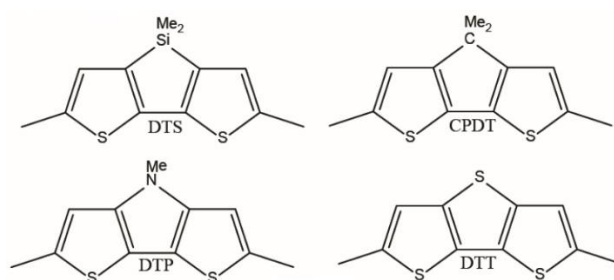


Figure 3: Chemical structures of some  $\pi$ -spacers. Adapted from Trang *et al.*<sup>11</sup>

#### b. Organometallics

Also called metal complexes, organometallics absorb in the UV-visible spectral region and show a wide band-gap. Nevertheless, when radical cations or anions are generated upon one-electron oxidation or reduction, the resulting metal-to-ligand or ligand-to-metal charge transfer process (MLCT or LMCT) displays a small HOMO-LUMO gap. This feature favors intense and broad absorptions in the NIR spectral region. One of the most studied NIR organometallics are ruthenium complexes.<sup>12–15</sup>

Among them, we can mention dinuclear ruthenium complexes derived from 1,2-dicarbonylhydrazine ligands showing intense metal-to-metal charge transfer band in the NIR region thanks to one of their three possible forms: Ru<sup>II</sup>/Ru<sup>III</sup> (Figure 4a).

Another important class of organometallics is metallodithiolene complexes which absorb intensively in the NIR region but weakly in the visible range. These complexes are completely colorless and could be used as visibly transparent absorbers for IR radiation or solar heat (Figure 4b).<sup>16,17</sup>

Metal complexes represent an important class of photosensitizers and catalysts for light harvesting materials. They can be incorporated into polymer side chains to control the structure, despite the possible side reactions with the active propagating species (Figure 4c).<sup>18–20</sup> Thus, metal complexes are integrated in the polymer backbone through different techniques: postpolymerization complexation, grafting onto strategy, or grafting through strategy using functional monomers.<sup>21</sup>

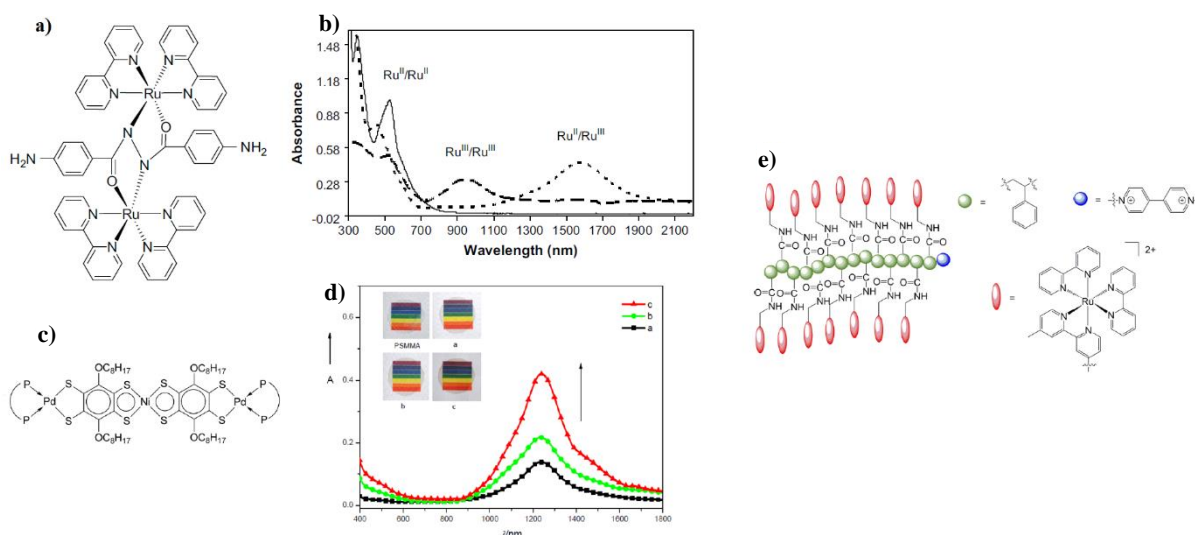


Figure 4: **a)** chemical structure of a dinuclear ruthenium complex and **b)** its corresponding absorption spectra in solution<sup>15</sup>; **c)** chemical structure of a multi-nuclear metallodithiolenes complex oligomer and **d)** its corresponding photos and absorption spectra in film<sup>16</sup>; **e)** chemical structure of a polymer backbone decorated with ruthenium side chains.<sup>18</sup>

### c. Conjugated polymers

In 1977, Heeger, MacDiarmid and Shirakawa<sup>22</sup> put  $\pi$ -conjugated organic macromolecules in the spotlight. These polymers are made of a linear series of overlapping  $p_z$  orbitals with  $sp^2$  or  $sp$  hybridization, thus generating a conjugated chain of delocalized electrons.<sup>23</sup> Then, semi-conducting polymers were further studied and several generations appeared. The first generation includes conjugated polymers with good conductivity but low processability. The second generation consists of conjugated polymers with alkyl chains to improve solubility and, hence, processability. Finally, the most recent generation comprises conjugated polymers with enhanced or new physical/chemical and catalytic properties. This last generation was developed to improve the optoelectronic properties to give high-performance electronic devices. Conjugated polymers designed to absorb in the near-infrared region are part of the third generation. These new  $\pi$ -conjugated organic macromolecules have generally a donor-acceptor alternating structure combining a strong electron-donating unit with a strong

electron-withdrawing unit. They present a band-gap smaller than 1.6 eV and they are called low band-gap polymers.

Like NIR small molecules, low band-gap polymers have been the subject of specific strategies to tune their band-gaps and to shift their absorption in the NIR region. Band-gap engineering is a way to obtain materials with specific properties for optoelectronic and bioimaging applications. The tools to control and tune the band-gap will be detailed later in this manuscript.

## 2) Applications

The materials previously presented have been developed for different applications in optoelectronics, bioimaging, and photonics. Materials absorbing in the NIR region and/or presenting a low band-gap are particularly attractive in organic photovoltaics (OPVs), organic photodetectors (OPDs), ambipolar organic field-effect transistors (OFETs), organic light-emitting diodes (OLEDs), bioimaging, and variable optical attenuators (VOAs) in photonics.

### a. Organic photovoltaics (OPVs)

The photovoltaic effect, also called the Becquerel effect, was first observed in 1839 and consists of the generation of voltage and electric current when a material is exposed to light.<sup>24</sup> The invention of solar cells results from this discovery. Even though silicon solar panels have been widely used for decades, new types of materials emerged to enhance performance while being cheaper, lighter, and more flexible: organic conjugated materials. The working principle of these organic solar cells is based on the absorption of photons generating excitons (*i.e.* electron-hole pairs) instead of free charges in the case of silicon solar cells (Figure 5). These excitons move within the material chain and/or between the chains (intermolecular transition, also called the hopping process), but, their lifetime being very short, they can only reach a maximum of 10 nm, which is called the maximum exciton diffusion length. Within this short period, the excitons can recombine or dissociate: the electron hole pairs are split into free charges. The dissociation of excitons occurs at the donor acceptor interface of the small molecule or the polymer if the difference in energy level of LUMO of donor and acceptor is higher than that of exciton binding energy (*i.e.* 0.2-0.3 eV). Then, the free charges are collected at the electrodes.<sup>25</sup>



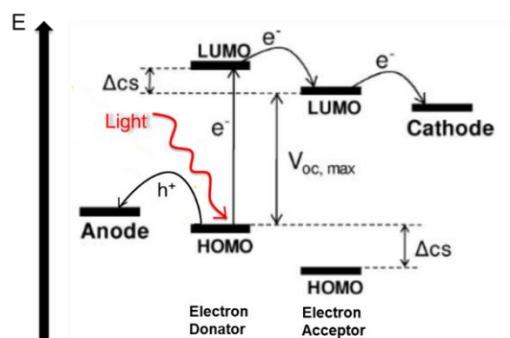
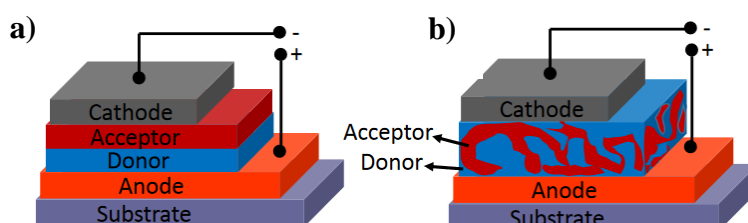


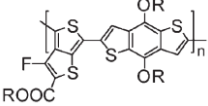
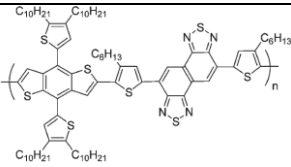
Figure 5: Scheme of the working principle of an organic solar cell

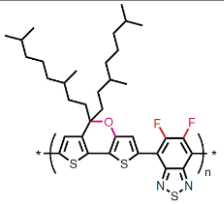
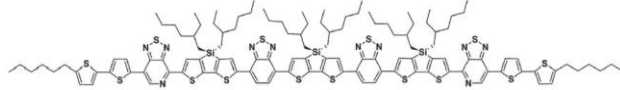
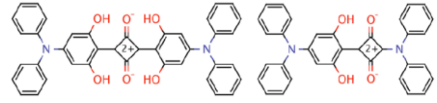
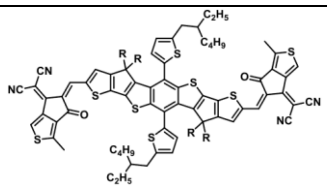
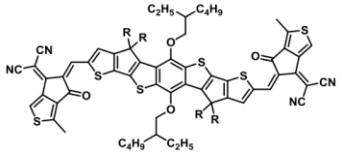
Performances of organic photovoltaic devices are assessed thanks to the power conversion efficiency (PCE) which is the product of short circuit current ( $J_{sc}$ ), open circuit voltage ( $V_{oc}$ ), and fill factor (FF) divided by the radiant flux density. An organic photovoltaic device can be classified by different junction types. The simplest one is the bi-layer heterojunction where an electron acceptor layer rests on an electron donor layer creating a single interface and they are sandwiched between two electrodes (Figure 6a).<sup>26</sup> However, as the photoactive layer is very thin, recombination losses between positive and negative charges are high and the number of excitons collected is low making this device structure the least efficient. Bulk heterojunction (BHJ) cells are now the most popular and efficient as they consist of a nanoscale blend of donor and acceptor materials increasing the interfacial area and improving charge generation and transport (Figure 6b).<sup>27</sup> In the literature, many examples of blends composed of the regioregular electron donor poly(3-hexylthiophene) (P3HT) and the electron acceptor [6,6]-phenyl C61-butyric acid methyl ester (PCBM) are reported.<sup>28,29</sup> Despite being the best seller research for a decade since its first report in 2002<sup>30</sup>, the P3HT:PCBM blend has shown some limitations in terms of efficiency.<sup>31</sup> Indeed, P3HT has a poor overlap between its absorption spectrum and the sun's irradiance spectrum limiting the harvest of a maximal number of photons. Moreover, PCBM is optically inert, has a poor absorption in the visible range, and has a low LUMO level leading to low  $V_{oc}$ .

Figure 6: Architectures of photoactive layer: **a)** bilayer heterojunction and **b)** bulk heterojunction. Adapted from Kumaresan *et al.*<sup>26</sup>

Thus, low band-gap polymers and small molecules were designed and synthesized to maximize the number of photons harvested from sunlight as the maximum photon flux is around 700 nm on the solar spectrum. The use of low band-gap polymers led to bulk heterojunction devices with PCE above 10%<sup>32</sup>. Liang *et al.* synthesized a star polymer based on the electron donor benzodithiophene (BDT) unit with a band-gap of 1.68 eV reaching 7.4%.<sup>33</sup> Wang *et al.* combined benzodithiophene units with electron acceptor naphthothiadiazole (NT) units and mixed it with PC<sub>71</sub>BM to achieve a PCE of 6%.<sup>34</sup> Low band-gap small molecules were employed to achieve similar performance.<sup>35–37</sup> Small molecules like squaraine dyes can be blended with compatible electron-acceptors to yield a new type of BHJ with PCE approaching 8%.<sup>38–41</sup> These small molecules can be employed as nonfullerene acceptors (NFAs), substituting the widely used fullerene acceptors (FAs), by bringing a complementary absorption to that of the polymer donor, which boosts sunlight harvesting and enhances the PCE.<sup>42,43</sup> Gao *et al.* developed two novel small molecule acceptors, BTTIC and BTOIC, with optical band-gaps of 1.47 eV and 1.39 eV respectively and blended them with the PBDB donor-polymer to achieve a 13 % PCE thanks to extended absorption to the NIR region.<sup>44</sup> Since 2017, the combination of low band-gap polymer donors and low band-gap non-fullerene acceptors has boosted the PCE to 17%.<sup>45–47</sup>

Table 1: Examples of chemical structures of low band-gap polymers and small molecules and their corresponding performances in organic photovoltaics. \* PCEs are obtained in blends with PC<sub>61</sub>BM or PC<sub>71</sub>BM.

Chemical structure	$\lambda_{\max}$ film (nm)	$E_g^{\text{opt}}$ (eV)	PCE* (%)	reference
	700	1.68	7.4	Liang <i>et al.</i> <sup>33</sup>
	750	1.58	6	Wang <i>et al.</i> <sup>34</sup>

	800	1.38	10.6	You <i>et al.</i> <sup>32</sup>
	780	1.41	7.6	Abdelsamie <i>et al.</i> <sup>36</sup> Liu <i>et al.</i> <sup>37</sup>
	720	1.55	8.3	Zimmerman <i>et al.</i> <sup>40</sup>
	759	1.47	13.18	Gao <i>et al.</i> <sup>44</sup>
	781	1.39	10.96	Gao <i>et al.</i> <sup>44</sup>

### b. Organic Photodetectors (OPDs)

Photodetectors are energy converting devices also called transducers: when light energy affects them, they automatically modify one of their features (bulk conductivity for photoresistors, luminescence for scintillators, etc). Their working principle is based on the conversion of absorbed photons into free charge carriers, followed by an electrical response that could be a change in voltage or current in electrical circuits.<sup>48</sup> They are found in environmental monitoring, astronomy, surveillance, machine vision, and cameras in smart phones. Photodetectors are divided in three main categories: photoconductors, photodiodes, and phototransistors. Their performance is assessed by comparing and defining specific features. The most important characteristics of a photodetector are the external quantum efficiency (EQE) expressed in % which represents the photoelectric conversion capability, the

photocurrent density (J) and the dark current density ( $J_d$ ) which correspond to the current density flowing through a photodetector device under illumination and in the dark, respectively.

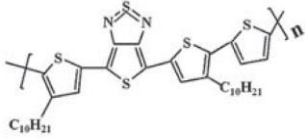
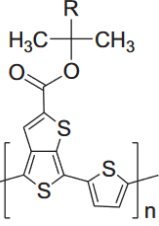
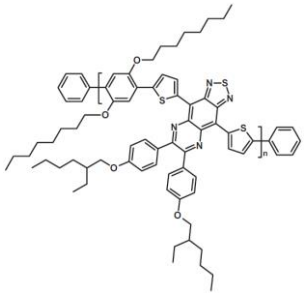
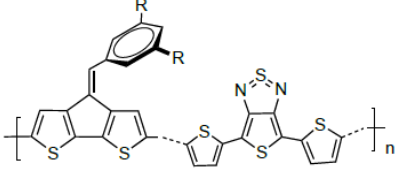
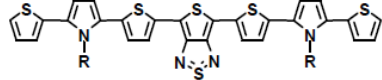
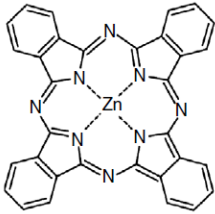
At first, photodetectors were based on inorganic semiconductors like silicon for their high charge-carrier mobility, small exciton binding energy, and high stability. However, they were replaced by organic semiconductors due to their complex and expensive manufacturing processes and mechanical inflexibility. Actually, organic semiconductors are composed of weak van der Waals forces between their molecules making them mechanically soft.

For NIR-light detection like in optical communication<sup>49</sup>, remote control<sup>50</sup>, nighttime surveillance<sup>51</sup>, and biomedicine<sup>52,53</sup>, organic photodetectors with a near-infrared response are indispensable. Low band-gap polymers or small molecules are crucial to fabricate this kind of device as they can improve their detection sensitivity and selectivity to capture very weak NIR signals.<sup>54</sup> Moreover, NIR-OPDs have lower cost and higher performance than inorganic photodetectors and only a very thin layer of the material is desired to fully absorb all the incident photons making their processability easier.<sup>55,56</sup>

Detectivities above  $10^{12}$  cm Hz<sup>1/2</sup>/W (or jones) have been obtained by using low band-gap polymers with a response up to 1450 nm (band-gap as low as 1 eV) by Gong *et al.* in 2009.<sup>57</sup> Two pioneering works also showed encouraging performances like Yao *et al.*<sup>58</sup> with a photodetector based on a polymer with a band-gap of 1.3 eV and a photoresponse peak at 1000 nm or Perzon *et al.* with a device based on a new polymer with a band-gap around 1 eV and a response up to 1200 nm.<sup>59</sup> More recently, London *et al.* synthesized a low band-gap donor-acceptor polymer presenting a band-gap of 0.74 eV with a photoresponse up to 1650 nm but with poor film quality and EQE.<sup>60</sup> Concerning low band-gap small molecules used in NIR photodetectors, Qi *et al.* studied two D-A-D low band-gap small molecules based on bis(2-thienyl)-*N*-alkylpyrrole (TPT) and thieno[3,4-*b*]thiadiazole (TTa) with band-gaps around 1.3 eV and used them in panchromatic photodetectors with a photoresponse from 300 to 1000 nm.<sup>61</sup> Moreover, Siegmund *et al.* mixed an electron donor organometallic zinc phthalocyanine (ZnPC) with an electron acceptor buckminsterfullerene (C<sub>60</sub>) and used an optical microcavity to obtain a NIR photodetector with an EQE above 20%.<sup>62</sup>

Now, some efforts have to be made in response time, detectivity, and smaller band-gap to hit the mid- and far-infrared light range.

Table 2: Examples of chemical structures of low band-gap polymers and small molecules and their corresponding performances in organic photodetectors

Chemical structure	Photoresponse max (nm)	Eg <sup>opt</sup> (eV)	EQE (%)	Detectivity max (Jones)	reference
	1450	0.8	26	$4.2 \cdot 10^{13}$	Gong <i>et al.</i> <sup>57</sup>
	1000	1.3	38	$2.6 \cdot 10^{11}$	Yao <i>et al.</i> <sup>58</sup>
	950	1.0	25	$5.0 \cdot 10^8$	Perzon <i>et al.</i> <sup>59</sup>
	1650	0.74	0.2	$10^9$	London <i>et al.</i> <sup>60</sup>
	1000	1.26	-	$1.7 \cdot 10^{11}$	Qi <i>et al.</i> <sup>61</sup>
	1100	1.52	23	$10^{11}$	Siegmund <i>et al.</i> <sup>62</sup>

c. Ambipolar Organic Field-Effect Transistors (OFETs)

Field-effect transistors (FETs) work like capacitors as they use an electric field to control the flow of current. A FET is composed of three terminals: a gate connecting two ohmic contacts, the source and the drain electrodes.<sup>63</sup> Actually, the charge-carriers enter the channel through the source, then the channel conductivity is modulated along the gate when a voltage is applied and finally the charge-carriers leave the channel through the drain. The most crucial factor to assess the performance of a field-effect transistor is the saturated charge carrier mobility ( $\mu_{\text{sat}}$ ).

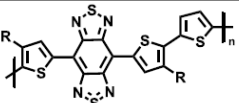
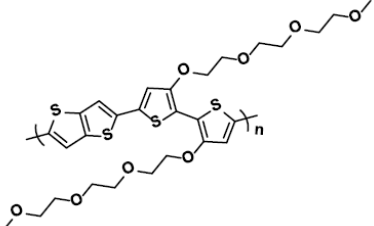
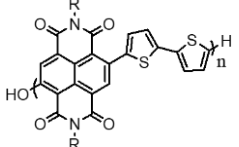
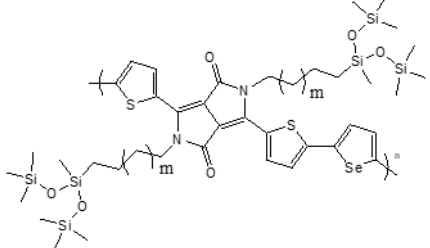
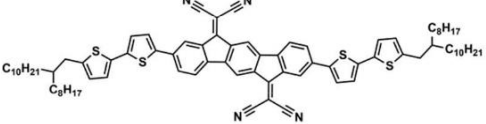
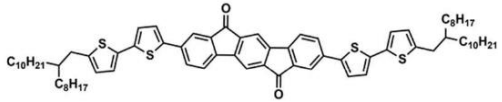
In the beginning, FET were based on metal-oxide semiconductors (MOSFET) and rapidly they became the most widely manufactured device in the world. However, to reduce costs of manufacturing while being more environmentally friendly, organic semiconductors were employed to fabricate thin film transistors. Organic field-effect transistors (OFETs) present several other advantages in comparison to inorganic FETs as they are lightweight, flexible, and solution processable. Among the OFETs, ambipolar transistors are particularly interesting as they can transport either holes or electrons depending on the polarity of the gate voltage. To obtain stable hole and electron transport (*i.e.* ambipolar properties), semiconductors in the active layer must have HOMO energy levels below -5.0 eV and LUMO levels close to or below -4.0 eV.<sup>64</sup> Therefore, energy gap between the HOMO and LUMO levels has to be narrow to utilize ambipolar OFETs in ideal optoelectronic applications. As a result, low band-gap materials, including the ones absorbing in the NIR region, are promising candidates.

Michinobu's group synthesized a benzobisthiadiazole-based polymer (BBT) enriched with an electron-rich thiophene unit reaching a band-gap of 0.75 eV and used it as ambipolar OFET with well-balanced ambipolar characteristics.<sup>65</sup> Giovannitti *et al.* also played on the side-chain engineering of a polymer based on bithiophene (2T) et thienothiophene (TT) units by functionalizing it with either alkoxy or ethylene glycol side chains.<sup>66</sup> The final materials showed interesting results when used in a device but only unipolar characteristic with a hole mobility of 0.95 cm<sup>2</sup>/V.s. Contrary to Giovannitti's group, Matsidik *et al.* prepared a low band-gap polymer based on naphthalene diimide units (NDI) and 2T units showing only electron mobilities up to 3 cm<sup>2</sup>/V.s.<sup>67</sup> One very good example of well-balanced high hole and electron mobilities is the work of Lee *et al.* with the successful synthesis of a diketopyrrolopyrrole-selenophene D-A copolymer decorated with siloxane side-chains and showing low band-gap features.<sup>68</sup> Concerning low band-gap small molecules, Ozdemir *et al.* built two D-A-D small

## Chapter 1: Materials absorbing in the near infrared region and their innovative applications

molecules based on indeno[1,2-*b*]fluorene-6,12-dione (IFDK) and indeno[1,2-*b*]fluorene-6,12-diylidene dimalononitrile (IFDM) acceptor units and  $\alpha$ -substituted bithiophene donor units presenting low band-gaps (1.21 and 1.65 eV) with reasonably balanced electron and hole mobilities.<sup>69</sup>

Table 3: Examples of chemical structures of low band-gap polymers and small molecules and their corresponding performances in organic field-effect transistors

Chemical structure	$E_g^{opt}$ (eV)	$\mu_{sat}^{hole}$ (cm <sup>2</sup> /V.s)	$\mu_{sat}^{electron}$ (cm <sup>2</sup> /v.s)	reference
	0.75	$7.2 \cdot 10^{-3}$	$1.5 \cdot 10^{-2}$	Wang <i>et al.</i> <sup>65</sup>
	1.65	0.95	-	Giovannitti <i>et al.</i> <sup>66</sup>
	1.38	-	3.2	Matsidik <i>et al.</i> <sup>67</sup>
	1.24	8.84	4.34	Lee <i>et al.</i> <sup>68</sup>
	1.21	0.01	0.13	Ozdemir <i>et al.</i> <sup>69</sup>
	1.65	0.01	0.02	Ozdemir <i>et al.</i> <sup>69</sup>

d. Organic Light-Emitting Diodes (OLEDs)

When a suitable voltage is applied through a LED, it emits light and the color of this light depends on the energy required for electrons within the material to cross the band-gap.<sup>70,71</sup> Development of organic light-emitting diodes (OLEDs) only started in 1987 with the work of Tang *et al.*<sup>72</sup> Since then, LEDs have been fabricated with semiconductor polymers<sup>73</sup> and small molecules making them flexible contrary to liquid crystal displays (LCDs) and conventional LEDs.<sup>74</sup>

Typically, organic light-emitting diode devices are structured with an emitter layer placed between two electrodes (anode and cathode). The working principle is, under an applied electric field, electrons and holes are injected from the electrodes to the active material to form excitons. Then these electron-hole pairs recombine and a radiative emission that generates photons occurs.<sup>75</sup> Performances of OLEDs are assessed by two quantum efficiencies: the internal quantum efficiency  $\eta_{\text{int}}$  (IQE) and the external quantum efficiency  $\eta_{\text{ext}}$  (EQE).<sup>76</sup> The luminescence efficiency (or quantum yield  $\Phi_{\text{PL}}$ ) is also a significant and realistic parameter to control the performance of an OLED device.

Developing materials able to produce near-infrared emissions are now the next target of research on OLEDs.<sup>77</sup> This new interest is particularly focused on the range from 700 to 1000 nm as it coincides with the biological tissue semitransparency window for biosensing applications and biomedical imaging. Actually, NIR light penetrates more easily than visible light in biological tissues and the clearer window is between 700 and 1000 nm to make *in vivo* imaging because above 1000 nm water and lipids absorb more prominently.<sup>78</sup> These NIR-OLEDs could also be used for space applications, short-range communications, night vision, security authentication technologies exploiting biometrics, and transmitters in visible light communication networks.<sup>79</sup> Moreover, using NIR materials for OLEDs devices increases their stability and durability as these materials require less energy than UV materials (*i.e.* 1.1-1.8 eV in the 700-1000 nm window). Hence, low band-gap materials are particularly interesting to fabricate NIR-OLEDs.

Baigent *et al.* presented the first polymer-based NIR-OLEDs in 1995 consisting of a thin film of a cyano copolymer with a narrow band-gap sandwiched between an indium-tin oxide (ITO) layer and a poly(*p*-phenylene vinylene) film. Even though the final device showed a low EQE, the emission range is located between 550 and 1000 nm.<sup>80,81</sup> Later on, Winder *et al.* synthesized a novel low band-gap polymer based on the electron deficient benzothiadiazole



(BT) unit and used it in an OLED device showing an emission range between 600 nm and 1100 nm.<sup>82</sup> Recently, Minotto *et al.* reported one of the highest EQEs in the 650-800 nm emission range by blending a diketopyrrolopyrrole (DPP) derivative and a fluorene-based polymer.<sup>83-85</sup> Yeddu *et al.* fabricated a NIR-OLED based on low band-gap polymer (1 eV) with an emission up to 1100 nm showing also characteristics of NIR-photodetector.<sup>86</sup> Near-infrared organometallics are also useful emitters in OLEDs as Shahaliazad *et al.* demonstrated with the efficient use of two neodymium complexes (Nd<sup>3+</sup>). After doping them with 1,3-bis(9-carbazolyl)benzene, the final OLED devices had emission peaks up to 13330 nm but with very low EQEs (0.022%).<sup>87</sup>

Table 4: Examples of chemical structures of low band-gap polymers and small molecules and their corresponding performances in organic light-emitting diodes

Chemical structure	Eg <sup>opt</sup> (eV)	EQE (%)	emission range (nm)	Φ <sub>PL</sub>	reference
	1.65	0.2	550-1000		Baigent <i>et al.</i> <sup>80</sup>
	1.6	1	600-1100		Winder <i>et al.</i> <sup>82</sup>
	1.6	2.7	650-800	31	Minotto <i>et al.</i> <sup>83</sup>
	2.3				
	1	2	1100		Yeddu <i>et al.</i> <sup>86</sup>
	-	0.022	850-1400		Shahaliazad <i>et al.</i> <sup>87</sup>

e. Variable Optical Attenuators (VOAs)

Variable optical attenuators play different role in wavelength-division multiplexing networks and in cross-connected nodes. They are useful to control optical signals and to regulate dynamic channel power. Usually, they operate at the telecommunication wavelengths (*e.g.*, 1330 and 1550 nm). Active materials in the NIR-II region are thereby perfect candidates for this application. Moreover, NIR-absorbing materials are most of the time electrochemically active or electrochromic, making them useful for switching devices like electrochromic VOAs as they can tune the electrical and optical properties.<sup>88</sup> Electrochromic materials are mostly found in domotic applications such as rear-view mirrors in cars or transparency controlled window.<sup>89</sup> The main point is to use materials that display reversible and stable optical changes at the telecommunication wavelengths.

Organometallics such as dinuclear ruthenium complexes have excellent NIR electrochromic properties, making them convenient for photonic applications.<sup>90</sup> Zhang *et al.* improved a NIR electrochromic attenuator by replacing the visible electrochromic ferrocene with the NIR-absorbing ruthenium complex and mixing it with a polycrystalline tungsten oxide.<sup>91</sup> Radical anions of conjugated diquinones are also reported in literature to have NIR-absorbing electrochromism. The use of specific polymers was proved by Zheng *et al.* as they fabricated an electrochromic VOA based on the layer-by-layer assembly of naphthalene-SO<sub>3</sub>-Na and the cationic polymer poly(diallyldimethylammonium) chloride (PDDA) operating in the NIR region from 1200 nm to 1900 nm.<sup>92</sup> He. *et al.* employed a low band-gap polymer ( $E_g = 1.57$  eV) based on nature-inspired bay-annulated indigo (BAI) as electron acceptor unit to build an electrochromic device that can switch reversibly in both the visible and NIR regions.<sup>93</sup>

f. Photoacoustic imaging

In the field of medical imaging, photoacoustic (PA) imaging is an emerging non-invasive technique based on the photoacoustic effect. This physical effect rests on the formation of sound or ultrasound waves resulting from light absorption. In PA imaging, a nanosecond-pulsed laser irradiates the tissues, the biomolecules within it (*e.g.* melanin, collagen, hemoglobin, DNA (deoxyribonucleic acid), etc.) absorb the light creating a time-varying thermal expansion-relaxation process responsible for the generation of acoustic waves. Depending on the molecule-based nanoparticle, different information is collected from tumor imaging to real-time drug detection (Figure 7).

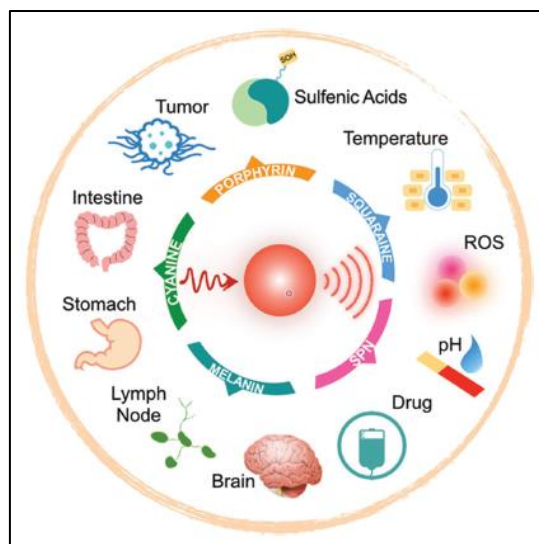


Figure 7: Advanced photoacoustic imaging applications depending on organic molecule based nanoparticles. Adapted from Jiang *et al.*<sup>95</sup>

The images obtained through the acquisition of these PA waves are of high-resolution because sound scatters less than light in biological tissues. Formally, PA imaging relies on visible light but recently NIR-I (700 to 1000 nm) and NIR-II (1000 to 1700 nm) regions were explored to offer high spatial resolution, deeper penetration depth, reduced optical absorption, and tissue scattering. The imaging depth is significantly improved as NIR region allows higher light excitation energy density. Moreover, using NIR light reduces tissue scattering: tissues are more transparent at longer wavelengths. To measure the tissue oxygenation, the level of oxyhemoglobin must be investigated and its maximum absorption is around 1064 nm. The biggest drawback of working in the NIR region is that water strongly absorbs between 1400 to 1500 nm.

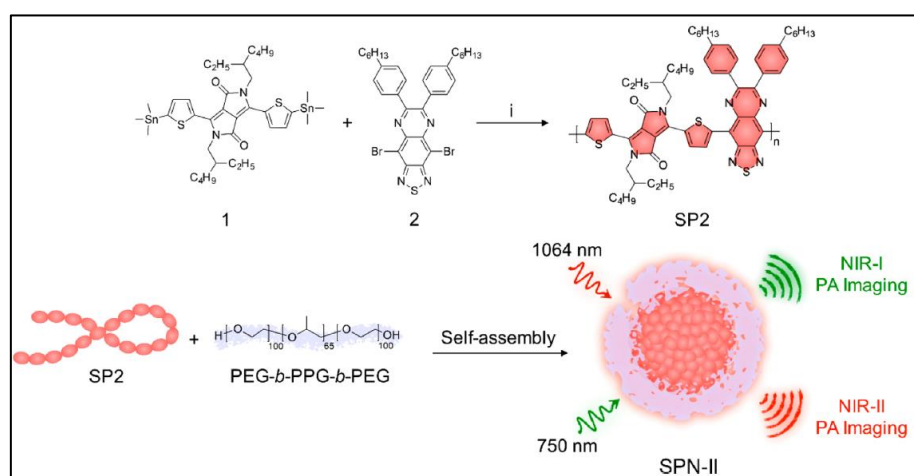


Figure 8: Preparation of donor-acceptor conjugated polymer SP2 and schematic illustration for preparation of nanoparticles SPN-II *via* nanoprecipitation method. Adapted from Jiang *et al.*<sup>96</sup>

To increase the PA signal generated upon irradiation, the use of effective contrast agents is necessary. These agents are based on organic or inorganic nanoparticles absorbing around 1064 nm because the commercially available and most used device is a 1064-nm nanosecond laser.<sup>94</sup> Organic nanoparticles absorbing in the NIR region have the main advantage to be biocompatible and to have size-independent optical properties in comparison to inorganic nanomaterials.<sup>95</sup> Jiang *et al.* reported the synthesis of contrast agent based on donor-acceptor conjugated polymer dispersed in water as nanoparticles thanks to the poly(ethylene glycol)-*b*-PPG-*b*-poly(ethylene glycol) PEG-*b*-PPG-*b*-PEG triblock copolymer surfactant (Figure 8). The final semi-conductive polymer nanoparticles absorb in both NIR-I and NIR-II regions while providing good images of brain vasculature in living rats.<sup>96</sup> In another example, Sun *et al.* developed nanoparticles based on a narrow band-gap D-A conjugated polymer (TBDOPV-DT) obtained by nanoprecipitation with the PEG-*b*-PDLLA block copolymer as surfactant.<sup>97</sup>

### g. Photodynamic therapy

Photodynamic therapy is a minimally invasive treatment for various malignant tumors. This therapy is divided in three phases: the introduction of a photosensitizer, the light irradiation on the lesion area, and the production of cytotoxic singlet oxygen ( $^1\text{O}_2$ ) and reactive oxygen species. Upon irradiation, the photosensitizer transfers its excited triplet state energy to molecular oxygen or substrates in its environment. The reactive oxygen species are able to destruct the tumor cells *via* oxidation, disruption of homeostasis, and ion transportation. This method avoids the use of toxic drugs or radioactive rays while limiting scars and speeding up healing.<sup>98</sup> Besides, most of the photosensitizers used for photodynamic therapy show a good selectivity for damaged tissues while avoiding the destruction of healthy tissues.<sup>99</sup> Up to now, this phenomenon remains unclear but some research suggests that the membrane of cancer cells is larger than healthy ones allowing more efficient accumulation of the photosensitizer.<sup>100</sup> Moreover, cancer cells overexpress receptor proteins and show higher concentration of glutathione with increase of the medium acidity.<sup>101</sup> These chemical and biochemical differences are exploited to enhance the selectivity of photosensitizers.

When the treatment uses photosensitizers activated by UV-visible light, it is only restricted to superficial lesions. To travel deeper into biological tissues and treat deep lesions, NIR-activated photosensitizer is needed. Several strategies are targeted by using small molecules, organic and inorganic nanoparticles. Yuan's group showed a mitochondria-targeting photodynamic therapy (mitochondria are the power source of each biological cells) by forming

nanoparticles based on a tetraphenylporphine-terminated amphiphilic copolymer poly(styrene)-*b*-(PS-*b*-POEGMA-TPP) and an iodinated boron dipyrromethene photosensitizer (BDPI) absorbing in the NIR region (Figure 9). The tetraphenylporphine and the BDPI were chosen because there are a superior mitochondrial-targeting ligand and a high singlet oxygen producer, respectively.<sup>102</sup>

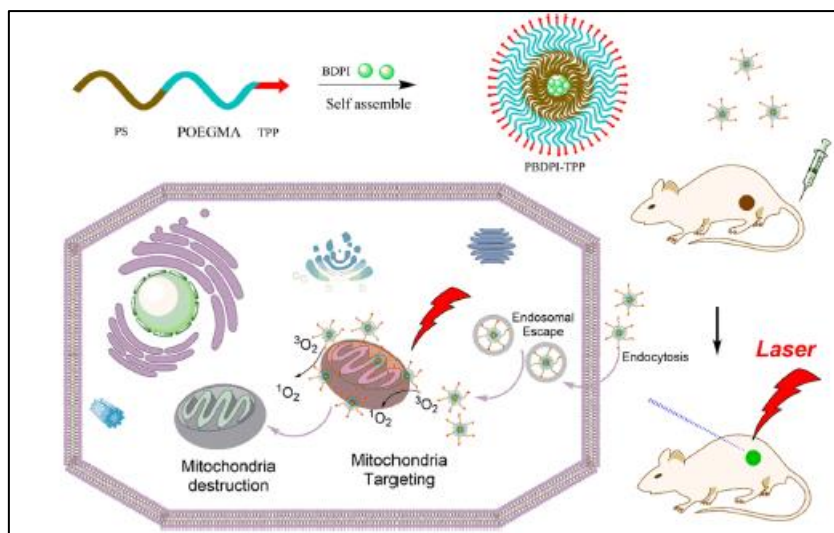


Figure 9: Schematic illustration of PBDPI-TPP nanoparticles for mitochondria-targeting NIR imaging photodynamic therapy. Adapted from Yuan *et al.*<sup>102</sup>

#### h. Photothermal therapy

In addition to photodynamic therapy, photothermal therapy is a minimal invasive therapy to treat tumors based on the irradiation of the targeted cells with a specific photosensitizer followed by the release of heat (*i.e.* artificial elevation of the tissue temperature).<sup>103</sup> The main difference in comparison to photodynamic therapy is that it does not require oxygen to kill the cancer cells. In fact, hyperthermia eradicates the cells *via* protein denaturation or rupture of the cellular membrane.<sup>104</sup> This kind of therapy presents the major advantage to remove cancerous cells by acting with minimal invasion to surrounding healthy cells and tissues. Usually, tissue damages are observed between 55 and 95°C and a lot of natural photothermal agents are already present in the human body such as hemoglobin and melanin. Again, NIR-absorbing agents are necessary to treat deeper biological tissues with high photothermal conversion efficiency while limiting their damages to healthy tissues.<sup>105</sup>

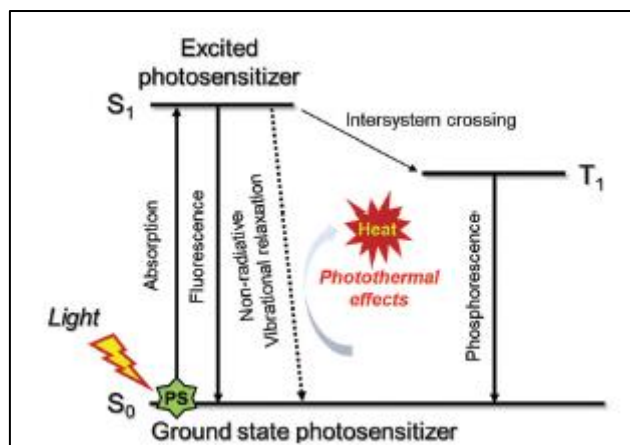


Figure 10: Working principle of organic photothermal agents. Adapted from Jung *et al.*<sup>103</sup>

Organic nanomaterials, particularly conjugated polymers, are preferred as they have better biocompatibility and lower cytotoxicity than inorganic photothermal agents. The working principle of photothermal effect in organic species is depicted in Figure 10. Upon photoexcitation, the lowest excited singlet state ( $S_1$ ) of organic materials has the possibility to decay directly back to the ground state ( $S_0$ ) or passing by the triplet state ( $T_1$ ) before going back to  $S_0$  (phosphorescence). The return to  $S_0$  can be achieved by emitting a photon (fluorescence) or through a nonradiative relaxation pathway. This second possibility is responsible for photothermal effects.

Fluorescent small molecules and organometallics such as cyanine, porphyrin, BODIPY and phthalocyanine can also be employed as NIR-absorbing photothermal agents.<sup>106,107</sup> Yet, they can show drawbacks: poor aqueous solubility, photobleaching, and low photothermal efficiency. Conjugated polymers can be used in multifunctional nanoplatforms to mix photothermal and drug delivery properties in combination for cancer therapy.<sup>108</sup> Semiconducting polymer nanoparticles (SPNPs) lead to excellent photothermal conversion efficiencies as they have interesting properties such as photostability, brightness, and cytotoxicity. Most of them are based on polyaniline (PANI)<sup>109</sup>, polypyrrole (PPy)<sup>110</sup>, PEDOT:PSS<sup>111</sup>, and conjugated D-A polymers<sup>112</sup>. Besides, hybrid nanocomposites composed of inorganic nanoparticles and polymers are also employed for theranostic agents in imaging guided photothermal therapy.<sup>113</sup>

Liu *et al.* synthesized a photothermal agent based on dopamine-melanin colloidal nanospheres (DPA-melanin CNSs) absorbing from the UV-visible to NIR regions with a high molar extinction coefficient at 808 nm. The final nanoagent showed a photothermal conversion

efficiency of 40% which is much higher than the one obtained for the widely used Au nanorods for cancer therapy (*i.e.* 22%).<sup>114</sup> Jing's group obtained water-stabilized nanoparticles with strong absorption in the NIR region showing photothermal conversion efficiency up to 32% *via* nanoprecipitation of a D-A-D small molecule based on thiadiazole with a biodegradable amphiphilic block copolymer (PEG-*b*-PDLLA).<sup>115</sup> More recently, Wang *et al.* synthesized nanoscale polymer metal-organic framework (MOF) hybrids based on the zirconium-MOF UiO-66 and polyaniline (PANI) showing 22% photothermal conversion efficiency upon NIR-light irradiation.<sup>116</sup> Recently, Wu *et al.* reported the synthesis of a NIR photothermal-responsive hydrogel based on a narrow band-gap semiconductor polymer and the poly(*N*-isopropylacrylamide) (PNIPAAm). Besides having a photothermal conversion efficiency around 27%, the composite hydrogels show a rapid and reversible mechanical shrinkage upon NIR-light irradiation making them the perfect candidates for drug delivery applications.<sup>117</sup>

Concerning this thesis project, materials absorbing in the spectral range 650-1000 nm are targeted in order to obtain active materials in the NIR region. This study will focus mainly on low band-gap polymers as it is the predominant research axis of the group.

## II. Low band-gap polymers

### 1) Definition and types

This novel type of  $\pi$ -conjugated organic macromolecule is particularly interesting because it marks the apparition of polymers presenting narrow optical band-gaps, tunable energy levels, and desired electronic properties. As previously mentioned, these so-called low band-gap polymers can even present a band-gap smaller than 1.6 eV and absorb in the near-IR range.

First generation conjugated polymers such as polyphenylenevinylenes (PPVs) and polythiophenes (PTs) display large optical band-gaps and are not efficient to harvest near-IR photons. Therefore, a major task for polymer chemists was to reduce the band-gap and to tune the energy levels of the conjugated polymers. In addition to  $\pi$ -conjugation length, band-gap engineering needs to take in account several important factors<sup>118</sup>:

- bond length alternation (BLA), which is the difference in length between single and double bonds. Low band-gap materials present reduced BLA.
- molecular planarity, which favors orbital overlap and electron delocalization.
- aromatic resonance energy, which influences the confinement or delocalization of the  $\pi$ -electron.
- substituent groups, which affect the electronic state, solubility, molecular stacking, and morphology of the entire material.
- intermolecular or interchain interactions, which alter the aggregation behavior and therefore the photophysical properties.
- oxidation and reduction states, as radical cations or anions influence the energy levels and intramolecular charge transfer.

One solution is to design polymers with larger  $\pi$ -conjugation by increasing chain length and fusing more aromatic rings in the backbone. But these strategies do not show the best results to control the band-gap and energy levels. As a result, two major chemistry design approaches were generated: stabilizing the quinoid resonance structure and taking advantage of donor-acceptor interactions.<sup>119</sup> Now, it has been proved that these two methods are more efficient when combined.

a. Conjugated quinoid type polymers

Generally, conjugated polymers exist under two resonance structures: aromatic and quinoid (Figure 11). When polymers adopt the quinoid structure, aromaticity is lost and there is no more stabilization energy: this structure is energetically less stable but presents a smaller band-gap. Some progress in the stabilization of the quinoid form have been reported by fusing another aromatic ring to the polymer backbone.<sup>120</sup> Indeed, this technique provides a large aromatic resonance stabilization energy and the band-gap is efficiently reduced.



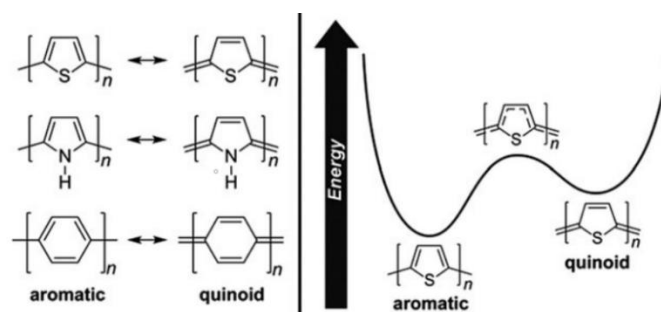


Figure 11: Aromatic vs quinoid resonance structures. Adapted from Rasmussen *et al.*<sup>119</sup>

Kobayashi *et al.* were the first to report the synthesis of a low band-gap poly(isathianaphthene) (PITN) by using the fused-ring approach. Actually, fusing a benzene ring to a thiophene enhanced the quinoidal nature of the polymer backbone and the band-gap reached 1 eV (Figure 12 left side).<sup>121</sup> After this successful synthesis, many low band-gap polymers were developed with the fused ring approach.<sup>122</sup> Liang *et al.* synthesized a polymer called PTB1 and achieved a band-gap of 1.62 eV by fusing thienothiophene (TT) moieties that are now well-known for stabilization of the quinoidal structure (Figure 12 center).<sup>123</sup> More recently, Osaka *et al.* fused two benzothiadiazole (BT) to one naphthobisthiadiazole (NTz) to a low band-gap polymer (PNTz4T) with a band-gap of 1.54 eV (Figure 12 right side).<sup>124</sup>

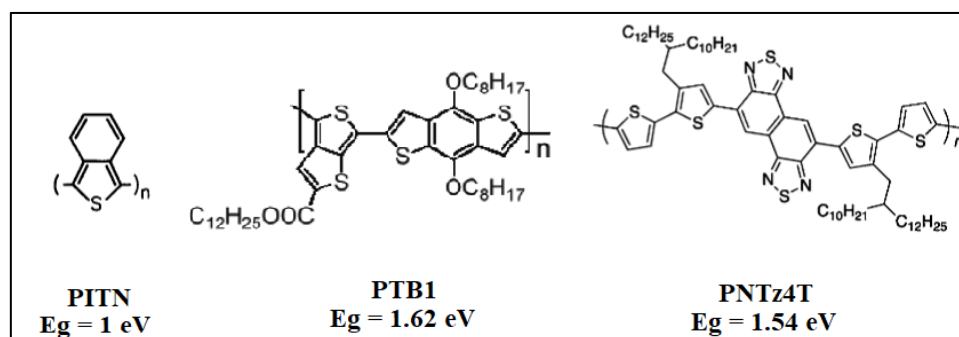


Figure 12: Chemical structures of some fused heterocycle-based low band-gap polymers. Adapted from Kobayashi *et al.*<sup>121</sup>, Liang *et al.*<sup>123</sup>, and Osaka *et al.*<sup>124</sup>

#### b. Donor-acceptor polymers

Another way to fine-tune the band-gap of conjugated polymers is the use of donor-acceptor interactions by alternating electron-donating (D) and electron-withdrawing (A) units on the polymer backbone.<sup>125</sup> This type of polymer is called “D-A” conjugated polymer where the HOMO of the donor segment interacts with the HOMO of the acceptor segment to create two new energy levels (same mechanism is observed for the LUMOs).<sup>126</sup> This mechanism is

called hybridization where a higher HOMO and a lower LUMO are produced, giving a narrower optical band-gap (Figure 13).

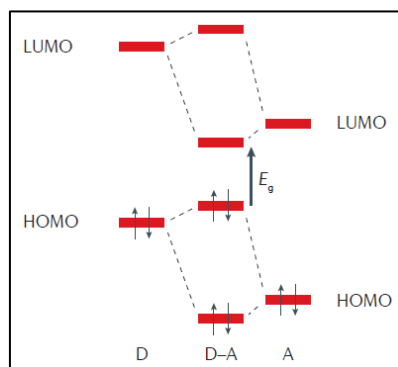


Figure 13: Hybridization of the energy levels of the D-A copolymer. Adapted from Li *et al.*<sup>125</sup>

The decrease in bond length alternation and therefore band-gap is also explained by the existence of two resonance forms that coexist within the polymer backbone ( $D-A \leftrightarrow D^+=A^-$ ).<sup>127</sup>

Havinga *et al.* were the first to report this approach with the synthesis of polysquaraines (PSA) and polycroconaines (PCA) presenting band-gaps of 0.4 eV and 1.15 eV, respectively (Table 5, entries 1 and 2).<sup>128,129</sup> From then on, researchers focused on the choice of donor and acceptor building blocks as they have a critical impact on the enhancement of band-gaps.<sup>130</sup> Among the strong electron-donating units, we found benzodithiophene (BDT), cyclopentadithiophene (CPDT), and dithienosilole (DTS) to only cite a few. On the side of strong electron-withdrawing units, we found benzothiadiazole (BT), diketopyrrolopyrrole (DPP), and diazapentalene (DAP) (Figure 14).

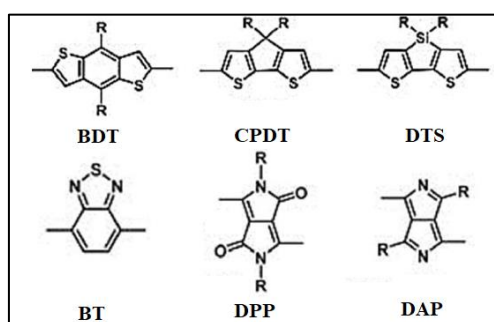
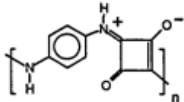
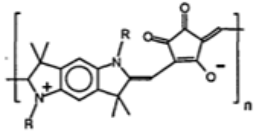
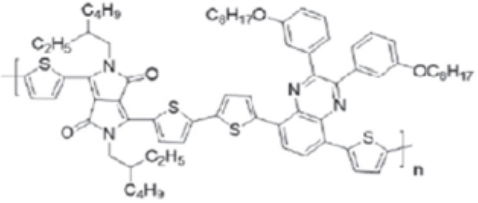
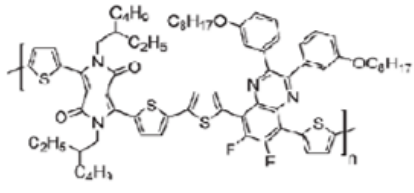
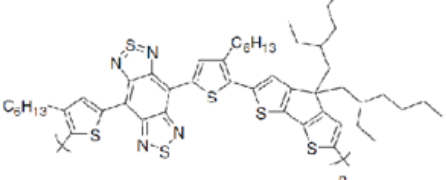


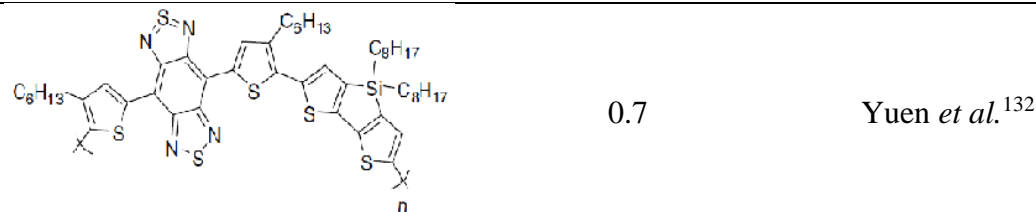
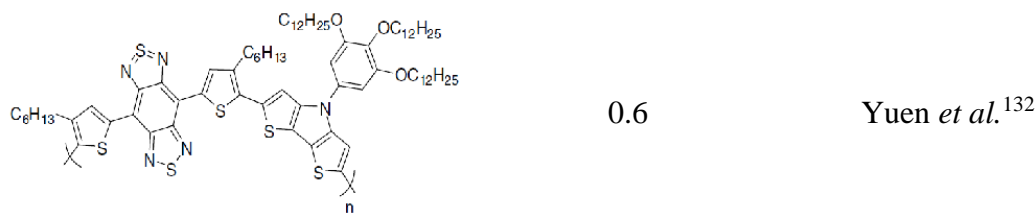
Figure 14: Chemical structures of some strong donor monomers (upper line) and strong acceptor monomers (bottom line).

Among these strong acceptors, the quinoxaline (Qx) is particularly interesting as it presents strong quinoid characteristics. Chochos *et al.* designed D-A<sub>1</sub>-D-A<sub>2</sub> low band-gap polymers containing the DPP unit as first acceptor (A<sub>1</sub>) and varying the second acceptor

monomer ( $A_2$ ) based on Qx units. The resulting materials called DPPBTQ $_x$ BT and DPPBTffQ $_x$ BT containing quinoxaline and difluoroquinoxaline units showed a band-gap of 1.36 eV and 1.39 eV, respectively (Table 5, entries 3 and 4).<sup>131</sup> Another interesting strong acceptor is the benzobisthiadiazole (BBT) which was employed by Yuen *et al.* to synthesize three low band-gap polymers (Table 5, entries 5, 6, and 7).<sup>132</sup> For all the resulting materials, the optical band-gaps are very low, below 0.8 eV. Even though BBT units have the disadvantage to yield inflexible polymers, Yuen *et al.* overcame this problem by adding hexyl side-groups on the polymer backbones.

Table 5: Chemical structures of some donor-acceptor low band-gap polymers. Adapted from Havinga *et al.*<sup>128,129</sup>, Chochos *et al.*<sup>131</sup>, and Yuen *et al.*<sup>132</sup>

Chemical structure	$E_g^{opt}$ (eV)	reference
	0.4	Havinga <i>et al.</i> <sup>128,129</sup>
	1.15	Havinga <i>et al.</i> <sup>128,129</sup>
	1.36	Chochos <i>et al.</i> <sup>131</sup>
	1.39	Chochos <i>et al.</i> <sup>131</sup>
	0.8	Yuen <i>et al.</i> <sup>132</sup>



## 2) Polycondensation

Step-growth or condensation polymerization is the main synthetic route to obtain low band-gap polymers. The basic principle of this kind of polymerization is the reaction of complementary reactive groups borne by difunctional monomers.<sup>133</sup> For instance, diacid and dialcohol monomers react to create a polyester. Monomers can react at any time in consecutive reactions, allowing macromolecules to grow, often followed by the elimination of a small molecule as a by-product (water in the case of the polyesterification).

The first condensation polymer was the Bakelite resins obtained through the condensation of phenol and formaldehyde and discovered by the Belgian chemist, Baekeland, in 1907. Then, Wallace Carothers and his coworkers found the now famous polymers, nylon and polyester, and established the fundamental principles and equations of step-growth polymerization: the so-called Carothers equation.<sup>134</sup>

Step-growth polymerization should not be confused with chain-growth polymerization as they are fundamentally different regarding their mechanisms, the way the molar mass increases as a function of monomer conversion, and their activation energy. In step-growth polymerizations, the reaction is activated by heat without chemical initiator. There is no initiation step as in chain-growth polymerizations. High molar mass chains are only produced at very high conversions, contrary to chain-growth polymerizations.<sup>135</sup>

Among the most important condensation polymers, we can cite polyesters, polycarbonates, polyamides, polyisocyanates, polysiloxanes, polysulfides, and polyether

ketones. Currently, investigations head towards click reactions, olefin metathesis, and multicomponent reactions.<sup>136</sup>

a. Theoretical consideration

Condensation polymers, also known as step-growth polymers, are obtained through a series of steps achieved by successive reactions between difunctional monomers.<sup>137</sup> Step-growth polymerizations involve monomers possessing chemical functions that can constitute covalent bonds with each other. When these functions are present in the same molecule, the monomer is called AB-monomer where A and B represent complementary reactive groups. When these functions are present in two difunctional molecules, the monomers are referred to AA and BB monomers (Figure 15).

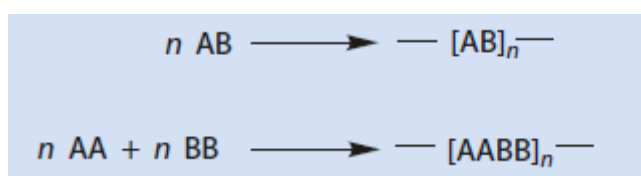


Figure 15: Schematic representation of the step-growth polymerization of AB-monomers and AA/BB monomers. Adapted from Koltzenburg *et al.*<sup>135</sup>

One of the most important factors used to characterize macromolecules is the number-average degree of polymerization obtained by dividing the initial number of reactive functions by the number of reactive functions at time  $t$ . By taking the example of a step-growth reaction involving two different functional groups A and B, the number-average degree of polymerization can be defined as follows:

$$DP_n = \frac{\nu_A^0}{\nu_A} = \frac{\nu_B^0}{\nu_B} \quad \text{Equation 1.3}$$

where  $\nu_A^0$  (or  $\nu_B^0$ ) represents the initial number of A functional groups (or B) and  $\nu_A$  (or  $\nu_B$ ) the number of A functional groups at time  $t$  (or B).

The extent of reaction, the conversion  $p$ , which represents the fraction of reacted functional groups in the reaction mixture is defined as:

$$p = 1 - \frac{\nu_A}{\nu_A^0} \quad \text{Equation 1.4}$$

Thus, the number average degree of polymerization can be written:

$$DP_n = \frac{1}{1-p} \quad \text{Equation 1.5}$$

As  $p$  increases,  $DP_n$  increases but it is very difficult to achieve full conversion (*i.e.*  $p=1$ ) since the monomers should be really pure, no side reaction should occur and the viscosity of the medium has to be limited. These are the reasons why polymers obtained through condensation polymerizations do not usually present very high molar masses (Figure 16).

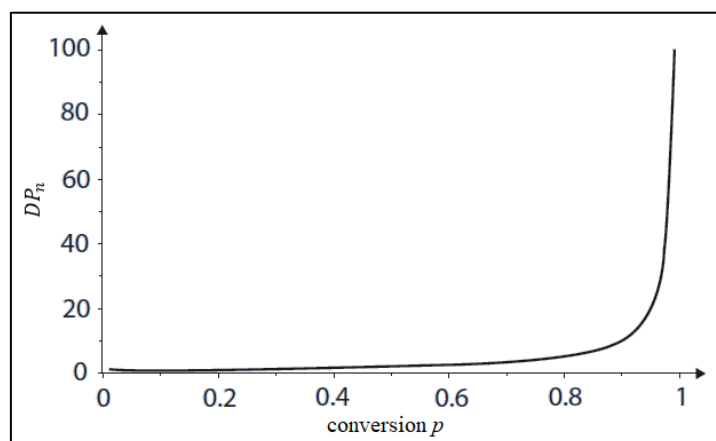


Figure 16: Dependence of the number average degree of polymerization on conversion for a step-growth polymerization. Adapted from Koltzenburg *et al.*<sup>135</sup>

In addition, the weight-average degree of polymerization can be defined as:

$$DP_w = \frac{1+p}{1-p} \quad \text{Equation 1.6}$$

These two characteristics describe, the molar mass dispersity,  $\mathfrak{D}$ , giving an idea of the width of a molar mass distribution, can be introduced as:

$$\mathfrak{D} = \frac{M_w}{M_n} = \frac{DP_w}{DP_n} = 1 + p \quad \text{Equation 1.7}$$

Where  $M_w$  and  $M_n$  stand for the weight-average molar mass and the number-average molar mass, respectively. Typically,  $\mathfrak{D}$  approaches 2 as the extent of reaction  $p$  tends towards 1.

When a condensation polymerization occurs with a stoichiometric imbalance between the numbers of reactive groups A and B, due to either incomplete purification or minor mishandling, the direct consequence is a decrease in the average degree of polymerization. The stoichiometric ratio  $r$ , always less than or equal to 1, is defined by:

$$r = \frac{\nu_A^0}{\nu_B^0} \quad \text{Equation 1.8}$$

From this ratio  $r$ , new relationships are obtained. The total number of chain ends ( $\nu_{ends}$ ) is given by summing the number of unreacted functional groups  $\nu_A$  and  $\nu_B$  after the reaction reaches the extent  $p$  :

$$\nu_{ends} = (1 - p)\nu_A^0 + (1 - pr)\nu_B^0 = \left(1 - p + \frac{1-pr}{r}\right)\nu_A^0 \quad \text{Equation 1.9}$$

As a result, we can define the total number of chains ( $\nu_{chains}$ ) which is half the number of chain ends:

$$\nu_{chains} = \frac{1}{2}\left(1 + \frac{1}{r} - 2p\right)\nu_A^0 \quad \text{Equation 1.10}$$

And the total number of repeat units ( $\nu_{repeat\ units}$ ) corresponding to the number of monomer molecules present initially:

$$\nu_{repeat\ units} = \frac{1}{2}\nu_A^0 + \frac{1}{2}\nu_B^0 = \frac{1}{2}\left(1 + \frac{1}{r}\right)\nu_A^0 \quad \text{Equation 1.11}$$

Finally, all these relationships lead to a new definition of the number-average degree of polymerization by dividing the number of repeat units  $\nu_{repeat\ units}$  by the number of chains  $\nu_{chains}$ :

$$DP_n = \frac{1+1/r}{1+1/r-2p} = \frac{1+r}{1+r-2pr} \quad \text{Equation 1.12}$$

For general polymers, the number-average molar mass  $M_n$  is found by multiplying the molar mass of the repeat unit  $M_0$  by the number-average degree of polymerization  $DP_n$ .<sup>138</sup> In the case of condensation polymers, this calculation requires more reflection and sometimes correction. Indeed, if we consider an AB monomer, the repeat unit is the  $ab$  entity with the elimination of one by-product molecule whereas if we consider the AA and BB monomers, the repeat unit is the  $aabb$  entity with the elimination of two by-product molecules, AA + BB. Hence, the number of  $aa + bb$  entity is twice the number of  $aabb$  entity. From this conclusion, the number average molar mass  $M_n$ , in the case of polymerization of AA and BB monomers, is obtained as follows:

$$M_n = \frac{(M_{AA} + M_{BB}) \times DP_n}{2} = \frac{M_0 \times DP_n}{2} \quad \text{Equation 1.13}$$

where  $DP_n$  is linked with the average molecular weight of the two kinds of monomer units in the structure.

b. Low band-gap polymerization technique

Low band-gap polymers are mainly polymerized by cross-coupling reactions/polycondensations with palladium catalysts.<sup>139</sup> The overall equation of cross-coupling polymerizations is defined in Figure 17, where M-R<sub>1</sub>-M represents a metal-organic AA monomer and X-R<sub>2</sub>-X an organic halide or triflate BB monomer.

These reactions are catalyzed by transition metal complexes, mostly palladium catalysts.<sup>140</sup> They are more stable than nickel catalysts despite having a tendency to break the catalyst/polymer  $\pi$ -complex.

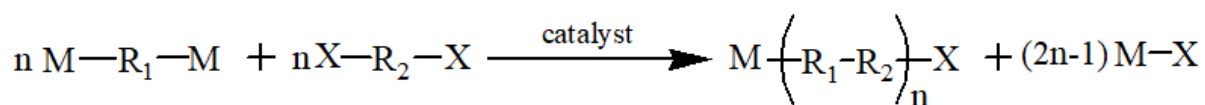


Figure 17: General equation of a cross-coupling polymerization

One of the most employed cross-coupling polycondensation is the Stille polycondensation which consists of the repetition of Stille reactions between two monomers to give a polymer. This coupling reaction involves an organostannane (also called organotin) and an organic electrophile to achieve a new C-C single bond. As it is part of the metal-catalyzed cross-coupling reaction family, like the Suzuki-Miyaura reaction, this reaction requires a palladium catalyst. The first reaction involving these reactants was reported by Eaborn *et al.* in 1976.<sup>141</sup> John K. Stille established the general features and mechanisms of the reaction, giving his name to it in 1978.<sup>142</sup> Today, the Stille reaction is considered as one of the most efficient methods to synthesize organic functional materials. It was only in the early 1980s that the Stille reaction was adapted to synthesize polymers through the polycondensation of di-organotin monomers and dihalide monomers. The first functional polymer synthesized with Stille polycondensation was the poly(phenylene-thiophene) (PPT).<sup>143</sup>



When this polymerization occurs *via* the AA/BB approach (Figure 18), it involves two different monomers: one substituted with two organotin functional groups and the other substituted with two halides or triflate.

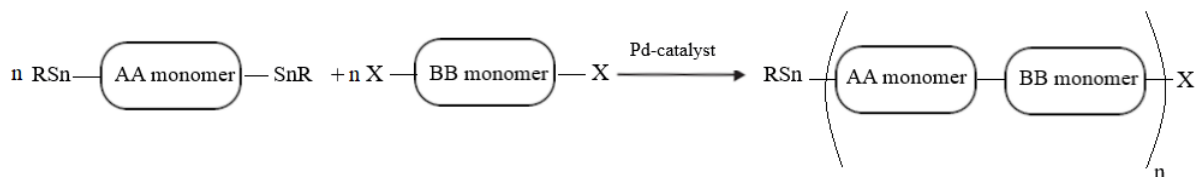


Figure 18: Schematic representation of the AA/BB Stille polycondensation

The catalytic cycle of the Stille reaction given below (Figure 19) is composed of several steps:

- an oxidative addition of organic electrophile  $R^1-X$  to a  $Pd(0)$  complex
- a transmetallation between the  $Pd$  complex and the organostannane  $R^2-SnMe_3$ , which is a slow process to form the intermediate  $R^1-LnPd(II)-R^2$
- a reductive elimination of the final product  $R^1-R^2$  through a *trans-cis* isomerization and the regeneration of the  $Pd(0)$  catalyst

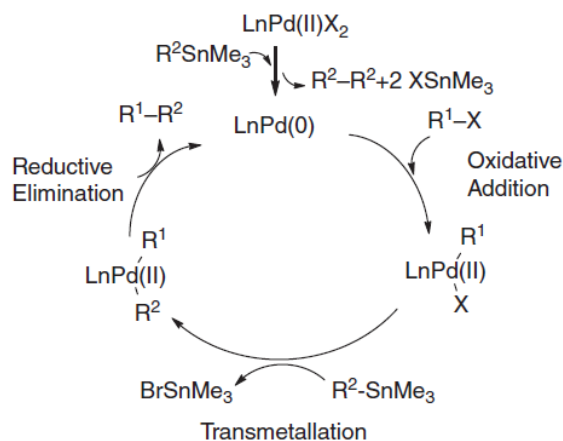


Figure 19 : Stille reaction catalytic cycle. Adapted from Carsten *et al.*<sup>145</sup>

During the first step, the oxidative addition of  $R^1-X$  to  $Pd(0)$  can be performed through a nucleophilic substitution 2 ( $S_N2$ ) for halides with a  $C(sp^3)-X$  or through a three-center transition state between the electrophile  $R^1-X$  and the active  $Pd(0)$  for halides with a  $C(sp^2)-X$ . The latter produces a kinetic product of *cis*- $[Pd(II)RXL_2]$  complex which isomerizes to a more thermodynamically stable *trans*- $[PdRXL_2]$  complex.<sup>144</sup>

The transmetallation step is different in the Stille reaction by analogy with other Pd-catalyzed cross-coupling reactions. Indeed, the organostannane  $R^2-SnMe_3$  reacts with the Pd complex giving a Sn-C bond cleavage and a Pd-C bond formation where the Sn-C bond is not as strong and as polar as other metal-carbon bonds (*e.g.* B-C bond in the Suzuki reaction).

Concerning the choice of the dihalide (or ditriflate), the diiodo monomers are often preferred as they are more reactive. Actually, a strong electron-rich di-organotin favors the transmetallation step and a strong electron-deficient dihalide or ditriflate promotes the oxidative addition. These two features combined facilitate the synthesis of polymers with high molar mass.

The active Pd(0) catalyst used during the first step is formed from a Pd(II) precursor by a reduction through an organostannane before entering the catalytic cycle. The most popular Pd(0) catalysts used for the Stille polycondensation are  $Pd(PPh_3)_4$  and  $Pd_2(dba)_3$ , the latter being more air-stable than the former.<sup>145</sup>  $PPh_3$  is commonly employed as a reducing agent when Pd(II) is used as the Pd source.<sup>146</sup> As in the Suzuki reaction, a combination of Pd catalysts and phosphine ligands is a familiar use to achieve high catalytic performance despite their sensitivity to trace amounts of oxygen and moisture. Recently, bulky phosphine ligands were found to be useful in every step of the catalytic cycle of the Stille reaction.<sup>147</sup>

Generally, Stille polycondensations are performed in common solvents such as benzene, toluene, xylene, THF, DMF, and chloroform ( $CHCl_3$ ). The solvent must be chosen according to its power of solubilisation of the organic reactants, the intermediates, and the growing polymer chain but also according to its power of stabilization of the catalyst. High-boiling solvents are preferred as the polycondensation requires high temperatures to promote the reaction and increase the solubility of the final polymer. Thus, toluene and chlorobenzene are the most common solvent used as they show high-boiling points and low polarities.

Some additives such as inorganic salts can be employed to accelerate the coupling (*e.g.* LiCl), to activate the organostannane (*e.g.* fluoride salts), and to increase the reaction rate (*e.g.* Cu(I) salts).

Unfortunately, some side reactions can occur during the Stille cross-coupling. Actually, if the reagents are not stable against high temperatures, they can decompose and lead to side reactions.<sup>148,149</sup>

The major advantages of the Stille polycondensation are the mild reaction conditions, the various usable functional groups, and the stereo- and regio-selectivities. Even though the organostannane monomer is quite stable against oxygen and moisture, its high neurotoxicity makes it a major drawback.<sup>67</sup> Occasionally, these stannylated products require time-consuming and skilled purifications. Phosphine ligands can cause issues too as they are sensitive to moisture and air, expensive, and toxic. Some responses have been formulated to make the Stille polycondensation greener, including for instance the use of recyclable and less toxic molecular stannanes. Finally, while the Stille polycondensation requires a precise stoichiometric balance, some monomers can be subjected to homocoupling causing defects in the polymer chains.<sup>150–154</sup> A new solution is coming to the surface to reach high molar mass polymers with low dispersities: microwave-assisted polymerizations.<sup>155</sup>

To conclude, in Stille reactions, the optimization of the reaction conditions is a crucial point to achieve high yields (*i.e.* high degrees of polymerization) and controlled dispersities to give high-quality polymers.

### 3) End functionalization in polycondensation

The introduction of functional groups at the beginning and/or at the end of each polymer chain broadens the range of possible applications. The functionalized polymers can, for example, be covalently attached to another polymer or to an inorganic/metal surface permitting the elaboration of new and multifunctional materials.<sup>156</sup> Several methodologies have been developed to functionalize the end of conjugated polymers made through a polycondensation and will be described below.

#### a. Monofunctional end-capper: a one-step strategy

The first methodology is the incorporation of a monofunctional reagent/end-capper in addition to the AA and BB monomers, from the beginning of the polymerization. Because of its monofunctional nature, this molecular end-capper ends the chain extension where it reacts and provides a new functionality (Figure 20). The major advantage of this procedure is its one-step behavior, saving time and materials. Frequently, this functionality at the end of the polymer chain can be chemically modified to complete further reactions (*e.g.* initiation of a second polymer by using the functionality as an initiator) or to be further grafted onto substrates and surfaces. The challenges in the end functionalization are the determination of the end-capping efficiency and the separation of functionalized and non-functionalized polymers.

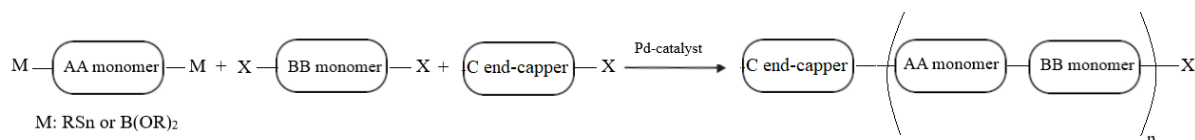


Figure 20: Schematic representation of the end-functionalization through molecular end-capper in Stille/Suzuki polycondensations.

From the theoretical point of view, by taking the example of a step-growth reaction involving two different functional groups A and B and a monofunctional reagent C as end-capper, the stoichiometric ratio  $r$ , presented in II. 2) a., must be redefined as follows:

$$r' = \frac{v_A^0}{v_B^0 + 2v_C^0} \quad \text{Equation 1.14}$$

where the factor 2 relative to the monofunctional reagent C is introduced to show it has the same effect on the  $DP_n$  as a difunctional reagent. Stoichiometric imbalance and/or the use of monofunctional reagents have a strong effect on the number average degree of polymerization  $DP_n$ .<sup>157</sup> Actually, the bigger the stoichiometric imbalance is, the lower average chain-length is.<sup>158</sup>

Schmücker *et al.* employed Suzuki polycondensation to synthesize and end-functionalize a poly(*p*-phenylene) (PPP) polymer by adding an alkoxyamine TIPNO (2,2,5-trimethyl-4-phenyl-3-azahexane-3-nitroxide) bearing a brominated phenyl moiety labelled as pBrStTIPNO in the mixture (Figure 23a). The bi-functional macroinitiator was used to initiate the polymerization of temperature-responsive blocks based on *N*-isopropylacrylamide (NIPAAm) (Figure 21).<sup>159</sup>

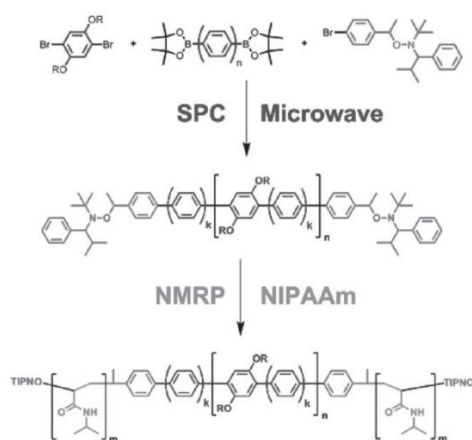


Figure 21: Syntheses scheme for PPP bi-functional macroinitiator and PNIPAAm-*b*-PPP-NIPAAm block copolymers. Adapted from Schmücker *et al.*<sup>159</sup>

Funston *et al.* end-capped a poly(arylene ethynylene) (PAE) with  $\alpha$ -terthiophene ( $T_3$ ) end-groups *via* Sonogashira coupling reaction. They chose to add the aryl iodide functional group in stoichiometric excess by increasing the amount of end-capper (0.1 eq compared to 1 eq for AA and BB monomers) and obtained moderate molar masses (*i.e.*  $M_n = 7200 \text{ g.mol}^{-1}$ ). The final material showed low band-gap characteristics since its cation radical absorption spectrum, obtained *via* pulse radiolysis study, showed two absorption bands a 640 nm and 1350 nm.<sup>160</sup> Dan *et al.* also showed a proper use of one pot synthesis *via* a polycondensation known as Michael addition by mixing a difunctional acrylate and a difunctional thiol with a monofunctional thiol. The final telechelic polymer was properly end-functionalized thanks to a good control of the stoichiometry balance.<sup>161</sup> Harris *et al.* showed one of the best example of this synthetic strategy in the literature. In their paper, they examined the end-capping efficacy by realizing multiple one-pot reactions implying a dibromofluorene monomer (F), a stannylated thienothiophene (TT), and several end-capping reagents such as bromobenzene, 4-bromotoluene, and 4-iodotoluene (Figure 22a). These end-cappers present different reactivity and thus led to different molar masses. They defined and quantified each polymer's end-groups by Matrix Assisted Laser Desorption Ionization Time-of-Flight analyses (MALDI-ToF) (Figure 22b) and it turned out that the polymer functionalized with bromofluorene showed the smallest amount of defects (Figure 23b).<sup>162</sup>

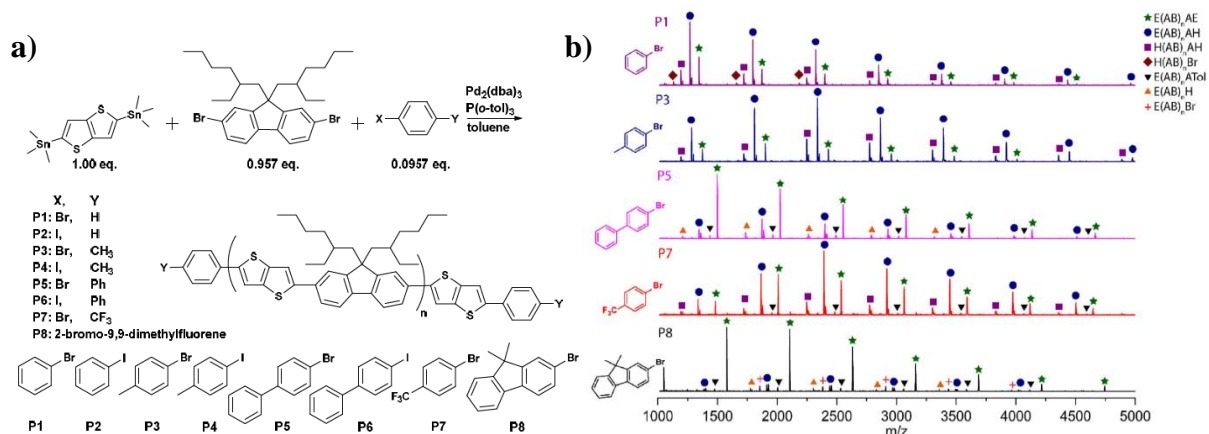


Figure 22: **a)** Syntheses scheme for several polymers with various end-capping reagents. **b)** Representative MALDI-ToF mass spectra of some corresponding end-functionalized polymers. Adapted from Harris *et al.*<sup>162</sup>

Wang *et al.* enhanced the optical properties of a D-A conjugated polymer based on bithiophene (bT) and diketopyrrolopyrrole (DPP) units by end-capping it with quinoxalino[2,3-*b*]porphyrin (QP). They employed a one-step strategy *via* Stille polycondensation and obtained

a bifunctionalized polymer showing an optical band-gap of 1.31 eV with a maximum absorption around 780 nm in thin films (Figure 23c).<sup>163</sup> Robb *et al.* also used a one-step strategy *via* Stille polycondensation to yield an end-functionalized D-A conjugated polymer with perylene diimide (PDI) units. By increasing the amount of bromine function, the final polymer was bifunctionalized and showed an optical band-gap around 1.41 eV (Figure 23d).<sup>164</sup>

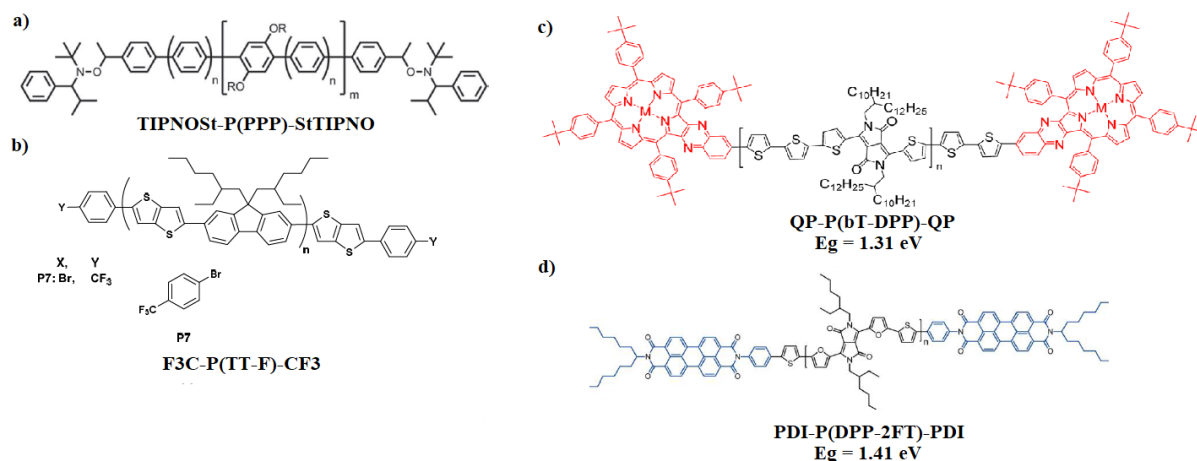


Figure 23: Chemical structures of end-functionalized conjugated polymers *via* the molecular end-capper technique: a)<sup>159</sup> in Suzuki polycondensation b)<sup>162</sup>, c)<sup>163</sup> and d)<sup>164</sup> in Stille polycondensation.

### b. *In situ* termination

In general, the *in situ* method is based on the exploitation of the high reactivity of the propagating species and the controlled nature of the polymerization. The most well-known example of this method is the end-functionalization of polythiophenes through Kumada catalyst-transfer polycondensation (KCTP). This controlled polymerization is based on the combination of thiophene monomer equipped with a Grignard reagent (MgX) and a halogen functionality with the Ni-catalyst initiator.

However, this method can be applied to step-growth polycondensations (Figure 24). The end-capping molecule is introduced in the reaction mixture after the subsequent polymerization to react with the chain ends. This technique is similar to the previously described method in the II. 3) a. section, but it exploits a monofunctional molecule which is introduced at the end of the polymerization step. In general, this method, when applied to step-growth polymerizations, relies on the introduction of one of the AA/BB monomers in slight stoichiometric excess to ensure that all the chains are terminated with the same reactive group (*e.g.* stannylated group). Then, the monofunctional quenching molecule (*e.g.* bromine group) is added to the mixture at

the end of the polymerization. Theoretically, if all the chains are stannyl terminated, all the monofunctional molecule bearing bromine groups will quench both chain ends. The advantage of this method is the highest probability to end-functionalize all the chains. Yet, this method can produce a mixture of end-capped and non-end-capped polymer chains if all the chains are not correctly terminated with stannylated groups, leading to time-consuming purifications. In addition, this technique is not a one-step procedure as the end-capping molecule is added at the end of the polymerization, increasing the chance to pollute the reaction medium.

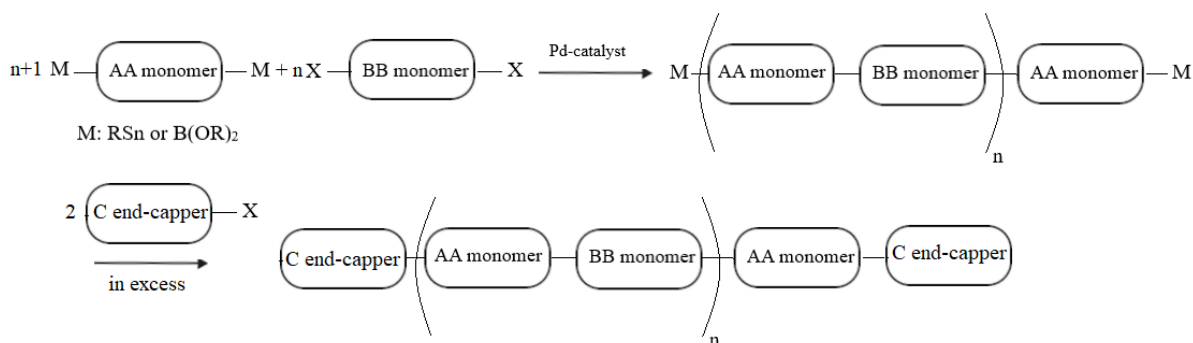


Figure 24: Schematic representation of the *in situ* end-functionalization in Stille/Suzuki polycondensation where the AA monomer is introduced in slight stoichiometric excess

Koldemir *et al.* successfully synthesized an end-capped D-A conjugated polymer based on dithienogermole (DTG) and benzothiadiazole (BT) by playing with stoichiometry and presenting an optical band-gap around 1.4 eV. Actually, they introduced the stannylate monomer DTG in a 1% excess in order to induce a stannylated chain termination due to the stoichiometric imbalance (Figure 27a). Then, they added the 4-iodotoluene end-capper in excess to quench all the stannyl terminations. After MALDI Mass Spectrometry (MALDI-MS) and Nuclear Magnetic Resonance (NMR) analyses, it turned out the exact identity of the chain ends was more complex due to debromination and/or destannylation.<sup>165</sup> Actually, most of the chain ends were monofunctionalized with the toluene (84%) but some chains were bifunctionalized with hydrogen (16%) (Figure 25b).

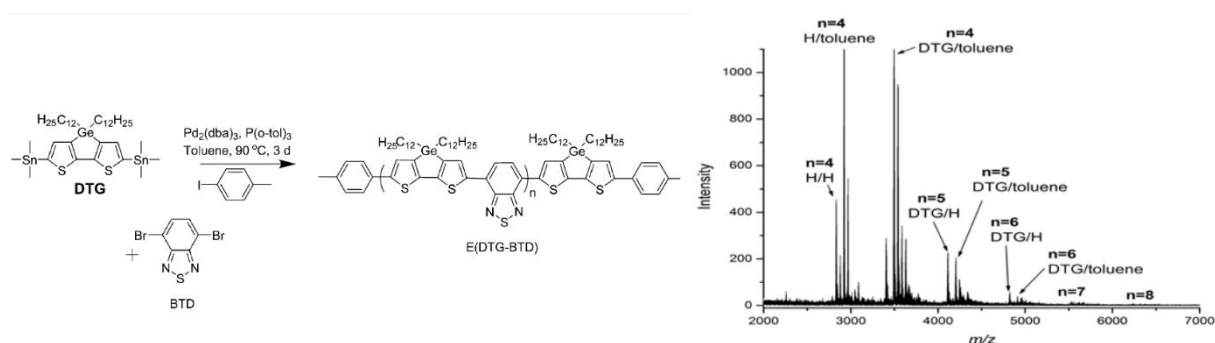


Figure 25: **a)** Synthesis scheme for end-functionalization of P(DTG-BTD) with 4-iodotoluene. **b)** Representative MALDI-ToF mass spectra of the corresponding end-functionalized polymer. Adapted from Koldemir *et al.*<sup>165</sup>

Park *et al.* prepared two end-functionalized D-A conjugated polymers based on bromobenzothiadiazole (BT) *via* microwave-assisted Stille polycondensation. They introduced the stannylate monomer in slight excess in each polymer batch. After polymerization and prior to quenching with methanol, the 2-bromothiophene (T) and the stannylated-thiophene (T) end-cappers were added subsequently in 4 equivalents and 8 equivalents, respectively. In the end, the final polymer P2 showed a moderate molar mass of 30 kg.mol<sup>-1</sup> with an optical band-gap around 1.4 eV (Figure 27b). By comparing with a non-functionalized polymer P1, X-ray photoelectron spectroscopy (XPS) was employed to determine the composition of the polymer P2 by probing peaks due to Sn and Br (Figure 26). Bazan's group concluded to a successful end-functionalization as no Sn and Br peaks were found on the core level XPS spectrum of P2, contrary to the one of the non-functionalized polymer.<sup>166,167</sup>

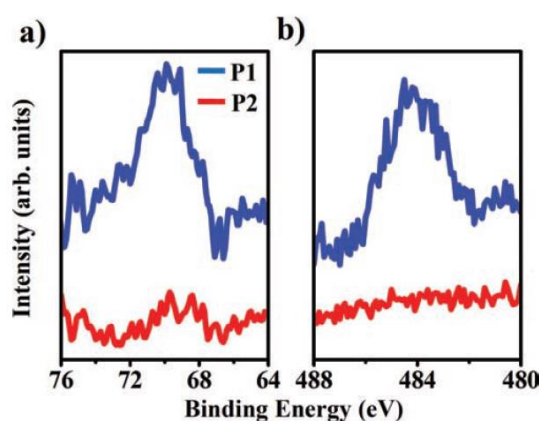


Figure 26: XPS spectra of **a)** Br 3d and **b)** Sn 3d<sub>5/2</sub> for the non-functionalized polymer P1 (blue) and the functionalized polymer P2 (red). Adapted from Park *et al.*<sup>166</sup>



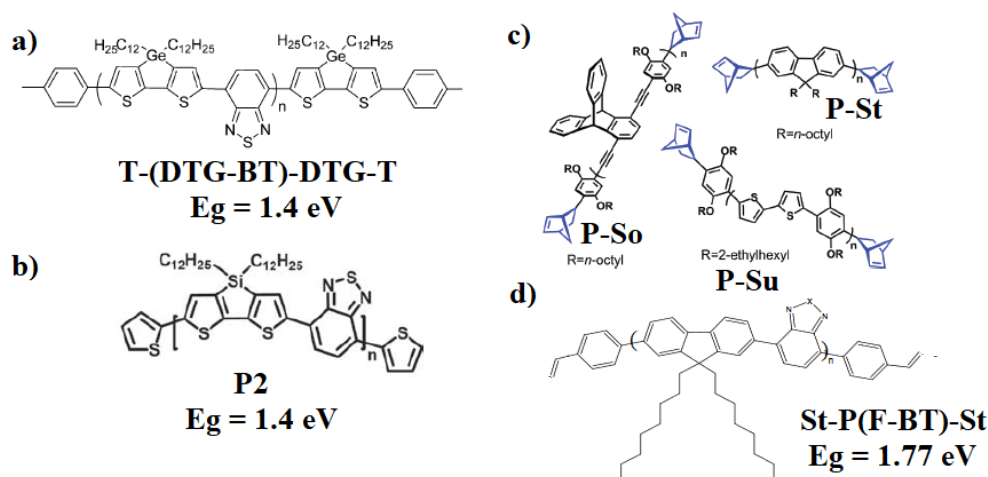


Figure 27: Chemical structures of end-functionalized conjugated polymers *via* the *in situ* termination: **a)**, **b)** in Stille polycondensation<sup>165-167</sup> **c)** in Sonogashira, Stille, Suzuki polycondensations for P-So, P-St, and P-Su, respectively<sup>168</sup> and **d)** in Suzuki polycondensation.<sup>169</sup>

Cox *et al.* also synthesized three D-A conjugated polymers P-St, P-Su, and P-So *via* Stille, Suzuki and Sonogashira polycondensations, respectively (Figure 27c). As for the previous examples cited, they introduced the dihaloarene monomer in slight excess to ensure that the polymer chains were terminated with an aryl halide and then, after polymerization, added the norbornadiene end-capper in the mixture. All of the polycondensations employed in this paper were equally successful as the end-capping procedure was based on hydroarylation reactions of norbornadiene using reductive conditions. Even though the subsequent polymers do not show low band-gap features, they were employed as macroinitiators to build triblock copolymers showing red emission photoluminescence in thin films.<sup>168</sup> Baycan Koyuncu *et al.* showed an excellent example of *in situ* functionalization of low band-gap polymers. Indeed, they synthesized a polymer with an optical band-gap around 1.77 eV based on benzothiadiazole (BT) units and fluorene (F) units *via* Suzuki polycondensation and added vinyl end-groups (4-bromostyrene and 4-vinylphenyl boronic acid) at the end of the reaction (Figure 27d). The presence of the end-groups was determined by using <sup>1</sup>H NMR: vinylic proton resonances were observed. Yet, this method is not completely efficient to assess the end-capping efficiency as it was used on non-purified polymers. Hence, the presence of the vinylic proton could come from 4-bromostyrene and 4-vinylphenyl boronic acid molecules that are not covalently linked to the polymer backbone.<sup>169</sup> More recently, Aivali *et al.* modified the chain ends of a carbazole-based low band-gap polymer made *via* Suzuki polycondensation thanks to the *in situ* method. At the end of the subsequent polymerization, they added 4-vinylphenylboronic acid and

bromobenzene in the mixture to introduce polymerizable double bonds at the end chain of the polymer and phenyl groups at the other end.  $^1\text{H}$  NMR and attenuated total reflectance (ATR) were used to confirm the introduction of the end double bonds after purification of the polymer but no functionalization rate could be calculated.<sup>170</sup>

### c. Post-polymerization modification

In this method, the end-modification of the polymer is performed in a second experimental procedure after the first polymerization and purification. In the general case, this strategy of modification presents several synthetic assets as the choice of the functional group is not as limited as in the two previous strategies. This technique also offers the possibility to select the functionalization on both chain-ends with the same or different end-groups (Figure 28).<sup>171</sup> Protected functional monomers can be polymerized to terminate all the end chains with a specific functionality. After purification, the functional groups are deprotected and modified. The post-polymerization modification can be done under various forms like cross-coupling reactions, Vilsmeier-Haack formylation, gaseous  $\text{CO}_2$  and hydrochloric acid treatments, lithiation, etc.<sup>172</sup>

However, this technique is arduous as the chain ends of a polymer obtained *via* a step-growth polymerization are most of the time quenched with hydrogen atoms after purification. Hence, the reaction of functional groups on deactivated chain ends is inaccessible. That is why very few examples of post-polymerization modification on low band-gap polymers are available in the literature. Most of these examples include catalyst transfer methods adapted to metal catalyzed cross-coupling polymerizations originally exhibiting a step-growth character.<sup>173</sup> Figure 28 represents the ideal case of post-polymerization modifications on step-growth polymers where the end chains are not deactivated and still bear stannyl, borane or halogen end groups.

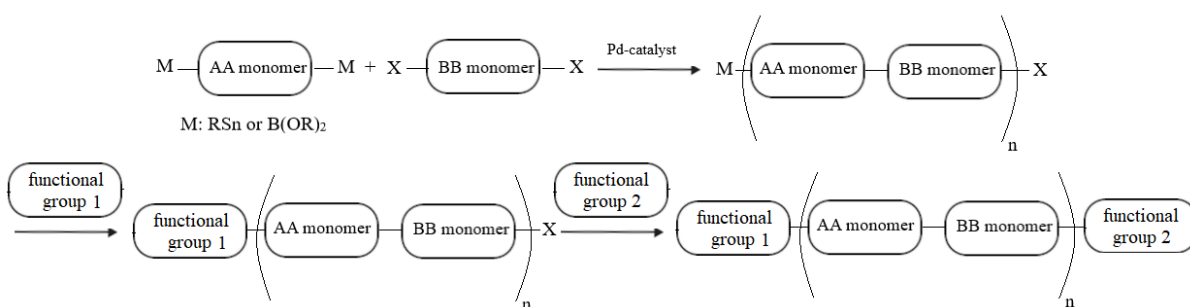


Figure 28: Schematic representation of the post-polymerization modification in Stille/Suzuki polycondensations.

Zang *et al.* synthesized a series of conjugated polymers end-functionalized on both chain ends *via* Suzuki catalyst transfer polycondensation and subsequent post-polymerization modifications (Figure 29). Actually, they designed multiple Pd(0)/*t*-Bu<sub>3</sub>P/*p*-TfOC<sub>6</sub>H<sub>4</sub>X catalytic systems bearing different dormant reactive sites where TfO stands for a triflate and X for an halogen and employed them in the polycondensations. Each resulting polymer bearing this functional triflate was subjected to another Suzuki polycondensation to modify their chain ends by using a 2-phenylaniline-based palladacycle complex. Thus, each triflate functional group was replaced by different arylboronic acids with functional groups such as fluorene, vinyl group, and cyanogen. The nature of chain ends was confirmed by MALDI-ToF analyses and NMR spectroscopy.<sup>174</sup>

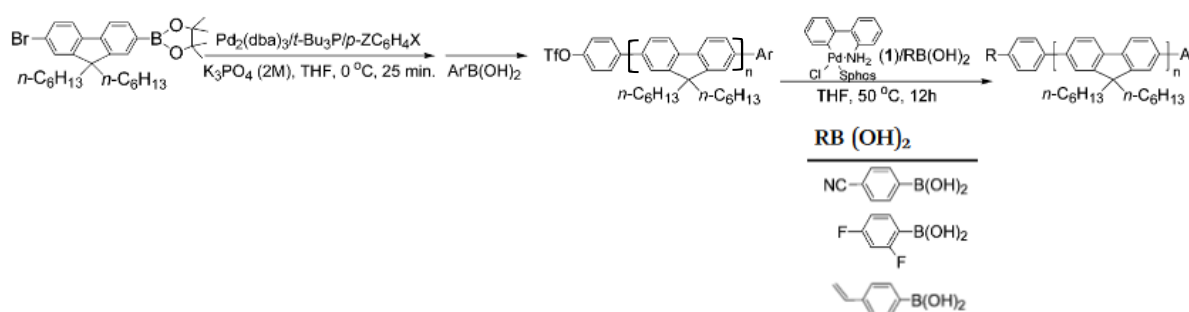


Figure 29: Chemical structures of end-functionalized conjugated polymers *via* post-polymerization modifications. Adapted from Zang *et al.*<sup>174</sup>

To sum up, low band-gap polymers are obtained through polycondensation following the Carothers equation and they can be functionalized at their chain ends. This end-functionalization, achievable *via* different synthetic methodologies, pave the way for new materials with notably hybrid materials.

### III. Hybrid materials involving low band-gap polymers

#### 1) Principle

Generally, a hybrid material is a composite of inorganic and organic compounds. This section will focus on hybrid materials made of conjugated polymers (CPs) and inorganic metals or carbon-based materials, covalently linked together. This kind of material is obtained by grafting CPs onto various kinds of inorganic substrates by means of diverse synthetic strategies and have attracted significant consideration in the past few years.<sup>175</sup> This new field of research

mainly arose to improve the interfaces between the different organic and inorganic layers superimposed in organic electronic devices in order to enhance their performances and lifetimes.<sup>176</sup> Among these interfaces, we can cite the ones between electrodes and the organic semiconductor layers affecting charge injection, charge transport, and charge recombination.<sup>175</sup> Solutions to reduce charge traps and to improve charge mobility are to coat an interlayer or to covalently modify the electrode surface. Indium tin oxide (ITO), a common material used in OLEDs and OPVs, is frequently used to design hybrid materials.

Interfaces between electron donors and acceptors within the bulk heterojunction of solar cells are also of great importance as they can hold a space-charge region where charge transport and charge recombination are inefficient. Incorporating n-type inorganic materials in the active layer as electron acceptors is one solution to increase the mobility creating a pathway for charges. The biggest advantage of inorganic materials is that they show a better stability against oxygen and moisture than organic materials making devices more stable. Among the possible inorganic materials presented in Figure 34, nanocrystals such as CdSe and CdTe are the most popular thanks to two features: they absorb visible light and they can complete the photocurrent. Among the possibilities, metal oxide nanoparticles such as ZnO and TiO<sub>2</sub> are also commonly used due to their morphologies and dimensions making them useful to complement the absorptions in the visible light and to obtain vertical structures which enhance the charge transport. Other inorganic materials can be employed like carbon nanotube (CNT), graphene, and graphene oxide (GO).

However, nanoparticles and nanocrystals present a risk of aggregation which can reduce the efficiency of charge transport leading to limited performance in hybrid-based devices. The formation of aggregates depends on the intimate mixing of active layer components. Hence, the deposition procedure is a crucial step that must be controlled. Moreover, the intimate mixing leans on the type and the area of nanoparticle surfaces. Grafting conjugated polymers onto these nanoparticles is the solution to modify and enhance their surface while improving the intimate mixing by suppressing the aggregation phenomenon.

Finally, hybrid materials including conjugated polymers have found great interest in other applications such as OLEDs, sensors, transistors or photocatalysts (Figure 30). Yet, these applications will not be developed in this literature chapter but readers can find more information in the following reviews.<sup>177–181</sup>

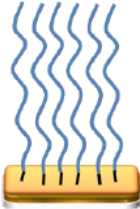
Substrate	Application
 <ul style="list-style-type: none"> <li>• Nanoparticles: Cadmium Selenium (<b>CdSe</b>), Cadmium Tellurium (<b>CdTe</b>), Zinc oxide (<b>ZnO</b>), Titanium oxide (<b>TiO<sub>2</sub></b>)</li> <li>• Indium Tin oxide (<b>ITO</b>)</li> <li>• Carbon materials : carbon nanotube (<b>CNT</b>), graphene, graphene oxide (<b>GO</b>)</li> <li>• Nanoparticles : Gold (<b>Au</b>), Silicon oxide (<b>SiO<sub>2</sub></b>)</li> </ul>	<ul style="list-style-type: none"> <li>• <b>OPV</b></li> <li>- Dye Synthesized Solar cells</li> <li>- Hybrid Solar Cells</li> <li>- Polymer Solar Cells</li> <li>• <b>OLED</b></li> <li>• <b>Sensors</b></li> <li>• <b>Other electronic devices</b></li> </ul>

Figure 30: Substrates grafted with conjugated polymers and their applications<sup>175</sup>

## 2) Grafting methodologies

Polymers can be attached to surfaces and nanoparticles *via* different methodologies: grafting from, grafting through, and grafting onto.<sup>182–184</sup>

### a. Grafting from

The grafting from method consists in the initiation of the polymerization from small initiator molecules covalently bound to the substrate as depicted in Figure 31. Hence, polymer chains grow from the surface thanks to monomers in the surrounding solution leading usually to highly dense polymer brushes.<sup>185</sup> High grafting densities can be reached as the diffusion of the monomer molecules to the growing chain-ends is not obstructed by steric hindrance. As the monomer concentration is not the same in the brush layer, dispersity of the chain lengths can end up large.

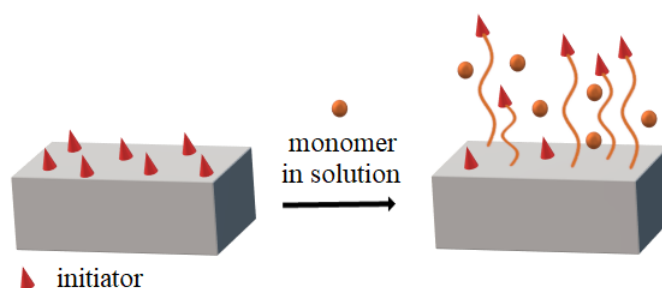


Figure 31: Schematic illustration of the grafting from technique

In this method, the initiator is first anchored to the surface and then the polymerization is executed with propagation and termination steps. Therefore, this methodology applies more in chain-growth polymerization. Yet, in the case of conjugated polymers, made through step-growth polymerizations, surface initiation is a more accurate term since the polymerization can occur in solution or from the surface. For instance, Awada *et al.* successfully initiated a Stille polycondensation from a surface by attaching a palladium-catalyst onto zinc oxide nanorods (NRs) (Figure 32). For the first time, they synthesized and anchored a low band-gap polymer based on dithienosilole (DTS) and benzothiadiazole (BT) units onto inorganic nanoparticles. They obtained a homogeneous organic shell on the NRs showing an optical band-gap of 1.51 eV.<sup>186</sup>

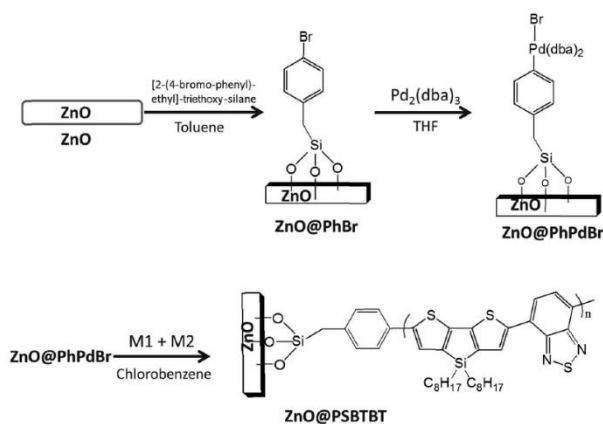


Figure 32: Synthetic methodology for grafting a low band-gap polymer onto zinc oxide nanoparticles *via* surface initiation. Adapted from Awada *et al.*<sup>186</sup>

#### b. Grafting through

The grafting through method is a less popular technique compared to the others. Actually, the working principle is similar to the grafting from method: small functional molecules are covalently attached to the surface. The difference is that these molecules are monomers instead of initiators. Thus, polymer chains do not grow necessarily from the surface as shown in Figure 33. Some initiator molecules are present in the bulk or in the solution, and polymer chains grow from it. Then, the polymer backbone will be anchored to the surface by reacting with the attached monomers. The propagation step can continue thanks to free monomers remaining in the solution. Generally, the grafting through method leads to uncontrolled grafting densities and dispersities. However, the grafting through method can lead to high grafting densities under suitable reaction conditions with, for instance, the supply of monomer directly from the substrate by using a dialysis membrane.<sup>184,185</sup>

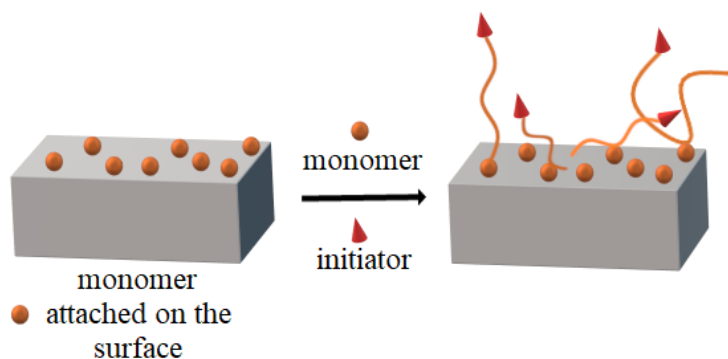


Figure 33: Schematic illustration of the grafting through technique

Despite being less popular than the other grafting methodologies, the grafting through technique brought some polymerizations back into fashion such as the Yamamoto coupling and the Heck coupling polymerizations. However, no example of low band-gap polymers grafted through an inorganic surface *via* Stille or Suzuki polycondensations are reported in the literature.

c. Grafting onto

The first use of the grafting onto method was reported by Mansky *et al.* who studied the grafting of end-functionalized random copolymers of styrene and methylmethacrylate onto silicon substrates.<sup>187</sup> The principle of this method is based on the reaction of reactive groups on the substrate with end-functional polymer chains as seen in Figure 34. Due to steric hindrance, the density of polymer brushes covalently linked to the substrate is rarely high as they form a macromolecular barrier. The limiting factor of this method is the diffusion of the premade chains to the surface.<sup>185</sup> Also, the dispersity can be low as the polymer chains are synthesized in a step prior to the grafting one.

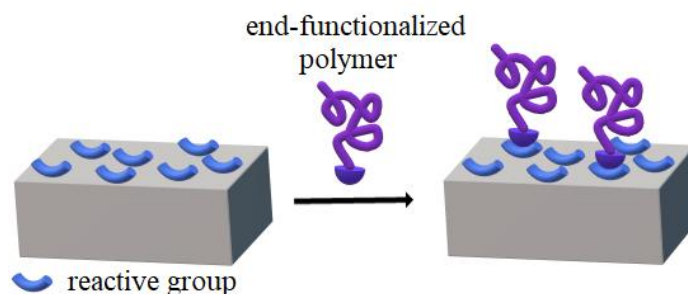


Figure 34: Schematic illustration of the grafting onto technique

This method requires a previously functionalized polymer either at the chain end or on the side chain. As soon as the functional group is properly inserted at the chain end of conjugated polymers, they are capable of reacting with the substrate. Sahu *et al.* synthesized one conjugated monomer and one conjugated polymer based on fluorene (F) with side-chains functionalized with thiol groups. Then, the thiol units were anchored to gold nanorods (NRs) yielding two distinct gold NRs surface-modified with monomer F and polymer PF. Both final materials showed red shifts in their absorption spectra in solution with maxima around 820 and 800 nm, respectively. Moreover, the photoluminescence emission was quenched in the case of the polymer PF as the energy transfers from the polymer backbone to the gold NRs as depicted on the right side of Figure 35.<sup>188,189</sup>

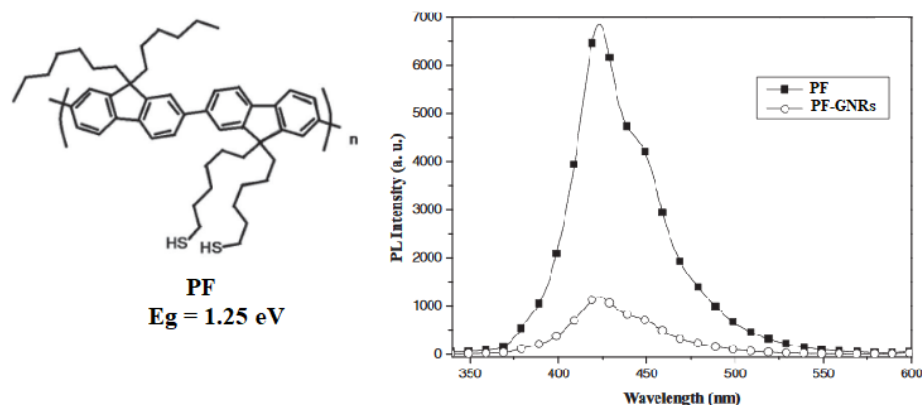


Figure 35: Chemical structure of thiol side-functionalized polyfluorene and its corresponding photoluminescence spectra bare and grafted onto gold nanorods. Adapted from Sahu *et al.*<sup>188</sup>

Compared to the other methodologies, the grafting onto technique appears to be the easiest to apply to hybrid materials involving low band-gap polymers. Indeed, one interesting advantage of this technique is the possibility to purify the end-functionalized polymer before grafting it. Moreover, the polymer can be fully characterized prior to grafting. It is one of the reasons why we employed it to graft low band-gap polymers onto nanoparticles later in this manuscript.

Hybrid materials based on low band-gap polymers are available thanks to the end-functionalization of polymers. However, other interesting materials are achievable thanks to this synthetic methodology such as block copolymers based on low band-gap polymers finding their several applications from photovoltaic devices to stimuli-responsive sensors.



## IV. Block copolymers involving low band-gap polymers

Block copolymers are composed of a linear combination of different monomer units in distinct sections. As morphology and crystallinity of conjugated polymers are determining factors to their optoelectronic properties, the employment of block copolymers based on CPs is of great importance. Block copolymers involving low band-gap polymers can be divided in two sub-parts: rod-rod block copolymers involving two different conjugated blocks and rod-coil block copolymers involving a low band-gap block and a non-conjugated block presenting a coil conformation. Several synthetic routes can be employed to obtain such complex structures with a variety of morphology and applications.<sup>191</sup>

### 1) Synthetic strategies

Depending on the choice of the synthetic approach, the resulting block copolymers can be used in different possible applications. Figure 36 presents the four major synthetic routes to obtain block copolymers: the macroinitiator, the macro end-capper copolymerization, the grafting-to methods, and finally the sequential monomer polymerization.

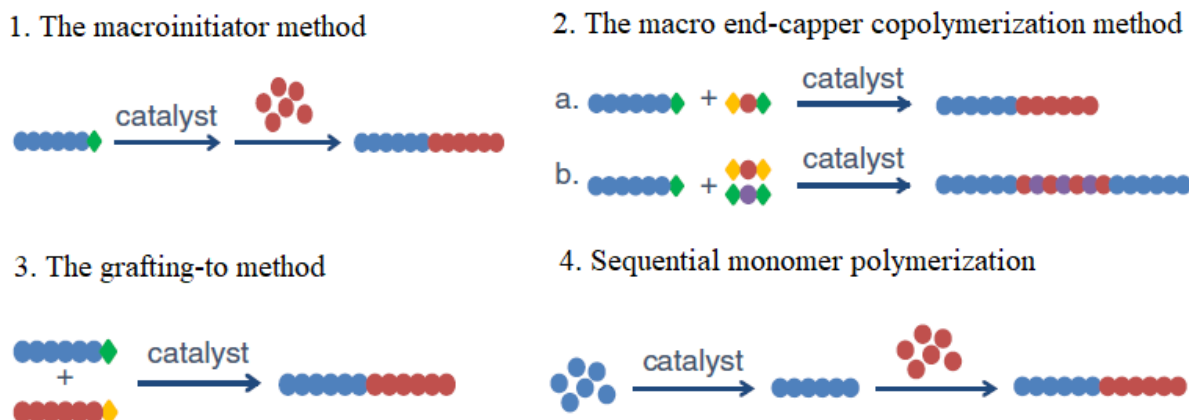


Figure 36: The different synthetic routes to obtain block copolymers. Adapted from Hardeman *et al.*<sup>156</sup>

#### a. The macroinitiator method

Also called the grafting-from method, the macroinitiator method aims to use an end-functionalized polymer as a macroinitiator to polymerize the second monomer (Figure 36. 1.). This method requires several steps, the first one being the elaboration of the macroinitiator. This synthesis can also be done from several postpolymerization reactions to obtain the desired initiator at the chain end.

This method has already led to both rod-rod and rod-coil block copolymers where the conjugated polymer plays the role of the macroinitiator.<sup>192</sup> Generally with rod-rod block copolymers, the macroinitiator bears a phenylbromo end-group which is further used in Pd-catalyzed polymerization<sup>193</sup> or in Kumada catalyst-transfer polycondensation (KCTP) after insertion of a Ni-catalyst in the C-Br chain end<sup>194</sup>. With rod-coil block copolymers, the conjugated macroinitiator typically needs more postpolymerization reactions. These additional steps influence the choice of the polymerization mechanism used for the second block. Quite often, the functional group present at the chain end of the first block is a reversible addition-fragmentation chain-transfer (RAFT) agent, but it is also quite common to find a nitroxide group or an alkyl halide as end-cappers to initiate the second block with a nitroxide-mediated polymerization (NMP) or an atom transfer radical polymerization (ATRP), respectively.<sup>195</sup>

For instance, Van de Wetering *et al.* end-functionalized a dioctylpoly(thienylenevinylene) (DO-PTV) with an aldehyde *via* successive Vilsmeier formylation (Figure 37). The low band-gap polymer, presenting an optical band-gap around 1.6 eV, was then transformed into a macroinitiator *via* a nucleophilic attack of a Grignard reagent, based on the alkoxyamine TIPNO (2,2,5-trimethyl-4-phenyl-3-azahexane-3-nitroxide), to the aldehyde group. The macroinitiator was later used for the copolymerization of the second block composed of a mixture of styrene (S) and chloromethylstyrene (CMS). However, at short polymerization times, the initiation of all polymer chains was incomplete. Finally, the CMS units can be further used to graft electron acceptors thanks to the chlorine functions in order to yield low band-gap donor-acceptor rod-coil block copolymer. Yet, Hadziioannou's group only reported the synthetic methodology without presenting a possible application of the final material.<sup>196,197</sup> This study is one of the few examples of rod-coil block copolymers based on low band-gap polymers made through the macroinitiator method available in the literature.

However, with the macroinitiator method, the biggest challenge is to separate the residual unreacted macroinitiators from the block copolymer. Indeed, the multiple postpolymerization reactions required to install the proper initiator at the chain end of the first block lead to a reduced yield, meaning that all the chains do not bear a functional group. Then, purifying a functionalized macromolecule from its non-functionalized counterpart is a big challenge. Moreover, the separation of the end-functionalized polymers and the macroinitiators is a very challenging step. Although this technique allows to control the polymerization of the second block, the macroinitiator can be subjected to side reactions and degradation phenomenon during the initiation of the second block.<sup>198</sup>

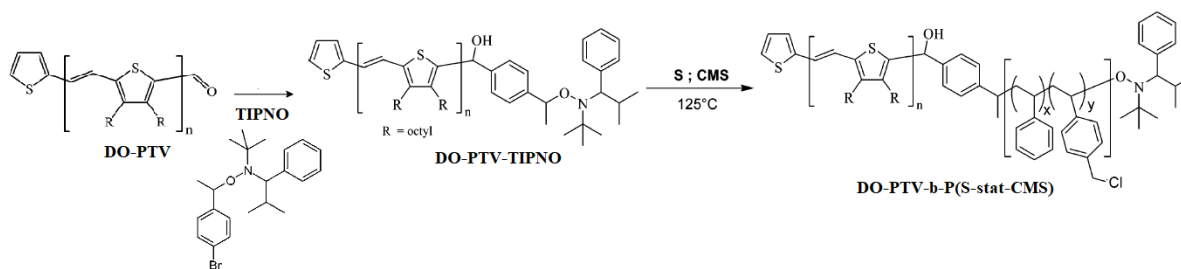


Figure 37: Synthesis of rod-coil block copolymer based on low band-gap polymer *via* the macroinitiator method. Adapted from Van de Wetering *et al.*<sup>196</sup>

#### b. The macro end-capper copolymerization method

In this strategy, an end-functional polymer is added, as a macro end-capper, in the step copolymerization of classical molecular monomers (Figure 36. 2.). This procedure is particularly employed for the synthesis of rod-rod block copolymers. It is important to keep in mind that the ratio of the macro end-capper influences the length of the second block. The functional group present at the chain end of the first block must be chosen according to the mechanism of the subsequent polymerization used for the second block. Within this method, two sub-categories must be distinguished: the one involving AB-type monomers leading only to diblock copolymers and the other involving AA-type and BB-type monomers leading to either diblock or triblock copolymers. Suzuki-Miyaura and Stille cross-coupling reactions were already applied to both categories with success.

For instance, Huang's group employed the macro end-capper copolymerization method to synthesize all-conjugated donor-acceptor block copolymers (Figure 38). They copolymerized mono bromo end-functionalized P3HT of various molar masses with AA and BB type monomers in a one-pot reaction *via* Stille polycondensation. The second block, called PNDIT2 and based on naphthalene-bis-(dicarboximide) (NDcI), shows low band-gap characteristics and the final material presents a band gap of 1.72 eV.<sup>199</sup> After purification by preparative SEC to remove the excess of unreacted P3HT, they yielded a mixture of triblock P3HT-*b*-PNDIT2-*b*-P3HT and diblock P3HT-*b*-PNDIT2. OPV devices made with these materials showed better performances than simple polymer blends. Actually, the block copolymers showed a PCE of 0.55% when annealed at 150°C and the polymer blends only exhibited a PCE of 0.05% with the same annealing conditions.<sup>200</sup> Lin *et al.* found a new tool to avoid residual homopolymer impurities during the preparation of macro end-capper of P3HTs. To reach a high degree of end-functionalization of the P3HT, they added LiCl during the Grignard metathesis polymerization (GRIM) to accelerate Grignard formation. Thus, high

molar mass block copolymers can be produced as a high amount of P3HT chains are end-functionalized and able to initiate the polymerization of the second block.<sup>193</sup>

Nevertheless, the challenge in the macro end-capper copolymerization method rests on the significant amount of homopolymer impurities remaining in the mixture at the end of the synthesis. In the case of macro end-capping, the final yield is significantly decreased probably due to the size of the end-capper and the big challenge is to make sure the polymer is properly functionalized.

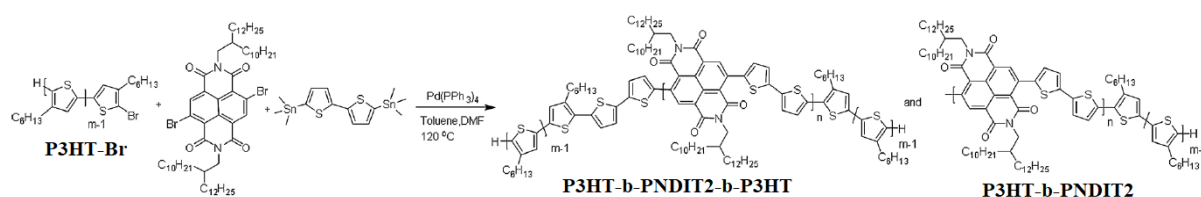


Figure 38: Synthesis of rod-rod block copolymer based on low band-gap polymer *via* the macro end-capper copolymerization method. Adapted from Wang *et al.*<sup>199</sup>

### c. The grafting-to method

Also called the end-functional polymers coupling method, the grafting-to method consists of the covalent combination of two end-functionalized homopolymers through a coupling reaction. This method requires the previous synthesis of the separate blocks both end-functionalized with the appropriate reactive molecule to further accomplish the coupling reaction (Figure 36. 3.). A purification step must be performed to separate the resulting block copolymer and residual parent homopolymers. While this technique allows to control the length of each block separately, it shows a major drawback as the combination efficiency of the coupling reaction between the two homopolymers is frequently low. This disadvantage is more prevalent for high molar masses, but it can be overcome by adding one of the two polymers in excess in the mixture.

As this method is based on the efficiency of the coupling reaction between the two polymers, a proper coupling reaction must be chosen to obtain high-yields and wide tolerance for various functional groups. The copper(I)-catalyzed azide-alkyne cycloaddition (CuAAC) click reaction meets all these criteria to synthesize rod-rod as well as rod-coil block copolymers. This coupling reaction requires both an azide and an acetylene end-functionalized polymers that can be obtained through either functional initiation followed by a deprotection reaction or

*in situ* functionalization. The Pd-catalyzed Suzuki coupling was used as a coupling reaction to obtain block copolymers with both a boronic ester and a halogen end-functionalized homopolymers. Heck coupling reaction and KCTP was also employed to synthesize block copolymers through the grafting-to method.

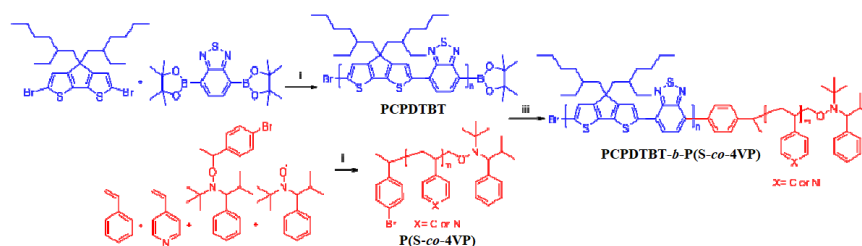


Figure 39: Synthesis of rod-coil block copolymer based on low band-gap polymer *via* the grafting-to method. Adapted from Zappia *et al.*<sup>201,202</sup>

For instance, Zappia *et al.* showed a good application of the grafting-to approach onto a low band-gap rod-coil block copolymer (Figure 39). They prepared separately a rod block PCPDTBT based on the benzothiadiazole unit and a coil block P(S-co-4VP) *via* a Suzuki polycondensation and a NMP, respectively. Each block bears a functional group at their chain end: a borolane end-group for the rod block and a phenyl bromine for the coil block. The latter was prepared *via* the chain-growth NMP of styrene (S) and 4-vinylpyridine (4VP), reported in previous work.<sup>201</sup> The two blocks were coupled *via* Suzuki condensation giving the rod-coil block copolymer. This unique technique, mixing step-growth and chain-growth polymerizations, showed its efficiency and the final material was blended with CdSe nanocrystals to tune the phase separation between the donor material (the rod block) and the acceptor material (the CdSe nanocrystals) in the photovoltaic active layer. Actually, the coil block interacts with the nanocrystals while being covalently bonded with the rod block. Thus, the block copolymer can be used as compatibilizer to enhance the hole transport and the charge extraction for photovoltaic devices.<sup>202</sup>

The grafting-to method brings several challenges in its synthetic pathway. Indeed, after the successful coupling of the two blocks, the residual unreacted homopolymers must be removed either by extraction exploiting the difference of solubility between homopolymers and copolymers or by preparative Size Exclusion Chromatography (SEC). In addition, sometimes the end-functionalization of both homopolymers can be incomplete and may generate low yield of coupling between the two blocks.

## d. Sequential monomer polymerization

The final methodology is a polymerization in two steps, with a sequential monomer addition. In fact, this method consists of the addition of the second monomer just after the complete consumption of the first monomer (Figure 36. 4.). As the polymerization is controlled throughout the whole process, this method leads to controlled molar masses and low dispersities with a high degree of control of the final structure. Generally, the sequential monomer addition is utilized for the synthesis of all-conjugated block copolymers implying KCTP, which is quite the only polymerization mechanism (for conjugated monomers) that follows a chain-growth behavior. This is also the limitation of this technique: the choice of monomer available is reduced as the polymerization mechanism must be the same for the two blocks.

For instance, Todd *et al.* worked on the one-pot synthesis of all-conjugated block copolymer *via* sequential monomer addition containing two rod segments: the poly(5,6-difluorobenzotriazole-*alt*-4-hexylthiophene) (PFBTzHT) block made through KCTP and the P3HT block initiated thanks to the Ni-terminated first block (Figure 40). The final block copolymer shows low band-gap behavior in thin films: bathochromic shifts are observed as the percentage of P3HT increases in the various block copolymer compositions. The major advantage of using controlled synthesis, contrary to conventional synthetic methods, is the obtaining of well-defined donor-acceptor conjugated polymers with narrow dispersities and predictable molar masses.<sup>203</sup>

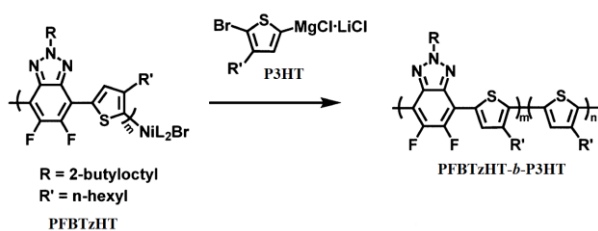


Figure 40: Synthesis of rod-rod block copolymer based on low band-gap polymer *via* the sequential monomer polymerization. Adapted from Todd *et al.*<sup>203</sup>

The sequential monomer addition is the less challenging approach as no purification is needed due to its one-pot character. Nevertheless, as mentioned before, this strategy is limited to chain-growth polymerizations.

## 2) Rod-rod block copolymers

The synthesis of rod-rod block copolymers is the subject of considerable attention since they can be used as donor-acceptor materials in all-polymer solar cells. In optoelectronic devices, it is also well-known that the maximum exciton diffusion length is around 10 nm before the actual charge separation, reinforcing the necessity of control on the nanoscale morphology to enhance device efficiencies.<sup>186</sup> Indeed, the use of block copolymers increases the donor-acceptor interface and promotes the exciton dissociation into free charge carriers. Compared to blends, all-conjugated block copolymers show self-assembly properties in thin films where the less soluble block aggregates first and the second block influences the nanoscale domain size of these aggregates. The nature and size of each block have an importance on the self-assembly behavior. Moreover, the donor-acceptor structure of these block copolymers can provide a broad light absorption to the visible-NIR region with the complementarity of the block absorption. Covalently linked donor and acceptor units enhance the control of the mesoscale assembly and interfacial structure. Single-component bulk heterojunction in OPVs are thermodynamically stable with tunable domain sizes improving the exciton dissociation and the charge extraction.<sup>205</sup> However, studies on fully conjugated D-A block copolymers involving a low band-gap block are rare in the literature as their synthesis remains challenging. As seen previously, rod-rod block copolymers can be done *via* different synthetic methodologies.

Concerning the macroinitiator method, only few examples of rod-rod block copolymers, involving at least one low band-gap block, synthesized through this technique were found in the literature. For instance, Wang *et al.* reported the synthesis of all-conjugated D-A-D triblock copolymers *via* this method. They synthesized a poly(*N,N'*-bis(2-decyltetradecyl)-1,4,5,8-naphthalene diimide-*co*-thiophene) (PNDITh-Br<sub>2</sub>) presenting bromine end-groups *via* a Stille polycondensation and showing a band gap of 1.5 eV. The chain ends were obtained by controlling the molar ratio in order to have the brominated monomer in slight excess compared to the stannylated one. Then, they used this polymer as a macroinitiator to initiate the KCTP of the second block composed of P3HT in presence of a Ni-catalyst. As the macroinitiator presents bromine functionality at each chain end, the resulting material is a triblock copolymer (Figure 41). The efficiency of the second polymerization was proved by SEC: the triblock shows an increase in  $M_n$  and a decrease of  $\bar{D}$  compared to the macroinitiator. Low dispersity (1.15) is the result of living nature of the KCTP process. As Higashihara's group focused on the synthetic methodology, they did not use the final material to fabricate OPV devices.<sup>206,207</sup>

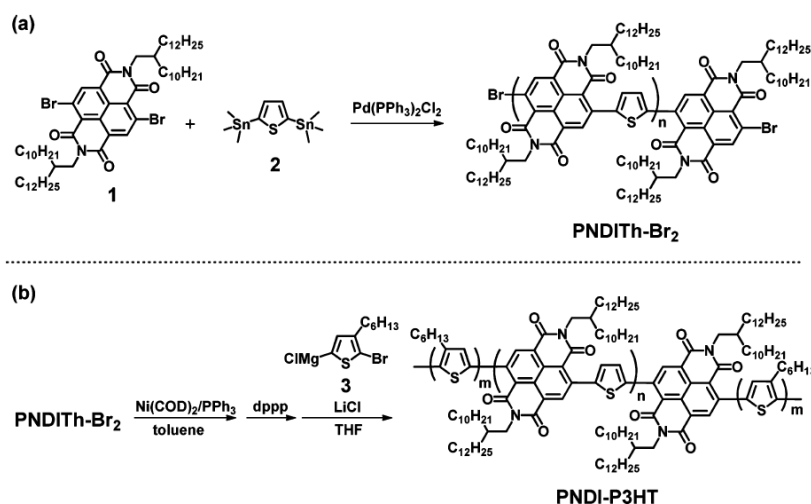


Figure 41: Synthetic routes for PNDIth-Br<sub>2</sub> (a), and all-conjugated ABA-type triblock copolymer *via* KCTP (b). Adapted from Wang *et al.*<sup>206,207</sup>

On the contrary, several examples of this kind of material made through the macro end-capper copolymerization method were reported. For instance, Nakabayashi *et al.* employed this method to yield a fully conjugated donor-acceptor triblock copolymer composed of P3HT block as donor and poly(naphthalene bisimide) (PNBI) block as acceptor segment, labelled as P3HT-PNBI-P3HT (Figure 42). First, P3HT blocks were synthesized *via* quasi-living Grignard metathesis polymerization and end-functionalized with bromine end-groups. Then, a Yamamoto coupling polymerization of the PNBI was performed by using the P3HT blocks as macro end-capper. The final triblock and impurities (coupled-P3HT, P3HT and PNBI homopolymers, P3HT-PNBI diblock copolymers) were separated by Soxhlet extraction with proper solvents. Thin films of the triblock copolymer show a low band-gap around 1.46 eV without thermal annealing and a lower band-gap around 1.39 eV when annealed 30 min at 200°C. After confirmation of the HOMO/LUMO levels by cyclic voltammetry (CV), the triblock copolymer was used as acceptor material in all-polymer solar cells by blending it with P3HT as donor material. The device showed a PCE of 1.28% when annealed at 200°C demonstrating the efficient use of PNBI as non-fullerene acceptor in all-polymer solar cells.<sup>208</sup>



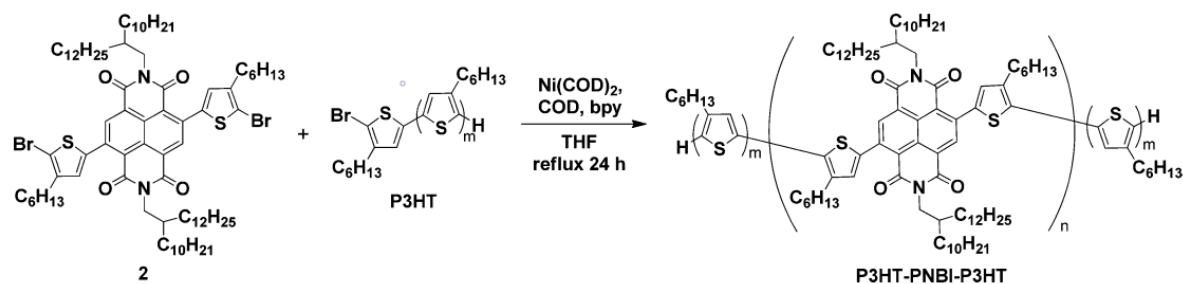


Figure 42: Synthetic route for P3HT-PNBI-P3HT fully conjugated donor-acceptor triblock copolymer. Adapted from Nakabayashi *et al.*<sup>208</sup>

Park *et al.* also used this technique to fabricate all-polymer solar cells by combining two different rigid blocks. This allows the block copolymer to absorb in a wide range within 300 and 800 nm. Actually, they synthesized a PBDT2T-*b*-N2200 rod-rod block copolymer fully conjugated with only step-growth polymerizations. The poly{[*N,N'*-bis(2-octyldodecyl)-naphthalene-1,4,5,8-bis(dicarboximide)-2,6-diyl]-*alt*-5,5'-(2,2'-bithiophene)} N2200 block, synthesized *via* Stille polycondensation, plays the role of the macro end-capper and two other monomers (benzodithiophene (BDT) and bithiophene carboxylate (2T)) were added to the mixture to polymerize the second block through a Stille polycondensation. The PBDT2T donor block has a wide band-gap (1.98 eV) and the N2200 acceptor block a narrow band-gap (1.47 eV). Hence, the final block copolymer presents an optical band-gap of 1.48 eV mostly thanks to the presence of the N2200 block. Furthermore, this highly crystalline D-A block copolymer shows a good solubility in nonhalogenated solvents. Thus, the final material was dissolved in toluene to make polymer solar cells showing a PCE of 6.43%, which is more than 2 times higher than that made with blended materials. The charge-carrier mobility was also measured and the block copolymer-based devices showed a good balance between hole and electron mobilities, reducing the bimolecular recombination and increasing the  $J_{SC}$  and FF values.<sup>209</sup>

Huang's group exploited a different technique, contrary to the previous examples, to purify the byproducts: preparative SEC. However, this method was not as effective as the Soxhlet extraction and they achieved a mixture of triblock and diblock. In their study, they employed the macro end-capper polymerization method in a one-pot reaction by Stille polycondensation with the synthesis of a fully conjugated D-A block copolymers P3HT-*b*-PBIT2 containing pyrene bisimide (PBI) and bithiophene (2T) (Figure 43). The final material exhibits low band-gap properties even though its band-gap reaches barely 1.6 eV. All-polymer solar cells were fabricated by using the block copolymer as single-component active layer and the final devices showed better PCE when thermally annealed (1% instead of 0.06% as-spun).

As Park *et al.*, they measured the hole and electron mobilities to study the charge transport properties of the devices and they obtained fair-enough balanced characteristics.<sup>210</sup>

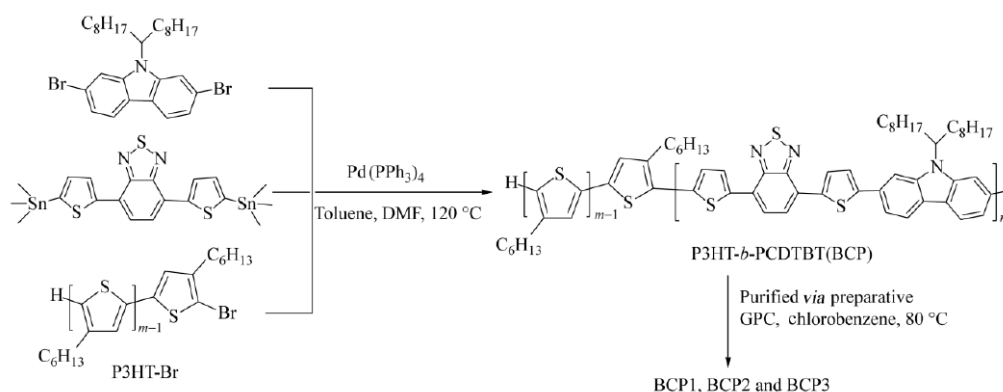


Figure 43: Synthetic route for fully conjugated D-A block copolymers P3HT-*b*-PBIT2. Adapted from Wang *et al.*<sup>210</sup>

Instead of using all-conjugated block copolymer in the active layer, Huang's group employed it as a compatibilizer in the active layer of polymer/fullerene BHJ solar cells. They reach a maximum PCE of 3.64%. Actually, they used poly(carbazole-*alt*-benzothiadiazole) (PCDTBT) ( $E_g^{\text{opt}} = 1.8 \text{ eV}$ ) to yield a D-A type fully conjugated block copolymer. An end-functional P3HT was exploited as a macro end-capper to copolymerize the block copolymer by Stille polycondensation in a one-pot reaction (Figure 47). Originally, the PCDTBT homopolymer has poor solubility in halogenated solvents but the introduction of P3HT into the backbone significantly improved the solubility. Unreacted free P3HT as well as PCDTBT homopolymer and oligomers were removed by Soxhlet extraction. The final material exhibits both of the P3HT and PCDTBT absorption features with an optical band-gap of 1.78 eV.<sup>211</sup> Aivali *et al.* also employed the PCDTBT to yield fully conjugated block copolymer as additives in the active layer but with a slight change in the synthetic methodology. In fact, they adapted the macro end-capper copolymerization method to a macromonomer. They used vinyl-functional oligomers of PCDTBT as macromonomers in a free radical polymerization (FRP) with 6-vinylphenyl-(2-pyridinyl)-4-phenyl-quinoline (vinyl-QPy) monomers.<sup>170</sup> The macromonomer PCDTBT presents a narrow band-gap (1.8 eV) and the block copolymers obtained by using azobisisobutyronitrile (AIBN) as the initiator were used as additives in mixtures of PCDTBT and PC<sub>71</sub>BM for active layers of OPVs.

Contrary to the previous examples, the work of Lee *et al.* was one of the rare studies to employ Suzuki-Miyaura polycondensation to provide fully conjugated rod-rod block

copolymers. The first block, based on benzothiadiazole (BT), was grown *via* this polymerization technique by mixing two AA and BB monomers with the second block P[3HT-*r*-3OT] playing the role of the macro end-capper. The efficiency of the chain extension was proved by shifts in the chromatogram toward higher molar mass (Figure 44. 1.). As seen in the previous examples, they fabricated solar cell devices by using the block copolymers as single-component active layers showing narrow band-gap characteristics (1.8 eV).<sup>212</sup> They reached a 2.6% PCE but with constant FF and  $V_{OC}$  due to bad contacts across all devices. Thus, the microphase separation is an important parameter to increase the short-circuit current.<sup>213</sup>

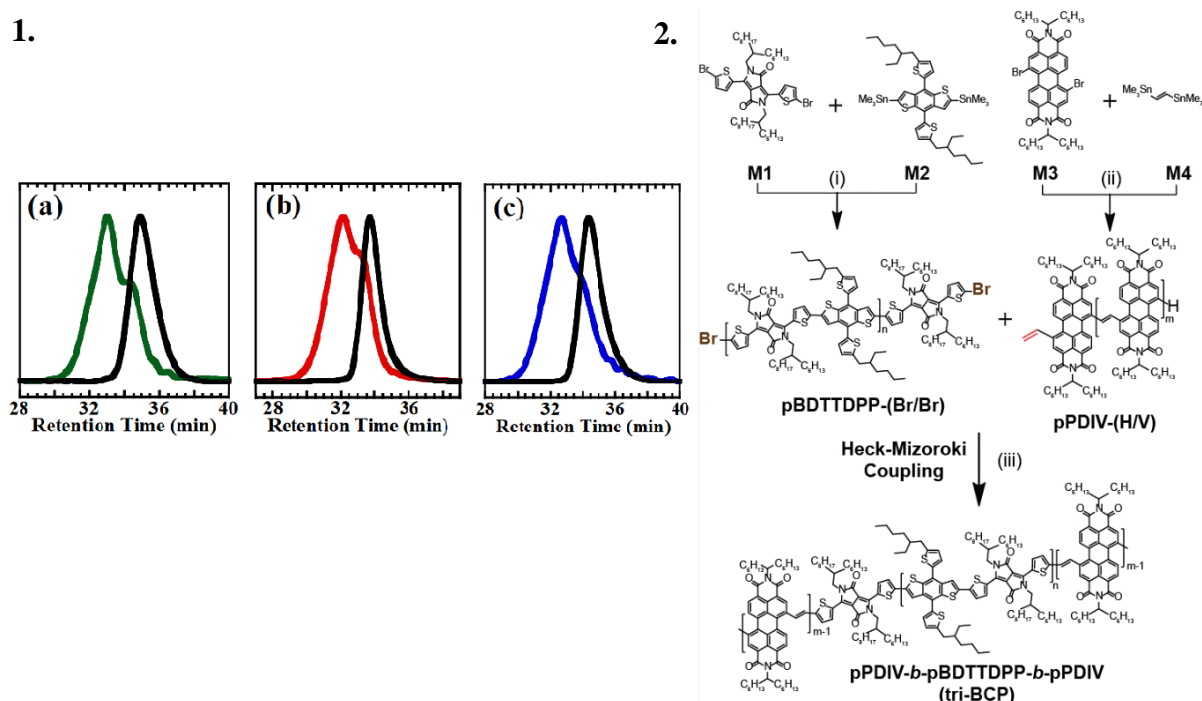


Figure 44: **1.** SEC chromatograms of P[3HT-*r*-3OT]-*b*-PFTBT block copolymers overlaid with P[3HT-*r*-3OT] macro end-capper (black). Adapter from Lee *et al.*<sup>213</sup> **2.** Synthetic route for fully conjugated D-A block copolymers pPDIV-*b*-pBDTTDPP-*b*-pPDIV. Adapted from Rahmanudin *et al.*<sup>214</sup>

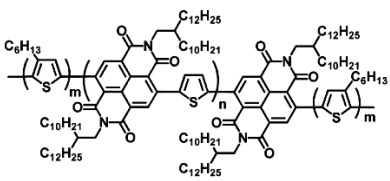
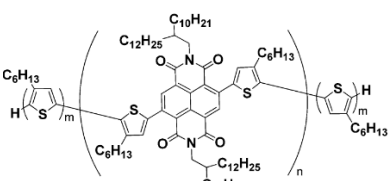
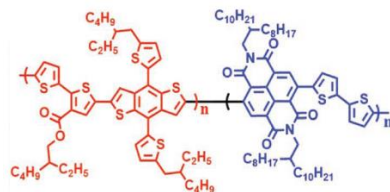
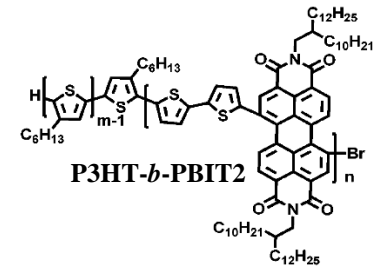
As seen above, the macro end-capper copolymerization method is a successful pathway and the most preferred route. Nevertheless, the grafting-to method has also been applied to obtain fully-conjugated rod-rod block copolymers involving low band-gap polymers. Rahmanudin *et al.* used this methodology to prepare fully conjugated triblock copolymers. Their synthetic strategy is focused on the synthesis of parent polymers based on diketopyrrolopyrrole (DPP) and perylenediimide (PDI) monomers through Stille polycondensation bearing either a vinyl or a bromine functions at the chain end (Figure 44. 2.). The vinyl function was introduced at the chain end of the first block labelled pPDIV by using

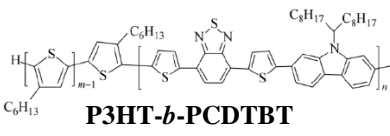
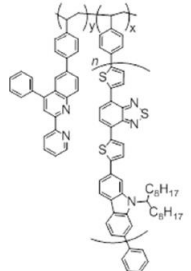
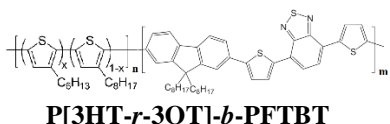
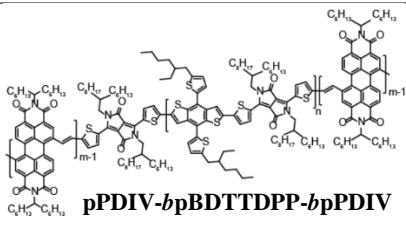
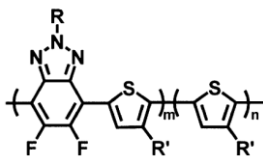
in slight excess the 1,2-bis(trimethylstannyl)ethene monomer. The bromine function was introduced at the chain end of the second block labelled pBDTTDPP with the same procedure by adding in excess the brominated DPP monomer. The presence of the end-groups was confirmed thanks to MALDI-ToF mass spectrometry analysis. However, both polymers presented low degrees of polymerization, which could be seen as a drawback. Yet, by using oligomers as coupling molecules, they have succeeded to increase the coupling yield as their solubility is better than polymers. Then, the corresponding low band-gap conjugated polymers pBDTTDPP (donor) and pPDIV (acceptor) were coupled *via* the Heck-Mizoroki coupling resulting in a triblock copolymer with a minor amount of unreacted macromonomers after purification by preparative SEC. Nevertheless, the comparison of polymers and purified triblock chromatograms showed an overlap of the molar mass distribution suggesting the presence of a minor amount of unreacted polymers. The final material was integrated in a single-component bulk heterojunction OPV device and shows a maximum absorbance at 600 nm in thin films with a band-gap around 1.37 eV and a PCE of 1.51%.<sup>214</sup>

Concerning sequential monomer polymerization, no further examples of rod-rod block copolymers involving a low band-gap block were found in the literature, except the work of Todd *et al.* detailed in the Section IV.1) d.

Even though all of the polymers presented above show narrow or low band-gap characteristics, none of them exhibited a maximum absorbance in the NIR region.

Table 6: Summary of the rod-rod block copolymers involving a low band-gap polymer reported in the literature: <sup>a</sup> determined by SEC; <sup>b</sup> optical band-gap of the block copolymer in thin films <sup>c</sup> optical band-gap of the low band-gap block

Chemical structure	Synthetic strategy	Mn <sup>a</sup> (kDa)	Đ	Eg <sup>opt,b</sup> (eV)	Application	Ref.
 <p><b>P3HT-<i>b</i>-PNDIth-<i>b</i>-P3HT</b></p>	Macroinitiator method	26.4	1.15			Wang <i>et al.</i> <sup>206,207</sup>
		27.0	1.20	1.5 <sup>c</sup>	-	
		33.7	1.29			
 <p><b>P3HT-<i>b</i>-PNBI-<i>b</i>-P3HT</b></p>	Macro end-capper copolymerization method	21.8	1.28	1.48	all-polymer solar cells	Nakabayashi <i>et al.</i> <sup>208</sup>
		26.0	1.60	1.39	max PCE: 1.28%	
 <p><b>PBdT2T-<i>b</i>-N2200</b></p>	Macro end-capper copolymerization method	33.3	3.21	1.48	all-polymer solar cells	Park <i>et al.</i> <sup>209</sup>
					max PCE: 6.43%	
 <p><b>P3HT-<i>b</i>-PBIT2</b></p>	Macro end-capper copolymerization method	25.2	1.23	1.63		Wang <i>et al.</i> <sup>210</sup>
		15.4	1.30	1.61		
		11.0	1.44	1.61	all-polymer solar cells max	
		28.3	1.17	1.83	PCE: 1%	
		15.0	1.45	1.61		
		12.3	1.54	1.61		

 <p><b>P3HT-<i>b</i>-PCDTBT</b></p>	Macro end-capper copolymerization method	49.9	1.30	1.78	additives in OPVs max PCE: 3.64%	Wang <i>et al.</i> <sup>211</sup>	
		33.4	1.28	1.80			
		24.8	1.25	1.86			
 <p><b>PCDTBT-<i>b</i>-PQPy</b></p>	Macromonomer copolymerization method	3.5	1.14	1.8 <sup>c</sup>	additives in OPVs	Aivali <i>et al.</i> <sup>170</sup>	
		5.7	1.16				
 <p><b>P[3HT-<i>r</i>-3OT]-<i>b</i>-PFTBT</b></p>	Macro end-capper copolymerization method	7.8	1.30	1.8 <sup>c</sup>	all-polymer solar cells max PCE: 2.6%	Lee <i>et al.</i> <sup>213</sup>	
		9.8	1.30				
		8.6	1.39				
 <p><b>pPDIV-<i>b</i>pBDTTPDPP-<i>b</i>pPDIV</b></p>	Grafting-to method	16.9	1.51	1.37	all-polymer solar cells max PCE: 1.51%	Rahmanudin <i>et al.</i> <sup>214</sup>	
 <p><b>PFBTzHT-<i>b</i>-P3HT</b></p>	Sequential monomer polymerization	18.1	1.24	-		Todd <i>et al.</i> <sup>203</sup>	
		12.1	1.31				1.8
		11.1	1.62				

## 3) Rod-coil block copolymers

Rod-coil block copolymers based on conjugated polymers were initially made to induce a higher solubility and a nanophase morphology. Indeed, conjugated polymers show relatively high stiffness and low solubility due to aggregation phenomenon caused by interchain  $\pi$ - $\pi$  orbital interactions.<sup>215</sup> Hence, the covalent linking of a coil block influences the organization of rod conjugated polymers and limits the aggregation phenomenon. As the coil and rod blocks tend to minimize their contact surface, they aggregate into domains that can be organized in several morphologies in bulk or in solution. They cannot separate at a macroscopic scale, contrary to simple blends, and the size of their self-organized domains has the same order of magnitude as the length of each block. The nanoscale morphologies (*e.g.* lamellar, spherical, cylindrical, vesicular, nanofiber, or microporous structures) are also influenced by the rod:coil ratio and the lengths of each block.<sup>216</sup> The microphase morphology depends on the volume fraction  $\chi$  of each block but also on the Maier-Saupe constant  $\omega$  giving an information on the rod-rod steric repulsion.<sup>217</sup> If the volume fraction of non-conjugated coil block increases, the conjugation length is reduced and the  $\pi$ -stacking can be lost resulting in a blue shift on the absorption spectrum.<sup>219,220</sup> The morphology is also affected by the choice of solvent, solution concentration, and substrate.<sup>216,221</sup>

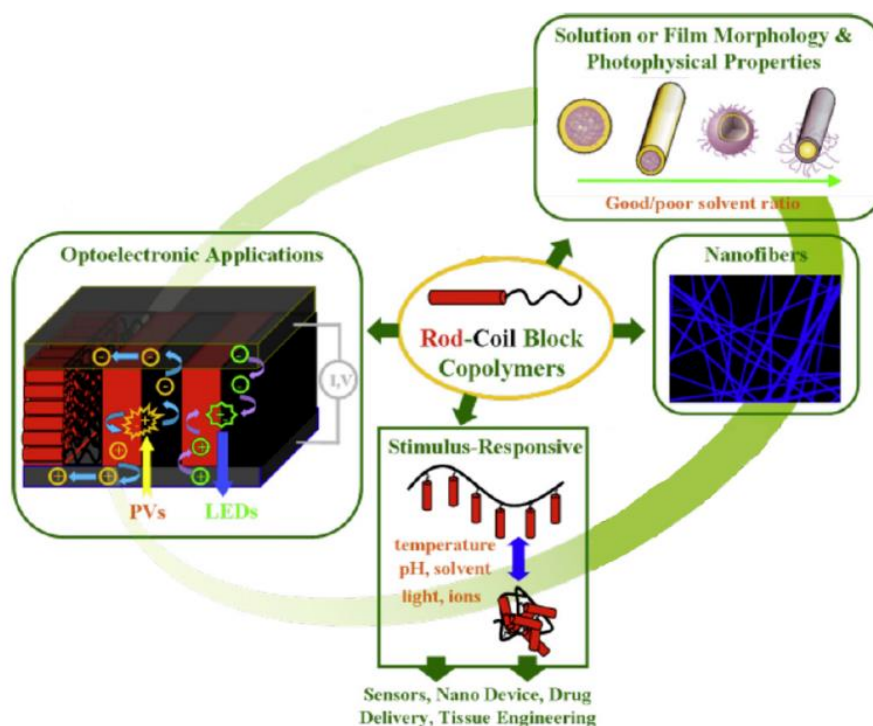


Figure 45: Morphology and applications of conjugated rod-coil block copolymers. Adapted from Liu *et al.*<sup>216</sup>

In photovoltaic applications, the charge separation can be improved by the use of rod-coil block copolymers as the typical size of their domains is in the same order as the maximum exciton diffusion length. Besides the size of the domains, the way the polymers aggregate and align themselves in three dimensions is particularly important to control the electronic and optoelectronic properties of the final material. The combination of the self-assembly properties with the functionality of the rod segments produce specific morphologies for optoelectronic applications such as OLEDs<sup>222</sup> and OFETs<sup>223</sup>. The incorporation of a coil block can enhance the energy transfer phenomenon and the spectral stability of the devices. Also, the use of a stimuli-responsive coil segment combined with a conjugated rod segment could lead to novel multifunctional sensory materials (Figure 45). A stimuli-responsive polymer is defined as a polymer that is subjected to a large and abrupt physical (temperature, solvent, light) or chemical (reactant, pH, ion) change in response to small external changes in the environmental conditions.

For all these reasons, the synthesis of rod-coil block copolymers is the subject of considerable attention but only a few studies involving a low band-gap rod block are reported in the literature as the synthesis of such block copolymer remains challenging.

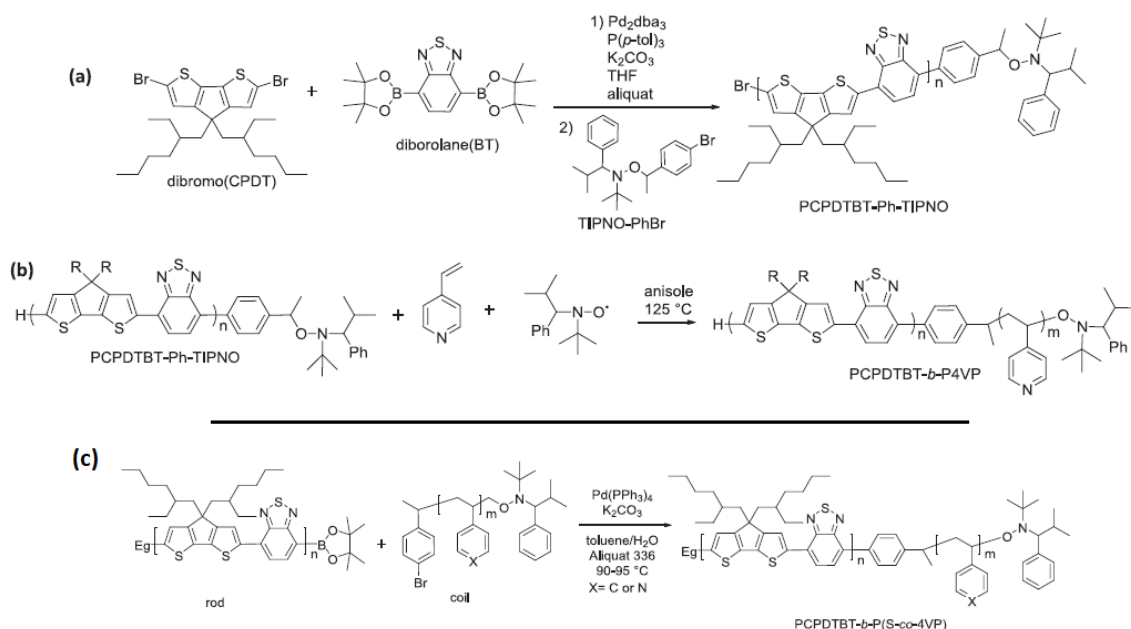


Figure 46: Synthetic routes for (a) the macroinitiator PCPDTBT-Ph-TIPNO, (b) the rod-coil block copolymer PCPDTBT-*b*-P4VP via the macroinitiator method, and (c) the rod-coil block copolymer PCPDTBT-*b*-P(*s-co*-4VP) via the grafting-to method. Adapted from Zappia *et al.*<sup>224</sup>



Concerning the macroinitiator method, as previously detailed in Section IV. 1) a., Van de Wetering *et al.* employed a low band-gap polymer as macroinitiator to synthesize a rod-coil block copolymer based on styrene and chloromethylstyrene. Then, Zappia *et al.* described a similar study involving a lower band-gap of the rod block. Actually, the low band-gap block PCPDTBT ( $E_g^{\text{opt}} = 1.5 \text{ eV}$ ) was end-functionalized with a phenyl bromine alkoxyamine based on TIPNO (Figure 46a). The rod block was only precipitated twice in the proper solvent and no further purification were carried out to avoid damages to the alkoxyamine at the chain end. The presence of the alkoxyamine was confirmed by MALDI-ToF analysis but unreactive species (*i.e.* rod block without the alkoxyamine at the chain end) appeared to be predominant.

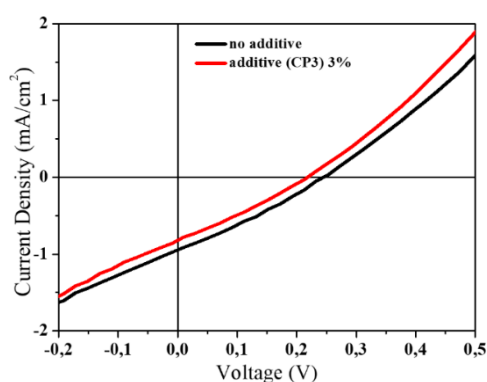


Figure 47: Current density vs voltage characteristics of hybrid solar cells based on CdSe nanocrystals/PCPDTBT homopolymer blend with no additive (black) and containing 1% of rod-coil block copolymer obtained *via* the grafting-to method. Adapted from Zappia *et al.*<sup>224</sup>

Yet, the polymerization of 4VP was performed starting from the macroinitiator *via* NMP and very short coil blocks were obtained due to the low concentration of radicals (Figure 46b). The final material was employed as a compatibilizer in hybrid blends of CdSe nanocrystals and PCPDTBT homopolymers to fabricate hybrid solar cells without annealing. The devices presented a PCE up to 1.16%. Furthermore, Zappia *et al.* depicted another synthetic route to produce rod-coil block copolymers based on the same low band-gap block PCPDTBT. In fact, they synthesized rod and coil blocks separately: the rod block was end-functionalized with borolane groups *via* Suzuki polycondensation and the coil block was prepared *via* NMP using the alkoxyamine TIPNO, the styrene and 4VP monomers. The coil block, bearing a brominated phenyl end-group, was coupled to the borolane group of the rod block *via* Suzuki coupling (Figure 46c). The remaining unreacted homopolymers were removed by several precipitations in different selective solvents and the final yields were decreased by 15-25%. The final material was also employed as compatibilizer in hybrid blends of CdSe nanocrystals and PCPDTBT homopolymers to fabricate hybrid solar cells but the devices showed low photocurrent and open

circuit voltage ( $V_{OC}$ ), and poor fill factor (FF) (Figure 47). Actually, these poor performances are due to the long coil insulating segments that hinder the charge mobility but reducing their length in the block copolymers resulted in short-circuits due to high roughness. Hence, the rod-coil block copolymers obtained through the grafting-to method were less efficient than the ones obtained through the macroinitiator method.<sup>224,225</sup>

More recently, Ferretti *et al.* employed the macroinitiator method described before to produce two amphiphilic low band-gap rod-coil block copolymers.<sup>224,225</sup> They used the same low band-gap block PCPDTBT as Zappia *et al.* to initiate the NMP of 4VP monomer. In addition, they also employed the grafting-to method to synthesize two more amphiphilic low band-gap rod-coil block copolymers based on the low band-gap block PCPDTBT end-functionalized with a borolane group and the coil block P4VP end-functionalized with a phenyl bromine alkoxyamine based on TIPNO. Both blocks were coupled by a Suzuki reaction. Finally, the four amphiphilic block copolymers were self-assembled into nanoparticles suspended in aqueous medium through miniemulsion approach, without using surfactant. The nanostructures are influenced by the composition and the length of the coil block but always present a spherical shape (Figure 48). Even though they did not show an application of these block copolymer-based nanoparticles, Destri's group hypothesized that this material could be used in the preparation of sustainable electronic devices such as OLEDs or OPVs or for bio-organic electronic application due to its aqueous processability.<sup>226</sup>

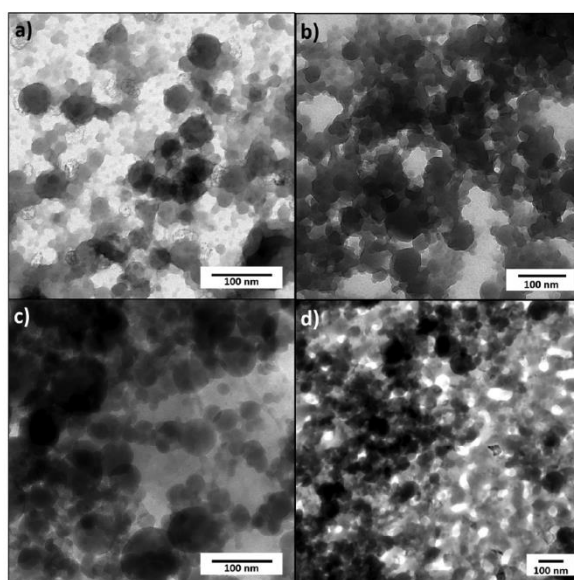
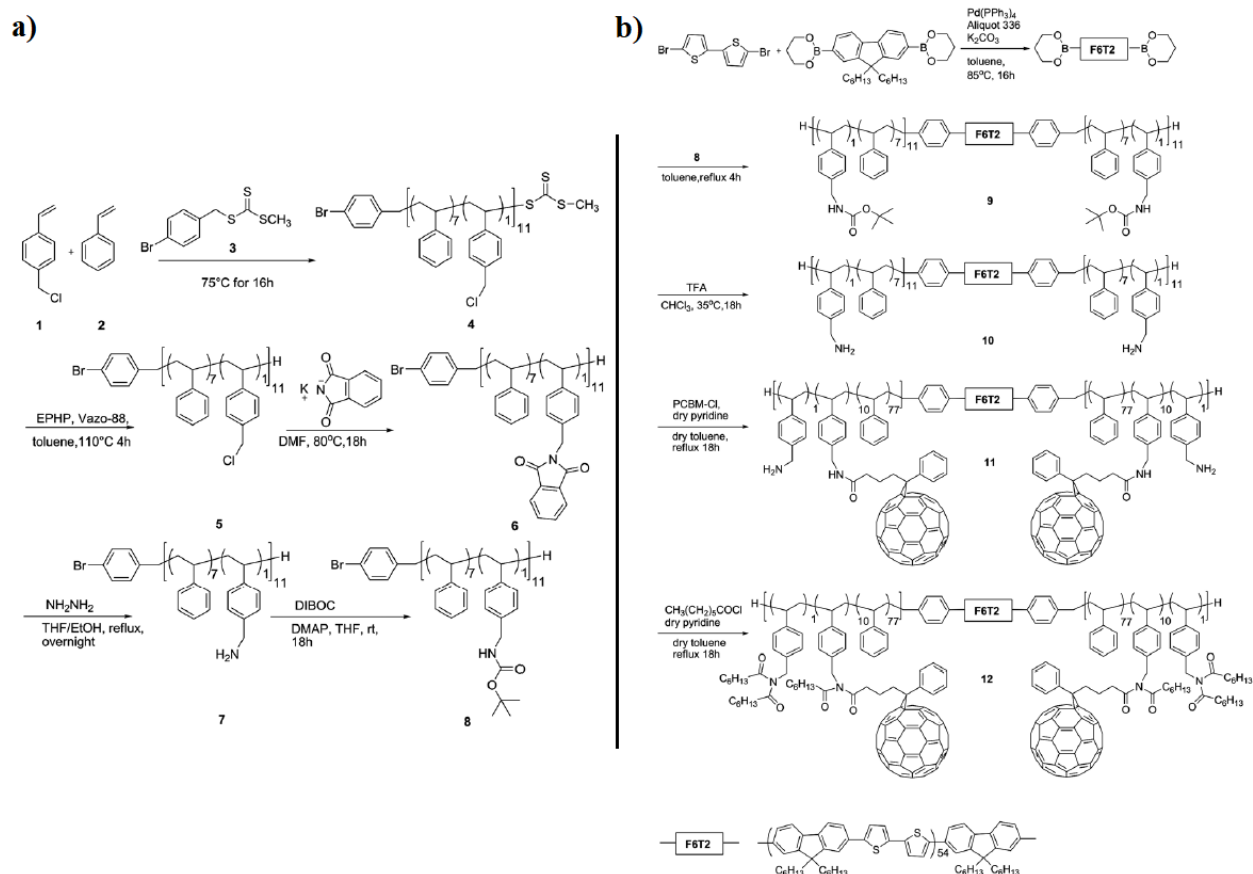


Figure 48: TEM images of rod-coil block copolymer-based water-processable nanoparticles films. Adapted from Ferretti *et al.*<sup>226</sup>

Even though Zappia *et al.* employed it, Ho *et al.* were among the first group to study the grafting-to method to synthesize rod-coil block copolymers based on low band-gap polymers. In their study, they reported the synthesis of an alkyne-terminated poly(diethylhexyloxy-*p*-phenylenevinylene) (DEH-PPV) showing a band gap of 1.6 eV and of an azido-terminated poly(methyl methacrylate) (PMMA) *via* a Siegrist polycondensation and an anionic polymerization, respectively. The two blocks were coupled by Huisgen cycloaddition with high yields due to an excess amount of the low band-gap block in the mixture. The unreacted homopolymers were removed by successive precipitations in proper solvents and SEC analysis proved the efficiency of the purification with the presence of a monomodal peak. The self-assembly of the final material was investigated by small-angle X-ray scattering (SAXS), wide-angle X-ray scattering (WAXS), transmission electron microscopy (TEM), polarized optical microscopy (POM), and differential scanning calorimetry (DSC). The results indicated that the material self-assembles into smectic-lamellar structures for low coil fraction (<53%) and into smectic-hexagonal structures for high coil fraction (>66%). Yet, the authors did not report a specific application for this rod-coil block copolymer.<sup>227</sup> As the previous example, Olsen *et al.* based their rod-coil block copolymers on the same low band-gap polymer DEH-PPV. They used the grafting-to method but the originality of their work rests on the use of anionic polymerization of isoprene to grow the coil block. Actually, the DEH-PPV block was injected at the end of the polymerization of the coil to terminate the living polyisoprene (PI). The excess of homopolymer was removed by precipitation and column chromatography purification. The self-assembly properties of the final material were studied by SAXS, WAXS, TEM, and POM. The block copolymers exhibit liquid crystalline characteristics as an isotropic phase with transitions to nematic and smectic phases were observed at high temperatures and coil fractions. The main goal of this study was to investigate the fundamental phase behavior in rod-coil systems so the authors did not report an application of this material.<sup>228</sup>

In closing, among all the possible applications of rod-coil block copolymers, Bicciochi *et al.* were the first to report the synthesis of such material comprising a donor and an acceptor as compatibilizers for full organic PVs. First, the coil block was obtained by copolymerization of styrene (S) and vinylbenzyl chloride (VBC) monomers under the control of the trithiocarbonate RAFT agent. The pendant benzyl chloride groups were transformed into free amine groups which were further protected with di-*tert*-butyldicarbonate (DIBOC) *via* post-polymerization modifications (Figure 49a). These functional groups were deprotected to attach fullerene (C<sub>60</sub>) on the coil block. Styrene was used as a comonomer to enhance the solubility

and to control the amount of C<sub>60</sub> by spacing the functional groups. Then the rod low band-gap block was synthesized by Suzuki polycondensation of bithiophene (2T) with slight excess of 9,9-dihexylfluorene-2,7-diboronic acid-*bis*-(1,3-propanediol)ester to end-functionalize the chain ends with boronic ester groups. The rod block F6T2 was grafted to the coil block P(S-*co*-VBC) by coupling between the functional groups and the final material appeared to be a coil-rod-coil triblock copolymer (Figure 49b).



Unreacted C<sub>60</sub> was removed by several filtrations and centrifugations. Even though the rod block presents a low band-gap of 1.77 eV, the final material does not show the same features: the maximum absorbance is reached at 450 nm in solution. The efficiency of the grafting-to method was assessed by SEC, Fourier-transform infrared spectroscopy, and fluorescence measurements. The latter showed a fluorescence quenching of the F6T2 block owing to electron-transfer processes with C<sub>60</sub>. The material was used as compatibilizer in various amounts to prepare OPV devices based on a blend of acceptor F6T2 and donor C<sub>60</sub>. The

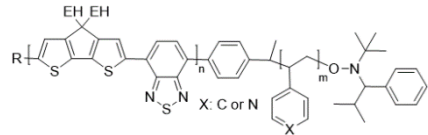
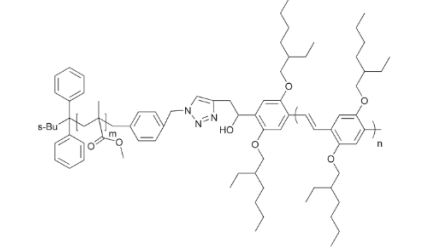
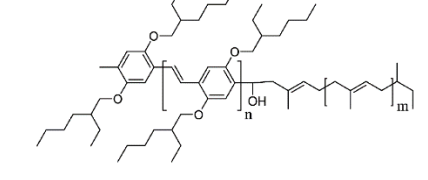
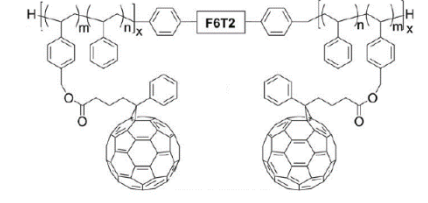
presence of the triblock copolymer enhanced the stability of the devices by increasing the residual efficiencies after 30 days.<sup>229,230</sup>

Concerning the macro end-capper polymerization method, no example of rod-coil block copolymers involving a low band-gap block was found in the literature.

Table 7: Summary of the rod-coil block copolymers involving a low band-gap polymer reported in the literature: <sup>a</sup> determined by SEC; <sup>b</sup> optical band-gap of the block copolymer in thin films <sup>c</sup> optical band-gap of the low band-gap block

Chemical structure	Synthetic strategy	Mn <sup>a</sup> (kDa)	Đ	Eg <sup>opt,b</sup> (eV)	Application	Ref.
 DO-PTV- <i>b</i> -P(S-co-CMS)	Macroinitiator method	5.1 31.3	2.5 1.7	1.6 <sup>c</sup>	-	Van de Wetering <i>et al.</i> <sup>196</sup>
 PCPDTBT- <i>b</i> -P4VP	Macroinitiator method	8.1	1.9	1.5 <sup>c</sup>	additives in OPVs max PCE: 1.16%	Zappia <i>et al.</i> <sup>224,225</sup>
 PCPDTBT- <i>b</i> -P(S-co-4VP) X = C or N	Grafting-to method	5.4 10.9 16.8	2.6 2.0 1.6	1.5 <sup>c</sup>	additives in OPVs no PCE	Zappia <i>et al.</i> <sup>224</sup>
 PCPDTBT- <i>b</i> -P4VP	Macroinitiator method	5.6 6.0	- -	1.5 <sup>c</sup>	Surfactant-free miniemulsion	Ferretti <i>et al.</i> <sup>229</sup>
 PCPDTBT- <i>b</i> -P4VP	Grafting-to method	16.2	1.4	1.5 <sup>c</sup>	Surfactant-free miniemulsion	Ferretti <i>et al.</i> <sup>226</sup>

## Chapter 1: Materials absorbing in the near infrared region and their innovative applications

 <p><b>PCPDTBT-<i>b</i>-P(S-co-4VP)</b></p>	Grafting-to method	14.6	1.9	1.5 <sup>c</sup>	Surfactant-free miniemulsion	Ferretti <i>et al.</i> <sup>226</sup>
 <p><b>PMMA-<i>b</i>-DEH-PPV</b></p>	Grafting-to method	-	-	1.6 <sup>c</sup>	-	Ho <i>et al.</i> <sup>227</sup>
 <p><b>DEH-PPV-<i>b</i>-PI</b></p>	Grafting-to method	-	-	1.6 <sup>c</sup>	-	Olsen <i>et al.</i> <sup>231</sup>
 <p><b>P(S-co-VBC-C60)-<i>b</i>-F6T2-<i>b</i>-P(S-co-VBC-C60)</b></p>	Grafting-to method	-	-	1.77 <sup>c</sup>	additives in OPVs for stability	Biccocchi <i>et al.</i> <sup>229,230</sup>

Even though all the polymers presented above show narrow or low band-gap characteristics, only one of them exhibits an absorbance maximum in the NIR region. Among the rod-rod and rod-coil block copolymers presented above, the recurring application is the optoelectronic devices. Nevertheless, block copolymers involving a low band-gap block could be employed in sensors<sup>231</sup>, stimuli-responsive applications<sup>232</sup>, photoacoustic imaging, photodynamic therapy, photothermal therapy, and variable optical attenuators.

## V. Conclusion

From this literature review, it appears that organic materials absorbing in the near infrared region form a major and multidisciplinary field of research with growing interest, particularly in the field of optoelectronic, bioimaging, and medical therapy. In addition to the fact that about 50% of solar energy takes place in the IR region, the interesting asset of working in this spectral range is that near infrared light penetrates biological tissues. Hence, a whole field of research has been developed thanks to small molecules, organometallics, and conjugated polymers absorbing in the near infrared.

Among conjugated polymers, low band-gap polymers have been the object of intensive research since their optoelectronic properties can be tuned by modifying their macromolecular structures. Indeed, several molecular engineering strategies have been developed in order to reduce their band-gap below 1.6 eV and tune their energy levels. Two major chemistry design approaches have been elaborated: the stabilization of the quinoid resonance structure by fusing aromatic rings, and the use of donor-acceptor interactions by alternating electron-donating (D) and electron-withdrawing (A) units on the polymer backbone. The general synthetic route to yield low band-gap polymers is step-growth or condensation polymerization involving palladium catalysts. These polymers are often polymerized by Stille polycondensation and functional groups can be introduced at the chain ends thanks to several methodologies.

End-functionalization of conjugated polymers helps to broaden the range of their applications. For instance, polymers can be covalently attached to inorganic/metal surfaces leading to the formation of hybrid materials. Yet, only few studies report the grafting of low band-gap polymers from, through or onto inorganic substrates. The development of such materials could improve greatly the performance and lifetime of active layers in optoelectronic devices.

Furthermore, the end-functionalization of conjugated polymers paves the way to block copolymers incorporating low band-gap polymers. Such materials are the subject of considerable interest as they can provide a broader light absorption in the NIR region and enhance the performance and stability of optoelectronic devices. In addition, rod-coil block copolymers can be applied to various applications, notably in the biomedical field, due to their self-assembly properties in solution and in thin films. Four major synthetic routes have been designed to obtain block copolymers and it appears that the macro end-capper copolymerization

method is the technique the most employed to yield rod-rod block copolymers involving a low band-gap block. Concerning rod-coil block copolymers, the macroinitiator technique is the method of choice, yet, only few studies report rod-coil block copolymers involving a low band-gap block with a maximum absorbance in the NIR region.

The work described in this manuscript remains on the end-functionalization of low band-gap polymers *via* the use of a monofunctional end-capper in a one-step procedure. The main objective of this study is the development of new materials based on low band-gap polymers absorbing in the spectral range 650-1000 nm in order to obtain active materials in the NIR region. Hence, the second chapter of this manuscript presents the synthesis of a new hybrid material by grafting a low band-gap polymer onto ZnO nanospheres *via* the grafting onto technique. In Chapters 3 and 4, the study focused on the design and the synthesis of rod-coil block copolymers involving a low band-gap block. Based on the literature review, two synthetic routes were employed: the macroinitiator method and the macro end-capper copolymerization method. Through several characterizations, possible applications for these block copolymers were proposed. Chapter 3 involved a coil block which induced filmogenic properties and its thermic and mass self-assembly properties were studied. On the contrary in Chapter 4, the self-assembly behavior of the block copolymer was examined in solution since the coil block was water soluble and led to the formation of micelles. The photothermal properties of these objects were investigated in different solvents.



## VI. References

- (1) Qi, J.; Qiao, W.; Wang, Z. Y. Advances in Organic Near-Infrared Materials and Emerging Applications. *Chem. Rec.* **2016**, *16* (3), 1531–1548. <https://doi.org/10.1002/tcr.201600013>.
- (2) Dou, L.; Liu, Y.; Hong, Z.; Li, G.; Yang, Y. Low-Band-gap Near-IR Conjugated Polymers/Molecules for Organic Electronics. *Chem. Rev.* **2015**, *115* (23), 12633–12665.
- (3) Coughlin, J. E.; Henson, Z. B.; Welch, G. C.; Bazan, G. C. Design and Synthesis of Molecular Donors for Solution-Processed High-Efficiency Organic Solar Cells. *Acc. Chem. Res.* **2014**, *47* (1), 257–270. <https://doi.org/10.1021/ar400136b>.
- (4) Wang, H.; Liu, F.; Bu, L.; Gao, J.; Wang, C.; Wei, W.; Russell, T. P. The Role of Additive in Diketopyrrolopyrrole-Based Small Molecular Bulk Heterojunction Solar Cells. *Adv. Mater.* **2013**, *25* (45), 6519–6525. <https://doi.org/10.1002/adma.201302848>.
- (5) Chen, Y.; Du, Z.; Chen, W.; Han, L.; Liu, Q.; Sun, M.; Yang, R. Near-Infrared Response Thienoisindigo-Based Small Molecule for Solution-Processed Bulk-Heterojunction Solar Cells. *Synth. Met.* **2014**, *187*, 24–29. <https://doi.org/10.1016/j.synthmet.2013.10.017>.
- (6) Aumaitre, C.; Rodriguez-Seco, C.; Jover, J.; Bardagot, O.; Caffy, F.; Kervella, Y.; López, N.; Palomares, E.; Demadrille, R. Visible and Near-Infrared Organic Photosensitizers Comprising Isoindigo Derivatives as Chromophores: Synthesis, Optoelectronic Properties and Factors Limiting Their Efficiency in Dye Solar Cells. *J. Mater. Chem. A* **2018**, *6* (21), 10074–10084. <https://doi.org/10.1039/C8TA01826J>.
- (7) Yang, D.; Yang, Q.; Yang, L.; Luo, Q.; Chen, Y.; Zhu, Y.; Huang, Y.; Lu, Z.; Zhao, S. A Low Band-gap Asymmetrical Squaraine for High-Performance Solution-Processed Small Molecule Organic Solar Cells. *Chem Commun* **2014**, *50* (66), 9346–9348. <https://doi.org/10.1039/C4CC03831B>.
- (8) Bura, T.; Leclerc, N.; Fall, S.; Lévêque, P.; Heiser, T.; Retailleau, P.; Rihn, S.; Mirloup, A.; Ziessel, R. High-Performance Solution-Processed Solar Cells and Ambipolar Behavior in Organic Field-Effect Transistors with Thienyl-BODIPY Scaffoldings. *J. Am. Chem. Soc.* **2012**, *134* (42), 17404–17407. <https://doi.org/10.1021/ja3072513>.
- (9) Ji, C.; Yin, L.; Li, K.; Wang, L.; Jiang, X.; Sun, Y.; Li, Y. D- $\pi$ -A- $\pi$ -D-Type Low Band Gap Diketopyrrolopyrrole Based Small Molecules Containing an Ethynyl-Linkage: Synthesis and Photovoltaic Properties. *RSC Adv.* **2015**, *5* (40), 31606–31614. <https://doi.org/10.1039/C5RA01946J>.
- (10) Lin, Z.; Huang, K.; Wang, Z.; Chen, X.; Sun, J.; Xu, Z.; He, T.; Yin, S.; Li, M.; Zhang, Q.; Qiu, H. Alkyl Side-Chain and Fluorination Engineering in the Indeno[1,2-b]Fluorene-Based Small-Molecule Acceptors for Efficient Non-Fullerene Organic Solar Cells. *Dyes Pigments* **2019**, *160*, 432–438. <https://doi.org/10.1016/j.dyepig.2018.08.039>.
- (11) Trang, N. V.; Dung, T. N.; Cuong, N. T.; Hai, L. T. H.; Escudero, D.; Nguyen, M. T.; Nguyen, H. M. T. Theoretical Study of a Class of Organic D- $\pi$ -A Dyes for Polymer Solar Cells: Influence of Various  $\pi$ -Spacers. *Crystals* **2020**, *10* (3), 163. <https://doi.org/10.3390/cryst10030163>.
- (12) Qi, Y.; Wang, Z. Y. Dendritic Mixed-Valence Dinuclear Ruthenium Complexes for Optical Attenuation at Telecommunication Wavelengths. *Macromolecules* **2003**, *36* (9), 3146–3151. <https://doi.org/10.1021/ma021018s>.

- (13) Wang, S.; Li, X.; Xun, S.; Wan, X.; Wang, Z. Y. Near-Infrared Electrochromic and Electroluminescent Polymers Containing Pendant Ruthenium Complex Groups. *Macromolecules* **2006**, *39*, 7502–7507. <https://doi.org/10.1021/ma061751>.
- (14) Xun, S.; LeClair, G.; Zhang, J.; Chen, X.; Gao, J. P.; Wang, Z. Y. Tuning the Electrical and Optical Properties of Dinuclear Ruthenium Complexes for Near Infrared Optical Sensing. *Org. Lett.* **2006**, *8* (8), 1697–1700. <https://doi.org/10.1021/ol060344f>.
- (15) Hasanain, F.; Wang, Z. Y. The Synthesis and Characterization of Near-Infrared Absorbing, Electrochromic Polyimides Containing a Dinuclear Ruthenium Complex in the Polymer Mainchain. *Dyes Pigments* **2009**, *83* (1), 95–101. <https://doi.org/10.1016/j.dyepig.2009.03.020>.
- (16) Liu, B.; Qiao, W.; Wang, Z. Y. Colorless Metallodithiolene Oligomers and Polymers with Intense Near- and Mid-Infrared Absorption. *RSC Adv.* **2015**, *5* (9), 6815–6822. <https://doi.org/10.1039/C4RA13039A>.
- (17) Chen, X.; Qiao, W.; Liu, B.; Ren, J.; Wang, Z. Synthesis and near Infrared Electrochromic Properties of Metallodithiolene Complexes. *Sci. China Chem.* **2017**, *60* (1), 77–83. <https://doi.org/10.1007/s11426-016-0252-x>.
- (18) Fang, Z.; Ito, A.; Keinan, S.; Chen, Z.; Watson, Z.; Rochette, J.; Kanai, Y.; Taylor, D.; Schanze, K. S.; Meyer, T. J. Atom Transfer Radical Polymerization Preparation and Photophysical Properties of Polypyridylruthenium Derivatized Polystyrenes. *Inorg. Chem.* **2013**, *52* (15), 8511–8520. <https://doi.org/10.1021/ic400520m>.
- (19) Fang, Z.; Ito, A.; Stuart, A. C.; Luo, H.; Chen, Z.; Vinodgopal, K.; You, W.; Meyer, T. J.; Taylor, D. K. Soluble Reduced Graphene Oxide Sheets Grafted with Polypyridylruthenium-Derivatized Polystyrene Brushes as Light Harvesting Antenna for Photovoltaic Applications. *ACS Nano* **2013**, *7* (9), 7992–8002. <https://doi.org/10.1021/nn403079z>.
- (20) Wang, Y.; Xu, S.; Chen, T.; Guo, H.; Liu, Q.; Ye, B.; Zhang, Z.; He, Z.; Cao, S. Synthesis and Preliminary Photovoltaic Behavior Study of a Soluble Polyimide Containing Ruthenium Complexes. *Polym. Chem.* **2010**, *1* (7), 1048. <https://doi.org/10.1039/c0py00096e>.
- (21) Schroot, R.; Jäger, M.; Schubert, U. S. Synthetic Approaches towards Structurally-Defined Electrochemically and (Photo)Redox-Active Polymer Architectures. *Chem. Soc. Rev.* **2017**, *46* (10), 2754–2798. <https://doi.org/10.1039/C6CS00811A>.
- (22) Shirakawa, H.; Louis, E. J.; MacDiarmid, A. G.; Chiang, C. K.; Heeger, A. J. Synthesis of Electrically Conducting Organic Polymers : Halogen Derivatives of Polyacetylene, (CH)<sub>n</sub>. *J. Chem. Soc. Chem. Commun.* **1977**, *16*, 578. <https://doi.org/10.1039/c39770000578>.
- (23) Attias, A.-J. Polymères conjugués et électronique organique. *Tech. Ing.* **2017**, *29*.
- (24) Copeland, W.; Black, I. O. D.; Garrett, A. B. THE PHOTOVOLTAIC EFFECT. *Chem. Rev.* **1942**, *31* (1), 177–226. <https://doi.org/10.1021/cr60098a004>.
- (25) Vivek, K. A. ORGANIC SOLAR CELLS: PRINCIPLES, MECHANISM AND RECENT DEVELOPMENTS. *Int. J. Res. Eng. Technol.* **2014**, *03* (09), 338–341. <https://doi.org/10.15623/ijret.2014.0309053>.
- (26) Kumaresan, P.; Vegiraju, S.; Ezhumalai, Y.; Yau, S.; Kim, C.; Lee, W.-H.; Chen, M.-C. Fused-Thiophene Based Materials for Organic Photovoltaics and Dye-Sensitized Solar Cells. *Polymers* **2014**, *6* (10), 2645–2669. <https://doi.org/10.3390/polym6102645>.
- (27) Brabec, C. J.; Sariciftci, N. S.; Hummelen, J. C. Plastic Solar Cells. *Adv. Funct. Mater.* **2001**, *11* (1), 15–26. [https://doi.org/10.1002/1616-3028\(200102\)11:1<15::AID-ADFM15>3.0.CO;2-A](https://doi.org/10.1002/1616-3028(200102)11:1<15::AID-ADFM15>3.0.CO;2-A).

- (28) Brabec, C. J.; Heeney, M.; McCulloch, I.; Nelson, J. Influence of Blend Microstructure on Bulk Heterojunction Organic Photovoltaic Performance. *Chem Soc Rev* **2011**, *40* (3), 1185–1199. <https://doi.org/10.1039/C0CS00045K>.
- (29) Ge, W. *An Overview on P3HT:PCBM, the Most Efficient Organic Solar Cell Material so Far*; 2009.
- (30) Schilinsky, P.; Waldauf, C.; Brabec, C. J. Recombination and Loss Analysis in Polythiophene Based Bulk Heterojunction Photodetectors. *Appl. Phys. Lett.* **2002**, *81* (20), 3885–3887. <https://doi.org/10.1063/1.1521244>.
- (31) Berger, P. R.; Kim, M. Polymer Solar Cells: P3HT:PCBM and Beyond. *J. Renew. Sustain. Energy* **2018**, *10* (1), 013508. <https://doi.org/10.1063/1.5012992>.
- (32) You, J.; Dou, L.; Yoshimura, K.; Kato, T.; Ohya, K.; Moriarty, T.; Emery, K.; Chen, C.-C.; Gao, J.; Li, G.; Yang, Y. A Polymer Tandem Solar Cell with 10.6% Power Conversion Efficiency. *Nat. Commun.* **2013**, *4* (1), 1446. <https://doi.org/10.1038/ncomms2411>.
- (33) Liang, Y.; Xu, Z.; Xia, J.; Tsai, S.-T.; Wu, Y.; Li, G.; Ray, C.; Yu, L. For the Bright Future-Bulk Heterojunction Polymer Solar Cells with Power Conversion Efficiency of 7.4%. *Adv. Mater.* **2010**, *22* (20), E135–E138. <https://doi.org/10.1002/adma.200903528>.
- (34) Wang, M.; Hu, X.; Liu, P.; Li, W.; Gong, X.; Huang, F.; Cao, Y. Donor–Acceptor Conjugated Polymer Based on Naphtho[1,2-*c*:5,6-*c'*]Bis[1,2,5]Thiadiazole for High-Performance Polymer Solar Cells. *J. Am. Chem. Soc.* **2011**, *133* (25), 9638–9641. <https://doi.org/10.1021/ja201131h>.
- (35) Lee, O. P.; Yiu, A. T.; Beaujuge, P. M.; Woo, C. H.; Holcombe, T. W.; Millstone, J. E.; Douglas, J. D.; Chen, M. S.; Fréchet, J. M. J. Efficient Small Molecule Bulk Heterojunction Solar Cells with High Fill Factors via Pyrene-Directed Molecular Self-Assembly. *Adv. Mater.* **2011**, *23* (45), 5359–5363. <https://doi.org/10.1002/adma.201103177>.
- (36) Abdelsamie, M.; Treat, N. D.; Zhao, K.; McDowell, C.; Burgers, M. A.; Li, R.; Smilgies, D.-M.; Stingelin, N.; Bazan, G. C.; Amassian, A. Toward Additive-Free Small-Molecule Organic Solar Cells: Roles of the Donor Crystallization Pathway and Dynamics. *Adv. Mater.* **2015**, *27* (45), 7285–7292. <https://doi.org/10.1002/adma.201503395>.
- (37) Liu, X.; Sun, Y.; Perez, L. A.; Wen, W.; Toney, M. F.; Heeger, A. J.; Bazan, G. C. Narrow-Band-Gap Conjugated Chromophores with Extended Molecular Lengths. *J. Am. Chem. Soc.* **2012**, *134* (51), 20609–20612. <https://doi.org/10.1021/ja310483w>.
- (38) Chen, Y.; Zhu, W.; Wu, J.; Huang, Y.; Facchetti, A.; Marks, T. J. Recent Advances in Squaraine Dyes for Bulk-Heterojunction Organic Solar Cells. *Org. Photonics Photovolt.* **2019**, *6* (1), 1–16. <https://doi.org/10.1515/oph-2019-0001>.
- (39) Hagfeldt, A.; Boschloo, G.; Sun, L.; Kloo, L.; Pettersson, H. Dye-Sensitized Solar Cells. *Chem. Rev.* **2010**, *110* (11), 6595–6663. <https://doi.org/10.1021/cr900356p>.
- (40) Zimmerman, J. D.; Lassiter, B. E.; Xiao, X.; Sun, K.; Dolocan, A.; Gearba, R.; Vanden Bout, D. A.; Stevenson, K. J.; Wickramasinghe, P.; Thompson, M. E.; Forrest, S. R. Control of Interface Order by Inverse Quasi-Epitaxial Growth of Squaraine/Fullerene Thin Film Photovoltaics. *ACS Nano* **2013**, *7* (10), 9268–9275. <https://doi.org/10.1021/nn403897d>.
- (41) Wang, S.; Hall, L.; Diev, V. V.; Haiges, R.; Wei, G.; Xiao, X.; Djurovich, P. I.; Forrest, S. R.; Thompson, M. E. N,N-Di Aryl Anilinosquaraines and Their Application to Organic Photovoltaics. *Chem. Mater.* **2011**, *23* (21), 4789–4798. <https://doi.org/10.1021/cm2020803>.

- (42) Lai, H.; Zhao, Q.; Chen, Z.; Chen, H.; Chao, P.; Zhu, Y.; Lang, Y.; Zhen, N.; Mo, D.; Zhang, Y.; He, F. Trifluoromethylation Enables a 3D Interpenetrated Low-Band-Gap Acceptor for Efficient Organic Solar Cells. *Joule* **2020**, *4* (3), 688–700. <https://doi.org/10.1016/j.joule.2020.02.004>.
- (43) Yan, C.; Barlow, S.; Wang, Z.; Yan, H.; Jen, A. K.-Y.; Marder, S. R.; Zhan, X. Non-Fullerene Acceptors for Organic Solar Cells. *Nat. Rev. Mater.* **2018**, *3* (3), 18003. <https://doi.org/10.1038/natrevmats.2018.3>.
- (44) Gao, W.; Liu, T.; Ming, R.; Luo, Z.; Wu, K.; Zhang, L.; Xin, J.; Xie, D.; Zhang, G.; Ma, W.; Yan, H.; Yang, C. Near-Infrared Small Molecule Acceptor Enabled High-Performance Nonfullerene Polymer Solar Cells with Over 13% Efficiency. *Adv. Funct. Mater.* **2018**, *28* (31), 1803128. <https://doi.org/10.1002/adfm.201803128>.
- (45) Cheng, P.; Yang, Y. Narrowing the Band Gap: The Key to High-Performance Organic Photovoltaics. *Acc. Chem. Res.* **2020**, *53* (6), 1218–1228. <https://doi.org/10.1021/acs.accounts.0c00157>.
- (46) Cui, Y.; Yao, H.; Zhang, J.; Xian, K.; Zhang, T.; Hong, L.; Wang, Y.; Xu, Y.; Ma, K.; An, C.; He, C.; Wei, Z.; Gao, F.; Hou, J. Single-Junction Organic Photovoltaic Cells with Approaching 18% Efficiency. *Adv. Mater.* **2020**, *32* (19), 1908205. <https://doi.org/10.1002/adma.201908205>.
- (47) National Renewable Energy Laboratory. *Best Research-Cell Efficiencies*; 2020.
- (48) Xu, Y.; Lin, Q. Photodetectors Based on Solution-Processable Semiconductors: Recent Advances and Perspectives. *Appl. Phys. Rev.* **2020**, *7* (1), 011315. <https://doi.org/10.1063/1.5144840>.
- (49) Clark, J.; Lanzani, G. Organic Photonics for Communications. *Nat. Photonics* **2010**, *4* (7), 438–446. <https://doi.org/10.1038/nphoton.2010.160>.
- (50) Zhang, H.; Jenatsch, S.; De Jonghe, J.; Nüesch, F.; Steim, R.; Véron, A. C.; Hany, R. Transparent Organic Photodetector Using a Near-Infrared Absorbing Cyanine Dye. *Sci. Rep.* **2015**, *5* (1), 9439. <https://doi.org/10.1038/srep09439>.
- (51) Sargent, E. H. Solar Cells, Photodetectors, and Optical Sources from Infrared Colloidal Quantum Dots. *Adv. Mater.* **2008**, *20* (20), 3958–3964. <https://doi.org/10.1002/adma.200801153>.
- (52) Tordera, D.; Peeters, B.; Delvitto, E.; Shanmugam, S.; Maas, J.; Riet, J.; Verbeek, R.; Laar, R.; Bel, T.; Haas, G.; Ugalde, L.; Breemen, A.; Katsouras, I.; Kronemeijer, A. J.; Akkerman, H.; Meulenkamp, E.; Gelinck, G. Vein Detection with Near-infrared Organic Photodetectors for Biometric Authentication. *J. Soc. Inf. Disp.* **2020**, *28* (5), 381–391. <https://doi.org/10.1002/jsid.891>.
- (53) Verstraeten, F.; Gielen, S.; Verstappen, P.; Raymakers, J.; Penxten, H.; Lutsen, L.; Vandewal, K.; Maes, W. Efficient and Readily Tuneable Near-Infrared Photodetection up to 1500 Nm Enabled by Thiadiazoloquinoxaline-Based Push-Pull Type Conjugated Polymers. *J. Mater. Chem. C* **2020**. <https://doi.org/10.1039/D0TC01435D>.
- (54) Wang, C.; Zhang, X.; Hu, W. Organic Photodiodes and Phototransistors toward Infrared Detection: Materials, Devices, and Applications. *Chem. Soc. Rev.* **2020**, *49* (3), 653–670. <https://doi.org/10.1039/C9CS00431A>.
- (55) Li, Q.; Guo, Y.; Liu, Y. Exploration of Near-Infrared Organic Photodetectors. *Chem. Mater.* **2019**, *31* (17), 6359–6379. <https://doi.org/10.1021/acs.chemmater.9b00966>.
- (56) Baeg, K.-J.; Binda, M.; Natali, D.; Caironi, M.; Noh, Y.-Y. Organic Light Detectors: Photodiodes and Phototransistors. *Adv. Mater.* **2013**, *25* (31), 4267–4295. <https://doi.org/10.1002/adma.201204979>.
- (57) Gong, X.; Tong, M.; Xia, Y.; Cai, W.; Moon, J. S.; Cao, Y.; Yu, G.; Shieh, C.-L.; Nilsson, B.; Heeger, A. J. High-Detectivity Polymer Photodetectors with Spectral

- Response from 300 Nm to 1450 Nm. *Science* **2009**, *325* (5948), 1665–1667. <https://doi.org/10.1126/science.1176706>.
- (58) Yao, Y.; Liang, Y.; Shrotriya, V.; Xiao, S.; Yu, L.; Yang, Y. Plastic Near-Infrared Photodetectors Utilizing Low Band Gap Polymer. *Adv. Mater.* **2007**, *19* (22), 3979–3983. <https://doi.org/10.1002/adma.200602670>.
- (59) Perzon, E.; Zhang, F.; Andersson, M.; Mammo, W.; Inganäs, O.; Andersson, M. R. A Conjugated Polymer for Near Infrared Optoelectronic Applications. *Adv. Mater.* **2007**, *19* (20), 3308–3311. <https://doi.org/10.1002/adma.200700557>.
- (60) London, A. E.; Huang, L.; Zhang, B. A.; Oviedo, M. B.; Tropp, J.; Yao, W.; Wu, Z.; Wong, B. M.; Ng, T. N.; Azoulay, J. D. Donor–Acceptor Polymers with Tunable Infrared Photoresponse. *Polym. Chem.* **2017**, *8* (19), 2922–2930.
- (61) Qi, J.; Ni, L.; Yang, D.; Zhou, X.; Qiao, W.; Li, M.; Ma, D.; Wang, Z. Y. Panchromatic Small Molecules for UV-Vis-NIR Photodetectors with High Detectivity. *J. Mater. Chem. C* **2014**, *2* (13), 2431. <https://doi.org/10.1039/c3tc32271h>.
- (62) Siegmund, B.; Mischok, A.; Benduhn, J.; Zeika, O.; Ullbrich, S.; Nehm, F.; Böhm, M.; Spoltore, D.; Fröb, H.; Körner, C.; Leo, K.; Vandewal, K. Organic Narrowband Near-Infrared Photodetectors Based on Intermolecular Charge-Transfer Absorption. *Nat. Commun.* **2017**, *8* (1), 15421. <https://doi.org/10.1038/ncomms15421>.
- (63) Horowitz, G. Organic Field-Effect Transistors. 13.
- (64) Yuen, J. D.; Wudl, F. Strong Acceptors in Donor–Acceptor Polymers for High Performance Thin Film Transistors. *Energy Environ. Sci.* **2013**, *6* (2), 392. <https://doi.org/10.1039/c2ee23505f>.
- (65) Wang, Y.; Hosokawa, R.; Mori, T.; Michinobu, T. Polarity Engineering of Benzobisthiadiazole-Based Polymer Thin Film Transistors by Variation of Electron Affinity of the Comonomers. *Bull. Chem. Soc. Jpn.* **2017**, *90* (9), 1041–1049. <https://doi.org/10.1246/bcsj.20170158>.
- (66) Giovannitti, A.; Sbircea, D.-T.; Inal, S.; Nielsen, C. B.; Bandiello, E.; Hanifi, D. A.; Sessolo, M.; Malliaras, G. G.; McCulloch, I.; Rivnay, J. Controlling the Mode of Operation of Organic Transistors through Side-Chain Engineering. *Proc. Natl. Acad. Sci.* **2016**, *113* (43), 12017–12022. <https://doi.org/10.1073/pnas.1608780113>.
- (67) Matsidik, R.; Komber, H.; Luzio, A.; Caironi, M.; Sommer, M. Defect-Free Naphthalene Diimide Bithiophene Copolymers with Controlled Molar Mass and High Performance via Direct Arylation Polycondensation. *J. Am. Chem. Soc.* **2015**, *137* (20), 6705–6711. <https://doi.org/10.1021/jacs.5b03355>.
- (68) Lee, J.; Han, A.-R.; Yu, H.; Shin, T. J.; Yang, C.; Oh, J. H. Boosting the Ambipolar Performance of Solution-Processable Polymer Semiconductors via Hybrid Side-Chain Engineering. *J. Am. Chem. Soc.* **2013**, *135* (25), 9540–9547. <https://doi.org/10.1021/ja403949g>.
- (69) Ozdemir, R.; Choi, D.; Ozdemir, M.; Kwon, G.; Kim, H.; Sen, U.; Kim, C.; Usta, H. Ultralow Band-gap Molecular Semiconductors for Ambient-Stable and Solution-Processable Ambipolar Organic Field-Effect Transistors and Inverters. *J. Mater. Chem. C* **2017**, *5* (9), 2368–2379. <https://doi.org/10.1039/c6tc05079d>.
- (70) Round, H. J. A Note on Carborundum. *Electr. World* **1907**, *49*, 309.
- (71) Holonyak, N.; Bevacqua, S. F. COHERENT (VISIBLE) LIGHT EMISSION FROM Ga(As<sub>1-x</sub>P<sub>x</sub>) JUNCTIONS. *Appl. Phys. Lett.* **1962**, *1* (4), 82–83. <https://doi.org/10.1063/1.1753706>.
- (72) Tang, C. W.; VanSlyke, S. A. Organic Electroluminescent Diodes. *Appl. Phys. Lett.* **1987**, *913* (51), 913–915. [https://doi.org/10.1007/978-3-642-93430-8\\_71](https://doi.org/10.1007/978-3-642-93430-8_71).

- (73) Burroughes, J. H.; Bradley, D. D. C.; Brown, A. R.; Marks, R. N.; Mackay, K.; Friend, R. H.; Burns, P. L.; Holmes, A. B. Light-Emitting Diodes Based on Conjugated Polymers. *Nature* **1990**, *347* (6293), 539–541. <https://doi.org/10.1038/347539a0>.
- (74) History of OLEDs. In *OLED Displays and Lighting*; John Wiley & Sons, Ltd: Chichester, UK, 2017; pp 1–11. <https://doi.org/10.1002/9781119040477.ch1>.
- (75) Fundamentals of OLEDs. In *OLED Displays and Lighting*; John Wiley & Sons, Ltd: Chichester, UK, 2017; pp 12–16. <https://doi.org/10.1002/9781119040477.ch2>.
- (76) Performance of OLEDs. In *OLED Displays and Lighting*; John Wiley & Sons, Ltd: Chichester, UK, 2017; pp 117–126. <https://doi.org/10.1002/9781119040477.ch7>.
- (77) Zampetti, A.; Minotto, A.; Cacialli, F. Near-Infrared (NIR) Organic Light-Emitting Diodes (OLEDs): Challenges and Opportunities. *Adv. Funct. Mater.* **2019**, *29* (21), 1807623. <https://doi.org/10.1002/adfm.201807623>.
- (78) Smith, A. M.; Mancini, M. C.; Nie, S. Second Window for in Vivo Imaging. *Nat. Nanotechnol.* **2009**, *4* (11), 710–711. <https://doi.org/10.1038/nnano.2009.326>.
- (79) Ibrahim-Ouali, M.; Dumur, F. Recent Advances on Metal-Based Near-Infrared and Infrared Emitting OLEDs. *Molecules* **2019**, *24* (7), 1412. <https://doi.org/10.3390/molecules24071412>.
- (80) Baigent, D. R.; Hamer, P. J.; Friend, R. H.; Moratti, S. C.; Holmes, A. B. Polymer Electroluminescence in the near Infra-Red. *Synth. Met.* **1995**, *71* (1–3), 2175–2176. [https://doi.org/10.1016/0379-6779\(94\)03208-N](https://doi.org/10.1016/0379-6779(94)03208-N).
- (81) Grimsdale, A. C.; Leok Chan, K.; Martin, R. E.; Jokisz, P. G.; Holmes, A. B. Synthesis of Light-Emitting Conjugated Polymers for Applications in Electroluminescent Devices. *Chem. Rev.* **2009**, *109* (3), 897–1091. <https://doi.org/10.1021/cr000013v>.
- (82) Winder, C.; Mühlbacher, D.; Neugebauer, H.; Serdar Sariciftci, N.; Brabec, C.; Janssen, R. A. J.; Kees Hummelen, J. Polymer Solar Cells and Infrared Light Emitting Diodes: Dual Function Low Band-gap Polymer. *Mol. Cryst. Liq. Cryst.* **2002**, *385* (1), 93–100. <https://doi.org/10.1080/713738797>.
- (83) Minotto, A.; Haigh, P. A.; Łukasiewicz, Ł. G.; Lunedei, E.; Gryko, D. T.; Darwazeh, I.; Cacialli, F. Visible Light Communication with Efficient Far-Red/near-Infrared Polymer Light-Emitting Diodes. *Light Sci. Appl.* **2020**, *9* (1), 70. <https://doi.org/10.1038/s41377-020-0314-z>.
- (84) Grzybowski, M.; Hugues, V.; Blanchard-Desce, M.; Gryko, D. T. Two-Photon-Induced Fluorescence in New  $\pi$ -Expanded Diketopyrrolopyrroles. *Chem. - Eur. J.* **2014**, *20* (39), 12493–12501. <https://doi.org/10.1002/chem.201402569>.
- (85) Wang, L.; Pan, C.; Liang, A.; Zhou, X.; Zhou, W.; Wan, T.; Wang, L. The Effect of the Backbone Structure on the Thermoelectric Properties of Donor-Acceptor Conjugated Polymers. *Polym. Chem.* **2017**, *8* (32), 4644–4650. <https://doi.org/10.1039/C7py01005b>.
- (86) Yeddu, V.; Seo, G.; Cruciani, F.; Beaujuge, P. M.; Kim, D. Y. Low-Band-Gap Polymer-Based Infrared-to-Visible Upconversion Organic Light-Emitting Diodes with Infrared Sensitivity up to 1.1 Mm. *ACS Photonics* **2019**, *6* (10), 2368–2374. <https://doi.org/10.1021/acsphotonics.9b00669>.
- (87) Shahalizard, A.; D'Aléo, A.; Andraud, C.; Sazzad, M. H.; Kim, D.-H.; Tsuchiya, Y.; Ribierre, J.-C.; Nunzi, J.-M.; Adachi, C. Near Infrared Electroluminescence from Nd(TTA) 3 Phen in Solution-Processed Small Molecule Organic Light-Emitting Diodes. *Org. Electron.* **2017**, *44*, 50–58. <https://doi.org/10.1016/j.orgel.2017.01.044>.
- (88) Wang, Z. Y.; Zhang, J.; Wu, X.; Birau, M.; Yu, G.; Yu, H.; Qi, Y.; Desjardins, P.; Meng, X.; Gao, J. P.; Todd, E.; Song, N.; Bai, Y.; Beaudin, A. M. R.; LeClair, G.

- Near-Infrared Absorbing Organic Materials. *Pure Appl. Chem.* **2004**, 76 (7–8), 1435–1443. <https://doi.org/10.1351/pac200476071435>.
- (89) Vergaz, R.; Barrios, D.; Sanchez-Pena, J. M.; Vazquez, C.; Pozo-Gonzalo, C.; Mecerreyes, D.; Pomposo, J. Variable Optical Attenuator Made by Using New Electrochromic Devices; Badenes, G., Abbott, D., Serpenguzel, A., Eds.; Sevilla, Spain, 2005; p 389. <https://doi.org/10.1117/12.608391>.
- (90) McDonagh, A. M.; Bayly, S. R.; Riley, D. J.; Ward, M. D.; McCleverty, J. A.; Cowin, M. A.; Morgan, C. N.; Varrazza, R.; Penty, R. V.; White, I. H. A Variable Optical Attenuator Operating in the Near-Infrared Region Based on an Electrochromic Molybdenum Complex. *Chem. Mater.* **2000**, 12 (9), 2523–2524. <https://doi.org/10.1021/cm001104b>.
- (91) Zhang, J. Near Infrared Electrochromic Variable Optical Attenuator Based on Ruthenium Complex and Polycrystalline Tungsten Oxide. *Chin. Sci. Bull.* **2005**, 50 (23), 2688. <https://doi.org/10.1360/04wb0116>.
- (92) Zheng, J.; Zheng, Y.; Wan, X. Near Infrared Electrochromic Variable Optical Attenuator Fabricated by Layer-by-Layer Assembly. *Chin. J. Polym. Sci.* **2011**, 29 (1), 117–123. <https://doi.org/10.1007/s10118-010-1007-5>.
- (93) He, B.; Neo, W. T.; Chen, T. L.; Klivansky, L. M.; Wang, H.; Tan, T.; Teat, S. J.; Xu, J.; Liu, Y. Low Band-gap Conjugated Polymers Based on a Nature-Inspired Bay-Annulated Indigo (BAI) Acceptor as Stable Electrochromic Materials. *ACS Sustain. Chem. Eng.* **2016**, 4 (5), 2797–2805. <https://doi.org/10.1021/acssuschemeng.6b00303>.
- (94) Upputuri, P. K.; Pramanik, M. Photoacoustic Imaging in the Second Near-Infrared Window: A Review. *J. Biomed. Opt.* **2019**, 24 (04), 1. <https://doi.org/10.1117/1.JBO.24.4.040901>.
- (95) Jiang, Y.; Pu, K. Advanced Photoacoustic Imaging Applications of Near-Infrared Absorbing Organic Nanoparticles. *Small* **2017**, 13 (30), 1700710. <https://doi.org/10.1002/smll.201700710>.
- (96) Jiang, Y.; Upputuri, P. K.; Xie, C.; Lyu, Y.; Zhang, L.; Xiong, Q.; Pramanik, M.; Pu, K. Broadband Absorbing Semiconducting Polymer Nanoparticles for Photoacoustic Imaging in Second Near-Infrared Window. *Nano Lett.* **2017**, 17 (8), 4964–4969. <https://doi.org/10.1021/acs.nanolett.7b02106>.
- (97) Sun, T.; Dou, J.-H.; Liu, S.; Wang, X.; Zheng, X.; Wang, Y.; Pei, J.; Xie, Z. Second Near-Infrared Conjugated Polymer Nanoparticles for Photoacoustic Imaging and Photothermal Therapy. *ACS Appl. Mater. Interfaces* **2018**, 10 (9), 7919–7926. <https://doi.org/10.1021/acsami.8b01458>.
- (98) Deng, K.; Li, C.; Huang, S.; Xing, B.; Jin, D.; Zeng, Q.; Hou, Z.; Lin, J. Recent Progress in Near Infrared Light Triggered Photodynamic Therapy. *Small* **2017**, 13 (44), 1702299. <https://doi.org/10.1002/smll.201702299>.
- (99) Allison, R. R.; Bagnato, V. S.; Sibata, C. H. Future of Oncologic Photodynamic Therapy. *Future Oncol.* **2010**, 6 (6), 929–940. <https://doi.org/10.2217/fon.10.51>.
- (100) Ucar, E.; Seven, O.; Lee, D.; Kim, G.; Yoon, J.; Akkaya, E. U. Selectivity in Photodynamic Action: Higher Activity of Mitochondria Targeting Photosensitizers in Cancer Cells. *ChemPhotoChem* **2019**, cptc.201800231. <https://doi.org/10.1002/cptc.201800231>.
- (101) Kwiatkowski, S.; Knap, B.; Przystupski, D.; Saczko, J.; Kędzierska, E.; Knap-Czop, K.; Kotlińska, J.; Michel, O.; Kotowski, K.; Kulbacka, J. Photodynamic Therapy – Mechanisms, Photosensitizers and Combinations. *Biomed. Pharmacother.* **2018**, 106, 1098–1107. <https://doi.org/10.1016/j.biopha.2018.07.049>.
- (102) Yuan, P.; Ruan, Z.; Yan, L. Tetraphenylporphine-Modified Polymeric Nanoparticles Containing NIR Photosensitizer for Mitochondria-Targeting and Imaging-Guided

- Photodynamic Therapy. *ACS Biomater. Sci. Eng.* **2020**, *6* (2), 1043–1051. <https://doi.org/10.1021/acsbio.3c01662>.
- (103) Jung, H. S.; Verwilt, P.; Sharma, A.; Shin, J.; Sessler, J. L.; Kim, J. S. Organic Molecule-Based Photothermal Agents: An Expanding Photothermal Therapy Universe. *Chem. Soc. Rev.* **2018**, *47* (7), 2280–2297. <https://doi.org/10.1039/C7CS00522A>.
- (104) Wang, J.; Qiu, J. A Review of Organic Nanomaterials in Photothermal Cancer Therapy. *Cancer Res. Front.* **2016**, *2* (1), 67–84. <https://doi.org/10.17980/2016.67>.
- (105) Sheng, W.; He, S.; Seare, W. J.; Almutairi, A. Review of the Progress toward Achieving Heat Confinement—the Holy Grail of Photothermal Therapy. *J. Biomed. Opt.* **2017**, *22* (8), 080901. <https://doi.org/10.1117/1.JBO.22.8.080901>.
- (106) Chen, Y.; Li, L.; Chen, W.; Chen, H.; Yin, J. Near-Infrared Small Molecular Fluorescent Dyes for Photothermal Therapy. *Chin. Chem. Lett.* **2019**, *30* (7), 1353–1360. <https://doi.org/10.1016/j.ccllet.2019.02.003>.
- (107) Liu, Y.; Bhattarai, P.; Dai, Z.; Chen, X. Photothermal Therapy and Photoacoustic Imaging via Nanotheranostics in Fighting Cancer. *Chem. Soc. Rev.* **2019**, *48* (7), 2053–2108. <https://doi.org/10.1039/C8CS00618K>.
- (108) Xu, L.; Cheng, L.; Wang, C.; Peng, R.; Liu, Z. Conjugated Polymers for Photothermal Therapy of Cancer. *Polym Chem* **2014**, *5* (5), 1573–1580. <https://doi.org/10.1039/C3PY01196>.
- (109) Zhou, J.; Lu, Z.; Zhu, X.; Wang, X.; Liao, Y.; Ma, Z.; Li, F. NIR Photothermal Therapy Using Polyaniline Nanoparticles. *Biomaterials* **2013**, *34* (37), 9584–9592. <https://doi.org/10.1016/j.biomaterials.2013.08.075>.
- (110) Yang, K.; Xu, H.; Cheng, L.; Sun, C.; Wang, J.; Liu, Z. In Vitro and In Vivo Near-Infrared Photothermal Therapy of Cancer Using Polypyrrole Organic Nanoparticles. *Adv. Mater.* **2012**, *24* (41), 5586–5592. <https://doi.org/10.1002/adma.201202625>.
- (111) MacNeill, C. M.; Wailes, E. M.; Levi-Polyachenko, N. H. A Comparative Study of the Photothermal Efficiency of Electrically Conducting Poly(3,4-Ethylenedioxythiophene)-Based Nanomaterials with Cancer Cells. *J. Nanosci. Nanotechnol.* **2013**, *13* (6), 3784–3791. <https://doi.org/10.1166/jnn.2013.7211>.
- (112) MacNeill, C. M.; Coffin, R. C.; Carroll, D. L.; Levi-Polyachenko, N. H. Low Band Gap Donor-Acceptor Conjugated Polymer Nanoparticles and Their NIR-Mediated Thermal Ablation of Cancer Cells. *Macromol. Biosci.* **2013**, *13* (1), 28–34. <https://doi.org/10.1002/mabi.201200241>.
- (113) Song, X.; Gong, H.; Yin, S.; Cheng, L.; Wang, C.; Li, Z.; Li, Y.; Wang, X.; Liu, G.; Liu, Z. Ultra-Small Iron Oxide Doped Polypyrrole Nanoparticles for In Vivo Multimodal Imaging Guided Photothermal Therapy. *Adv. Funct. Mater.* **2014**, *24* (9), 1194–1201. <https://doi.org/10.1002/adfm.201302463>.
- (114) Liu, Y.; Ai, K.; Liu, J.; Deng, M.; He, Y.; Lu, L. Dopamine-Melanin Colloidal Nanospheres: An Efficient Near-Infrared Photothermal Therapeutic Agent for In Vivo Cancer Therapy. *Adv. Mater.* **2013**, *25* (9), 1353–1359. <https://doi.org/10.1002/adma.201204683>.
- (115) Sun, T.; Qi, J.; Zheng, M.; Xie, Z.; Wang, Z.; Jing, X. Thiadiazole Molecules and Poly(Ethylene Glycol)-Block-Polylactide Self-Assembled Nanoparticles as Effective Photothermal Agents. *Colloids Surf. B Biointerfaces* **2015**, *136*, 201–206. <https://doi.org/10.1016/j.colsurfb.2015.09.020>.
- (116) Wang, W.; Wang, L.; Li, Y.; Liu, S.; Xie, Z.; Jing, X. Nanoscale Polymer Metal-Organic Framework Hybrids for Effective Photothermal Therapy of Colon Cancers. *Adv. Mater.* **2016**, *28* (42), 9320–9325. <https://doi.org/10.1002/adma.201602997>.



- (117) Wu, Y.; Wang, K.; Huang, S.; Yang, C.; Wang, M. Near-Infrared Light-Responsive Semiconductor Polymer Composite Hydrogels: Spatial/Temporal-Controlled Release via a Photothermal “Sponge” Effect. *ACS Appl. Mater. Interfaces* **2017**, *9* (15), 13602–13610. <https://doi.org/10.1021/acsami.7b01016>.
- (118) Bundgaard, E.; Krebs, F. Low Band Gap Polymers for Organic Photovoltaics. *Sol. Energy Mater. Sol. Cells* **2007**, *91* (11), 954–985. <https://doi.org/10.1016/j.solmat.2007.01.015>.
- (119) Rasmussen, S. Low-Band-gap Polymers. In *Encyclopedia of Polymeric Nanomaterials*; Kobayashi, S., Müllen, K., Eds.; Springer Berlin Heidelberg: Berlin, Heidelberg, 2013; pp 1–13. [https://doi.org/10.1007/978-3-642-36199-9\\_5-1](https://doi.org/10.1007/978-3-642-36199-9_5-1).
- (120) Liu, C.; Wang, K.; Gong, X.; Heeger, A. J. Low Band-gap Semiconducting Polymers for Polymeric Photovoltaics. *Chem. Soc. Rev.* **2016**, *45* (17), 4825–4846. <https://doi.org/10.1039/C5CS00650C>.
- (121) Kobayashi, M.; Colaneri, N.; Boysel, M.; Wudl, F.; Heeger, A. J. The Electronic and Electrochemical Properties of Poly(Isothianaphthene). *J. Chem. Phys.* **1985**, *82* (12), 5717–5723. <https://doi.org/10.1063/1.448559>.
- (122) Xu, T.; Yu, L. How to Design Low Band-gap Polymers for Highly Efficient Organic Solar Cells. *Mater. Today* **2014**, *17* (1), 11–15. <https://doi.org/10.1016/j.mattod.2013.12.005>.
- (123) Liang, Y.; Wu, Y.; Feng, D.; Tsai, S.-T.; Son, H.-J.; Li, G.; Yu, L. Development of New Semiconducting Polymers for High Performance Solar Cells. *J. Am. Chem. Soc.* **2009**, *131* (1), 56–57. <https://doi.org/10.1021/ja808373p>.
- (124) Osaka, I.; Shimawaki, M.; Mori, H.; Doi, I.; Miyazaki, E.; Koganezawa, T.; Takimiya, K. Synthesis, Characterization, and Transistor and Solar Cell Applications of a Naphthobisthiadiazole-Based Semiconducting Polymer. *J. Am. Chem. Soc.* **2012**, *134* (7), 3498–3507. <https://doi.org/10.1021/ja210687r>.
- (125) Li, G.; Chang, W.-H.; Yang, Y. Low-Band-gap Conjugated Polymers Enabling Solution-Processable Tandem Solar Cells. *Nat. Rev. Mater.* **2017**, *2* (8). <https://doi.org/10.1038/natrevmats.2017.43>.
- (126) Brus, V. V.; Lee, J.; Luginbuhl, B.; Ko, S.; Bazan, G. C.; Nguyen, T. Solution-Processed Semitransparent Organic Photovoltaics: From Molecular Design to Device Performance. *Adv. Mater.* **2019**, 1900904. <https://doi.org/10.1002/adma.201900904>.
- (127) Bakhshi, A. K.; Kaur, A.; Arora, V. Molecular Engineering of Novel Low Band Gap Conducting Polymers. *INDIAN J CHEM* **2012**, *13*.
- (128) Havinga, E. E.; ten Hoeve, W.; Wynberg, H. Alternate Donor-Acceptor Small-Band-Gap Semiconducting Polymers; Polysquaraines and Polycroconaines. *Synth. Met.* **1993**, *55* (1), 299–306. [https://doi.org/10.1016/0379-6779\(93\)90949-W](https://doi.org/10.1016/0379-6779(93)90949-W).
- (129) van Mullekom, H. Developments in the Chemistry and Band Gap Engineering of Donor–Acceptor Substituted Conjugated Polymers. *Mater. Sci. Eng. R Rep.* **2001**, *32* (1), 1–40. [https://doi.org/10.1016/S0927-796X\(00\)00029-2](https://doi.org/10.1016/S0927-796X(00)00029-2).
- (130) Gao, Y.; Liu, M.; Zhang, Y.; Liu, Z.; Yang, Y.; Zhao, L. Recent Development on Narrow Band-gap Conjugated Polymers for Polymer Solar Cells. *Polymers* **2017**, *9* (12), 39. <https://doi.org/10.3390/polym9020039>.
- (131) Chochos, C. L.; Drakopoulou, S.; Katsouras, A.; Squeo, B. M.; Sprau, C.; Colsmann, A.; Gregoriou, V. G.; Cando, A.-P.; Allard, S.; Scherf, U.; Gasparini, N.; Kazerouni, N.; Ameri, T.; Brabec, C. J.; Avgeropoulos, A. Beyond Donor-Acceptor (D-A) Approach: Structure-Optoelectronic Properties-Organic Photovoltaic Performance Correlation in New D-A<sub>1</sub>-D-A<sub>2</sub> Low-Band-gap Conjugated Polymers. *Macromol. Rapid Commun.* **2017**, *38* (7), 1600720. <https://doi.org/10.1002/marc.201600720>.

- (132) Yuen, J. D.; Kumar, R.; Zakhidov, D.; Seifert, J.; Lim, B.; Heeger, A. J.; Wudl, F. Ambipolarity in Benzobisthiadiazole-Based Donor-Acceptor Conjugated Polymers. *Adv. Mater.* **2011**, n/a-n/a. <https://doi.org/10.1002/adma.201101134>.
- (133) Yokozawa, T.; Ohta, Y. Transformation of Step-Growth Polymerization into Living Chain-Growth Polymerization. *Chem. Rev.* **2016**, *116* (4), 1950–1968. <https://doi.org/10.1021/acs.chemrev.5b00393>.
- (134) Billiet, L.; Fournier, D.; Du Prez, F. Step-Growth Polymerization and ‘Click’ Chemistry: The Oldest Polymers Rejuvenated. *Polymer* **2009**, *50* (16), 3877–3886. <https://doi.org/10.1016/j.polymer.2009.06.034>.
- (135) Koltzenburg, S.; Maskos, M.; Nuyken, O. *Polymer Chemistry*; Springer Berlin Heidelberg: Berlin, Heidelberg, 2017. <https://doi.org/10.1007/978-3-662-49279-6>.
- (136) Dove, A. P.; Meier, M. A. R. Step-Growth Polymerization in the 21st Century. *Macromol. Chem. Phys.* **2014**, *215* (22), 2135–2137. <https://doi.org/10.1002/macp.201400512>.
- (137) Hiemenz, P. C.; Lodge, T. *Polymer Chemistry*, 2nd ed.; CRC Press: Boca Raton, 2007.
- (138) Hamaide, T. Du bon usage du degré de polymérisation en nombre. 6.
- (139) Koizumi, T.; Kanbara, T. Cross-Coupling Polymerization. In *Organometallic Reactions and Polymerization*; Osakada, K., Ed.; Lecture Notes in Chemistry; Springer Berlin Heidelberg: Berlin, Heidelberg, 2014; Vol. 85, pp 271–301. [https://doi.org/10.1007/978-3-662-43539-7\\_8](https://doi.org/10.1007/978-3-662-43539-7_8).
- (140) Xu, S.; Kim, E. H.; Wei, A.; Negishi, E. Pd- and Ni-Catalyzed Cross-Coupling Reactions in the Synthesis of Organic Electronic Materials. *Sci. Technol. Adv. Mater.* **2014**, *15* (4), 044201. <https://doi.org/10.1088/1468-6996/15/4/044201>.
- (141) Dua, S. S.; Eaborn, C.; Walton, R. M. REACTIONS OF ORGANIC HALIDES WITH R<sub>3</sub>MMR<sub>3</sub> COMPOUNDS (M = Si, Ge, Sn) IN THE PRESENCE OF TETRAKIS(TRIARYLPHOSPHINE) PALLADIUM. 3.
- (142) Milstein, D.; Stille, J. K. A General, Selective, and Facile Method for Ketone Synthesis from Acid Chlorides and Organotin Compounds Catalyzed by Palladium. *J. Am. Chem. Soc.* **1978**, *3*.
- (143) Yu, L.; Bao, Z.; Cai, R. Conjugated, Liquid Crystalline Polymers. *Angew. Chem. Int. Ed. Engl.* **1993**, *32* (9), 1345–1347. <https://doi.org/10.1002/anie.199313451>.
- (144) Espinet, P.; Echavarren, A. M. The Mechanisms of the Stille Reaction. *Angew. Chem. Int. Ed.* **2004**. <https://doi.org/10.1002/anie.200300638>.
- (145) Carsten, B.; He, F.; Son, H. J.; Xu, T.; Yu, L. Stille Polycondensation for Synthesis of Functional Materials. *Chem. Rev.* **2011**, *111* (3), 1493–1528. <https://doi.org/10.1021/cr100320w>.
- (146) Amatore, C.; El Kaïm, L.; Grimaud, L.; Jutand, A.; Meignié, A.; Romanov, G. Kinetic Data on the Synergetic Role of Amines and Water in the Reduction of Phosphine-Ligated Palladium(II) to Palladium(0). *Eur. J. Org. Chem.* **2014**, *2014* (22), 4709–4713. <https://doi.org/10.1002/ejoc.201402519>.
- (147) Cordovilla, C.; Bartolomé, C.; Martínez-Illarduya, J. M.; Espinet, P. The Stille Reaction, 38 Years Later. *ACS Catal.* **2015**, *5* (5), 3040–3053. <https://doi.org/10.1021/acscatal.5b00448>.
- (148) Menzel, K.; Fu, G. C. Room-Temperature Stille Cross-Couplings of Alkenyltin Reagents and Functionalized Alkyl Bromides That Possess  $\beta$  Hydrogens. *J. Am. Chem. Soc.* **2003**, *125* (13), 3718–3719. <https://doi.org/10.1021/ja0344563>.
- (149) Huang, H.; Jiao, G.; Liu, S.; Li, Q.; Shi, X.; Fu, N.; Wang, L.; Zhao, B.; Huang, W. Unprecedented Side Reactions in Stille Coupling: Desired Ones for Stille

- Polycondensation. *Chem. Commun.* **2015**, 51 (87), 15846–15849. <https://doi.org/10.1039/C5CC05404D>.
- (150) Vangerven, T.; Verstappen, P.; Patil, N.; D’Haen, J.; Cardinaletti, I.; Benduhn, J.; Van den Brande, N.; Defour, M.; Lemaux, V.; Beljonne, D.; Lazzaroni, R.; Champagne, B.; Vandewal, K.; Andreasen, J. W.; Adriaensens, P.; Breiby, D. W.; Van Mele, B.; Vanderzande, D.; Maes, W.; Manca, J. Elucidating Batch-to-Batch Variation Caused by Homocoupled Side Products in Solution-Processable Organic Solar Cells. *Chem. Mater.* **2016**, 28 (24), 9088–9098. <https://doi.org/10.1021/acs.chemmater.6b04143>.
- (151) Van den Brande, N.; Defour, M.; Liu, Z.; Verstappen, P.; Nies, E.; Maes, W.; Van Assche, G.; Van Mele, B. Homocoupling Defects of a Small Donor Molecule for Organic Photovoltaics: Quantification of the Eutectic State Diagram by Rapid Heat–Cool Differential Scanning Calorimetry. *J. Phys. Chem. C* **2019**, 123 (36), 22634–22642. <https://doi.org/10.1021/acs.jpcc.9b06336>.
- (152) Vangerven, T.; Verstappen, P.; Drijkoningen, J.; Dierckx, W.; Himmelberger, S.; Salleo, A.; Vanderzande, D.; Maes, W.; Manca, J. V. Molar Mass versus Polymer Solar Cell Performance: Highlighting the Role of Homocouplings. *Chem. Mater.* **2015**, 27 (10), 3726–3732. <https://doi.org/10.1021/acs.chemmater.5b00939>.
- (153) Heintges, G. H. L.; Janssen, R. A. J. On the Homocoupling of Trialkylstannyl Monomers in the Synthesis of Diketopyrrolopyrrole Polymers and Its Effect on the Performance of Polymer-Fullerene Photovoltaic Cells. *RSC Adv.* **2019**, 9 (28), 15703–15714. <https://doi.org/10.1039/C9RA02670C>.
- (154) Pirotte, G.; Kesters, J.; Cardeynals, T.; Verstappen, P.; D’Haen, J.; Lutsen, L.; Champagne, B.; Vanderzande, D.; Maes, W. The Impact of Acceptor-Acceptor Homocoupling on the Optoelectronic Properties and Photovoltaic Performance of PDTSQ<sub>x</sub> ff Low Band-gap Polymers. *Macromol. Rapid Commun.* **2018**, 39 (14), 1800086. <https://doi.org/10.1002/marc.201800086>.
- (155) Tierney, S.; Heeney, M.; McCulloch, I. Microwave-Assisted Synthesis of Polythiophenes via the Stille Coupling. *Synth. Met.* **2005**, 148 (2), 195–198. <https://doi.org/10.1016/j.synthmet.2004.09.015>.
- (156) Hardeman, T.; Van Den Eede, M.-P.; Verheyen, L.; Koeckelberghs, G. Controlled Synthesis of Conjugated Polymers and Block Copolymers. In *Synthetic Methods for Conjugated Polymers and Carbon Materials*; Leclerc, M., Morin, J.-F., Eds.; Wiley-VCH Verlag GmbH & Co. KGaA: Weinheim, Germany, 2017; pp 97–130. <https://doi.org/10.1002/9783527695959.ch3>.
- (157) Ebdon, J. R. Principles of Polymerization George Odian John Wiley and Sons, Inc., New York, 1991. Pp. 768, Price E47.50. ISBN 0-471-61020-8. *Polym. Int.* **1993**, 30 (2), 281–281. <https://doi.org/10.1002/pi.4990300223>.
- (158) Knoester, H. Theoretical Derivation of the Molecular Weight Distribution of End-Capped Linear Condensation Polymers. *Macromol. Theory Simul.* **2009**, 18 (1), 61–69. <https://doi.org/10.1002/mats.200800062>.
- (159) Schmücker, S.; Kuckling, D. Enhanced Preparation of Alkoxyamine-Functionalized Poly(*p*-Phenylene)s and Their Use as Macroinitiators for the Synthesis of Stimuli-Responsive Coil-Rod-Coil Block Copolymers. *Macromol. Chem. Phys.* **2012**, 213 (16), 1725–1734. <https://doi.org/10.1002/macp.201200178>.
- (160) Funston, A. M.; Silverman, E. E.; Miller, J. R.; Schanze, K. S. Charge Transfer through Terthiophene End-Capped Poly(Arylene Ethynylene)s. *J. Phys. Chem. B* **2004**, 108 (5), 1544–1555. <https://doi.org/10.1021/jp0364396>.
- (161) Dan, K.; Ghosh, S. Stimuli Responsive Triblock Copolymers by Chain-Growth Polymerization from Telechelic Macroinitiators Prepared via a Step-Growth

- Polymerization. *Polym Chem* **2014**, *5* (12), 3901–3909.  
<https://doi.org/10.1039/C4PY00078A>.
- (162) Harris, J. D.; Carter, K. R. A One-Pot Strategy to Improve End-Capping Efficacy in Stille Poly-Condensations. *Polym. Chem.* **2018**, *9* (9), 1132–1138.  
<https://doi.org/10.1039/C7PY01761H>.
- (163) Wang, L.; Qiao, Z.; Gao, C.; Liu, J.; Zhang, Z.-G.; Li, X.; Li, Y.; Wang, H. End-Capping Effect of Quinoxalino[2,3-*b*]Porphyrin on Donor–Acceptor Copolymer and Improved Performance of Polymer Solar Cells. *Macromolecules* **2016**, *49* (10), 3723–3732. <https://doi.org/10.1021/acs.macromol.6b00507>.
- (164) Robb, M. J.; Montarnal, D.; Eisenmenger, N. D.; Ku, S.-Y.; Chabinye, M. L.; Hawker, C. J. A One-Step Strategy for End-Functionalized Donor–Acceptor Conjugated Polymers. *Macromolecules* **2013**, *46* (16), 6431–6438.  
<https://doi.org/10.1021/ma401255d>.
- (165) Koldemir, U.; Puniredd, S. R.; Wagner, M.; Tongay, S.; McCarley, T. D.; Kamenov, G. D.; Müllen, K.; Pisula, W.; Reynolds, J. R. End Capping Does Matter: Enhanced Order and Charge Transport in Conjugated Donor–Acceptor Polymers. *Macromolecules* **2015**, *48* (18), 6369–6377.  
<https://doi.org/10.1021/acs.macromol.5b01252>.
- (166) Park, J. K.; Jo, J.; Seo, J. H.; Moon, J. S.; Park, Y. D.; Lee, K.; Heeger, A. J.; Bazan, G. C. End-Capping Effect of a Narrow Band-gap Conjugated Polymer on Bulk Heterojunction Solar Cells. *Adv. Mater.* **2011**, *23* (21), 2430–2435.  
<https://doi.org/10.1002/adma.201004629>.
- (167) Kim, S.; Park, J. K.; Park, Y. D. Charge Transport Behaviors of End-Capped Narrow Band Gap Polymers in Bottom-Contact Organic Field-Effect Transistors. *RSC Adv* **2014**, *4* (74), 39268–39272. <https://doi.org/10.1039/C4RA05873A>.
- (168) Cox, J. R.; Kang, H. A.; Igarashi, T.; Swager, T. M. Norbornadiene End-Capping of Cross-Coupling Polymerizations: A Facile Route to Triblock Polymers. *ACS Macro Lett.* **2012**, *1* (2), 334–337. <https://doi.org/10.1021/mz200205k>.
- (169) Baycan Koyuncu, F.; Davis, A. R.; Carter, K. R. Emissive Conjugated Polymer Networks with Tunable Band-Gaps via Thiol–Ene Click Chemistry. *Chem. Mater.* **2012**, *24* (22), 4410–4416. <https://doi.org/10.1021/cm302790a>.
- (170) Aivali, S.; Kakogianni, S.; Anastasopoulos, C.; Andreopoulou, A.; Kallitsis, J. Copolymers and Hybrids Based on Carbazole Derivatives and Their Nanomorphology Investigation. *Nanomaterials* **2019**, *9* (2), 133. <https://doi.org/10.3390/nano9020133>.
- (171) Handa, N. V.; Serrano, A. V.; Robb, M. J.; Hawker, C. J. Exploring the Synthesis and Impact of End-Functional Poly(3-Hexylthiophene). *J. Polym. Sci. Part Polym. Chem.* **2015**, *53* (7), 831–841. <https://doi.org/10.1002/pola.27522>.
- (172) Sun, H.; Zhang, S.; Yang, Y.; Li, X.; Zhan, H.; Cheng, Y. Excellent Control of Perylene Diimide End Group in Polyfluorene via Suzuki Catalyst Transfer Polymerization. *Macromol. Chem. Phys.* **2016**, *217* (24), 2726–2735.  
<https://doi.org/10.1002/macp.201600412>.
- (173) Aplan, M. P.; Gomez, E. D. Recent Developments in Chain-Growth Polymerizations of Conjugated Polymers. *Ind. Eng. Chem. Res.* **2017**, *56* (28), 7888–7901.  
<https://doi.org/10.1021/acs.iecr.7b01030>.
- (174) Zhang, H.-H.; Hu, Q.-S.; Hong, K. Accessing Conjugated Polymers with Precisely Controlled Heterobifunctional Chain Ends via Post-Polymerization Modification of the OTf Group and Controlled Pd(0)/*t*-Bu<sub>3</sub>P-Catalyzed Suzuki Cross-Coupling Polymerization. *Chem. Commun.* **2015**, *51* (80), 14869–14872.  
<https://doi.org/10.1039/C5CC06188A>.

- (175) Bousquet, A.; Awada, H.; Hiorns, R. C.; Dagrón-Lartigau, C.; Billon, L. Conjugated-Polymer Grafting on Inorganic and Organic Substrates: A New Trend in Organic Electronic Materials. *Prog. Polym. Sci.* **2014**, *39* (11), 1847–1877. <https://doi.org/10.1016/j.progpolymsci.2014.03.003>.
- (176) Dayal, S.; Kopidakis, N.; Olson, D. C.; Ginley, D. S.; Rumbles, G. Photovoltaic Devices with a Low Band Gap Polymer and CdSe Nanostructures Exceeding 3% Efficiency. *Nano Lett.* **2010**, *10* (1), 239–242. <https://doi.org/10.1021/nl903406s>.
- (177) Al-Asbahi, B. Influence of SiO<sub>2</sub>/TiO<sub>2</sub> Nanocomposite on the Optoelectronic Properties of PFO/MEH-PPV-Based OLED Devices. *Polymers* **2018**, *10* (7), 800. <https://doi.org/10.3390/polym10070800>.
- (178) Nguyen, T.-P. Polymer-Based Nanocomposites for Organic Optoelectronic Devices. A Review. *Surf. Coat. Technol.* **2011**, *206* (4), 742–752. <https://doi.org/10.1016/j.surfcoat.2011.07.010>.
- (179) Wang, S.; Kang, Y.; Wang, L.; Zhang, H.; Wang, Y.; Wang, Y. Organic/Inorganic Hybrid Sensors: A Review. *Sens. Actuators B Chem.* **2013**, *182*, 467–481. <https://doi.org/10.1016/j.snb.2013.03.042>.
- (180) Kagan, C. R. Organic-Inorganic Hybrid Materials as Semiconducting Channels in Thin-Film Field-Effect Transistors. *Science* **1999**, *286* (5441), 945–947. <https://doi.org/10.1126/science.286.5441.945>.
- (181) Liras, M.; Barawi, M.; de la Peña O’Shea, V. A. Hybrid Materials Based on Conjugated Polymers and Inorganic Semiconductors as Photocatalysts: From Environmental to Energy Applications. *Chem. Soc. Rev.* **2019**, *48* (22), 5454–5487. <https://doi.org/10.1039/C9CS00377K>.
- (182) Giussi, J. M.; Cortez, M. L.; Marmisollé, W. A.; Azzaroni, O. Practical Use of Polymer Brushes in Sustainable Energy Applications: Interfacial Nanoarchitectonics for High-Efficiency Devices. *Chem. Soc. Rev.* **2019**, *48* (3), 814–849. <https://doi.org/10.1039/C8CS00705E>.
- (183) Wang, S.; Wang, Z.; Li, J.; Li, L.; Hu, W. Surface-Grafting Polymers: From Chemistry to Organic Electronics. *Mater. Chem. Front.* **2020**, *4* (3), 692–714. <https://doi.org/10.1039/C9QM00450E>.
- (184) Murugan, P.; Krishnamurthy, M.; Jaisankar, S. N.; Samanta, D.; Mandal, A. B. Controlled Decoration of the Surface with Macromolecules: Polymerization on a Self-Assembled Monolayer (SAM). *Chem. Soc. Rev.* **2015**, *44* (10), 3212–3243. <https://doi.org/10.1039/C4CS00378K>.
- (185) Mohammadi Sejoubsari, R.; Martinez, A. P.; Kutes, Y.; Wang, Z.; Dobrynin, A. V.; Adamson, D. H. “Grafting-Through”: Growing Polymer Brushes by Supplying Monomers through the Surface. *Macromolecules* **2016**, *49* (7), 2477–2483. <https://doi.org/10.1021/acs.macromol.6b00183>.
- (186) Awada, H.; Bousquet, A.; Dagrón-Lartigau, C.; Billon, L. Surface-Initiated Polymerization of A–A/B–B Type Conjugated Monomers by Palladium-Catalyzed Stille Polycondensation: Towards Low Band Gap Polymer Brushes. *RSC Adv.* **2015**, *5* (96), 78436–78440. <https://doi.org/10.1039/C5RA08027D>.
- (187) Mansky, P. Controlling Polymer-Surface Interactions with Random Copolymer Brushes. *Science* **1997**, *275* (5305), 1458–1460. <https://doi.org/10.1126/science.275.5305.1458>.
- (188) Sahu, D.; Chu, H.-C.; Yang, P.-J.; Lin, H.-C. Surface Modification of Gold Nanorods by Grafting Fluorene-Based Conjugated Copolymers Containing Thiol-Pendants. *Macromol. Chem. Phys.* **2012**, *213* (15), 1550–1558. <https://doi.org/10.1002/macp.201100550>.

- (189) Kim, S. H.; Singu, B. S.; Yoon, K. R. Synthesis and Surface Modification of Hybrid Multiblock Gold–Nickel–Polypyrrole Nanorods by Poly(Fluorene) and Their Optical Properties. *J. Ind. Eng. Chem.* **2015**, *30*, 174–182. <https://doi.org/10.1016/j.jiec.2015.05.019>.
- (190) Strover, L. T.; McCulloch, B.; Ho, V.; Segalman, R.; Malmström, J.; McGillivray, D. J.; Sejdic, J. T. Tuning the Optoelectronic Properties of P3EHT Block Copolymers by Surface Modification. *Int. J. Nanotechnol.* **2017**, *14* (1/2/3/4/5/6), 540. <https://doi.org/10.1504/IJNT.2017.082481>.
- (191) Wang, J.; Higashihara, T. Synthesis of All-Conjugated Donor–Acceptor Block Copolymers and Their Application in All-Polymer Solar Cells. *Polym. Chem.* **2013**, *4* (22), 5518–5526.
- (192) Wu, W.-C.; Chen, C.-Y.; Lee, W.-Y.; Chen, W.-C. Stimuli-Responsive Conjugated Rod-Coil Block Copolymers: Synthesis, Morphology, and Applications. *Polymer* **2015**, *65*, A1–A16. <https://doi.org/10.1016/j.polymer.2015.03.035>.
- (193) Lin, Y.-H.; Smith, K. A.; Kempf, C. N.; Verduzco, R. Synthesis and Crystallinity of All-Conjugated Poly(3-Hexylthiophene) Block Copolymers. *Polym Chem* **2013**, *4* (2), 229–232. <https://doi.org/10.1039/C2PY20830J>.
- (194) Asawapirom, U.; Güntner, R.; Forster, M.; Scherf, U. Semiconducting Block Copolymers—Synthesis and Nanostructure Formation. *Thin Solid Films* **2005**, *477* (1–2), 48–52. <https://doi.org/10.1016/j.tsf.2004.08.155>.
- (195) Brochon, C.; Hadziioannou, G. Controlled Radical Polymerizations as Versatile Synthetic Routes for Conjugated Rod-Coil Block Copolymers and Their Use as Active Polymer Semiconducting Materials in Flexible Organic Electronic Devices and Systems. In *Controlled/Living Radical Polymerization: Progress in ATRP*; Matyjaszewski, K., Ed.; ACS Symposium Series; American Chemical Society: Washington DC, 2009; Vol. 1023, pp 243–256. <https://doi.org/10.1021/bk-2009-1023.ch017>.
- (196) Van De Wetering, K.; Brochon, C.; Ngov, C.; Hadziioannou, G. Design and Synthesis of a Low Band Gap Conjugated Macroinitiator: Toward Rod–Coil Donor–Acceptor Block Copolymers. *Macromolecules* **2006**, *39* (13), 4289–4297. <https://doi.org/10.1021/ma060497i>.
- (197) Stalmach, U.; de Boer, B.; Videlot, C.; van Hutten, P. F.; Hadziioannou, G. Semiconducting Diblock Copolymers Synthesized by Means of Controlled Radical Polymerization Techniques. *J. Am. Chem. Soc.* **2000**, *122* (23), 5464–5472. <https://doi.org/10.1021/ja000160a>.
- (198) Tao, Y.; McCulloch, B.; Kim, S.; Segalman, R. A. The Relationship between Morphology and Performance of Donor–Acceptor Rod–Coil Block Copolymer Solar Cells. *Soft Matter* **2009**, *5* (21), 4219. <https://doi.org/10.1039/b907836c>.
- (199) Wang, S.; Jin, X.; Yao, B.; Wang, P.; Du, X.; Dong, L.; Wang, X.; Zhu, X.; Huang, W. Well-Defined Structures and Nanoscale Morphology for All-Conjugated BCPs. *Micro Nano Lett.* **2019**, *14* (8), 928–931. <https://doi.org/10.1049/mnl.2019.0002>.
- (200) Wang, S.; Jin, X.; Yao, B.; Du, X.; Dong, L.; Wang, X.; Huang, W. Influence of the Molecular Weight in P3HT Block on Fully Conjugated Block Copolymers. *Synth. Met.* **2019**, *253*, 20–25. <https://doi.org/10.1016/j.synthmet.2019.04.025>.
- (201) Di Mauro, A. E.; Toscanini, M.; Piovani, D.; Samperi, F.; Curri, M. L.; Corricelli, M.; De Caro, L.; Siliqi, D.; Comparelli, R.; Agostiano, A.; Destri, S.; Striccoli, M. Segmented Poly(Styrene-Co-Vinylpyridine) as Multivalent Host for CdSe Nanocrystal Based Nanocomposites. *Eur. Polym. J.* **2014**, *60*, 222–234. <https://doi.org/10.1016/j.eurpolymj.2014.09.010>.

- (202) Zappia, S.; Destri, S.; Striccoli, M.; Curri, M. L.; di Mauro, A. E.; Ameer, Z.; Maruccio, G.; Rizzo, A.; Mastria, R. Morphological Study of CdSe Nanocrystals Passivated with a Low Band Gap Rod-Coil Diblock Copolymer for Hybrid Solar Cells. *Adv. Sci. Technol.* **2014**, *93*, 235–240. <https://doi.org/10.4028/www.scientific.net/AST.93.235>.
- (203) Todd, A. D.; Bielawski, C. W. Controlled Synthesis of an Alternating Donor–Acceptor Conjugated Polymer via Kumada Catalyst-Transfer Polycondensation. *ACS Macro Lett.* **2015**, *4* (11), 1254–1258. <https://doi.org/10.1021/acsmacrolett.5b00505>.
- (204) He, M.; Qiu, F.; Lin, Z. Conjugated Rod–Coil and Rod–Rod Block Copolymers for Photovoltaic Applications. *J. Mater. Chem.* **2011**, *21* (43), 17039–17048.
- (205) Lee, Y.; Gomez, E. D. Challenges and Opportunities in the Development of Conjugated Block Copolymers for Photovoltaics. *Macromolecules* **2015**, *48* (20), 7385–7395. <https://doi.org/10.1021/acs.macromol.5b00112>.
- (206) Wang, J.; Ueda, M.; Higashihara, T. Synthesis and Morphology of All-Conjugated Donor-Acceptor Block Copolymers Based on Poly(3-Hexylthiophene) and Poly(Naphthalene Diimide). *J. Polym. Sci. Part Polym. Chem.* **2014**, *52* (8), 1139–1148. <https://doi.org/10.1002/pola.27097>.
- (207) Wang, J.; Ueda, M.; Higashihara, T. Synthesis of All-Conjugated Donor–Acceptor–Donor ABA-Type Triblock Copolymers via Kumada Catalyst-Transfer Polycondensation. *ACS Macro Lett.* **2013**, *2* (6), 506–510. <https://doi.org/10.1021/mz400143y>.
- (208) Nakabayashi, K.; Mori, H. All-Polymer Solar Cells Based on Fully Conjugated Block Copolymers Composed of Poly(3-Hexylthiophene) and Poly(Naphthalene Bisimide) Segments. *Macromolecules* **2012**, *45* (24), 9618–9625. <https://doi.org/10.1021/ma302170e>.
- (209) Park, S. H.; Kim, Y.; Kwon, N. Y.; Lee, Y. W.; Woo, H. Y.; Chae, W.; Park, S.; Cho, M. J.; Choi, D. H. Significantly Improved Morphology and Efficiency of Nonhalogenated Solvent-Processed Solar Cells Derived from a Conjugated Donor–Acceptor Block Copolymer. *Adv. Sci.* **2020**, *7* (4), 1902470. <https://doi.org/10.1002/advs.201902470>.
- (210) Wang, S.; Yang, Q.; Tao, Y.; Guo, Y.; Yang, J.; Liu, Y.; Zhao, L.; Xie, Z.; Huang, W. Fully Conjugated Block Copolymers for Single-Component Solar Cells: Synthesis, Purification, and Characterization. *New J. Chem.* **2016**, *40* (2), 1825–1833. <https://doi.org/10.1039/C5NJ02636A>.
- (211) Wang, S.; Liu, Y.; Yang, J.; Tao, Y.; Guo, Y.; Cao, X.; Zhang, Z.; Li, Y.; Huang, W. Orthogonal Solubility in Fully Conjugated Donor-Acceptor Block Copolymers: Compatibilizers for Polymer/Fullerene Bulk-Heterojunction Solar Cells. *Chin. J. Polym. Sci.* **2017**, *35* (2), 207–218. <https://doi.org/10.1007/s10118-017-1889-6>.
- (212) Grieco, C.; Aplan, M. P.; Rimshaw, A.; Lee, Y.; Le, T. P.; Zhang, W.; Wang, Q.; Milner, S. T.; Gomez, E. D.; Asbury, J. B. Molecular Rectification in Conjugated Block Copolymer Photovoltaics. *J. Phys. Chem. C* **2016**, *120* (13), 6978–6988. <https://doi.org/10.1021/acs.jpcc.6b00103>.
- (213) Lee, Y.; Aplan, M. P.; Seibers, Z. D.; Xie, R.; Culp, T. E.; Wang, C.; Hexemer, A.; Kilbey, S. M.; Wang, Q.; Gomez, E. D. Random Copolymers Allow Control of Crystallization and Microphase Separation in Fully Conjugated Block Copolymers. *Macromolecules* **2018**, *51* (21), 8844–8852. <https://doi.org/10.1021/acs.macromol.8b01859>.
- (214) Rahmanudin, A.; Yao, L.; Sekar, A.; Cho, H.-H.; Liu, Y.; Lhermitte, C. R.; Sivula, K. Fully Conjugated Donor–Acceptor Block Copolymers for Organic Photovoltaics via

- Heck–Mizoroki Coupling. *ACS Macro Lett.* **2019**, *8* (2), 134–139.  
<https://doi.org/10.1021/acsmacrolett.8b00932>.
- (215) de Cuendias, A.; Hiorns, R. C.; Cloutet, E.; Vignau, L.; Cramail, H. Conjugated Rod-Coil Block Copolymers and Optoelectronic Applications: Conjugated Rod-Coil Block Copolymers. *Polym. Int.* **2010**, *59* (11), 1452–1476. <https://doi.org/10.1002/pi.2915>.
- (216) Liu, C.-L.; Lin, C.-H.; Kuo, C.-C.; Lin, S.-T.; Chen, W.-C. Conjugated Rod–Coil Block Copolymers: Synthesis, Morphology, Photophysical Properties, and Stimuli-Responsive Applications. *Prog. Polym. Sci.* **2011**, *36* (5), 603–637.  
<https://doi.org/10.1016/j.progpolymsci.2010.07.008>.
- (217) Kallitsis, J. K.; Andreopoulou, A. K. Rigid–Flexible and Rod–Coil Copolymers. In *Polymer Science: A Comprehensive Reference*; Elsevier, 2012; pp 725–773.  
<https://doi.org/10.1016/B978-0-444-53349-4.00177-1>.
- (218) Kuo, C.-C.; Liu, C.-L.; Chen, W.-C. Morphologies and Photophysical Properties of Conjugated Rod-Coil Block Copolymers. In *Complex Macromolecular Architectures*; Hadjichristidis, N., Hirao, A., Tezuka, Y., Du Prez, F., Eds.; John Wiley & Sons (Asia) Pte Ltd: Singapore, 2011; pp 593–622.  
<https://doi.org/10.1002/9780470825150.ch19>.
- (219) Lin, C.-H.; Tung, Y.-C.; Ruokolainen, J.; Mezzenga, R.; Chen, W.-C. Poly[2,7-(9,9-Dihexylfluorene)]-Block-Poly(2-Vinylpyridine) Rod–Coil and Coil–Rod–Coil Block Copolymers: Synthesis, Morphology and Photophysical Properties in Methanol/THF Mixed Solvents. *Macromolecules* **2008**, *41* (22), 8759–8769.  
<https://doi.org/10.1021/ma8016629>.
- (220) Tung, Y.-C.; Wu, W.-C.; Chen, W.-C. Morphological Transformation and Photophysical Properties of Rod-Coil Poly[2,7-(9,9-Dihexylfluorene)]-Block-Poly(Acrylic Acid) in Solution. *Macromol. Rapid Commun.* **2006**, *27* (21), 1838–1844. <https://doi.org/10.1002/marc.200600518>.
- (221) Olsen, B.; Segalman, R. Self-Assembly of Rod–Coil Block Copolymers. *Mater. Sci. Eng. R Rep.* **2008**, *62* (2), 37–66. <https://doi.org/10.1016/j.mser.2008.04.001>.
- (222) Lu, S.; Liu, T.; Ke, L.; Ma, D.-G.; Chua, S.-J.; Huang, W. Polyfluorene-Based Light-Emitting Rod–Coil Block Copolymers. *Macromolecules* **2005**, *38* (20), 8494–8502.  
<https://doi.org/10.1021/ma050267o>.
- (223) Sauv e, G.; McCullough, R. D. High Field-Effect Mobilities for Diblock Copolymers of Poly(3-Hexylthiophene) and Poly(Methyl Acrylate). *Adv. Mater.* **2007**, *19* (14), 1822–1825. <https://doi.org/10.1002/adma.200602368>.
- (224) Zappia, S.; Mendichi, R.; Battiato, S.; Scavia, G.; Mastria, R.; Samperi, F.; Destri, S. Characterization of Amphiphilic Block-Copolymers Constituted of a Low Band Gap Rigid Segment (PCPDTBT) and P4VP Based Coil Block Synthesized by Two Different Strategies. *Polymer* **2015**, *80*, 245–258.  
<https://doi.org/10.1016/j.polymer.2015.10.062>.
- (225) Zappia, S.; Di Mauro, A. E.; Mastria, R.; Rizzo, A.; Curri, M. L.; Striccoli, M.; Destri, S. Rod-Coil Block Copolymer as Nanostructuring Compatibilizer for Efficient CdSe NCs/PCPDTBT Hybrid Solar Cells. *Eur. Polym. J.* **2016**, *78*, 352–363.  
<https://doi.org/10.1016/j.eurpolymj.2016.03.021>.
- (226) Ferretti, A. M.; Zappia, S.; Scavia, G.; Giovanella, U.; Villafiorita-Monteleone, F.; Destri, S. Surfactant-Free Miniemulsion Approach for Low Band Gap Rod-Coil Block Copolymer Water-Processable Nanoparticle Fabrication: Film Preparation and Morphological Characterization. *Polymer* **2019**, *174*, 61–69.  
<https://doi.org/10.1016/j.polymer.2019.04.055>.
- (227) Ho, C.-C.; Lee, Y.-H.; Dai, C.-A.; Segalman, R. A.; Su, W.-F. Synthesis and Self-Assembly of Poly(Diethylhexyloxy-*p*-Phenylenevinylene)-*b*-Poly(Methyl



- Methacrylate) Rod–Coil Block Copolymers. *Macromolecules* **2009**, *42* (12), 4208–4219. <https://doi.org/10.1021/ma802551v>.
- (228) Olsen, B. D.; Segalman, R. A. Structure and Thermodynamics of Weakly Segregated Rod–Coil Block Copolymers. *Macromolecules* **2005**, *38* (24), 10127–10137. <https://doi.org/10.1021/ma051468v>.
- (229) Bicciochi, E.; Haeussler, M.; Rizzardo, E.; Scully, A. D.; Ghiggino, K. P. Donor-Acceptor Rod-Coil Block Copolymers Comprising Poly[2,7-(9,9-Dihexylfluorene)-*Alt* -Bithiophene] and Fullerene as Compatibilizers for Organic Photovoltaic Devices. *J. Polym. Sci. Part Polym. Chem.* **2015**, *53* (7), 888–903. <https://doi.org/10.1002/pola.27514>.
- (230) Bicciochi, E.; Chen, M.; Rizzardo, E.; Ghiggino, K. P. Synthesis of a Rod–Coil Block Copolymer Incorporating PCBM. *Polym Chem* **2013**, *4* (1), 53–56. <https://doi.org/10.1039/C2PY20507F>.
- (231) Schweicher, G.; Garbay, G.; Jouclas, R.; Vibert, F.; Devaux, F.; Geerts, Y. H. Molecular Semiconductors for Logic Operations: Dead-End or Bright Future? *Adv. Mater.* **2020**, *32* (10), 1905909. <https://doi.org/10.1002/adma.201905909>.
- (232) Kumari, P.; Bera, M. K.; Malik, S.; Kuila, B. K. Amphiphilic and Thermoresponsive Conjugated Block Copolymer with Its Solvent Dependent Optical and Photoluminescence Properties: Toward Sensing Applications. *ACS Appl. Mater. Interfaces* **2015**, *7* (23), 12348–12354. <https://doi.org/10.1021/am507266e>.

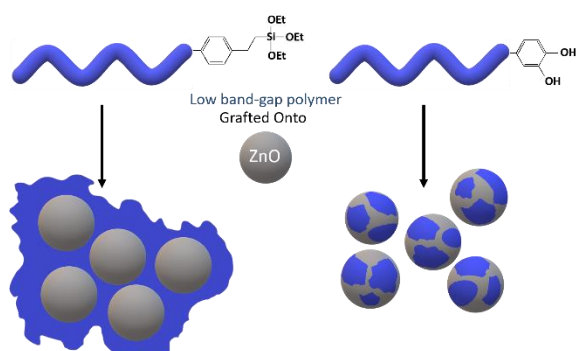
# Chapter 2

## Chapter 2: Low band-gap polymer brushes: influence of the end-group on the morphology of core-shell nanoparticles

Most of the content of this chapter has been published in *Reactive and Functional Polymers*:

Adèle Gapin, Hisham Idriss, Sylvie Blanc, Laurent Billon, Marie-Hélène Delville, Antoine Bousquet, Christine Lartigau-Dagron, Low band-gap polymer brushes: Influence of the end-group on the morphology of core-shell nanoparticles, *Reactive and Functional Polymers*, 2020, 155, 104700, <https://doi.org/10.1016/j.reactfunctpolym.2020.104700>

### Abstract



An efficient strategy is described to prepare electron donor/acceptor hybrid nanoparticles by anchoring a low band-gap polymer onto zinc oxide spheres. Functional macromolecules, bearing triethoxysilane or catechol terminal groups, were synthesized by polycondensation, using a ternary blend reaction, i.e. mixing two

monomers and an end-capper. Importantly, and in agreement with Carothers theory, the amount of end-capper allowed control over the chain molar mass. ZnO spherical nanoparticles were then grafted with the polymer chains and TEM images confirmed that core@shell materials were formed. The surface morphology of these hybrid materials was dependent on the anchoring agent. When silane functionalized polymers were used, cross-linked aggregates were obtained due to competition between self-condensation of silanes and reaction with ZnO surface hydroxyl groups. On the contrary, well-dispersed core-shell particles were synthesized with catechol polymers as anchoring agents. This grafting onto methodology led to patchy nanoparticles on which both zinc oxide and polymer surfaces were accessible. The optical properties of the hybrid material were ascertained by UV-visible absorption and photoluminescence to show specific quenching of the polymer fluorescence by the metal oxide.

## Table of Contents

I. Introduction:.....	108
II. Results and discussion: .....	111
1) Synthesis of end-functional low band-gap polymers. ....	111
2) Grafting of P(DTS-BT) on the surface of zinc oxide nanoparticles.....	118
3) Photophysics of the hybrid nanoparticles. ....	123
4) Elaboration of photovoltaic devices. ....	125
III. Conclusion .....	127
IV. References.....	128

## I. Introduction:

The development of conjugated polymers (CPs) was very active in the last decades with the discovery of their electrical conductivity and their use in optoelectronic devices such as polymer solar cells (PSCs)<sup>1</sup>, organic field effect transistors (OFETs)<sup>2</sup> or photodetectors (PDs)<sup>3</sup>. In the field of PSCs, the improvement of the active layer efficiency was the topic of intensive research.<sup>4</sup> The bulk heterojunction is based on the blend of electron donors (conjugated polymers) and electron acceptors. Within the electron donors, low band-gap (LBG) conjugated polymers have nowadays outperformed classical CPs thanks to their well-localized absorption in the solar spectrum due to a band-gap smaller than 1.6 eV and their number of delocalized  $\pi$  electrons.<sup>5</sup> Their ability to harvest more photons than classical CPs comes from their chemical structure made of an alternation of two co-monomers, an electron-rich monomer, which produces a rise of the polymer HOMO energy level and an electron-deficient monomer inducing a lowering of the polymer LUMO energy level.<sup>6,7</sup> Concerning electron acceptors, fullerene derivatives showed limited stability and challenges recently emerged.<sup>8,9</sup> Among them, metal oxide nanoparticles, especially titanium dioxide (TiO<sub>2</sub>) and zinc oxide (ZnO)<sup>10</sup>, are studied because of their low toxicity (unlike cadmium selenide) and the possibility of tailoring their electronic properties by doping or changing their morphologies and dimensions.

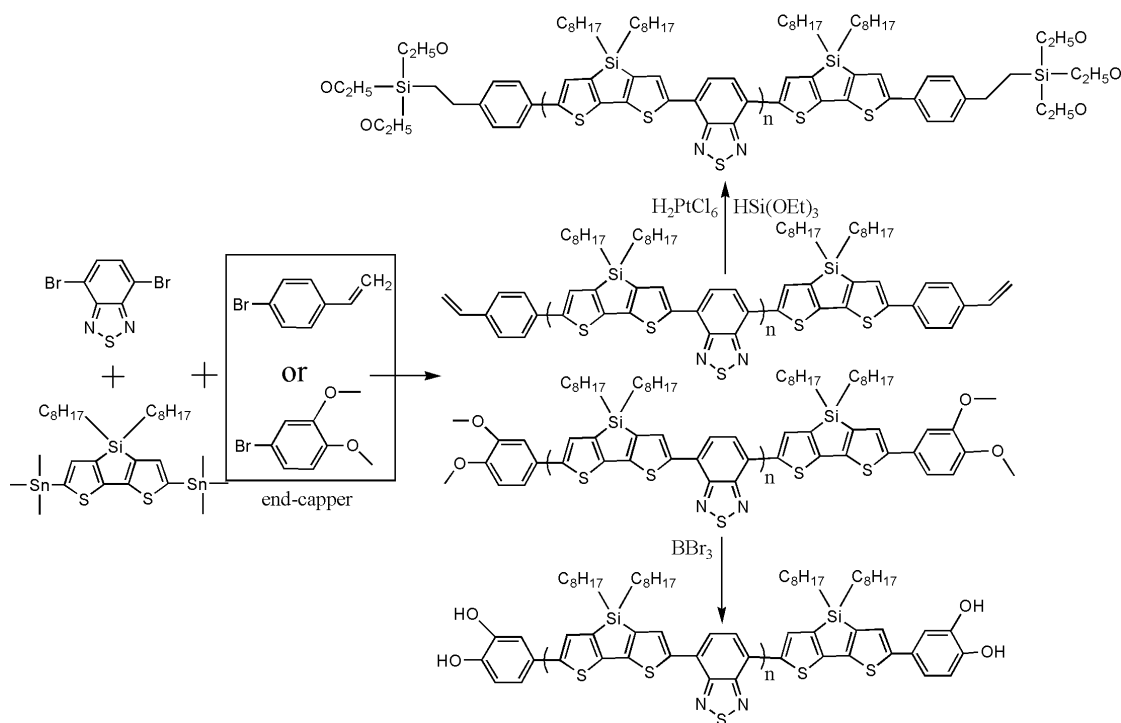
Consequently hybrid solar cells, composed of a bulk heterojunction between an inorganic material as an acceptor and a conjugated polymer as a donor matrix, came out.<sup>11,12</sup> Recently, hybrid materials based on conjugated polymers were successfully developed in which the macromolecules were covalently attached to the surface of an inorganic material.<sup>13</sup> These novel materials raised promises of enhanced interfacial properties<sup>14,15</sup> with the optimization of particles dispersion, charge injection or transport.<sup>16-18</sup> Chen *et al.* reported the elaboration of core-shell nanoparticles presenting a poly[4,4'-bis(2-ethylhexyl)-dithienosilol-2,6-diyl]-*alt*-(2,1,3-benzothiadiazol-4,7-diyl) (PSBTBT-NH<sub>2</sub>) corona grafted on cadmium telluride (CdTe) tetrapod.<sup>19</sup> This hybrid material has been used as the active layer of solar cell and a 3.2% power conversion efficiency was achieved. Awada *et al.* grafted poly(3-hexylthiophene) (P3HT) to replace the hydrophilic blend PEDOT/PSS (poly(ethylenedioxythiophene)-poly(styrene sulfonate)) used as hole transporting layer in photovoltaic devices. The water penetration in the cell was then impeded which significantly improved lifetime of device.<sup>20</sup> Pioneering studies showed the potential of these technologies in photovoltaics but their performances are limited by the difficulty of the hybrid material synthesis.<sup>19,21-24</sup> Indeed, most of the inorganics are

## Chapter 2: Low band-gap polymer brushes: influence of the end-group on the morphology of core-shell nanoparticles

grafted with the well-known P3HT because its polymerization is based on a chain-growth mechanism, allowing an easy end-capping<sup>25</sup> with anchoring functions such as silane, thiols or carboxylic acids.<sup>26-29</sup> On the contrary, LBG polymers are synthesized *via* a step-growth mechanism and their end-functionalization is more challenging and reports are scarce.<sup>30-33</sup> In a previous publication, we reported the use of surface-initiated polycondensation to grow low band-gap polymers brushes from of metal oxide nanorods.<sup>34</sup> By using this technique, a high polymer grafting density has been obtained with a homogeneous polymer corona surrounding the inorganic core. Actually, this is not the ideal morphology for photovoltaic application since it hinders electron percolation between acceptor domains (particle cores).<sup>13</sup>

Therefore, effort has been made in this study to reduce the grafting density in order to obtain patchy particles in which both polymer and metal oxide surfaces can be reached by electron and hole. This chapter describes a methodology to end-functionalize low band-gap polymers with triethoxysilane or catechol groups in order to bind metal oxide surfaces (Scheme 1). These functions have been inserted at the end of the poly[(4,4'-bis(2-ethylhexyl)dithieno-[3,2-b:2',3'-d]silole)-2,6-diyl-alt-(2,1,3-benzothiadiazole)-4,7-diyl] P(DTS-BT) by using a ternary blend of comonomers in the polycondensation media. The influence of the end-capper quantity on the molar mass and the chain functionality is described. Then, polymer chains were grafted, to create an organic corona around the zinc oxide nanoparticles (NPs). Synthesis, morphological, electronic properties, and photovoltaic performances are finally discussed.

## Chapter 2: Low band-gap polymer brushes: influence of the end-group on the morphology of core-shell nanoparticles



Scheme 1: Synthetic methodology for the end-capping of low band-gap polymers (considering a complete conversion)

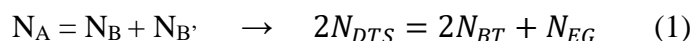
In the context of the PhD project, this first chapter was a way to learn, understand, and develop skills in the field of Stille polycondensation with monomers easy to synthesize. It was an upstream preparation prior to the other chapters. Thus, this chapter was used to understand and master the end-functionalization of conjugated polymers with different small molecules and study the influence of the stoichiometry of the end-capper on the length of the chains. This project also aimed at carrying on research in the topic of grafting low band-gap polymers onto specific substrates in the framework of the previous studies conducted in the team. Indeed, Awada *et al.* employed the grafting from technique to anchor a P(DTS-BT) onto zinc oxide nanorods but they obtained high grafting densities with crosslinking phenomenon between the nanoparticles.<sup>34</sup> Hence, this chapter was developed to bring new methodologies to graft low band-gap polymers onto nanoparticles with lower grafting densities and obtain patchy particles.

## II. Results and discussion:

In this synthetic part, a low band-gap was end-functionalized with a reactive end-capper and grafted onto ZnO nanospheres.

### 1) Synthesis of end-functional low band-gap polymers.

In this study, 4,7-dibromo-2,1,3-benzothiadiazole (BT) and 4,4'-bis(2-ethyl-hexyl)-5,5'-bis(trimethyltin)-dithieno[3,2-b:2',3'-d]silole (DTS) have been polymerized *via* a Stille cross-coupling reaction, using a Pd<sup>0</sup> catalyst and 4-bromostyrene as an end-capper (monofunctional) to synthesize a vinyl end-functionalized polymer. This copolymer was chosen for its broad absorption, high hole mobility, good photochemical stability and a reasonable power conversion efficiency of 5.1 %.<sup>35</sup> Monomers were obtained with high purity (synthesis and characterization in Chapter 5: Experimental Part). 4-bromostyrene was selected as an appropriate end-capper due to its Stille polymerizable bromophenyl group and the presence of the alkene allowing unambiguous characterization of the resulting end-functional material. In this kind of reaction, the stoichiometry of monomer to end-capping unit is a key factor that determines the length of the chain and the degree of end-group introduction. In this chapter, the stoichiometry of the reagents was maintained according to equation 1:



In which  $N_A$ ,  $N_B$ ,  $N_{B'}$  represent the mole number of stannate functions and bromide groups pertaining to the BT monomer and to the end-capping agent, respectively.  $N_{DTS}$ ,  $N_{BT}$  and  $N_{EG}$  define the mole number of DTS and BT monomers and bromostyrene end-groups (EG), respectively. By following this stoichiometry, the total number of aryl bromides is equal to the total number of aryl stannanes and the formation of chains bearing 4-bromostyrene is promoted. The number average degree of polymerization ( $DP_n$ ) of polymers obtained in the case of an A-A and B-B polycondensation, like DTS and BT, with an end-capper agent, can be predicted using the Carothers equation (eq 2)<sup>36,37</sup>:

$$\overline{DP}_n = \frac{1+r}{1+r-2rp} \quad (2)$$

In which  $r$  is the ratio of monomer groups, and  $p$  is the conversion. It should be noted that in this equation,  $DP_n$  counts the number of DTS + BT units, so it is twice the number of repeat



units  $n$  used in the calculation of the number average molar mass  $M_n$ . Therefore,  $M_n$  can be calculated as follows:

$$\bar{M}_n = M_0 \frac{\overline{DPn}}{2} = \frac{M_0}{2} \frac{1+r}{1+r-2rp} \quad (3)$$

Where  $M_0$  is the molar mass of the repeat unit. When monofunctional reagent (as the end-capping agent) is introduced, the monomer group ratio is defined by the equation 4<sup>38</sup>:

$$r = \frac{N_A}{N_B+2N_{B'}} = \frac{2N_{DTS}}{2N_{BT}+2N_{EG}} = \frac{N_{DTS}}{N_{BT}+N_{EG}} \quad (4)$$

Where the factor 2 relative to  $N_{B'}$  enters in the equation because the end-capper reagent has the same effect on the degree of polymerization than a difunctional monomer therefore is two times more effective.

Three end-functional polymers were synthesized in chlorobenzene by varying the initial bromostyrene molar equivalent  $N_{EG} = 0, 0.08$  and  $0.16$  (Table 1). After purification by precipitation and Soxhlet extraction (as indicated in the experimental part), <sup>1</sup>H NMR, Size-exclusion chromatography (SEC) and MALDI-ToF analyses were performed to characterize these polymers. First, we used NMR not only to verify the proton structure of the polymer but also to calculate the ratio between the repetitive units and the end-group ( $n_{DTSBT}/n_{EG}$ , Table 1). By comparing the integral of the peak at 5.8 ppm corresponding to the vinyl double bond (styrene, d Figure 1) to the signal from 7.7 to 8.4 ppm referring to the aromatic protons of DTS and BT units (f and g in Figure 1), we estimated this  $n_{DTSBT}/n_{EG}$  ratio in the final polymers. For P(DTS-BT)-BrS<sub>(1)</sub>, which is the polymer synthesized with a bromostyrene (BrS) molar equivalent of 0.08, this ratio was 7. Thanks to the Carothers equation (2), the theoretical  $DP_n$  was calculated to be 49 (at 100 % conversion), corresponding to 24 DTS-BT repetitive units. Since bromostyrene has been included in the stoichiometry (equation 1), styrene units should be at both end-chains for a 100 % conversion. Therefore, for this polymer, the theoretical  $n_{DTSBT}/n_{EG}$  ratio is 12 (reported in Table 1). The difference between the theory and the experiment may be due to conversion, since a theoretical 98 % conversion leads to a repetitive unit (DTS-BT) to styrene ratio of 7.

## Chapter 2: Low band-gap polymer brushes: influence of the end-group on the morphology of core-shell nanoparticles

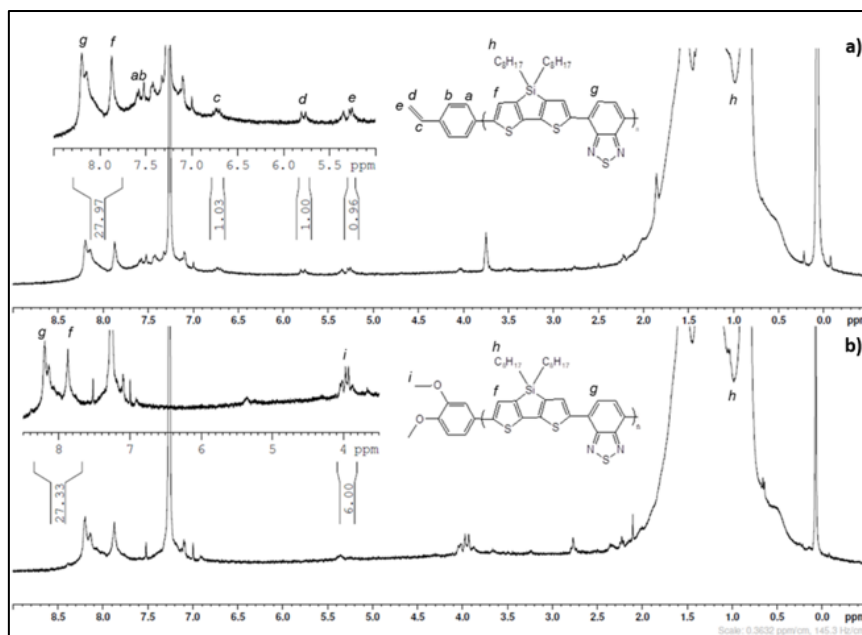


Figure 1: <sup>1</sup>H NMR spectra of P(DTS-BT)-BrS<sub>(1)</sub> (a) and P(DTS-BT)-BrV (b) (400 MHz, CDCl<sub>3</sub>)

For P(DTS-BT)-BrS<sub>(2)</sub>, a bromostyrene molar equivalent of 0.16 was used to study the possibility to tune the molar mass of the sample. From the <sup>1</sup>H NMR spectrum (Figure 2) the DTS-BT/styrene ratio is decreased to 5 which is really close to the theoretical value of 7 repetitive units given by Carothers equation. If the ratio of repeat units to vinyl bonds can be calculated, no information can be provided on the effective number of end-groups per polymer chain.

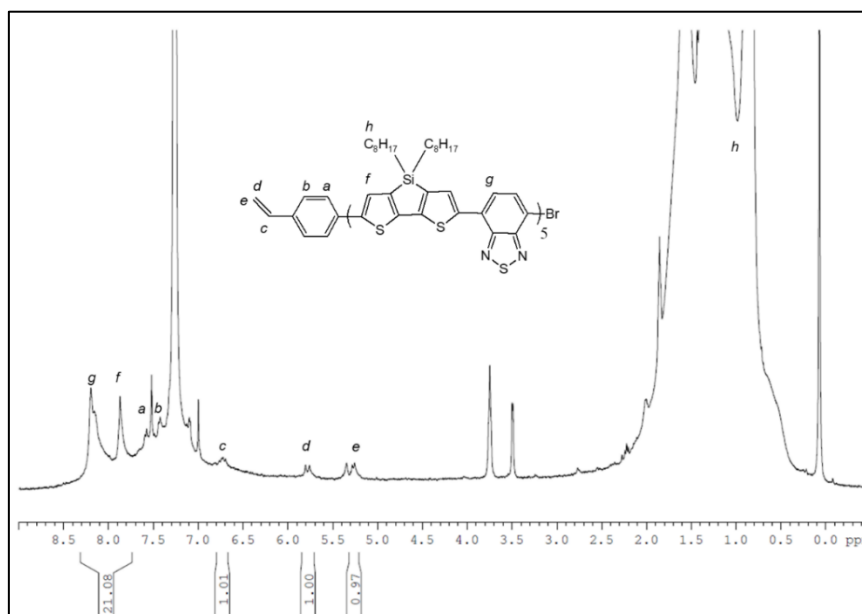


Figure 2: <sup>1</sup>H NMR spectrum (400MHz, CDCl<sub>3</sub>) of P(DTS-BT)-BrS<sub>(2)</sub>

Table 1: Macromolecular characteristics of the synthesized copolymers.

Polymer	$r^a$	$N_{DTS}^b$	$N_{BT}^b$	$N_{EG}^b$	$n_{DTSBT}/n_{EG}^c$	$n_{DTSBT}/n_{EG}^d$	$Mn_{th}^c$	$Mn^d$	$Mn^e$	$Mw^e$	$\mathcal{D}^e$
P(DTS-BT)	1	1	1	0	$\infty$	-	$\infty$	-	5 000	9 200	1.8
P(DTS-BT)-BrS <sub>(1)</sub>	0.96	1	0.96	0.08	12	7	13 300	7 900	4 800	8 800	1.8
P(DTS-BT)-BrS <sub>(2)</sub>	0.93	1	0.92	0.16	7	5	7 200	5 700	4 500	8 800	2.0
P(DTS-BT)-BrV	0.94	1	0.94	0.12	9	7	9 200	8 000	4 000	8 000	2.0

<sup>a</sup> feed ratio calculated according to equation (3), <sup>b</sup> molar equivalent; <sup>c</sup> calculated from the Carothers equation (2) and based on the hypothesis of 100 % conversion, i.e. 2 end-group per chains; <sup>d</sup> based on <sup>1</sup>H NMR; <sup>e</sup> measured by SEC with a UV detector at 678 nm.

Therefore MALDI-ToF analysis was performed and allowed defining and quantifying chain end-groups. As a technique limitation, only low molar mass chains can be analyzed ( $M \leq 3000 \text{ g.mol}^{-1}$ , see Figure 3). Figure 4 shows a zoom of the P(DTS-BT)-BrS<sub>(2)</sub> sample for the populations with a  $1900 \leq M \leq 2500 \text{ g.mol}^{-1}$ . Several populations appeared and it was not possible to assign them all. However, populations with abundance higher than 10 % were identified. Thus, several information from the mass spectrum can be extracted as the presence of di-capped, mono-capped and non-functionalized chains. For example, the assigned peaks with green circle, blue triangle and yellow star have been assigned to non-functionalized, mono-capped and end-capped chains, respectively, on the basis of the styrene molar mass difference. From the overall MALDI-ToF spectrum, a quantification of each population can be estimated with 28 % of difunctionalized  $\alpha, \omega$ -styrene chains, 47 % of mono-functionalized and 25 % of non-functionalized. Therefore, a total of 75 % of the chains were styrene end-capped, in agreement with the <sup>1</sup>H NMR spectrum showing that the conversion was not total. Moreover, some DTS homo-coupling was detected as already shown by Harris *et al.*<sup>33</sup>

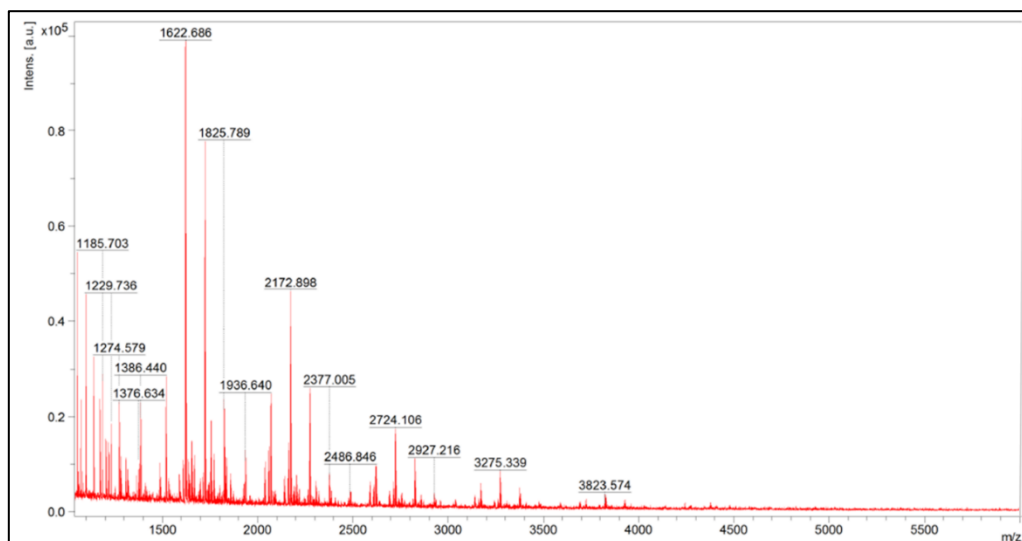


Figure 3: MALDI-TOF general spectrum of P(DTS-BT)-BrS<sub>(2)</sub>

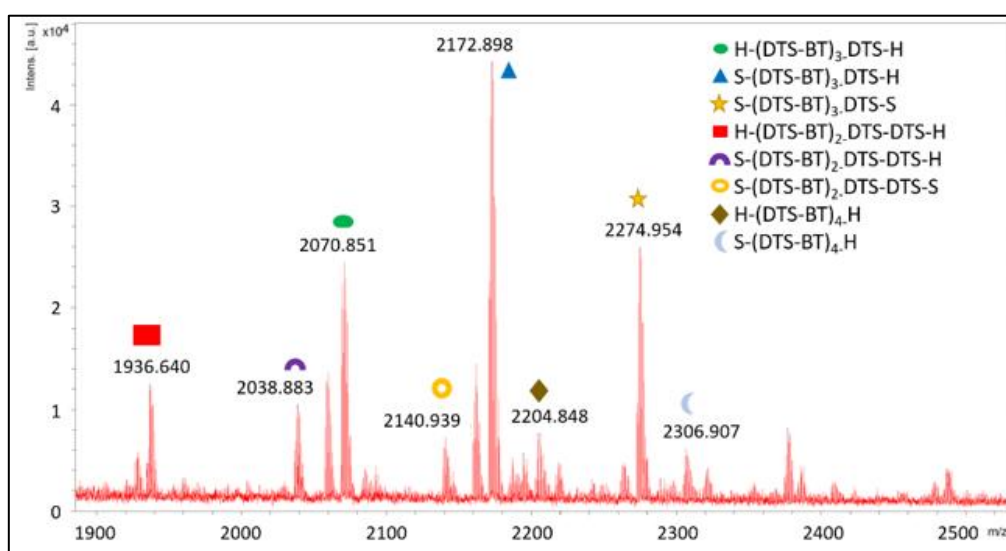


Figure 4: MALDI-ToF zoom spectra of P(DTS-BT)-BrS<sub>(2)</sub> for the populations with a  $1900 \leq M \leq 2500 \text{ g.mol}^{-1}$

Size exclusion chromatography was performed on both polymers (Figure 5) and reasonable dispersity values around  $\mathcal{D} = 2$  were obtained.  $M_n$  and  $M_w$  from 4000 to 9200  $\text{g.mol}^{-1}$  were calculated from conventional calibration using polystyrene samples.

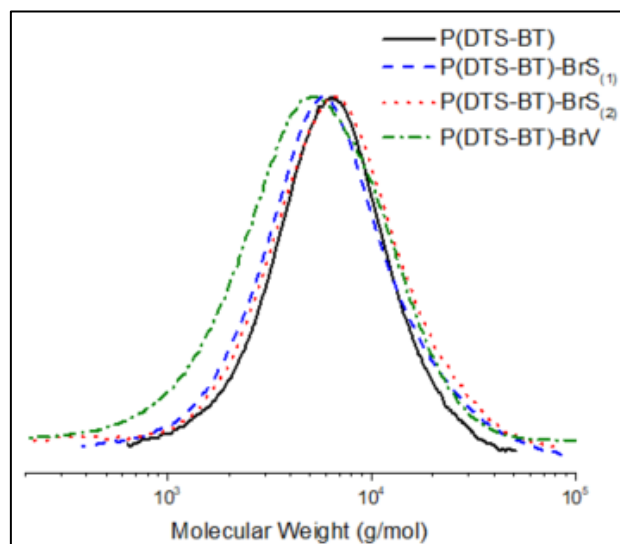


Figure 5: SEC chromatograms of the copolymers synthesized in this study (UV detector)

Using UV-visible spectrophotometry, the maximum absorption was found at 680 nm and the optical band gap evaluated at 1.51 eV (estimated from the low energy band edge of the optical spectrum,  $\lambda_{\text{onset}} = 820$  nm,  $E_g = 1240/\lambda_{\text{onset}}$  eV, Figure 6). Comparison of absorption spectra with literature confirmed that the degree of polymerization was high enough to reach the maximum conjugation length.<sup>39</sup> The end-functionalized copolymers showed a shoulder at 850 nm while the homopolymer does not present such behavior. This result could be due to the different solubility of the functionalized copolymers in which the  $\pi$ -stacking phenomenon is favored.

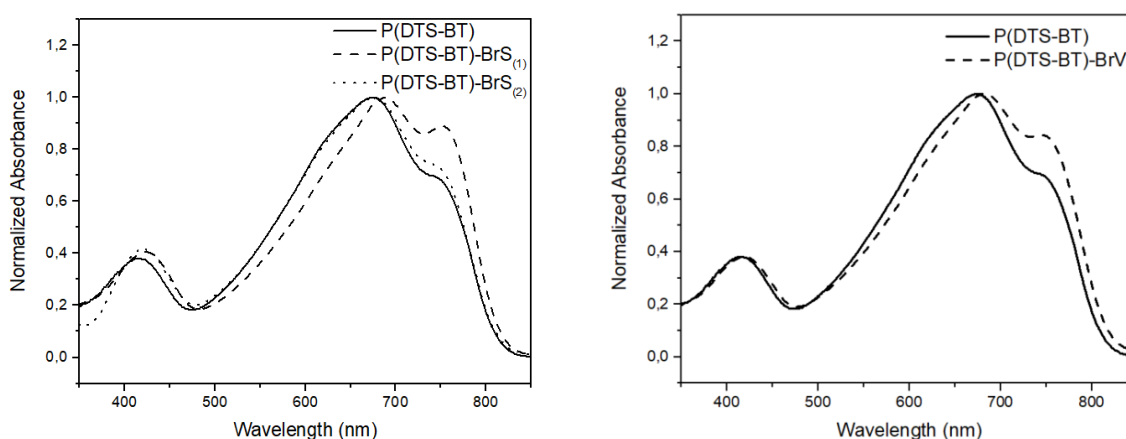


Figure 6: UV-visible absorption spectra of chloroform solutions of P(DTS-BT), P(DTS-BT)-BrS<sub>(1)</sub>, P(DTS-BT)-BrS<sub>(2)</sub>, and P(DTS-BT)-BrV

## Chapter 2: Low band-gap polymer brushes: influence of the end-group on the morphology of core-shell nanoparticles

Further post-functionalization *via* hydrosilylation of the vinyl moiety was performed under dry conditions to modify the alkene into a triethoxysilane end-group in quantitative yields. This group is well known to react by hydrolysis-condensation with hydroxyl surface functions of metal oxide materials.  $^1\text{H}$  NMR (Figure 7) was used to follow the conversion of the alkene to the triethoxysilane function. Triethoxysilane-terminated P(DTS-BT) (named P(DTS-BT)-Si from now on) spectrum showed complete disappearance of the alkene protons in the 5.00- 6.00 ppm range as well as the appearance of a peak at 3.86 ppm corresponding to the O-CH<sub>2</sub> of the silane end-chain. Due to the high sensitivity of the Si-OEt moiety to hydrolysis, the silane end-functionalized polymers (Si-P(DTS-BT)) were stored in a glove box under inert atmosphere.

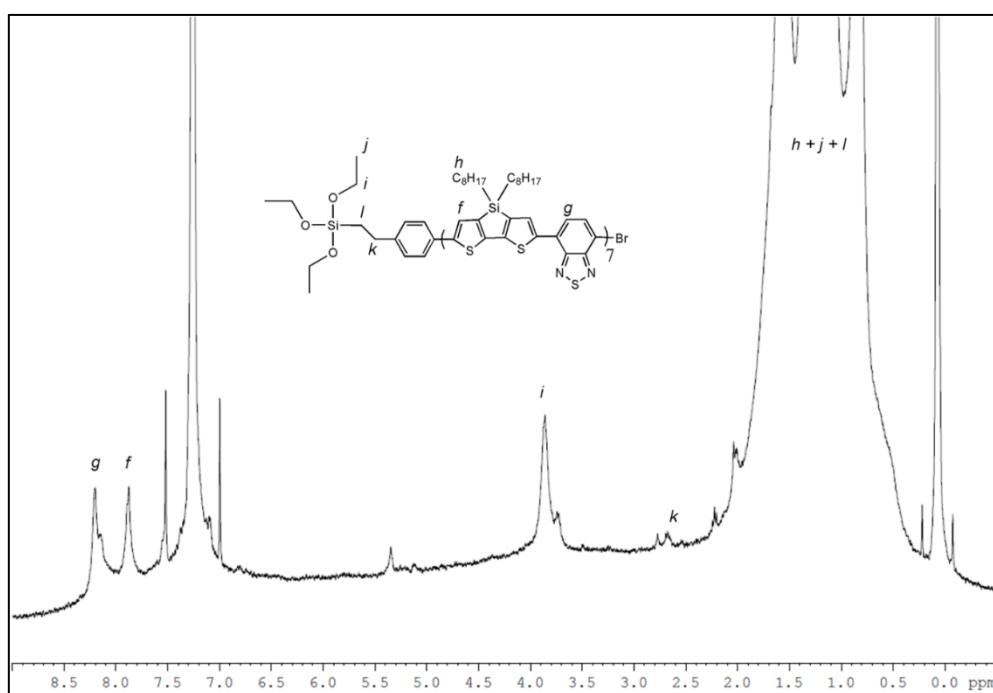


Figure 7:  $^1\text{H}$  NMR spectrum (400MHz,  $\text{CDCl}_3$ ) of triethoxysilane-terminated P(DTS-BT)

Following the exact same strategy of ternary blend, we functionalized P(DTS-BT) with the second end-capper, 4-bromoveratrole (P(DTS-BT)-BrV, see Scheme 1). The same characterization techniques were applied to this polymer.  $^1\text{H}$  NMR spectrum in Figure 1b shows in addition to the peaks assigned to the polymer, a peak at 4 ppm characteristic of the CH<sub>3</sub> of 4-bromoveratrole. The ratio of repetitive unit/end-capper was determined to be 7, very close to the theoretical value of 9 (Figure 1 and Table 1). This end-group is of great interest because methoxy groups can easily be deprotected to a catechol moiety which is then used to bind on metal oxide surfaces (named Cat-P(DTS-BT) from now on).<sup>40,41</sup>

2) Grafting of P(DTS-BT) on the surface of zinc oxide nanoparticles.

The spherical ZnO nanoparticles (NPs) (diameter = 20 nm) synthesized from the method described by Seow *et al.*<sup>42</sup> (described in chapter 5 and performed in ICMCB University of Bordeaux by Dr. Marie-Hélène Delville's group) were dispersed in CHCl<sub>3</sub> and mixed with an excess of silane terminated polymer (1 chain/nm<sup>2</sup>). The blend was heated at 60°C under vigorous stirring for 10 hours. Then the NPs were washed from unreacted polymer by several dispersion-centrifugation cycles in chloroform until the UV-visible spectrum of the supernatant was clear of any polymer absorption. These core@shell NPs (named ZnO@Si-P(DTS-BT) and ZnO@Cat-P(DTS-BT)) were characterized by thermogravimetric analysis (TGA) under nitrogen with a heating rate of 10 °C.min<sup>-1</sup> in order to follow the thermal degradation of the organic part and quantify the amount of P(DTS-BT) covalently linked to the NPs (Figure 8). The bare ZnO NPs showed a weight loss of 0.95 % between 100 and 550 °C corresponding to the loss of remaining chemically adsorbed water, while for pure P(DTS-BT) a weight loss of about 42 % was observed between 350 and 550°C. Figure 8 shows that the overall weight losses for the two hybrid materials, ZnO@Si-P(DTS-BT) and ZnO@Cat-P(DTS-BT), were 7.4 % and 2.2 %, respectively. From these values and by using the following formula:

$$\text{weight \% grafted P(DTS - BT)} = \frac{(\text{weight loss ZnO@PDTSBT}) - (\text{weight loss bare ZnO})}{\text{weight loss of P(DTS-BT)}} \times 100 \quad (5)$$

the weight percentage of the polymer brushes in the hybrid was calculated to be 15.4 % and 3 % for ZnO@Si-P(DTS-BT) and ZnO@Cat-P(DTS-BT), respectively.

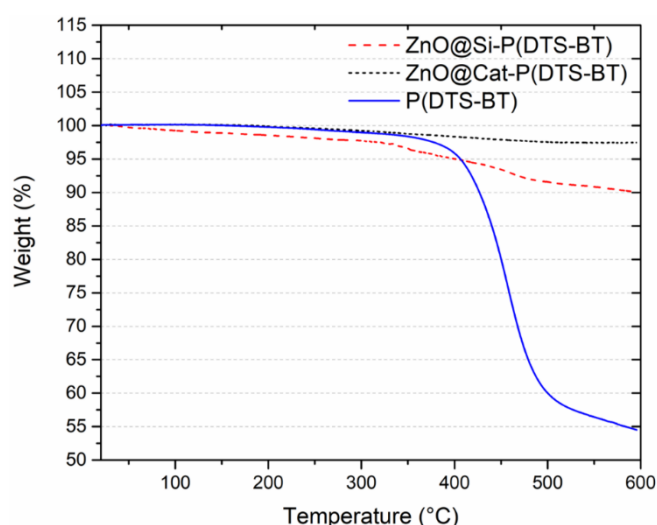


Figure 8: Thermogravimetric analysis of P(DTS-BT), grafted ZnO@Si-P(DTS-BT) and ZnO@Cat-P(DTS-BT) NPs under nitrogen at a heating rate of 10 °C.min<sup>-1</sup>

TEM was used to observe the morphology of the hybrid materials and evaluate the thickness of the grafted P(DTS-BT) layer onto the ZnO NPs surface. Figure 9a presents the image of bare zinc oxide spherical nanoparticles. The particle diameters were measured and the size distribution presented in Figure 10a showed that the average particle diameter is  $20 \pm 5$  nm.

In Figure 9b the image of the ZnO@Si-P(DTS-BT) is shown. Aggregates of few hundreds nanometers can be observed in low magnification picture (Figure 11) and at higher magnification, inside the aggregates the particles seemed embedded in a polymer matrix. Indeed, despite dilution, agitation or sonification we could not observe proper images of isolated nanoparticles and only aggregates were obtained. Zinc oxide particles seemed to be embedded in a polymer matrix. It is well-known in the literature that the triethoxysilane group, whose functionality is three, upon hydrolysis can self-condense leading to the formation of multilayers or crosslinked materials.<sup>43,44</sup> Moreover, in the synthesized macromolecules, as shown by MALDI-ToF, 28% of the chains bear a silane function at both ends. Therefore, during the grafting step, a crosslinking of polymer chains occurs, hence forming a matrix around the inorganic particles. This phenomenon is concomitant with their anchoring on the surface of the particles (Figure 12) with the presence of large aggregates containing both polymer multilayers and crystallized ZnO. On the contrary, when catechol end-terminal chains were used to graft zinc oxide particles, the TEM images in Figures 9c and d showed a  $3 \pm 1$  nm thick organic layer around the NPs without crosslinking.

Isolated particles bearing a heterogeneous polymer layer can easily be seen in the pictures, therefore the ZnO@Cat-P(DTS-BT) is the only sample presenting a core@shell structure. Indeed, on the TEM images, the polymer layer (light grey), does not completely cover the dark grey zinc oxide nanoparticles. Moreover, in Figure 13, an increase of the nanoparticle roughness is observed due to the presence of the polymer and even odd extra protuberances. Thus, patchy particles are obtained with a majority of the zinc oxide surface covered with polymer chains. The core@shell structure of the ZnO@Cat-P(DTS-BT) was also confirmed by the global increase of the nanoparticles size (Figure 10b). This heterogeneity can be of great interest in photovoltaic applications where both good dispersion and electron percolation between inorganic acceptor particles are targeted.



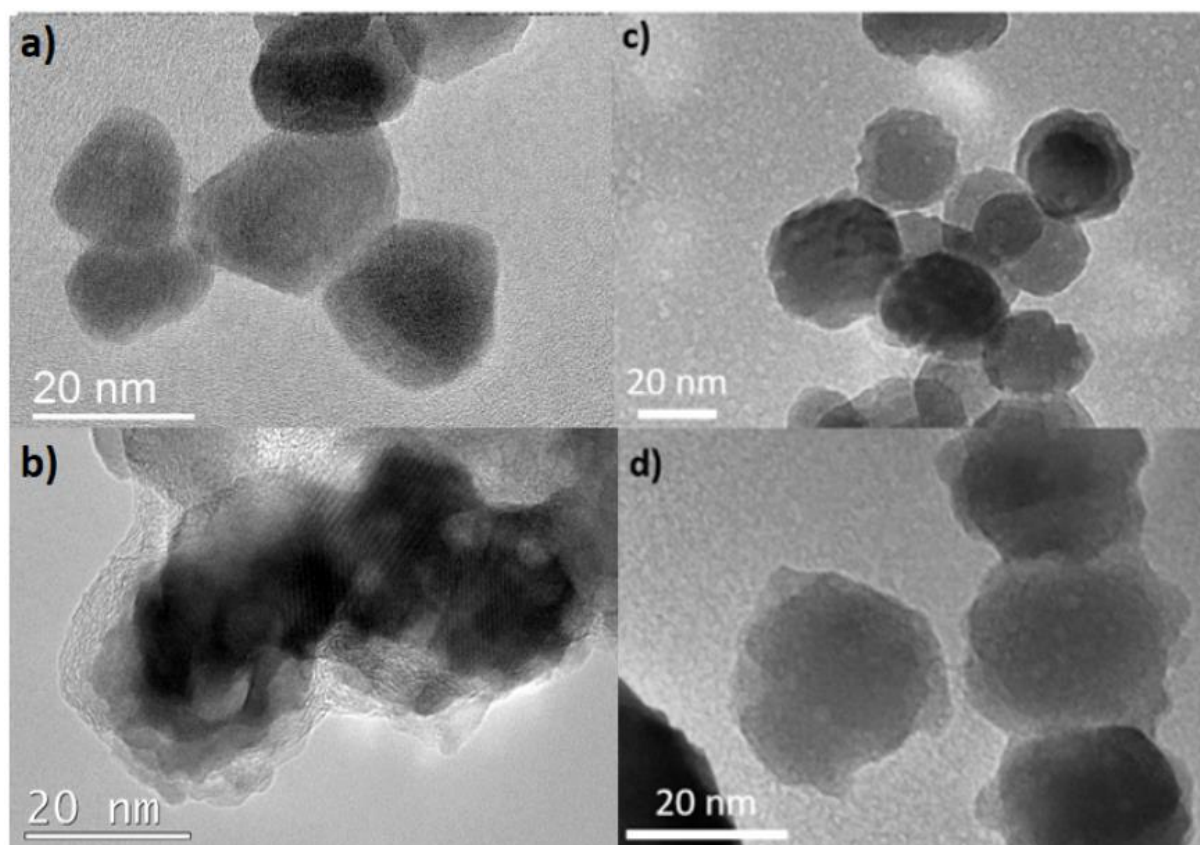


Figure 9: TEM images of a) bare ZnO NPs b) ZnO@SiP(DTS-BT) c) and d) ZnO@CatP(DTS-BT)

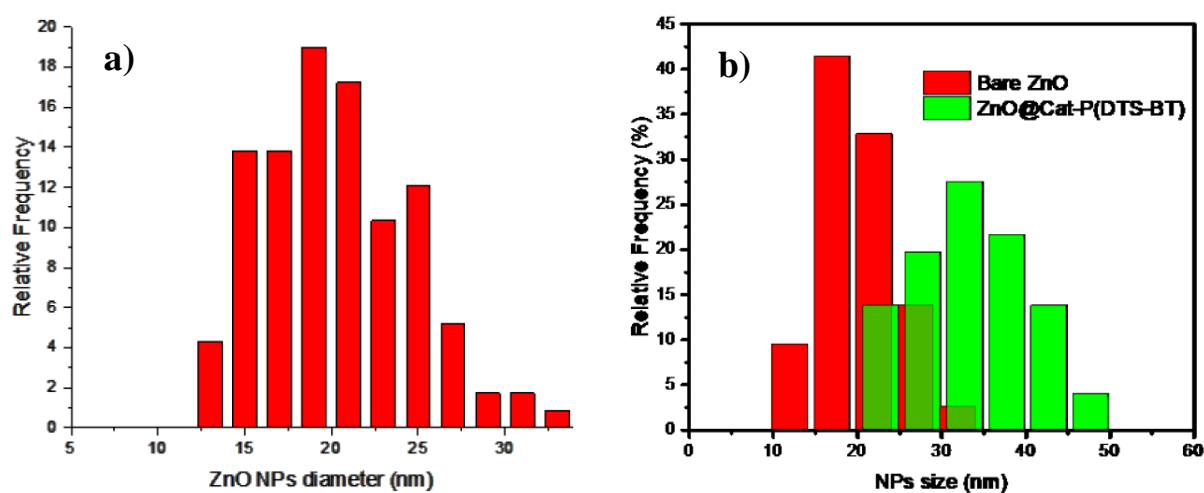


Figure 10: Size distribution of bare ZnO NPs a) and comparison with ZnO@Cat-P(DTS-BT) b) based on the statistical measurements of 120 NPs

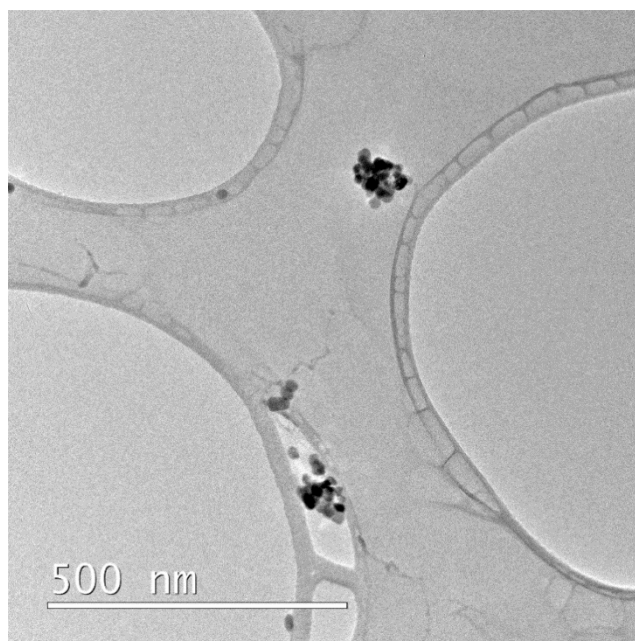


Figure 11: TEM image of ZnO@Si-P(DTS-BT) sample in which agglomerates of 100 nm can be observed

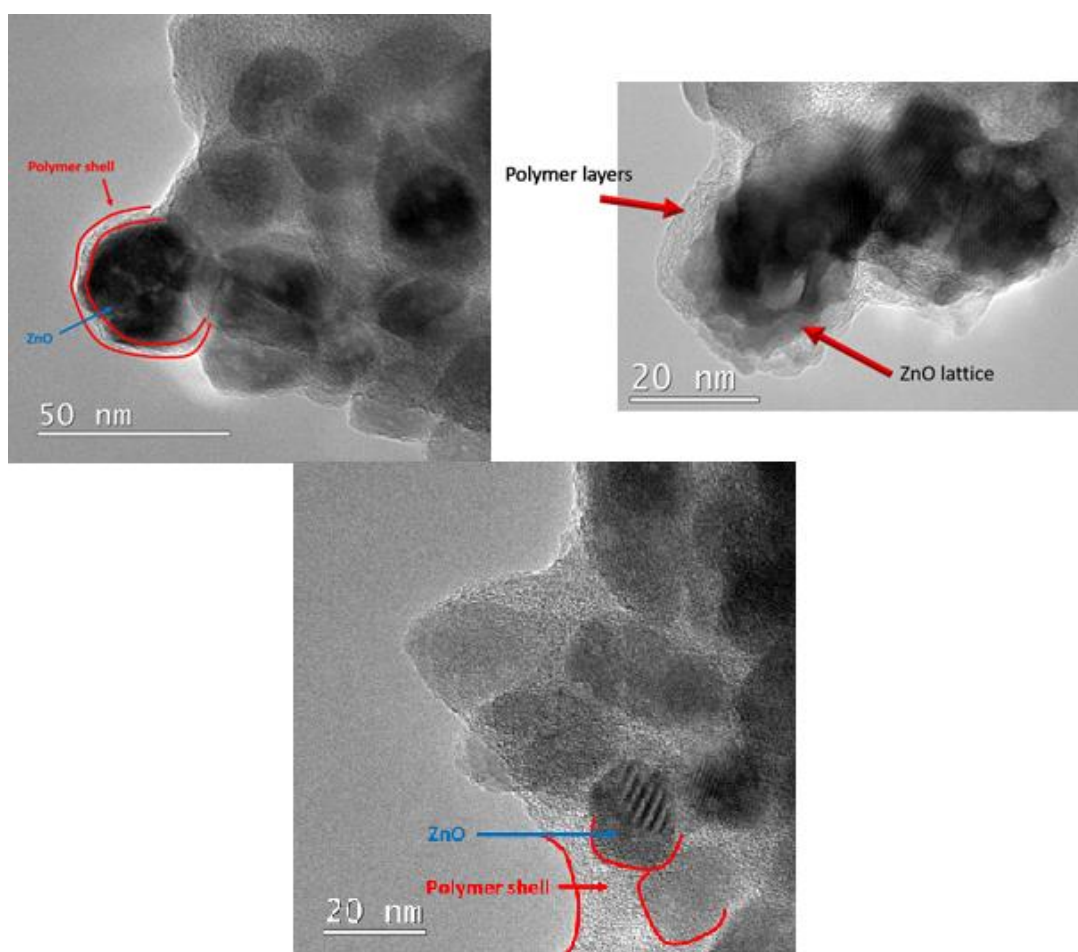


Figure 12: TEM images of ZnO@Si-P(DTS-BT) sample

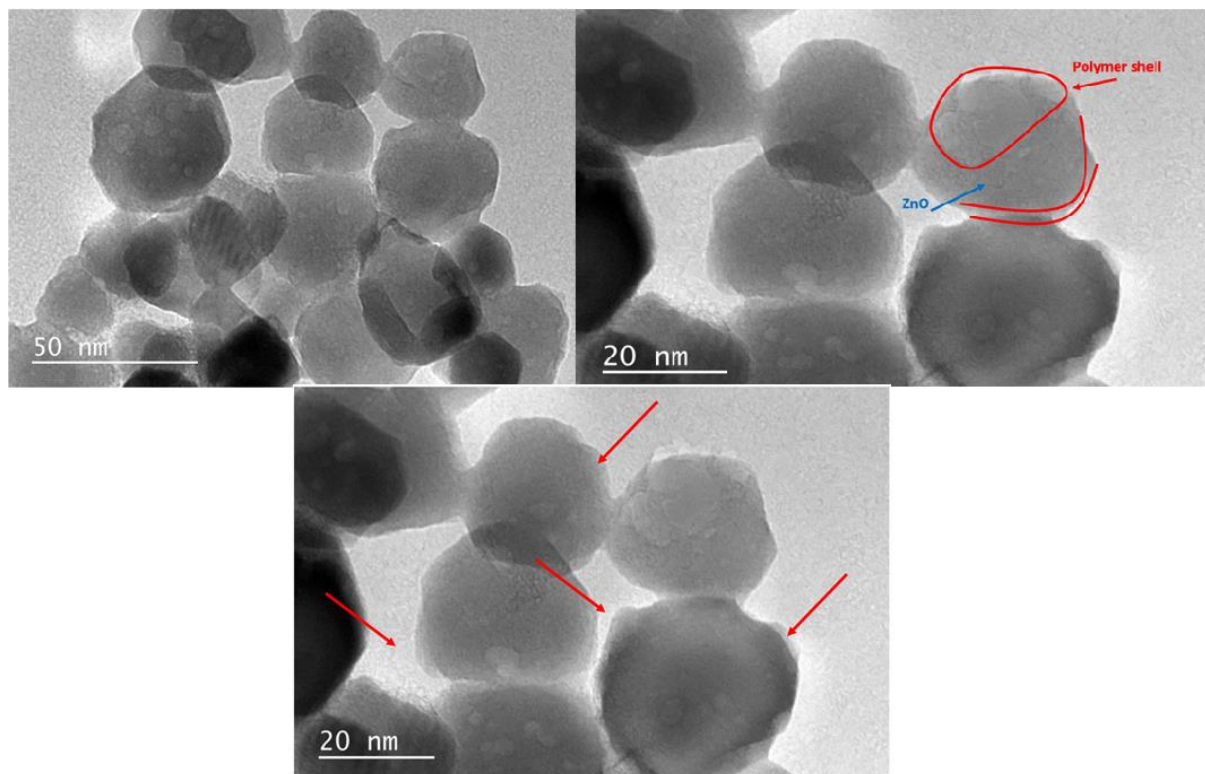


Figure 13: TEM images of ZnO@Cat-P(DTS-BT) sample

The nanoparticles specific surface area (SSA) was calculated to  $53 \text{ m}^2 \cdot \text{g}^{-1}$ . Actually, the nanoparticles are crystallized and non-agglomerated given the synthesis used to elaborate them and so they can be considered as perfect spheres of radius  $R = 10 \text{ nm}$ . Then, their volume  $V$  was calculated to be  $4190 \text{ nm}^3$  and their surface  $S$  to be  $1.26 \cdot 10^{-15} \text{ m}^2$ . Since their density  $\rho$  is  $5.6 \text{ g} \cdot \text{cm}^{-3}$ , their mass  $m$  was calculated to be  $2.3 \cdot 10^{-17} \text{ g}$  and their specific surface area (SSA) was deduced from the equation given below:

$$SSA = \frac{S}{m} \quad (6)$$

Since the weight fraction of P(DTS-BT) ( $f_{WP(DTS-BT)}$ ) was extracted from TGA, the surface grafting density ( $\sigma$ ) of the polymer was calculated *via* the equation :

$$\sigma = \frac{\frac{f_{WP(DTS-BT)}}{1-f_{WP(DTS-BT)}} \times N_{Av}}{\bar{M}_n \times SSA} \quad \text{where } N_{Av} \text{ is the Avogadro constant} \quad (7)$$

ZnO@Si-P(DTS-BT) exhibits crosslinking, thus it would be a nonsense to calculate a grafting density, but for the ZnO@Cat-P(DTS-BT) samples, the grafting density is  $0.05 \text{ chain/nm}^2$ , corresponding to 60 polymer chains per ZnO NP. This value is typically associated to polymer brushes in the “mushroom” regime, in which the space between grafted molecules is higher than two times the gyration radius of the polymer chain.<sup>45</sup> This low grafting density could be explained by the volume of the macromolecular grafting agent, which produces a high steric

hindrance at the metal oxide surface during the immobilization procedure. Since TEM images showed that the grafting is heterogeneous, therefore there are some areas on the particles where the chain density is lower than the average 0.05 chain per nm and others where the density is higher.

### 3) Photophysics of the hybrid nanoparticles.

The core@shell nanoparticles were then characterized by UV-visible absorption and photoluminescence (PL spectroscopy). Figure 14a presents the absorption spectra of pure polymer P(DTS-BT), the grafted ZnO@P(DTS-BT) and a mixture of bare ZnO with P(DTS-BT). In this last case, the ratio of both components was calculated to match the mass ratio found by TGA for the grafted NPs. Therefore, the absorbance of the mixture and the hybrid ZnO@P(DTS-BT) should match the maxima of absorbance at 680 nm and 370 nm for the polymer and the ZnO NPs, respectively. The comparison between the mixture and the hybrid absorption spectra revealed an increase of the absorption intensity at 750 nm when the polymer is covalently linked to the nanoparticle. This effect has been previously reported in the literature by Kiriya's group with P3HT-functionalized silica particles and was attributed to the establishment of  $\pi$ - $\pi$  interactions due to the proximity of anchored polymer chains.<sup>46</sup> The same bathochromic effect is well known in conjugated polymer films. Moreover, the maximum at 369 nm, characteristic of ZnO NPs (present in the ZnO/polymer physical mixture) exhibits a discernible blue shift of about 6 nm in the case of ZnO@P(DTS-BT) spectrum. This is due to variation in the dielectric environment of the oxide surface by the grafted macromolecules.<sup>47</sup> In a previous publication, our group reported the anchoring of this polymer on zinc oxide nanorods by surface-initiated polymerization. The same features with a maximum at 680 nm and a shoulder at 750 nm were observed.<sup>34</sup>

Figure 14b presents the PL spectra of the polymer, the blend polymer/bare ZnO particles and the ZnO@P(DTS-BT), under an incident light of  $\lambda = 670$  nm (Figure 15 shows the corresponding excitation spectra). Since the HOMO/LUMO levels of the polymer and the ZnO have already been reported at -5.25/-3.45<sup>48</sup> and -7.4/-3.9 eV<sup>49</sup> respectively, an electron transfer was expected upon irradiation, from the LUMO level of the polymer to the ZnO one. The main signal of the polymer spectrum from 700 to 830 nm is a typical emission of the P(DTS-BT) backbone that arises from the relaxation of excited  $\pi$ -electrons to the ground state. When the physical blend was analyzed, the PL intensity remained the same, meaning that no energy

## Chapter 2: Low band-gap polymer brushes: influence of the end-group on the morphology of core-shell nanoparticles

transfer occurred from the polymer to the nanoparticles. The main explanation for this behavior is that the concentration of the materials in chloroform is too low to induce an interaction. However, in comparison, the photoluminescence of the core@shell particles was drastically quenched. Indeed the intimacy of the hybrid components allows the electron transfer from polymer to zinc oxide.<sup>50</sup>

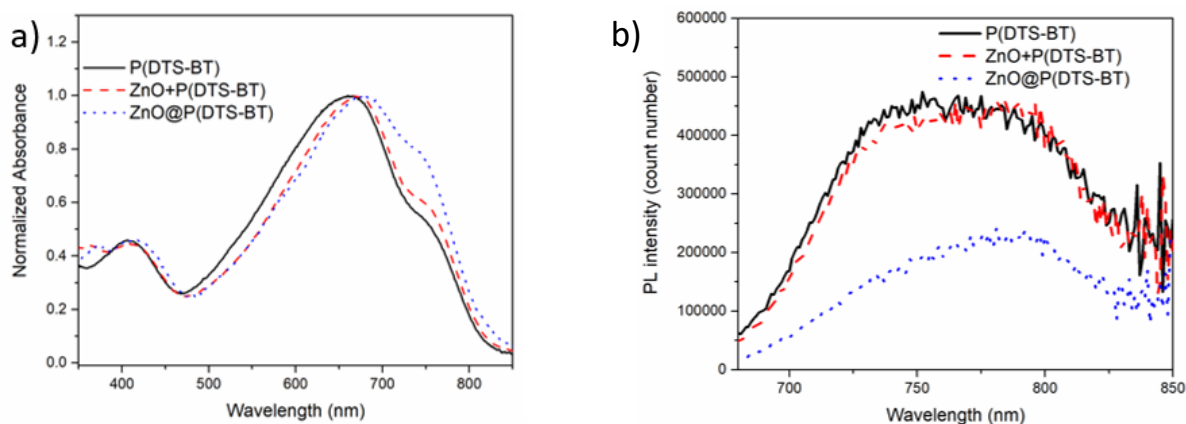


Figure 14: a) UV-visible absorption and b) photoluminescence ( $\lambda_{\text{ex}} = 670 \text{ nm}$ ) emission spectra of chloroform solutions of P(DTS-BT), grafted ZnO@P(DTS-BT) particles, and a mixture composed of bare ZnO and P(DTS-BT)

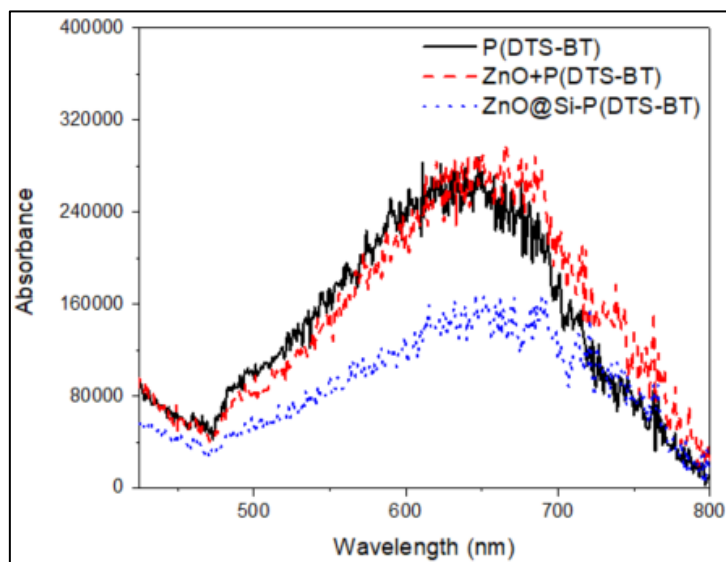


Figure 15: Photoluminescence excitation ( $\lambda_{\text{em}} = 820 \text{ nm}$ ) spectra of chloroform solutions of P(DTS-BT), grafted ZnO@P(DTS-BT) particles and a mixture composed of bare ZnO and P(DTS-BT)

#### 4) Elaboration of photovoltaic devices.

A binary blend composed of the grafted nanoparticles and a donor polymer P(DTS-BT) were tested as active layers of inverted solar cell devices. Actually, all of the devices have the same structure: indium tin oxide (ITO)/ZnO/ZnO@Cat-P(DTS-BT):P(DTS-BT)/MoO<sub>3</sub>/Ag (Figure 16). Two solutions were prepared, one in chlorobenzene and the other in chloroform, by blending the grafted nanoparticles ZnO@P(DTS-BT) (C = 15 g/L) with P(DTS-BT) (C = 10 g/L) with a weight ratio 60:40. The solutions in chlorobenzene were stirred for 1h at 90°C and then for 16h at 55°C. The solutions in chloroform were stirred for 1h at 70°C and then for 16h at 55°C. The binary solutions were spin-coated on the previously cleaned ITO substrates at different speeds (1000, 750, and 500 rpm for the chlorobenzene solutions and 3000, 2000, 1500, and 1000 rpm for the chloroform solutions) for 60s.

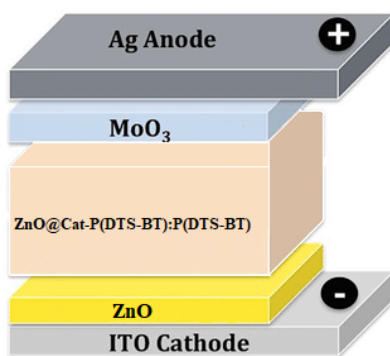


Figure 16: Device architecture of inverted structure of the fabricated organic solar cells

The current-voltage (I-V) characteristic of the devices were recorded in the dark and under illumination (AM 1.5 G, 1000 W/m<sup>2</sup>). In most of the cases, the photovoltaic performances were very low. Slightly better devices were obtained using chloroform solution and 3000 rpm as spin-coating speed. Figure 17a presents the current density *versus* voltage characteristics in the dark of these devices. Devices 2 and 3 (green and blue curves, respectively) are short-circuited because of an electrical contact between the electrode due the creation of a pin-hole appeared in the active layer during the deposition. On the contrary, devices 1 and 4 (black and red curves, respectively) produced uniform films without pin-holes. Hence, the J-V curves of devices 1 and 4 in the dark are not short-circuited. This result highlights that the active layer formation needs to be improved.

Figure 17b presents the current density *versus* voltage characteristics of devices 1 and 4 under illumination. The photovoltaic performances are really weak (below 0.001%) but in the best case the short circuit current J<sub>SC</sub> was calculated to be 0.34 mA.cm<sup>-2</sup> with an open circuit

## Chapter 2: Low band-gap polymer brushes: influence of the end-group on the morphology of core-shell nanoparticles

voltage  $V_{OC}$  of 11 mV and a fill factor FF of 0.32%. This result could be explained by the nanomorphology of the photoactive layer.<sup>51</sup> Actually, the photovoltaic properties depend heavily on these criteria as the nanomorphological arrangement of donor and acceptor domains (*i.e.* the formation of a large interfacial area) can have an influence on the excitonic dissociation efficiency.<sup>52</sup> In addition, the charge carrier transport and collection are closely related to the formation of percolated pathways. Yet, these features are not always controlled in hybrid material devices due to agglomeration of the nanoparticles into large aggregates. In this project, only the ZnO@Cat-P(DTS-BT) were studied because of their core@shell structure: the heterogeneity of the polymer layer on the nanoparticles can enhance the electron percolation. Even if no large aggregates were observed *via* TEM, it is possible that smaller aggregates (*i.e.* less than 20 nanoparticles) are present and hinder the percolation phenomenon. Besides, nanospheres are not the best choice to increase the percolation, it is the nanorods or nanowires that are the best to achieve vertical nanostructures.

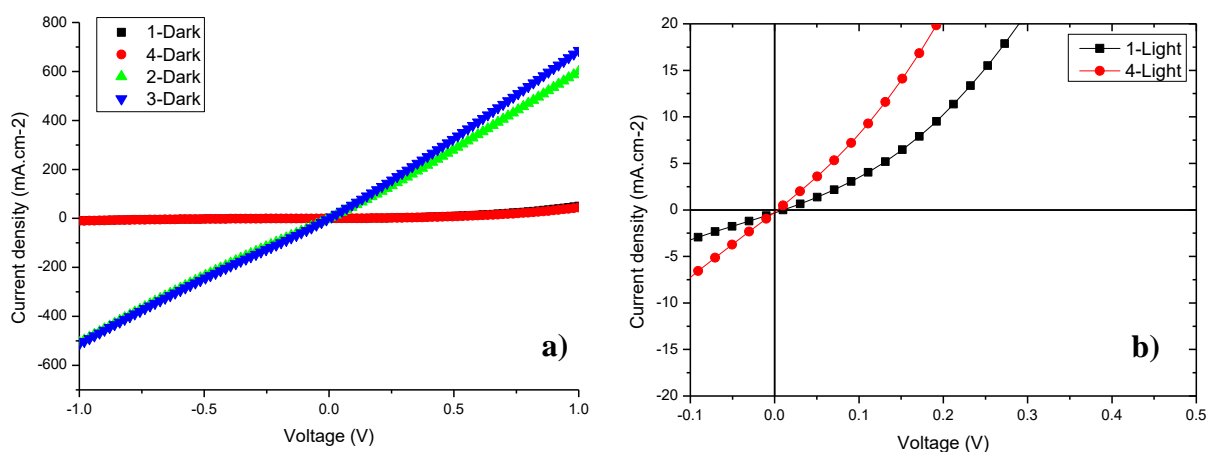


Figure 17: Current density *versus* voltage characteristics **a)** in the dark and **b)** under illumination of the inverted solar cell devices ITO/ZnO/ ZnO@P(DTS-BT):P(DTS-BT)/MoO<sub>3</sub>/Ag

In addition, poor efficiencies could be related to weak mobilities leading to deficient charge transport.

Due to time, amount of material and access to the lab, we could not investigate further photovoltaic cells made with the grafted nanoparticles. However, it would have been interesting to perform photoluminescence analysis of the thin films of the binary blend ZnO@Cat-P(DTS-BT):P(DTS-BT) in order to check the effective electron transfer from polymer to zinc oxide. The analysis of the mobilities could be of great interest to know if the charge transport can be tuned.

### III. Conclusion

The use of a ternary blend of comonomers is an efficient methodology to synthesize end-functional low band-gap polymers bearing surface anchoring groups. Triethoxysilane and catechol terminated macromolecules were successfully obtained and  $^1\text{H}$  NMR and MALDI-ToF techniques were used to identify and quantify the end-functionality. And, more importantly, in agreement with the theory, the amount of mono-functional monomer (styrene or bromoveratrole) controls the chains molar mass. ZnO spherical nanoparticles were then grafted by the polymer chains and TEM confirmed that hybrid materials were formed. The surface morphology of the hybrid materials was anchoring agent dependent. When silane functionalized polymers are used, cross-linked aggregates made of NPs embedded in a matrix are obtained due to the competition between self-condensation of silanes and reaction with ZnO surface hydroxyl groups. On the contrary, well-dispersed core-shell particles were synthesized with catechol polymer as anchoring agent. The grafting onto methodology led to patchy nanoparticles with partial coverage on which both zinc oxide and polymer surfaces are accessible. Photoelectronic characterizations were conducted on these hybrid materials and showed absorption features that were not present on polymer/particle physical mixture, thus proving specific interactions between core and shell. Finally, photoluminescence revealed the potential of these functionalized particles for photovoltaics with a remarkable quenching of the polymer fluorescence by zinc oxide NPs. Photovoltaic performances of inverted solar cells containing the hybrid material in its active layer were evaluated and showed a really weak efficiency.



## IV. References

- (1) Cui, C.; Li, Y. High-Performance Conjugated Polymer Donor Materials for Polymer Solar Cells with Narrow-Band-gap Nonfullerene Acceptors. *Energy & Environmental Science* **2019**, *12* (11), 3225–3246. <https://doi.org/10.1039/C9EE02531F>.
- (2) Yang, J.; Zhao, Z.; Wang, S.; Guo, Y.; Liu, Y. Insight into High-Performance Conjugated Polymers for Organic Field-Effect Transistors. *Chem* **2018**, *4* (12), 2748–2785. <https://doi.org/10.1016/j.chempr.2018.08.005>.
- (3) Xu, Y.; Lin, Q. Photodetectors Based on Solution-Processable Semiconductors: Recent Advances and Perspectives. *Applied Physics Reviews* **2020**, *7* (1), 011315. <https://doi.org/10.1063/1.5144840>.
- (4) Nelson, J. Polymer:Fullerene Bulk Heterojunction Solar Cells. *Materials Today* **2011**, *14* (10), 462–470. [https://doi.org/10.1016/S1369-7021\(11\)70210-3](https://doi.org/10.1016/S1369-7021(11)70210-3).
- (5) Liu, C.; Wang, K.; Gong, X.; Heeger, A. J. Low Band-gap Semiconducting Polymers for Polymeric Photovoltaics. *Chemical Society Reviews* **2016**, *45* (17), 4825–4846. <https://doi.org/10.1039/C5CS00650C>.
- (6) Khelifi, W.; Awada, H.; Brymora, K.; Blanc, S.; Hirsch, L.; Castet, F.; Bousquet, A.; Lartigau-Dagron, C. Halochromic Switch from the 1st to 2nd Near-Infrared Window of Diazapentalene–Dithienosilole Copolymers. *Macromolecules* **2019**. <https://doi.org/10.1021/acs.macromol.9b00675>.
- (7) Brymora, K.; Khelifi, W.; Blanc, S.; Hirsch, L.; Bousquet, A.; Lartigau-Dagron, C.; Castet, F. Comprehensive Theoretical and Experimental Study of near Infrared Absorbing Copolymers Based on Dithienosilole. *Polymer Chemistry* **2020**. <https://doi.org/10.1039/D0PY00330A>.
- (8) Bertho, S.; Janssen, G.; Cleij, T. J.; Conings, B.; Moons, W.; Gadisa, A.; D’Haen, J.; Goovaerts, E.; Lutsen, L.; Manca, J.; Vanderzande, D. Effect of Temperature on the Morphological and Photovoltaic Stability of Bulk Heterojunction Polymer:Fullerene Solar Cells. *Solar Energy Materials and Solar Cells* **2008**, *92* (7), 753–760. <https://doi.org/10.1016/j.solmat.2008.01.006>.
- (9) Liu, Y.; Zhao, J.; Li, Z.; Mu, C.; Ma, W.; Hu, H.; Jiang, K.; Lin, H.; Ade, H.; Yan, H. Aggregation and Morphology Control Enables Multiple Cases of High-Efficiency Polymer Solar Cells. *Nature Communications* **2014**, *5* (1). <https://doi.org/10.1038/ncomms6293>.
- (10) Bouclé, J.; Ravirajan, P.; Nelson, J. Hybrid Polymer–Metal Oxide Thin Films for Photovoltaic Applications. *Journal of Materials Chemistry* **2007**, *17* (30), 3141. <https://doi.org/10.1039/b706547g>.
- (11) Xu, T.; Qiao, Q. Conjugated Polymer–Inorganic Semiconductor Hybrid Solar Cells. *Energy & Environmental Science* **2011**, *4* (8), 2700. <https://doi.org/10.1039/c0ee00632g>.
- (12) Beek, W. J. E.; Wienk, M. M.; Janssen, R. A. J. Efficient Hybrid Solar Cells from Zinc Oxide Nanoparticles and a Conjugated Polymer. *Advanced Materials* **2004**, *16* (12), 1009–1013. <https://doi.org/10.1002/adma.200306659>.
- (13) Bousquet, A.; Awada, H.; Hiorns, R. C.; Dagron-Lartigau, C.; Billon, L. Conjugated-Polymer Grafting on Inorganic and Organic Substrates: A New Trend in Organic Electronic Materials. *Progress in Polymer Science* **2014**, *39* (11), 1847–1877. <https://doi.org/10.1016/j.progpolymsci.2014.03.003>.
- (14) Miozzo, L.; Yassar, A.; Horowitz, G. Surface Engineering for High Performance Organic Electronic Devices: The Chemical Approach. *Journal of Materials Chemistry* **2010**, *20* (13), 2513. <https://doi.org/10.1039/b922385a>.

- (15) Ma, H.; Yip, H.-L.; Huang, F.; Jen, A. K.-Y. Interface Engineering for Organic Electronics. *Advanced Functional Materials* **2010**, *20* (9), 1371–1388. <https://doi.org/10.1002/adfm.200902236>.
- (16) Ishii, H.; Sugiyama, K.; Ito, E.; Seki, K. Energy Level Alignment and Interfacial Electronic Structures at Organic/Metal and Organic/Organic Interfaces. *Advanced Materials* **1999**, *11* (8), 605–625. [https://doi.org/10.1002/\(SICI\)1521-4095\(199906\)11:8<605::AID-ADMA605>3.0.CO;2-Q](https://doi.org/10.1002/(SICI)1521-4095(199906)11:8<605::AID-ADMA605>3.0.CO;2-Q).
- (17) Gooding, J. J.; Ciampi, S. The Molecular Level Modification of Surfaces: From Self-Assembled Monolayers to Complex Molecular Assemblies. *Chemical Society Reviews* **2011**, *40* (5), 2704. <https://doi.org/10.1039/c0cs00139b>.
- (18) Tada, A.; Geng, Y.; Nakamura, M.; Wei, Q.; Hashimoto, K.; Tajima, K. Interfacial Modification of Organic Photovoltaic Devices by Molecular Self-Organization. *Physical Chemistry Chemical Physics* **2012**, *14* (11), 3713. <https://doi.org/10.1039/c2cp40198c>.
- (19) Chen, H.-C.; Lai, C.-W.; Wu, I.-C.; Pan, H.-R.; Chen, I.-W. P.; Peng, Y.-K.; Liu, C.-L.; Chen, C.-hsien; Chou, P.-T. Enhanced Performance and Air Stability of 3.2% Hybrid Solar Cells: How the Functional Polymer and CdTe Nanostructure Boost the Solar Cell Efficiency. *Advanced Materials* **2011**, *23* (45), 5451–5455. <https://doi.org/10.1002/adma.201102775>.
- (20) Awada, H.; Mattana, G.; Tournebize, A.; Rodriguez, L.; Flahaut, D.; Vellutini, L.; Lartigau-Dagron, C.; Billon, L.; Bousquet, A.; Chambon, S. Surface Engineering of ITO Electrode with a Functional Polymer for PEDOT:PSS-Free Organic Solar Cells. *Organic Electronics* **2018**, *57*, 186–193. <https://doi.org/10.1016/j.orgel.2018.03.004>.
- (21) Goodman, M. D.; Xu, J.; Wang, J.; Lin, Z. Semiconductor Conjugated Polymer–Quantum Dot Nanocomposites at the Air/Water Interface and Their Photovoltaic Performance. *Chemistry of Materials* **2009**, *21* (5), 934–938. <https://doi.org/10.1021/cm803248j>.
- (22) Li, F.; Du, Y.; Chen, Y.; Chen, L.; Zhao, J.; Wang, P. Direct Application of P3HT-DOPO@ZnO Nanocomposites in Hybrid Bulk Heterojunction Solar Cells via Grafting P3HT onto ZnO Nanoparticles. *Solar Energy Materials and Solar Cells* **2012**, *97*, 64–70. <https://doi.org/10.1016/j.solmat.2011.09.002>.
- (23) Jung, J.; Yoon, Y. J.; Lin, Z. Semiconducting Organic–Inorganic Nanocomposites by Intimately Tethering Conjugated Polymers to Inorganic Tetrapods. *Nanoscale* **2016**, *8* (16), 8887–8898. <https://doi.org/10.1039/C6NR00269B>.
- (24) Geng, H.; Wang, M.; Han, S.; Peng, R. Enhanced Performance of Hybrid Photovoltaic Devices via Surface-Modifying Metal Oxides with Conjugated Polymer. *Solar Energy Materials and Solar Cells* **2010**, *94* (3), 547–553. <https://doi.org/10.1016/j.solmat.2009.11.022>.
- (25) Handa, N. V.; Serrano, A. V.; Robb, M. J.; Hawker, C. J. Exploring the Synthesis and Impact of End-Functional Poly(3-Hexylthiophene). *Journal of Polymer Science Part A: Polymer Chemistry* **2015**, *53* (7), 831–841. <https://doi.org/10.1002/pola.27522>.
- (26) Lee, D.; Jang, D.-J. Charge-Carrier Relaxation Dynamics of Poly(3-Hexylthiophene)-Coated Gold Hybrid Nanoparticles. *Polymer* **2014**, *55* (21), 5469–5476. <https://doi.org/10.1016/j.polymer.2014.08.069>.
- (27) Awada, H.; Medlej, H.; Blanc, S.; Delville, M.-H.; Hiorns, R. C.; Bousquet, A.; Dagron-Lartigau, C.; Billon, L. Versatile Functional Poly(3-Hexylthiophene) for Hybrid Particles Synthesis by the Grafting onto Technique: Core@shell ZnO Nanorods. *Journal of Polymer Science Part A: Polymer Chemistry* **2014**, *52* (1), 30–38. <https://doi.org/10.1002/pola.26964>.
- (28) Awada, H.; Mezzasalma, L.; Blanc, S.; Flahaut, D.; Dagron-Lartigau, C.; Lyskawa, J.; Woisel, P.; Bousquet, A.; Billon, L. Biomimetic Mussel Adhesive Inspired Anchor to

- Design ZnO@Poly(3-Hexylthiophene) Hybrid Core@Corona Nanoparticles. *Macromolecular Rapid Communications* **2015**, *36* (16), 1486–1491. <https://doi.org/10.1002/marc.201500184>.
- (29) Boon, F.; Desbief, S.; Cutaia, L.; Douhéret, O.; Minoia, A.; Ruelle, B.; Clément, S.; Coulembier, O.; Cornil, J.; Dubois, P.; Lazzaroni, R. Synthesis and Characterization of Nanocomposites Based on Functional Regioregular Poly(3-Hexylthiophene) and Multiwall Carbon Nanotubes. *Macromolecular Rapid Communications* **2010**, *31* (16), 1427–1434. <https://doi.org/10.1002/marc.201000183>.
- (30) Wang, L.; Qiao, Z.; Gao, C.; Liu, J.; Zhang, Z.-G.; Li, X.; Li, Y.; Wang, H. End-Capping Effect of Quinoxalino[2,3-*b'*]Porphyrin on Donor–Acceptor Copolymer and Improved Performance of Polymer Solar Cells. *Macromolecules* **2016**, *49* (10), 3723–3732. <https://doi.org/10.1021/acs.macromol.6b00507>.
- (31) Robb, M. J.; Montarnal, D.; Eisenmenger, N. D.; Ku, S.-Y.; Chabynyc, M. L.; Hawker, C. J. A One-Step Strategy for End-Functionalized Donor–Acceptor Conjugated Polymers. *Macromolecules* **2013**, *46* (16), 6431–6438. <https://doi.org/10.1021/ma401255d>.
- (32) Koldemir, U.; Puniredd, S. R.; Wagner, M.; Tongay, S.; McCarley, T. D.; Kamenov, G. D.; Müllen, K.; Pisula, W.; Reynolds, J. R. End Capping Does Matter: Enhanced Order and Charge Transport in Conjugated Donor–Acceptor Polymers. *Macromolecules* **2015**, *48* (18), 6369–6377. <https://doi.org/10.1021/acs.macromol.5b01252>.
- (33) Harris, J. D.; Carter, K. R. A One-Pot Strategy to Improve End-Capping Efficacy in Stille Poly-Condensations. *Polymer Chemistry* **2018**, *9* (9), 1132–1138. <https://doi.org/10.1039/C7PY01761H>.
- (34) Awada, H.; Bousquet, A.; Dagrón-Lartigau, C.; Billon, L. Surface-Initiated Polymerization of A–A/B–B Type Conjugated Monomers by Palladium-Catalyzed Stille Polycondensation: Towards Low Band Gap Polymer Brushes. *RSC Advances* **2015**, *5* (96), 78436–78440. <https://doi.org/10.1039/C5RA08027D>.
- (35) Hou, J.; Chen, H.-Y.; Zhang, S.; Li, G.; Yang, Y. Synthesis, Characterization, and Photovoltaic Properties of a Low Band Gap Polymer Based on Silole-Containing Polythiophenes and 2,1,3-Benzothiadiazole. *Journal of the American Chemical Society* **2008**, *130* (48), 16144–16145. <https://doi.org/10.1021/ja806687u>.
- (36) Flory, P. J. Molecular Size Distribution in Linear Condensation Polymers<sup>1</sup>. *Journal of the American Chemical Society* **1936**, *58* (10), 1877–1885. <https://doi.org/10.1021/ja01301a016>.
- (37) Knoester, H. Theoretical Derivation of the Molecular Weight Distribution of End-Capped Linear Condensation Polymers. *Macromolecular Theory and Simulations* **2009**, *18* (1), 61–69. <https://doi.org/10.1002/mats.200800062>.
- (38) Hiemenz, P. C.; Lodge, T. *Polymer Chemistry*, 2nd ed.; CRC Press: Boca Raton, 2007.
- (39) Beek, W. J. E.; Wienk, M. M.; Janssen, R. A. J. Hybrid Solar Cells from Regioregular Polythiophene and ZnO Nanoparticles. *Advanced Functional Materials* **2006**, *16* (8), 1112–1116. <https://doi.org/10.1002/adfm.200500573>.
- (40) Faure, E.; Falentin-Daudré, C.; Jérôme, C.; Lyskawa, J.; Fournier, D.; Woisel, P.; Detrembleur, C. Catechols as Versatile Platforms in Polymer Chemistry. *Progress in Polymer Science* **2013**, *38* (1), 236–270. <https://doi.org/10.1016/j.progpolymsci.2012.06.004>.
- (41) Ye, Q.; Zhou, F.; Liu, W. Bioinspired Catecholic Chemistry for Surface Modification. *Chemical Society Reviews* **2011**, *40* (7), 4244. <https://doi.org/10.1039/c1cs15026j>.
- (42) Seow, Z. L. S.; Wong, A. S. W.; Thavasi, V.; Jose, R.; Ramakrishna, S.; Ho, G. W. Controlled Synthesis and Application of ZnO Nanoparticles, Nanorods and Nanospheres

- in Dye-Sensitized Solar Cells. *Nanotechnology* **2009**, *20* (4), 045604. <https://doi.org/10.1088/0957-4484/20/4/045604>.
- (43) Wicks, Z. W. *Organic Coatings: Science and Technology*, 3rd ed.; Wiley-Interscience: Hoboken, N.J, 2007.
- (44) Tillet, G.; Boutevin, B.; Ameduri, B. Chemical Reactions of Polymer Crosslinking and Post-Crosslinking at Room and Medium Temperature. *Progress in Polymer Science* **2011**, *36* (2), 191–217. <https://doi.org/10.1016/j.progpolymsci.2010.08.003>.
- (45) Kim, M.; Schmitt, S.; Choi, J.; Krutty, J.; Gopalan, P. From Self-Assembled Monolayers to Coatings: Advances in the Synthesis and Nanobio Applications of Polymer Brushes. *Polymers* **2015**, *7* (7), 1346–1378. <https://doi.org/10.3390/polym7071346>.
- (46) Senkovskyy, V.; Tkachov, R.; Beryozkina, T.; Komber, H.; Oertel, U.; Horecha, M.; Bocharova, V.; Stamm, M.; Gevorgyan, S. A.; Krebs, F. C.; Kiriya, A. “Hairy” Poly(3-Hexylthiophene) Particles Prepared via Surface-Initiated Kumada Catalyst-Transfer Polycondensation. *Journal of the American Chemical Society* **2009**, *131* (45), 16445–16453. <https://doi.org/10.1021/ja904885w>.
- (47) Xu, J.; Wang, J.; Mitchell, M.; Mukherjee, P.; Jeffries-EL, M.; Petrich, J. W.; Lin, Z. Organic–Inorganic Nanocomposites via Directly Grafting Conjugated Polymers onto Quantum Dots. *Journal of the American Chemical Society* **2007**, *129* (42), 12828–12833. <https://doi.org/10.1021/ja074133x>.
- (48) Medlej, H.; Awada, H.; Abbas, M.; Wantz, G.; Bousquet, A.; Grelet, E.; Hariri, K.; Hamieh, T.; Hiorns, R. C.; Dagnon-Lartigau, C. Effect of Spacer Insertion in a Commonly Used Dithienosilole/Benzothiadiazole-Based Low Band Gap Copolymer for Polymer Solar Cells. *European Polymer Journal* **2013**, *49* (12), 4176–4188. <https://doi.org/10.1016/j.eurpolymj.2013.09.025>.
- (49) Liu, B.; Lan, L.; Liu, Y.; Tao, H.; Li, H.; Xu, H.; Zou, J.; Xu, M.; Wang, L.; Peng, J.; Cao, Y. Improved Performance of Quantum Dot Light-Emitting Diodes by Hybrid Electron Transport Layer Comprised of ZnO Nanoparticles Doped Organic Small Molecule. *Organic Electronics* **2019**, *74*, 144–151. <https://doi.org/10.1016/j.orgel.2019.06.035>.
- (50) Malgas, G. F.; Motaung, D. E.; Mhlongo, G. H.; Nkosi, S. S.; Mwakikunga, B. W.; Govendor, M.; Arendse, C. J.; Muller, T. F. G. The Influence of ZnO Nanostructures on the Structure, Optical and Photovoltaic Properties of Organic Materials. *Thin Solid Films* **2014**, *555*, 100–106. <https://doi.org/10.1016/j.tsf.2013.08.012>.
- (51) Wright, M.; Uddin, A. Organic–Inorganic Hybrid Solar Cells: A Comparative Review. *Solar Energy Materials and Solar Cells* **2012**, *107*, 87–111. <https://doi.org/10.1016/j.solmat.2012.07.006>.
- (52) Yu, G.; Gao, J.; Hummelen, J. C.; Wudl, F.; Heeger, A. J. Polymer Photovoltaic Cells: Enhanced Efficiencies via a Network of Internal Donor-Acceptor Heterojunctions. *Science* **1995**, *270* (5243), 1789–1791. <https://doi.org/10.1126/science.270.5243.1789>.
- (53) Saunders, B. R. Hybrid Polymer/Nanoparticle Solar Cells: Preparation, Principles and Challenges. *Journal of Colloid and Interface Science* **2012**, *369* (1), 1–15. <https://doi.org/10.1016/j.jcis.2011.12.016>.
- (54) Jung, J.; Yoon, Y. J.; He, M.; Lin, Z. Organic-Inorganic Nanocomposites Composed of Conjugated Polymers and Semiconductor Nanocrystals for Photovoltaics. *J. Polym. Sci. Part B: Polym. Phys.* **2014**, *52* (24), 1641–1660. <https://doi.org/10.1002/polb.23612>.

# Chapter 3

## Table of Contents

I. Introduction.....	134
II. Results and discussion .....	136
1) Synthesis of the acceptor monomer .....	136
2) Synthesis of rod-coil block copolymers <i>via</i> the macroinitiator method.....	140
a. Synthesis of the rod alternating copolymers .....	140
b. Synthesis of the macroinitiators .....	146
c. Synthesis of the rod-coil block copolymers.....	151
3) Synthesis of rod-coil block copolymers <i>via</i> the macro end-capper copolymerization method .....	157
a. Synthesis of a second generation alkoxyamine.....	158
b. Synthesis of the coil homopolymer.....	160
c. Functionalization of the coil homopolymer .....	163
d. Synthesis of the rod-coil block copolymer .....	165
4) Optical, thermal, and structural properties .....	170
a. Optical properties .....	170
b. Thermal properties .....	176
c. Structural properties .....	183
III. Conclusion .....	188
IV. References.....	190

## I. Introduction

In this chapter, the main goal is to extend the possible applications of IR-absorbing polymer by designing a rod-coil diblock copolymer. From our experience, polymers for electronic devices like photovoltaics should present a high solubility to be easily deposited as films. Frequently, conjugated polymer solubility is low and can lead to the formation of aggregates or nano holes (pinhole) which could reduce device efficiencies.<sup>1,2</sup> To solve this problem, we want to introduce a block copolymer with filmogenic properties as additive to improve the film morphology, the mechanical properties and processability of the active layer. The copolymer would be based on the *n*-butyl acrylate monomer as soft filmogenic block<sup>3</sup> and the second block would be based on a IR-absorbing polymer compatible with the active layer. According to the literature, no block copolymers have been synthesized with an absorbing block in the near infrared and no rod-coil block copolymers based on low band-gap rod block and *n*-butyl acrylate coil block have been reported in literature.

Such materials can be obtained by various synthetic routes described in Chapter 1 and in this work, we decided to focus on two strategies: the macroinitiator method and the macro end-capper copolymerization method. The first method (Scheme 2), based on the work of Brochon *et al.*<sup>4</sup>, involves the use of a functional rod block used as macroinitiator in the controlled radical polymerization of *n*-butyl acrylate (*n*BA). The second method (Scheme 8) involves the synthesis of a functional P(*n*BA) further used as a macro end-capper in the cross-coupling Stille polycondensation of conjugated monomers. In both synthetic routes, a polycondensation composed of three components, two monomers and one monofunctional reagent were performed. All the knowledge acquired during the study of the grafted nanoparticles, reported in Chapter 2, has been of great benefit during these experiments.

Then, the optical, thermal, and structural properties of the different materials used in this chapter were studied. It was expected that the incorporation of a coil block would improve the solubility of the block copolymers, reducing the formation of aggregates and decreasing the  $\pi$ -stacking. This phenomenon was observed by Visible-NIR spectrophotometry and the molar absorption coefficient were also calculated. Solid-state properties of the block copolymer films were studied as well. For optoelectronic properties of photovoltaic devices, the control over the structure and morphology in solid state is important as the charge transport proceeds by means of hopping across the medium at intrachain and interchain levels.<sup>5</sup> Hence, the conjugation length is a determining factor for intra- and interchain transports. The incorporation of

### Chapter 3: Rod-coil block copolymers with filmogenic properties based on low band-gap conjugated polymers

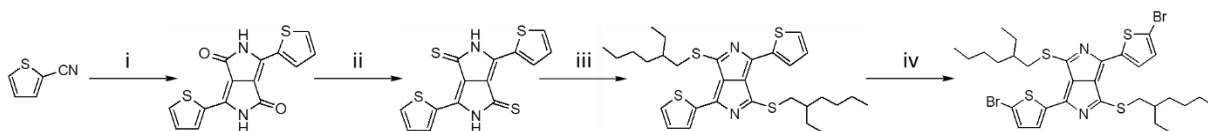
insulating coil block could decrease the conjugation length by decreasing  $\pi$ -stacking and thus increasing the hopping distance between neighboring chains or grains. The thermal stability was assessed by thermogravimetric analysis and the thermal transitions were studied by differential scanning calorimetry. Interestingly, liquid crystalline transitions were observed for two materials. Grazing incidence wide-angle X-ray scattering (GIWAXS) analyses were performed to give a detailed structural study on these specific materials in order to confirm the liquid crystalline behavior.



## II. Results and discussion

### 1) Synthesis of the acceptor monomer

The 2,5-diazapentalene (DAP) monomer was chosen for its strong electron-accepting characteristic and its broad absorption in the NIR region. This monomer is derived from the 1,4-diketopyrrolo[3,4-*c*]pyrrole (DPP) chromophore<sup>6</sup> and its synthesis was previously reported by our research group in 2019.<sup>7</sup> The synthesis of the DAP monomer has been performed in 4 steps. The first step corresponds to the formation of the DPP core followed by a thionation to obtain the DAP core. Then, solubilizing lateral chains were introduced *via* a thioalkylation step and the last step consists in a dibromination to functionalize the monomer.



Scheme 1: Synthetic routes to 2,5-diazapentalene monomer: (i) sodium, iron chloride, *t*-amyl alcohol, di-isopropylsuccinate; (ii) Lawesson's reagent, chlorobenzene; (iii) K<sub>2</sub>CO<sub>3</sub>, acetone, ethylhexylbromide; (iv) *N*-bromosuccinimide, chloroform

The first step (i) of the synthetic route (Scheme 1) consists in the synthesis of 3,6-dithiophene-2-yl-2,5-dihydropyrrolo[3,4-*c*]pyrrole-1,4-dione (DPP) and was first reported and patented by Iqbal *et al.*<sup>8,9</sup> In this one-pot reaction, two equivalents of 2-thiophene-carbonitrile react with di-isopropylsuccinate through a pseudo-Stobbe type condensation in basic medium.<sup>10</sup> The reaction temperature was chosen to be around 85°C with a slow addition of the di-isopropylsuccinate in the mixture (drop-by-drop) to hinder the nucleophilic addition of the anion formed by the ester of succinate at low temperature. The conjugated bicyclic molecule was purified by precipitation in cold methanol followed by a filtration step and several washings with methanol and deionized water. The final isolated and purified product is a red powder obtained with a good yield (85%). The thiophene spacers reduce the steric hindrance, increase planarity, and improve carrier mobility while the lactam (cyclic amide) groups boost the electronic affinity of the molecule by their electron-accepting effects.

In Figure 1, the <sup>1</sup>H NMR spectrum shows a singlet at 11.19 ppm corresponding to the protons (a) on the lactam groups, two doublets at 8.17 and 7.91 ppm associated with the

### Chapter 3: Rod-coil block copolymers with filmogenic properties based on low band-gap conjugated polymers

aromatic protons (b) and (c) of the thiophene, and a doublet of doublets centered at 7.26 ppm belonging to the aromatic protons (d) of the thiophene.

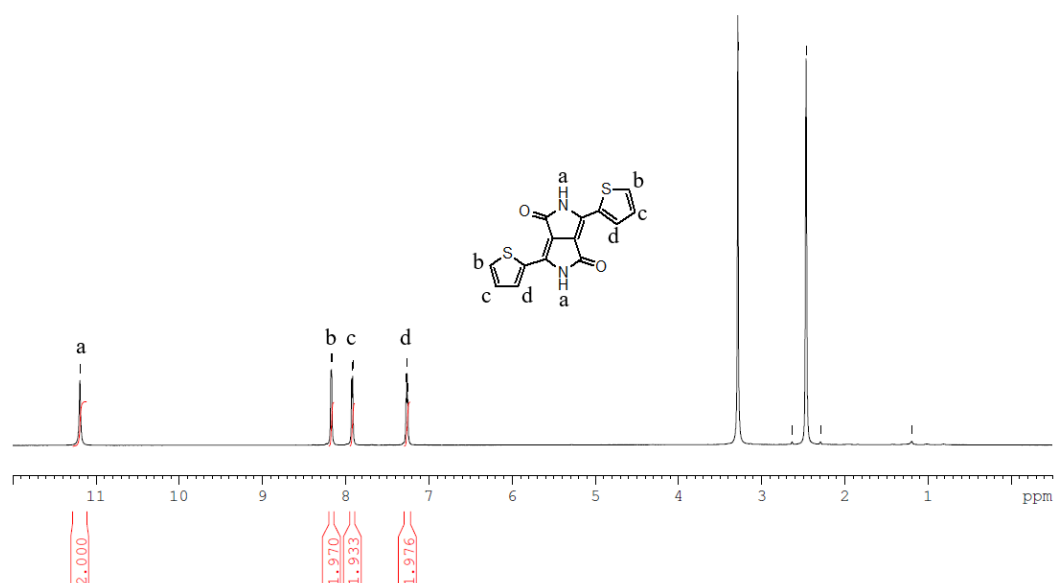


Figure 1: <sup>1</sup>H NMR spectrum of 3,6-dithiophene-2-yl-2,5-dihydropyrrolo[3,4-c]pyrrole-1,4-dione DPP molecule (400 MHz, d<sub>6</sub>-DMSO)

The second step (ii) of the synthetic route (Scheme 1) is the thionation reaction where oxygen atoms are substituted by sulfur atoms following the synthesis reported by Wang *et al.*<sup>11</sup> and Stas *et al.*<sup>12</sup> This reaction occurs in presence of the Lawesson's reagent in chlorobenzene reflux *via* a mechanism similar to a Wittig reaction.<sup>13</sup> The end of the thionation reaction is indicated by a clear change of the solution color, turning from dark red to dark green. The thionated molecule was precipitated in cold methanol and purified several times *via* Soxhlet extraction in ethanol to eliminate the phosphorus residues which could degrade the monomer. The final isolated and purified product is a dark green powder obtained with a good yield (93%).

In Figure 2, the <sup>1</sup>H NMR spectrum presents a singlet at 12.81 ppm corresponding to the protons (a) on the nitrogen atoms, a singlet at 8.99 ppm, a doublet of doublets centered at 7.39 ppm, and another doublet of doublets centered at 8.06 ppm associated with the aromatic protons (b), (c), and (d) of the thiophene, respectively. The successful substitution of the oxygen atoms by sulfur atoms is confirmed by the chemical shift (shielding) of the protons peaks compared to the <sup>1</sup>H NMR of the DPP molecule (Figure 1).

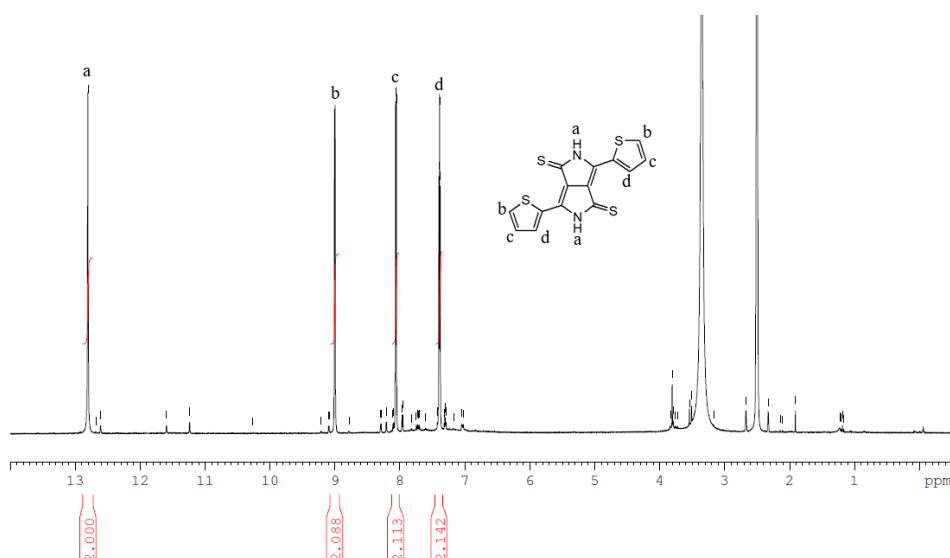


Figure 2:  $^1\text{H}$  NMR spectrum of 2,5-diazapentalene DAP molecule (400 MHz,  $d_6$ -DMSO)

The third step (iii) of the synthetic route (Scheme 1) is the *S*-alkylation to introduce alkyl side-chains used to enhance the solubility of the monomer. Hence, ethylhexylbromide was added drop-wise to the monomer previously solubilized in acetone. This alkyl chain was chosen to bring good solubility of the monomer in general organic solvents such as tetrahydrofuran (THF), dichloromethane (DCM), and chloroform ( $\text{CHCl}_3$ ). Potassium carbonate was added to the mixture to work in basic conditions. The alkyl chains could be installed *via* a *N*-alkylation, but the reactivity of the *S*-alkylation is higher: the latter occurs in priority. The monomer was purified by evaporating the acetone *via* rotary evaporator and by flash chromatography using silica gel. The chosen eluent was a mixture of cyclohexane and DCM (1:1). The final isolated and purified product is a purple powder obtained with good yield (63%).

In Figure 3, the  $^1\text{H}$  NMR spectrum shows the three aromatic protons (a), (b), and (c) of the thiophene between 7.23 and 8.12 ppm. The multiplet centered at 3.58 ppm corresponds to the two aliphatic protons (d) in  $\alpha$  position of sulfur atoms confirming the successful *S*-alkylation of the DAP molecule.

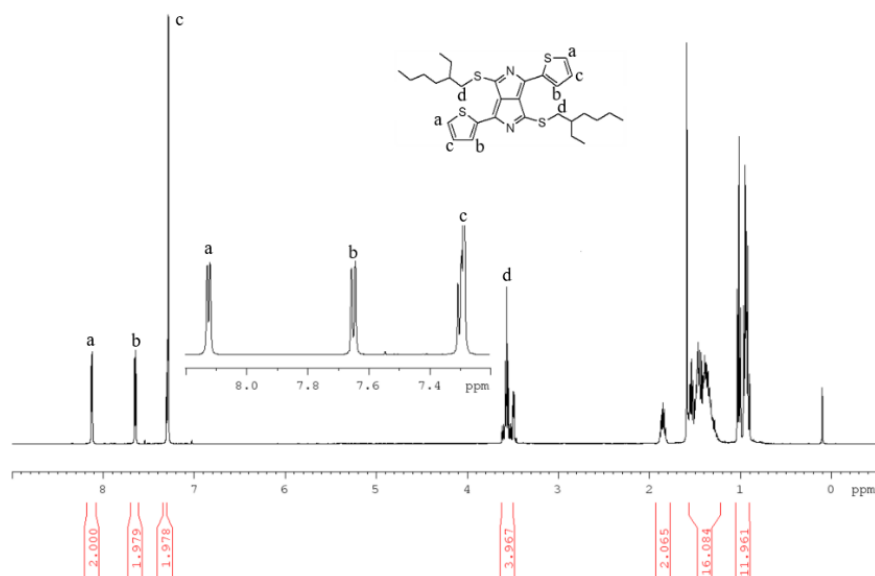


Figure 3:  $^1\text{H}$  NMR spectrum of alkylated 2,5-diazapentalene DAP molecule (400 MHz,  $\text{CDCl}_3$ )

The final step (iv) of the synthetic route (Scheme 1) is the bromination in  $\alpha$  position of the thiophene groups. As this reaction is very sensitive to light, this step was completed in the dark. *N*-bromosuccinimide was added to the alkylated product solubilized in chloroform and the reaction was followed *via* thin-layer chromatography (TLC) in a mixture of cyclohexane and chloroform (1:1). The brominated product was precipitated in cold methanol and the final isolated product is a green powder obtained with a reasonable yield (54%).

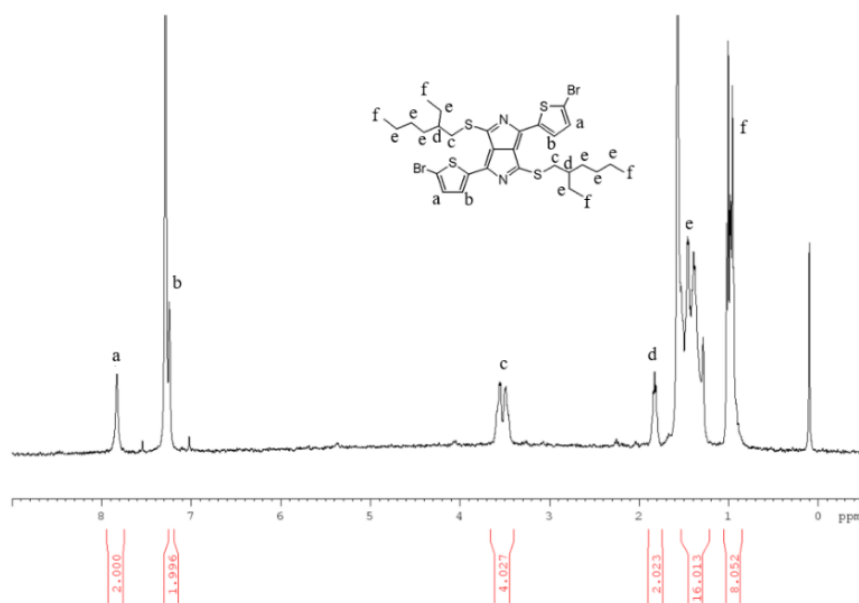


Figure 4:  $^1\text{H}$  NMR spectrum of dibrominated 2,5-diazapentalene DAP monomer (400 MHz,  $\text{CDCl}_3$ )

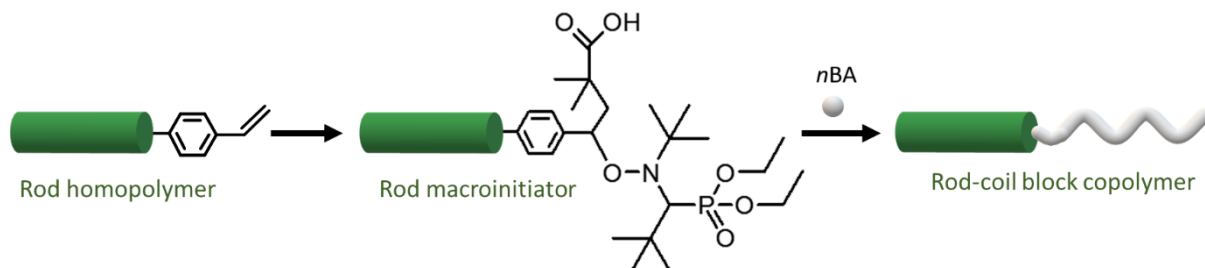
## Chapter 3: Rod-coil block copolymers with filmogenic properties based on low band-gap conjugated polymers

In Figure 4, the  $^1\text{H}$  NMR spectrum presents only two aromatic protons (a) and (b) of the thiophene at 7.83 and 7.24 ppm, respectively. The proton (a) at 8.12 ppm of the alkylated product (Figure 3) disappeared indicating the successful dibromination on the thiophene units. The multiplet centered at 3.52 ppm corresponds to the two aliphatic protons (c) in  $\alpha$  position of sulfur atoms and the multiplet centered at 1.82 ppm corresponds to the aliphatic proton (d) in  $\beta$  position of sulfur atoms. The multiplet centered at 1.38 ppm belongs to the eight aliphatic protons (e) and the multiplet centered at 0.98 ppm belongs to the four aliphatic protons (f).

The acceptor monomer was successfully synthesized and then was employed in the synthesis of donor-acceptor low band-gap polymers.

### 2) Synthesis of rod-coil block copolymers *via* the macroinitiator method

In this first synthetic strategy, a low band-gap polymer was end-functionalized with a reactive end-capper which was then modified into a nitroxide initiator. Finally, the macroinitiator was employed to initiate the polymerization of a coil block (Scheme 2).



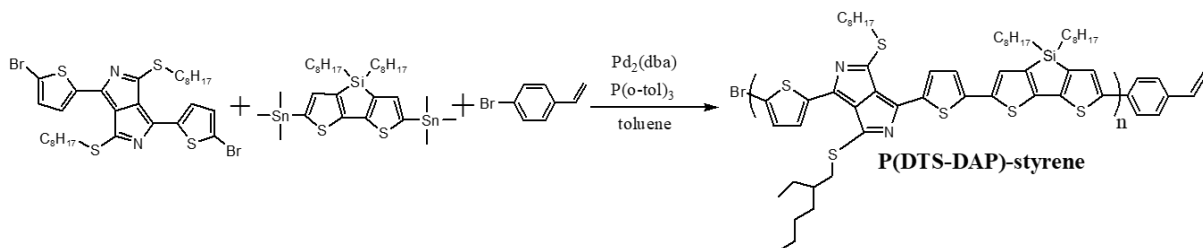
Scheme 2: Synthetic methodology for rod-coil block copolymer *via* the macroinitiator method

#### a. Synthesis of the rod alternating copolymers

The dibrominated 2,5-diazapentalene (DAP) and the distannylated 4,4'-bis(2-ethylhexyl)-5,5'-bis(trimethyltin)-dithieno[3,2-b:2',3'-d]silole (DTS) monomers were polymerized *via* a Stille cross-coupling polycondensation, using a  $\text{Pd}^0$  catalyst ( $\text{Pd}_2(\text{dba})_3$ ), the tri(*o*-tolyl)phosphine ligand ( $\text{P}(\text{o-tol})_3$ ), and the 4-bromostyrene as an end-capper (monofunctional) to synthesize a styrenic end-functionalized polymer (Scheme 3). The synthetic details are reported in the experimental part (Chapter 5). The monomer DTS was selected for its strong electron-donating behavior, good photochemical stability and the presence of alkyl chains on the Si atom that enhance the polymer solubility.<sup>14</sup> In the literature, it is reported that donor-

### Chapter 3: Rod-coil block copolymers with filmogenic properties based on low band-gap conjugated polymers

acceptor copolymers based on the DTS unit present a low energy level of the LUMO due to the effective orbital mixing of the Si-C  $\pi^*$  orbital with the  $\pi^*$  orbital of the butadiene fragment.<sup>15</sup> In addition, they show better optoelectronic properties in devices compared to the one based on the cyclopentadithiophene (CPDT) unit as the introduction of silicon stabilizes the diene HOMO.<sup>16</sup> It has to be reminded that the DTS donor monomer was purchased from 1-Material and used without further purification.



Scheme 3: Synthetic methodology for styrenic end-functionalized rod alternating copolymer

As in Chapter 2, 4-bromostyrene was selected as an appropriate end-capper due to its Stille polymerizable bromophenyl group and the presence of the styrene unit allowing unambiguous characterization of the resulting end-functional material. Most importantly, this styrene unit allows radical polymerization. The stoichiometry of the reagents was maintained according to the Carothers equation introduced in Chapter 2:

$$N_A = N_B + N_{B'} \quad \rightarrow \quad 2N_{DTS} = 2N_{DAP} + N_{EG} \quad (1)$$

In which  $N_A$ ,  $N_B$ ,  $N_{B'}$  represent the mole number of stannate functions and bromide groups pertaining to the DAP monomer and to the end-capping agent, respectively.  $N_{DTS}$ ,  $N_{DAP}$  and  $N_{EG}$  define the mole number of DTS and DAP monomers and 4-bromostyrene end-groups (EG), respectively. By following this stoichiometry, the total number of aryl bromides is equal to the total number of aryl stannanes and the formation of chains bearing 4-bromostyrene is promoted. The Stille polycondensation was performed under inert atmosphere in dry toluene and followed by the precipitation of the polymer in cold ethanol. After filtration, the polymer was purified by Soxhlet extraction in ethanol to remove impurities such as metallic byproducts, catalysts, ligands and unreacted monomers. This technique is also useful to divide in several fractions the polymer chains according to the chosen solvent. Through this division, the oligomers ( $n \leq 2$ ) can be isolated in one fraction (labelled as the ethanol fraction) and the longer polymer chains in other fractions. Hence, two different fractions were obtained: one in THF and the other in CHCl<sub>3</sub>. Three end-functional polymers were obtained by slightly varying the initial end-capper molar equivalent  $N_{EG} = 0.081$ ,  $0.062$  and  $0.078$  (Table 1) and were isolated in THF fractions. The final polymers were recovered with good yields (92%, 92%, and 83%, respectively) and

### Chapter 3: Rod-coil block copolymers with filmogenic properties based on low band-gap conjugated polymers

were labelled as P(DTS-DAP)-S. Yields are calculated as the ratio of the THF fraction weight on the theoretical polymer weight. For all the alternating copolymers, the THF fraction was the major fraction (average yield: 89%) and the CHCl<sub>3</sub> fraction was considered as the minor fraction (average yield: 11%). It is also possible that the ethanol fraction contains small chains (*i.e.* oligomers). The chloroform fraction was not employed and not analyzed for the rest of the study. Indeed, the solubilization of this last fraction was difficult and some characterization techniques were not possible such as SEC in THF. In addition, the material must be soluble in toluene for the following synthetic steps. Therefore, all the following analyses have been performed on the THF fraction, which obviously led to a lack of information about the full polymer sample.

<sup>1</sup>H NMR was performed to verify the proton structure of the polymers and to calculate the ratio between the repetitive units and the end-group ( $n_{DTSDAP}/n_{EG}$ , Table 1). In Figure 5, the <sup>1</sup>H NMR spectrum, obtained at 80°C to enhance the solubility of the polymer chains, shows two areas assigned to the thiophene groups: the first zone between 7.81 and 8.41 ppm belongs to the aromatic protons (a) and the second zone between 7.39 and 7.72 ppm is related to the aromatic protons (b) and (c). The multiplet centered at 3.63 ppm corresponds to the two aliphatic protons (d) in  $\alpha$  position of sulfur atoms on the alkyl chains. The CH, CH<sub>2</sub>, and CH<sub>3</sub> protons of the alkyl chains have their chemical shifts between 0.65 and 2.04 ppm. The peaks at 6.56, 5.61 and 5.10 ppm coincide with the styrenic protons (e), (f) and (g), respectively. The integral of the proton (g) was compared to the integral of the protons (d) centered at 3.63 ppm in order to estimate the  $n_{DTSDAP}/n_{EG}$  ratio in the final polymers. In Figure 5, the integral of the protons (d) ( $I_d$ ) is equal to 20 and the integral of the proton (g) ( $I_g$ ) is equal to 1. Hence, the  $n_{DTSDAP}/n_{EG}$  ratio was calculated from the following equation:

$$n_{DTSDAP}/n_{EG} = \frac{I_d/4}{I_g} \quad (2)$$

The  $n_{DTSDAP}/n_{EG}$  ratio was found to be equal to 5 and was reported in Table 1. The same calculation was applied to the two other alternating copolymers and the corresponding ratio were reported in Table 1.

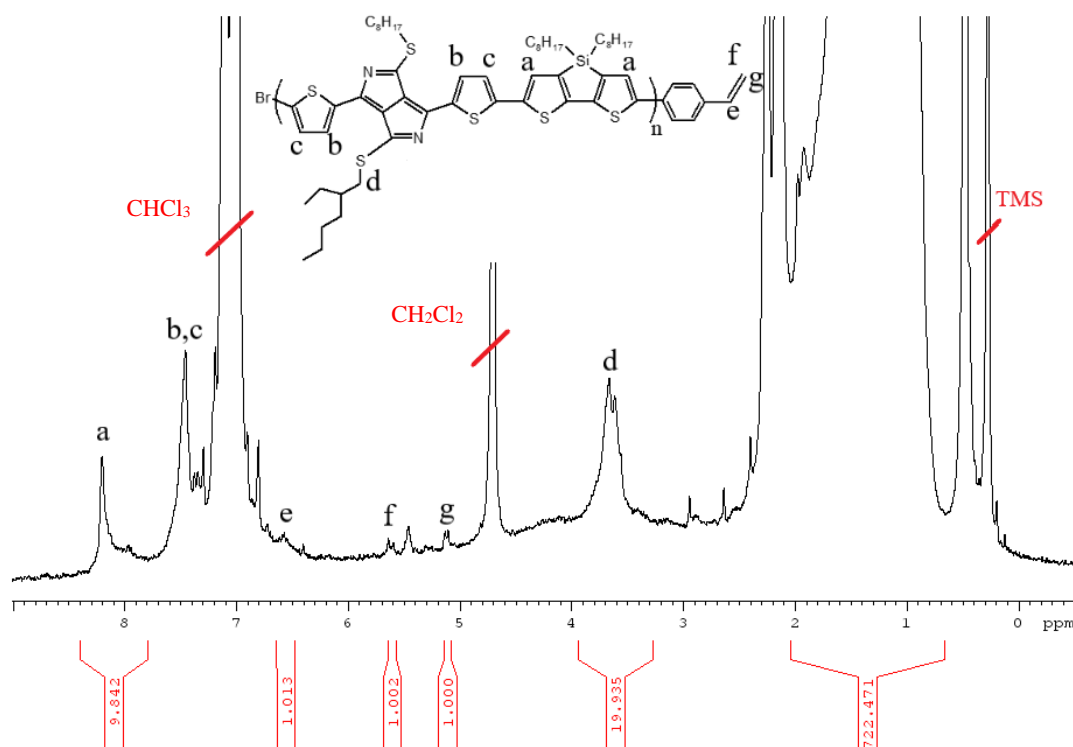


Figure 5:  $^1\text{H}$  NMR spectrum of the styrenic end-functionalized  $\text{P}(\text{DTS-DAP})_5\text{-S}$  alternating copolymer (400 MHz, toluene- $d_8$ )

The  $n_{\text{DTS}/n_{\text{EG}}}$  ratio in the final alternating copolymers were also calculated from Carothers equation below and reported in Table 1:

$$\overline{DP}_n = \frac{1+r}{1+r-2rp} \quad (3)$$

In which  $r$  is the ratio of monomer groups, and  $p$  is the conversion. It should be noted that in this equation,  $\overline{DP}_n$  counts the number of DTS + DAP units, so it is twice the number of repeat units  $n$  used in the calculation of the number average molar mass  $M_n$ . Therefore,  $M_n$  can be calculated as follows:

$$\overline{M}_n = M_0 \frac{\overline{DP}_n}{2} = \frac{M_0}{2} \frac{1+r}{1+r-2rp} \quad (4)$$

Where  $M_0$  is the molar mass of the repeat unit. When monofunctional reagent (as the end-capping agent) is introduced, the monomer group ratio is defined by the following equation:

$$r = \frac{N_A}{N_B+2N_{B'}} = \frac{2N_{\text{DTS}}}{2N_{\text{DAP}}+2N_{\text{EG}}} = \frac{N_{\text{DTS}}}{N_{\text{DAP}}+N_{\text{EG}}} \quad (5)$$



### Chapter 3: Rod-coil block copolymers with filmogenic properties based on low band-gap conjugated polymers

Where the factor 2 relative to  $N_B$  enters in the equation because the end-capper reagent has the same effect on the degree of polymerization than a difunctional monomer therefore is two times more effective.

The ratios obtained *via*  $^1\text{H}$  NMR were found to be slightly different compared to the theory. For the polymer analyzed in Figure 5, the  $n_{\text{DTSDAP}}/n_{\text{EG}}$  ratio was estimated to be 5. Thanks to the Carothers equation, the theoretical  $\text{DP}_n$  of the same polymer was calculated to be 50 (at 100% conversion), corresponding to 25 DTS-DAP repetitive units. Since bromostyrene has been included in the stoichiometry, styrene units should be at both end-chains for a 100% conversion. Therefore, for this polymer, the theoretical  $n_{\text{DTSDAP}}/n_{\text{EG}}$  ratio is 12 (Table 1). The difference between the theory and the experiment may be due to conversion, since a theoretical 97% conversion leads to a repetitive unit (DTS-DAP) to styrene ratio of 5. The molar masses  $M_n$  were calculated from the theory and compared to the molar masses  $M_n$  directly calculated from the ratio  $n_{\text{DTSDAP}}/n_{\text{EG}}$  obtained *via*  $^1\text{H}$  NMR with the hypothesis that each chain bore one end-capper. For the alternating copolymer  $\text{P}(\text{DTS-DAP})_5\text{-S}$  (entry 2, Table 1), the molar mass  $M_n$ , calculated from  $^1\text{H}$  NMR, and with the hypothesis that only one styrene is present on the chain, is equal to  $5000 \text{ g}\cdot\text{mol}^{-1}$ . Theoretically, a molar mass of  $24000 \text{ g}\cdot\text{mol}^{-1}$  can be reached at 100% of conversion. For all the alternating copolymers, the experimental molar masses deviated from the theoretical ones due to several parameters: incomplete conversion, the approximation that each chain is monofunctionalized for a conversion below 100%, and finally, the fact that only the THF fraction was analyzed while the  $\text{CHCl}_3$  fraction contains the highest molar masses. As previously detailed in Chapter 1, high molar masses are difficult to reach in step-growth polycondensation as the conversion increases exponentially with the  $\text{DP}_n$  and full conversions are rarely achieved.

In the case of the  $\text{P}(\text{DTS-DAP})_7\text{-S}$  (entry 4, Table 1), the theoretical molar mass is also reduced because the stoichiometry has not been experimentally reached: bromide groups are in slight excess compared to stannate functions.

Table 1: Macromolecular characteristics of the synthesized alternating copolymers

Polymer	$r^a$	$N_{DTS}^b$	$N_{DAP}^b$	$N_{EG}^b$	$n_{DTS DAP}$ $/n_{EG}^c$	$n_{DTS DAP}$ $/n_{EG}^d$	$Mn$ $th^c$ ( $g \cdot mol^{-1}$ )	$Mn^d$ ( $g \cdot mol^{-1}$ )	$p$
P(DTS-DAP)	1	0.5	0.5	0	$\infty$	-	$\infty$		
P(DTS-DAP) <sub>5</sub> -S	0.96	1	0.959	0.081	12	5	24000	5000	0.975
P(DTS-DAP) <sub>9</sub> -S	0.97	1	0.969	0.062	16	9	31000	9000	0.987
P(DTS-DAP) <sub>7</sub> -S	0.95	1	0.978	0.078	9	7	17000	7000	0.99

<sup>a</sup> feed ratio calculated according to Carothers equations, <sup>b</sup> molar fraction; <sup>c</sup> calculated from Carothers equations and based on the hypothesis that 100% of conversion is reached; <sup>d</sup> based on <sup>1</sup>H NMR

The three end-functional alternating copolymers were characterized by size-exclusion chromatography (SEC) in THF equipped with a UV-Visible detector set at  $\lambda = 700$  nm (Figure 6). Reasonable dispersity values between 1.5 and 1.7 and  $M_n$  and  $M_w$  from 4600 to 18200  $g \cdot mol^{-1}$  were calculated from conventional calibration using polystyrene standards. As depicted in Figure 6, the three alternating copolymers displayed the same molar masses. This result could be due to an incomplete solubility of the polymer chains in THF. Indeed, the filter used prior to injection was slightly coloured and the longest chains may have been retained.

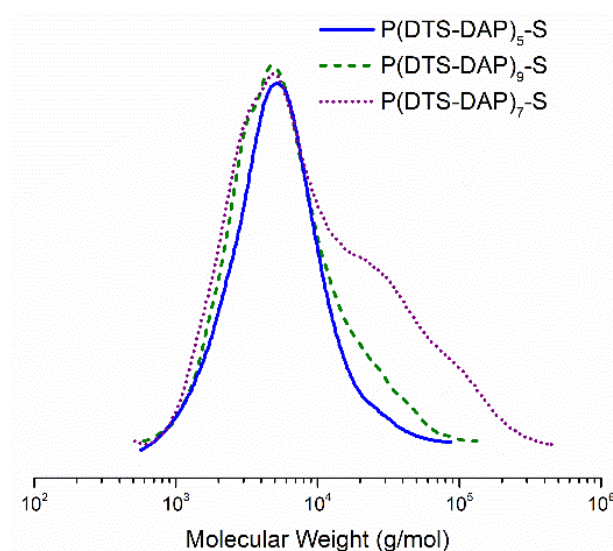
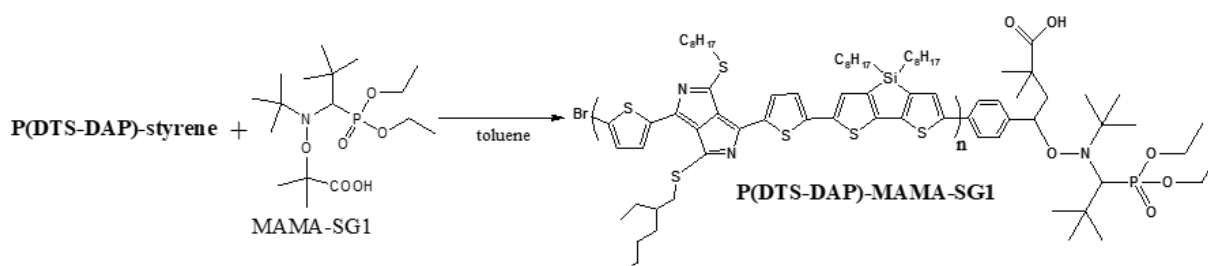


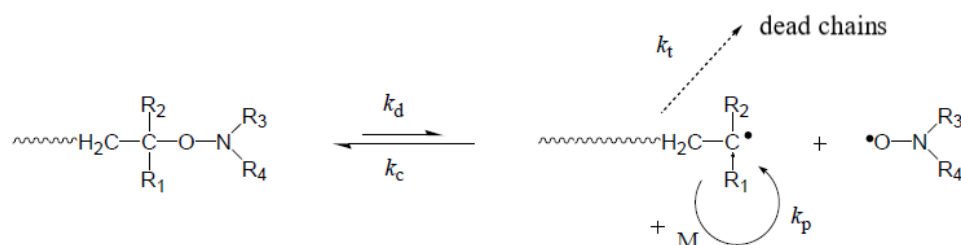
Figure 6: SEC-THF chromatograms of the three styrenic end-functionalized P(DTS-DAP)-S alternating copolymers (UV-Visible detector set at 700 nm)

b. Synthesis of the macroinitiators



Scheme 4: Synthetic methodology for nitroxide end-functionalized rod alternating copolymer: a macroinitiator

The three styrenic end-functionalized rod alternating copolymers were transformed into macroinitiators by converting the styrenic end-groups into alkoxyamine initiating groups (Scheme 4). The nitroxide-mediated polymerization (NMP) is a controlled method of radical polymerization, easy to carry out, which enables the synthesis of polymers with controlled molar masses and well-defined architectures.<sup>17,18</sup> This control is achieved with dynamic equilibration between dormant alkoxyamines and actively propagating radicals (Scheme 5).<sup>19</sup> As usual nitroxides (R<sub>1</sub>)(R<sub>2</sub>)N-O are too stable due to the relocation of the free electron on the nitrogen or oxygen atoms, they cannot initiate a polymerization.<sup>20</sup> When coupled to more reactive radicals, nitroxides become alkoxyamines where the C-O bond can break homolytically at elevated temperature. The fragmentation gives two compounds: a transient alkyl (R<sub>3</sub>)<sup>•</sup> and a stable nitroxide radical (R<sub>1</sub>)(R<sub>2</sub>)N-O<sup>•</sup>.<sup>21</sup> In this thesis project, we employed the MAMA-SG1 (BlocBuilder ®), kindly provided by Arkema (France). The nitroxide SG1 was discovered and patented by Grimardi *et al.* in 1996 and is also called DEPN, *N-tert-butyl-N-(1-diethylphosphono-2,2-dimethylpropyl) nitroxide*.<sup>22,23</sup> As for the MAMA-SG1 alkoxyamine, its synthesis was patented in 2010 and has been commercialized by Arkema ever since.<sup>24</sup>

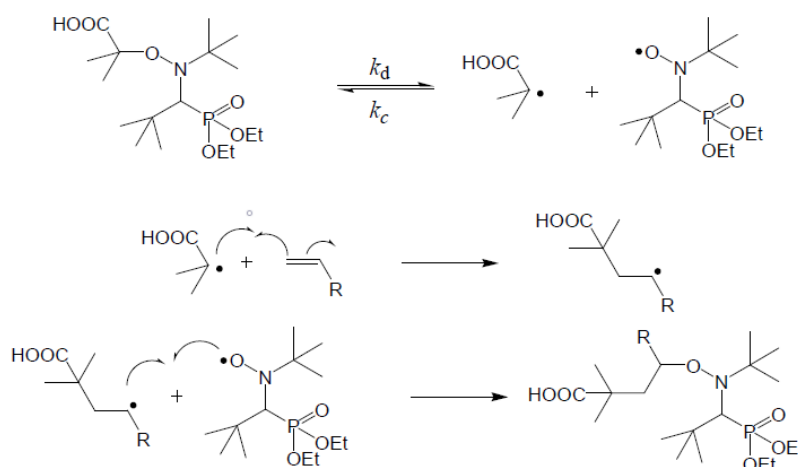


Scheme 5: Activation/deactivation equilibrium in nitroxide-mediated polymerization where  $k_d$  stands for dissociation constant and  $k_c$  for recombination constant. Adapted from Blas<sup>13</sup>

Polymer end groups originally prepared by step-growth polymerization have already been converted into initiating sites. Zhang *et al.* and Gaynor *et al.* transformed poly(ether

### Chapter 3: Rod-coil block copolymers with filmogenic properties based on low band-gap conjugated polymers

sulfone)s with OH end groups into atom transfer radical polymerization (ATRP) initiators using an excess of 2-bromoisobutyryl bromide.<sup>25,26</sup> Furthermore, Mennicken *et al.* reported the conversion of polycarbonate with hydroxy end groups into an ATRP macroinitiator by esterification.<sup>27</sup> Van de Wetering *et al.* transformed a dioctylpoly(thienylenevinylene) with aldehyde end groups *via* a nucleophilic attack of a Grignard reagent based on TIPNO (2,2,5-trimethyl-4-phenyl-3-azahexane-3-nitroxide) to yield an alkoxyamine macroinitiator for NMP.<sup>28</sup> Despite numerous examples of TIPNO macroinitiators available in the literature, their production includes several synthetic steps. One solution to reduce the number of steps in the synthetic procedure is to employ the 1,2 addition of MAMA-SG1 onto olefins to prepare a second generation alkoxyamine (Scheme 6).<sup>29</sup> By addition of a radical species to an olefin, alkyl radicals are produced and they can trap the aminoxyl radical *in situ*.<sup>21</sup> The dissociation temperature of second generation alkoxyamines is much higher than the first one of MAMA-SG1, therefore monoaddition and not polymerization is produced at low temperatures. For instance, Dufils *et al.* synthesized several second generation alkoxyamines derived from various activated olefins, such as *n*-butyl acrylate (*n*BA), acrylic acid (AA), and styrene (S).<sup>30</sup> This technique can be applied to the preparation of macroinitiators.



Scheme 6: 1,2-addition of MAMA-SG1 onto an activated olefin. Adapted from Blas<sup>13</sup>

Hence, for the transformation of the three styrenic end-functionalized rod alternating copolymers, we employed the 1,2 addition of MAMA-SG1 onto styrenic end groups. The alkoxyamine MAMA-SG1 was added in slight excess (2.5 eq compared to the polymer chains) to a solution of styrenic end-functionalized polymer P(DTS-DAP)-S and the mixture was heated at 100°C as the dissociation temperature zone of the MAMA-SG1 is located around this temperature. The synthesis took place under inert atmosphere and in dry chloroform to ensure

### Chapter 3: Rod-coil block copolymers with filmogenic properties based on low band-gap conjugated polymers

a good solubility of the rod alternating copolymer. The synthetic details are reported in the experimental part (Chapter 5). The macroinitiator was precipitated in cold ethanol, filtered and washed with ethanol to remove the unreacted alkoxyamines. The final macroinitiators were obtained with yields comprised between 55 and 61% and were labelled as P(DTS-DAP)-MAMA-SG1. Lower yields were obtained, compared to the yields of the alternating copolymers, maybe due to the change of macromolecule solubility. In fact, the macroinitiators presented a higher solubility due to the presence of the MAMA-SG1 at the chain ends. Hence, during the precipitation, it could be possible that some chains have been solubilized in ethanol and lost which explains the reduced yields.

$^1\text{H}$  NMR was performed to verify the proton structure of the macroinitiators. In Figure 7, the  $^1\text{H}$  NMR spectrum of one of the macroinitiators, obtained at  $80^\circ\text{C}$  to enhance the solubility of the polymer chains, shows two areas assigned to the thiophene groups: the first zone between 8.1 and 8.27 ppm belongs to aromatic protons (a) and the second zone between 7.38 and 7.56 ppm is related to aromatic protons (b) and (c). The multiplet centered at 3.62 ppm corresponds to the two aliphatic protons (d) in the  $\alpha$  position of sulfur atoms on the alkyl chains. The multiplet centered at 3.25 ppm belongs to four aliphatic protons (h) on the phosphonic ester chain ends. The integral of the proton (h) was compared to the integral of the protons (d) centered at 3.63 ppm in order to estimate the  $n_{\text{DTS-DAP}}/n_{\text{EG}}$  ratio in the final polymers. The ratios  $n_{\text{DTS-DAP}}/n_{\text{MAMA}}$  of the macroinitiators were found to be similar to the ratios  $n_{\text{DTS-DAP}}/n_{\text{EG}}$  of the alternating copolymers, meaning that all styrene units have been converted into MAMA-SG1 units. Nevertheless, the superimposition of the  $^1\text{H}$  NMR spectra of the styrenic end-functionalized polymer P(DTS-DAP)<sub>5</sub>-S and the macroinitiator P(DTS-DAP)<sub>5</sub>-MAMA-SG1 in Figure 7 shows that the signals at 6.56, 5.61 and 5.10 ppm pertaining to the parent styrene end-functionalized polymer have not completely disappeared. From this result, we calculated the conversion of styrenic protons into MAMA-SG1 alkoxyamines according to this equation:

$$\text{functionalization yield} = \frac{I_{h/4}}{I_{f/1} + I_{h/4}} \times 100 = 83 \quad (6)$$

Here, it should be emphasized that the integration of the signals at 6.56, 5.61 and 5.10 ppm was difficult to take because of the weak intensity compared to the baseline, and may be overestimated. Therefore, we can conclude that at least 83% of the chains are now functionalized with MAMA-SG1 alkoxyamines.

## Chapter 3: Rod-coil block copolymers with filmogenic properties based on low band-gap conjugated polymers

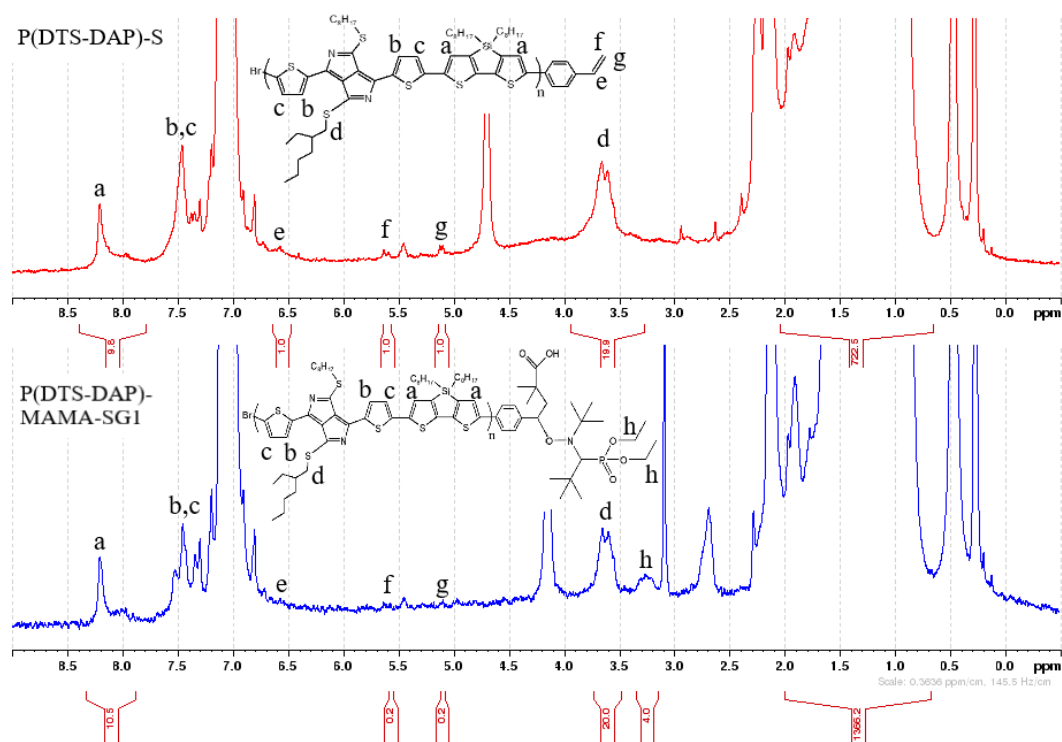


Figure 7: Superimposition of <sup>1</sup>H NMR spectra of the styrenic end-functionalized P(DTS-DAP)<sub>5</sub>-S alternating copolymer and the nitroxide end-functionalized P(DTS-DAP)<sub>5</sub>-MAMA-SG1 macroinitiator (400 MHz, toluene-d<sub>8</sub>)

The three macroinitiators were characterized by size-exclusion chromatography (SEC) in THF equipped with a UV-Visible detector set at  $\lambda = 700$  nm (Figure 8). Dispersity values between 2.1 and 2.4 and  $M_n$  and  $M_w$  from 6200 to 16100 g.mol<sup>-1</sup> were calculated from conventional calibration using polystyrene standards and are reported in Table 2. Generally, molar masses and dispersities of macroinitiators are higher than the ones found for the rod alternating copolymers (also reported in Table 2). We explained it by the enhancement of the solubility of polymer chains thanks to the presence of the MAMA-SG1 alkoxyamines at the chain ends that allows the solvation of the complete sample in THF. Molar masses obtained by SEC deviate slightly from the ones obtained *via* <sup>1</sup>H NMR due to the polystyrene calibration.

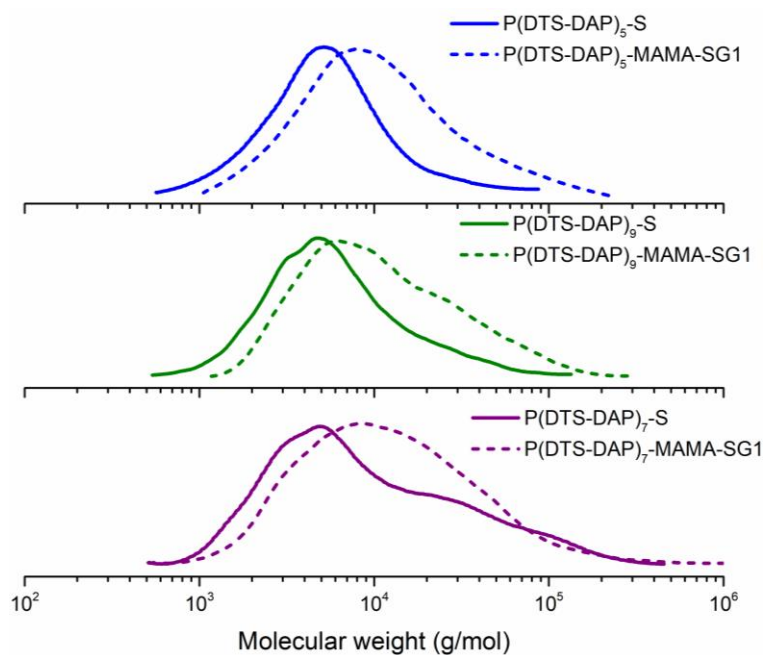


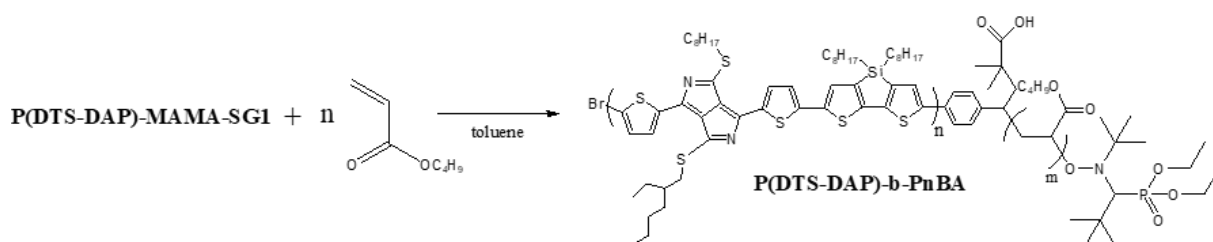
Figure 8: Superimposition of the SEC-THF chromatograms of the three styrenic end-functionalized P(DTS-DAP)-S alternating copolymers and the three nitroxide end-functionalized P(DTS-DAP)-MAMA-SG1 macroinitiators (UV-Visible detector set at 700 nm)

Table 2: Macromolecular characteristics of the macroinitiators

Polymer	$M_n^a$	$M_n^b$	$M_w^b$	$\bar{D}^b$
P(DTS-DAP) <sub>5</sub> -S	5000	4600	6900	1.5
P(DTS-DAP) <sub>9</sub> -S	9000	5100	8800	1.7
P(DTS-DAP) <sub>7</sub> -S	7000	12400	18200	1.5
P(DTS-DAP) <sub>5</sub> -MAMA-SG1	5400	6200	13000	2.1
P(DTS-DAP) <sub>9</sub> -MAMA-SG1	9400	7000	15700	2.2
P(DTS-DAP) <sub>7</sub> -MAMA-SG1	7400	6700	16100	2.4

<sup>a</sup> based on the <sup>1</sup>H NMR and with the hypothesis that each chain bore one end-capper; <sup>b</sup> measured by SEC with a UV-Visible detector at 700 nm

c. Synthesis of the rod-coil block copolymers



Scheme 7: Synthetic methodology for rod-coil block copolymer *via* the macroinitiator method

The three nitroxide end-functionalized macroinitiators were employed to initiate the polymerization of *n*-butyl acrylate (*n*BA) *via* nitroxide-mediated polymerization (NMP) (Scheme 7). The use of a controlled radical polymerization is an asset in the synthesis of block copolymers as it makes it more efficient with greater degree of control without by-products and with tolerant synthetic process conditions compared to free-radical polymerizations (FRP).<sup>31,32</sup> *n*-Butyl acrylate was chosen to build the coil block as it provides easy processability towards thin films and shows low glass-transition temperature ( $T_g$ ).<sup>33</sup> Hence, for the first batch, *n*BA was added in large excess, 4700 eq compared to the macroinitiator chains, to a solution of nitroxide end-functionalized macroinitiator P(DTS-DAP)<sub>5</sub>-MAMA-SG1 in toluene. Since NMP is usually carried out above 110°C, solvents with high boiling point are preferred. Here, toluene was the solvent of choice because of its high boiling point (110°C) and it does not contain any chlorine atoms (in comparison with chlorobenzene-based solvents), which can lead to transfer in radical polymerization.<sup>34–36</sup> However, the solubility of the P(DTS-DAP)<sub>5</sub>-MAMA-SG1 was not great and a large amount of toluene was needed to achieve an acceptable sample (33 mg of polymer in 4 mL). Since the volume was high, and to keep a suitable concentration in monomer for polymerization ( $C = 3.35 \text{ mol.L}^{-1}$ ), a substantial amount of monomer had to be inserted (around 5000 eq compared to the macroinitiator chains). The polymerization kinetics were followed by <sup>1</sup>H NMR by withdrawing samples at predefined times. After calculation of the conversion  $p$  by using the integral of one of the monomer peaks and integral of one of the polymer peaks (detailed in Chapter 5), semi-logarithmic kinetic of  $\ln((1-p)^{-1})$  *versus* time was plotted (Figure 9, blue squares). If the polymerization is controlled, a linear evolution of  $\ln((1-p)^{-1})$  *versus* time proves that the concentration of active propagating species is constant throughout the polymerization balancing the rates of activation and deactivation.<sup>37</sup> In the case of the polymerization of *n*BA with the P(DTS-DAP)<sub>5</sub> macroinitiator at 115°C, the kinetic plot presents a plateau at very low conversion and an upward curvature after 3000 min of polymerization. This phenomenon is characteristic of a slow initiation.<sup>38</sup> As



the experimental conditions play a crucial role on the success of the polymerization<sup>39</sup>, we hypothesized that the polymerization temperature was too low to completely activate the macroinitiator. Thus, two other batches of NMP of rod-coil block copolymers were set up with two solutions of nitroxide end-functionalized macroinitiators P(DTS-DAP)<sub>7</sub>-MAMA-SG1 and P(DTS-DAP)<sub>9</sub>-MAMA-SG1 in toluene. *n*BA was added in large excess (5000 and 6600 eq, respectively) to each solution and the mixtures were heated at 125°C and 130°C, respectively. The polymerization kinetics were followed by <sup>1</sup>H NMR and semi-logarithmic kinetic plots of  $\ln((1-p)^{-1})$  versus time are presented in Figure 9 (purple circles and green triangles). At both 125°C and 130°C, the kinetic plots present a linear evolution (even though, at 125°C, the last point slightly deviates from linearity). However, no conclusion can be clearly made about this kinetic plot as it contains only few points and stops at low conversions around 13%. Although the controlled behavior of the polymerizations was not well-established, the temperature increase showed an enhancement of the initiation step as it improves the activation and the solubilization of the macroinitiators in toluene.

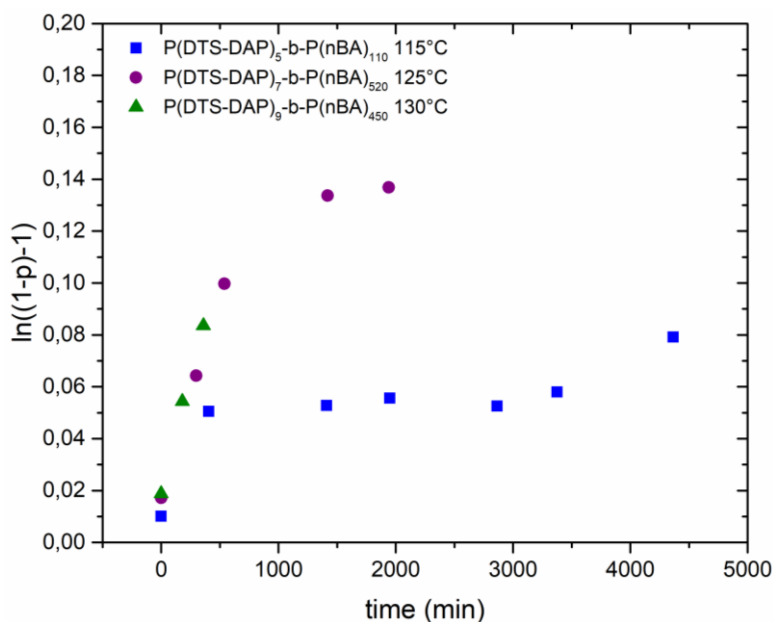


Figure 9: Semi-logarithmic kinetic plots of  $\ln((1-p)^{-1})$ , where  $p$  represents the overall monomer conversion, versus time for *n*-butyl acrylate (*n*BA) polymerizations via NMP with macroinitiators P(DTS-DAP)-MAMA-SG1

The block copolymers were purified by simple evaporation of monomers and solvent, solubilization in a good solvent and drying. The final conversions are 8% at 115°C, 13% at 125°C, and 8% at 130°C but, since the monomer equivalents were high, reasonable chain lengths are reached.

### Chapter 3: Rod-coil block copolymers with filmogenic properties based on low band-gap conjugated polymers

$^1\text{H}$  NMR was performed to verify the proton structure of the purified block copolymers. In Figure 10, the  $^1\text{H}$  NMR spectrum of one of the block copolymers, obtained at  $60^\circ\text{C}$  to enhance the solubility of the rod polymer chains in tetrachloroethane ( $\text{C}_2\text{D}_2\text{Cl}_4$ ), shows one area assigned to the thiophene protons (a), (b), and (c) of the rod block between 6.86 and 8.17 ppm. The large peak at 4.07 ppm corresponds to the two aliphatic protons (e) in  $\alpha$  position of the ester function of *n*-butyl acrylate in the coil block. Other peak centered at 2.35 ppm belongs to the protons (f) of *n*-butyl acrylate in the coil block. The integral of the protons (a), (b), and (c) was calibrated at 30 protons and was compared to the integral of the protons (e) to estimate a number average degree of polymerization ( $\text{DP}_n$ ) of the coil block. For the polymerization performed at  $115^\circ\text{C}$ , the integral of the two protons (e) is equal to 220 while the integral of the six protons (a), (b), and (c) is equal to 30. Hence, the  $\text{DP}_n$  of the coil block is equal to 110. The  $\text{DP}_n$  of the other block copolymers were estimated with the same calculation. The  $\text{DP}_n$  of the rod and coil blocks were calculated from  $^1\text{H}$  NMR and reported in Table 3. Generally, the three block copolymers present short rod blocks and long coil blocks.

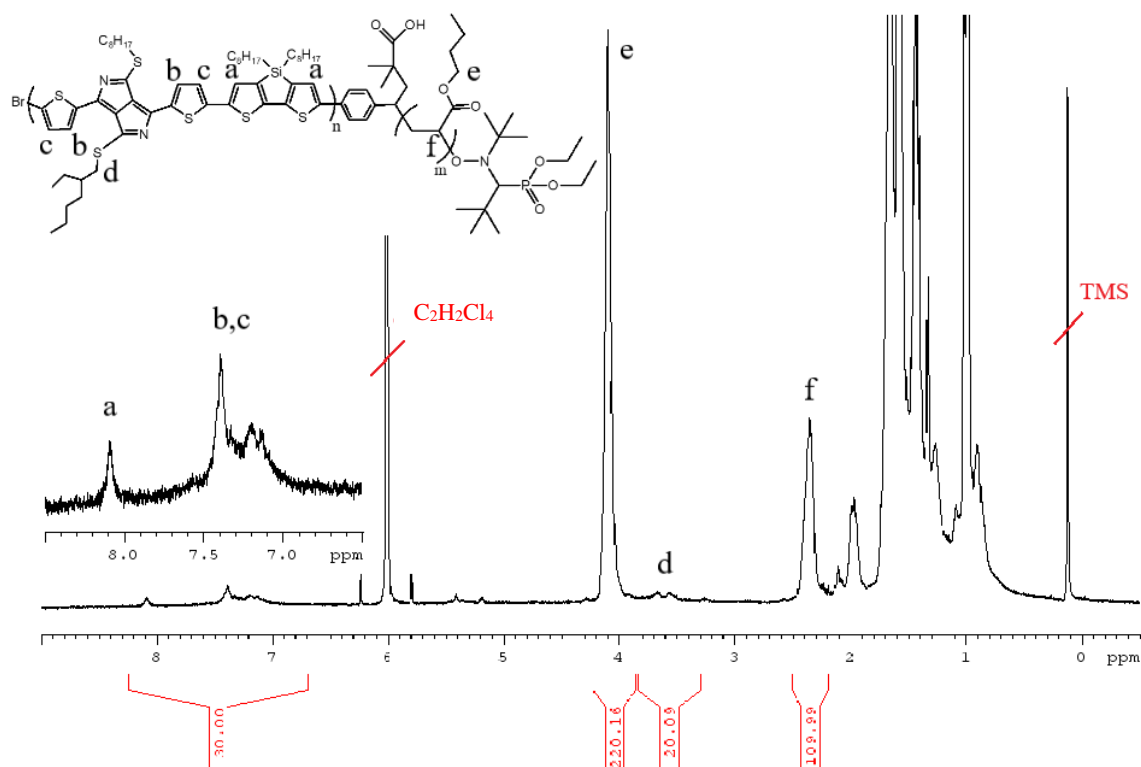


Figure 10:  $^1\text{H}$  NMR spectrum of the rod-coil block copolymer  $\text{P}(\text{DTS-DAP})_5\text{-}b\text{-P}(\text{nBA})_{110}$  (400 MHz,  $\text{C}_2\text{D}_2\text{Cl}_4$ )

NMR diffusion-ordered spectroscopy (DOSY) was performed in the same solvent as  $^1\text{H}$  NMR in order to assess the effective formation of the  $\text{P}(\text{DTS-DAP})\text{-}b\text{-P}(\text{nBA})$  block

### Chapter 3: Rod-coil block copolymers with filmogenic properties based on low band-gap conjugated polymers

copolymers by NMP. By correlating the coefficient spots of each component with their corresponding chemical shifts, DOSY NMR allows the identification of different components by means of the acquisition of two-dimensional spectra.<sup>40</sup> The produced two-dimensional correlation map presents chemical shifts on the horizontal axis and diffusion coefficients on the vertical axis.<sup>41</sup> This technique has been already employed in our laboratory<sup>42,43</sup> as DOSY NMR is a powerful tool to characterize and to prove the formation of block copolymers.<sup>44</sup> This method, sometimes called “NMR chromatography”, is a very sensitive technique capable of detecting traces in complex mixtures. In Figure 11, the DOSY NMR spectrum of the rod-coil block copolymer P(DTS-DAP)<sub>5</sub>-*b*-P(nBA)<sub>110</sub> shows a zoomed view of the DOSY experiment with the related <sup>1</sup>H spectrum projected on the top. The <sup>1</sup>H NMR spectrum has already been explained above (Figure 10). On the DOSY map, the signals corresponding to P(DTS-DAP) and P(nBA) blocks seem to be aligned but the vertical axis presents a wide diffusion coefficient and a double population in the -9.5;-10.2 region. This result cannot confirm the formation of a pure block copolymer but rather suggests the presence of a mixture of residual macroinitiator and block copolymer.

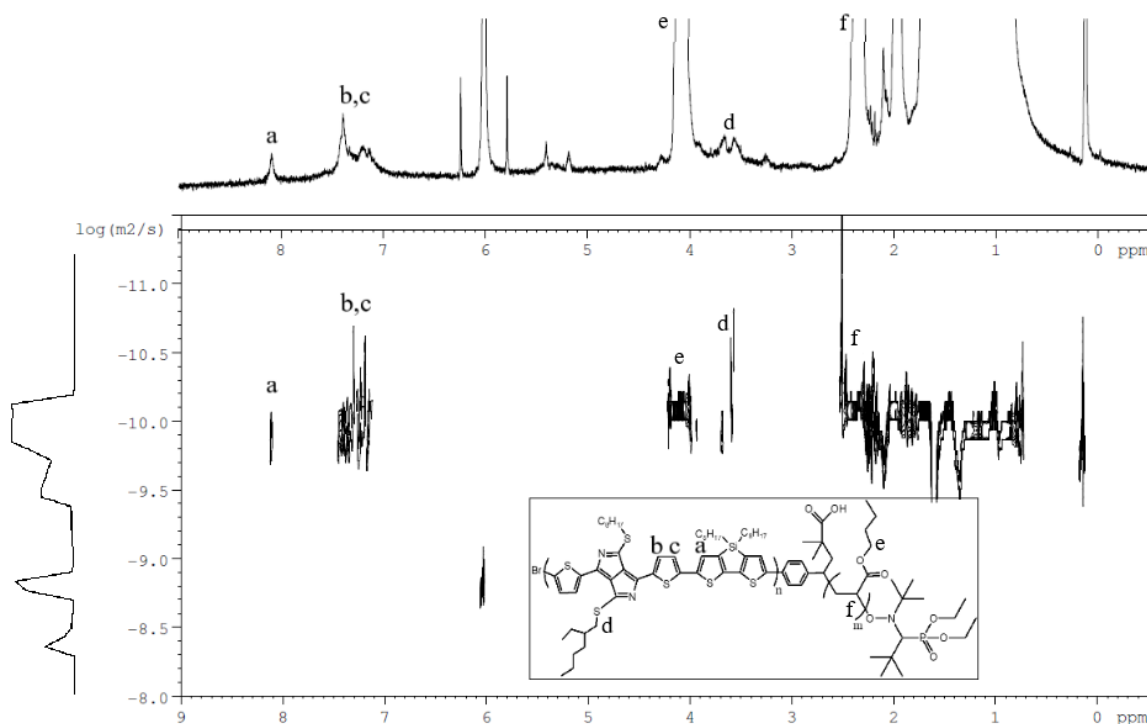


Figure 11: NMR DOSY spectrum of the rod-coil block copolymer P(DTS-DAP)<sub>5</sub>-*b*-P(nBA)<sub>110</sub> (400 MHz, C<sub>2</sub>D<sub>2</sub>Cl<sub>4</sub>)

The three rod-coil block copolymers were characterized by size-exclusion chromatography (SEC) in THF equipped with a UV-Visible detector set at  $\lambda = 700$  nm (Figure

12). Dispersity values between 1.9 and 4.6 and  $M_n$  and  $M_w$  from 43500 to 57950  $\text{g}\cdot\text{mol}^{-1}$  were calculated from conventional calibration using polystyrene standards and are reported in Table 3. On chromatograms, bimodal distributions are observable. This result is in agreement with what was shown in DOSY NMR with the double population. The superimposition of SEC traces of the styrenic end-functionalized  $\text{P}(\text{DTS-DAP})_7\text{-S}$  alternating copolymer, the nitroxide end-functionalized  $\text{P}(\text{DTS-DAP})_7\text{-MAMA-SG1}$  macroinitiator, and the rod-coil block copolymer  $\text{P}(\text{DTS-DAP})_7\text{-}b\text{-P}(\text{nBA})_{520}$  in Figure 13 confirms that the peak at lower molar masses correspond to residual  $\text{P}(\text{DTS-DAP})$  homopolymer.

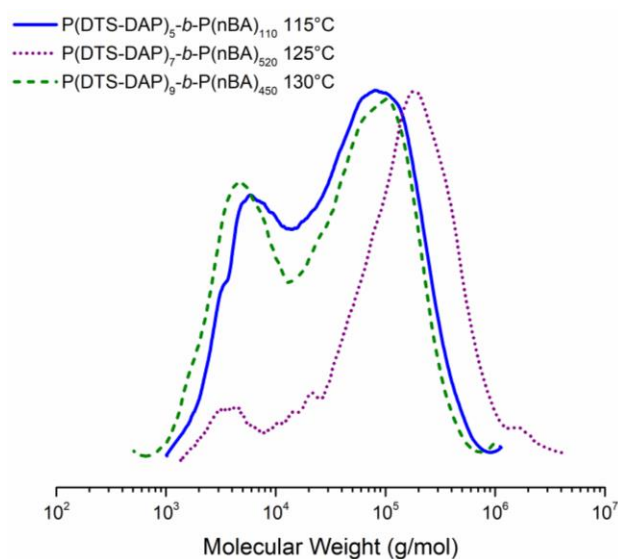


Figure 12: SEC-THF chromatograms of the three rod-coil block copolymers  $\text{P}(\text{DTS-DAP})\text{-}b\text{-P}(\text{nBA})$  (UV-visible detector set at 700 nm)

In Figure 13, the shift of the block copolymer SEC chromatogram towards higher molar masses proves that the macroinitiator was chain extended by the  $\text{P}(\text{nBA})$  coil block. However, the maximum of the low molar masses shoulder on the chromatogram of the block copolymer has the same abscissa than the residual peak of the low band-gap homopolymer. This result means that the final material is composed of a mixture of residual unreacted rod blocks and block copolymers. The same observations were made for the other rod-coil block copolymers,  $\text{P}(\text{DTS-DAP})_5\text{-}b\text{-P}(\text{nBA})_{110}$  and  $\text{P}(\text{DTS-DAP})_9\text{-}b\text{-P}(\text{nBA})_{450}$ . Yet, the shoulders are more intense for these two block copolymers.

As reported in Chapter 1, it is a challenge to separate alternating copolymers from block copolymers. Nevertheless, we tried so by purifying the final block copolymers *via* Soxhlet extraction with methanol in which the  $\text{P}(\text{DTS-DAP})$  is insoluble but the block copolymer is soluble, given that the hot methanol solution gained color during the purification. In Figure 13, the chromatogram of the purified block copolymer is superimposed to the one of the

### Chapter 3: Rod-coil block copolymers with filmogenic properties based on low band-gap conjugated polymers

macroinitiator and the non-purified mixture: the residual peak, pertaining to the homopolymer, is no longer present and the peak of the block copolymer is alone. This purification was successful as the P(*n*BA) coil block is giving solubility in methanol to the block copolymer.

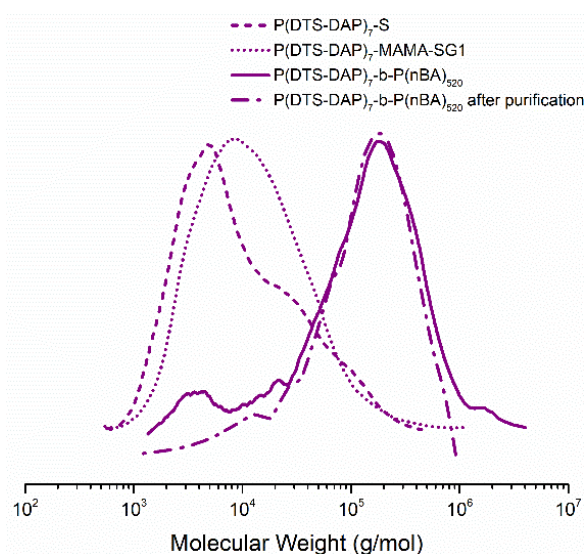


Figure 13: SEC-THF chromatograms of the styrenic end-functionalized P(DTS-DAP)<sub>7</sub>-S alternating copolymer, the P(DTS-DAP)<sub>7</sub>-MAMA-SG1 macroinitiator, and the rod-coil block copolymer P(DTS-DAP)<sub>7</sub>-*b*-P(*n*BA)<sub>520</sub> before and after purification (UV-visible detector set at 700 nm)

The molar masses obtained by SEC-THF are quite consistent with the results obtained from <sup>1</sup>H NMR, except for the first block copolymer P(DTS-DAP)<sub>5</sub>-*b*-P(*n*BA)<sub>110</sub>.

Table 3: Macromolecular characteristics of the rod-coil block copolymers

Copolymer	$Mn_{rod}^a$	$DPn_{rod}^a$	$Mn_{coil}^a$	$DPn_{coil}^a$	$Mn^b$	$Mw^b$	$\mathcal{D}^b$
	( $g \cdot mol^{-1}$ )		( $g \cdot mol^{-1}$ )		( $g \cdot mol^{-1}$ )	( $g \cdot mol^{-1}$ )	
P(DTS-DAP) <sub>5</sub> - <i>b</i> -P( <i>n</i> BA) <sub>110</sub>	5000	5	14100	110	43700	92000	2.1
P(DTS-DAP) <sub>9</sub> - <i>b</i> -P( <i>n</i> BA) <sub>450</sub>	9000	9	57600	450	45900	93000	2.0
P(DTS-DAP) <sub>7</sub> - <i>b</i> -P( <i>n</i> BA) <sub>520</sub>	7000	7	66500	520	89000	216000	2.4

<sup>a</sup> based on the <sup>1</sup>H NMR; <sup>b</sup> measured by SEC with a UV-Visible detector at 700 nm

In this first part, three rod-coil block copolymers were synthesized *via* the macroinitiator method and are detailed in Table 3. The advantage of this methodology is the synthesis and characterization of a well-defined end-functionalized low band-gap polymer prior to produce

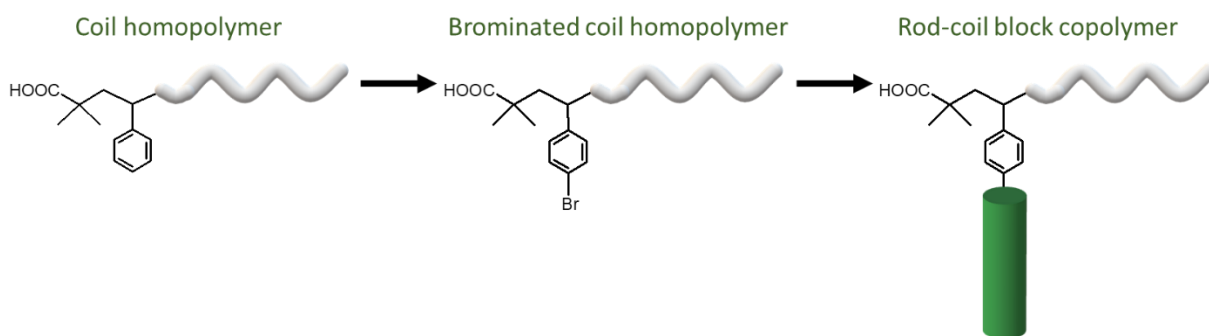
### Chapter 3: Rod-coil block copolymers with filmogenic properties based on low band-gap conjugated polymers

block copolymer. The use of a nitroxide macroinitiator is advantageous to perform the polymerization of the second block *via* NMP. The installation of such nitroxide at the chain end of a low band-gap polymer was possible thanks to the intermolecular radical 1,2 addition which avoid numerous synthetic steps. However, the obtaining of short coil block could not be reached as the *n*BA monomer was introduced in large excess. The use of such high equivalent number of monomers was dictated by the relatively poor solubility of the macroinitiator in toluene. Purification with a Soxhlet extraction in methanol was efficient to remove the unreacted low band-gap homopolymers and pure block copolymers were obtained.

The main limitation of this methodology is the difficulty to produce P(*n*BA) coil block with low molar masses given the 5000-fold excess of monomer compared to macroinitiator. Therefore, in the following part, we used the macro end-capper copolymerization method to produce block copolymer with smaller coil block.

#### 3) Synthesis of rod-coil block copolymers *via* the macro end-capper copolymerization method

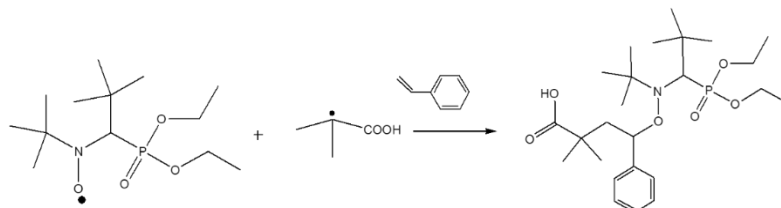
In this second synthetic strategy, a coil P(*n*BA) homopolymer was synthesized and its chain end was then modified into a brominated one. Finally, the brominated coil homopolymer was employed as a macro end-capper in the polycondensation of the low band-gap rod block (Scheme 8).



Scheme 8: Synthetic methodology for rod-coil block copolymer *via* the macro end-capper copolymerization method

a. Synthesis of a second generation alkoxyamine

A second generation alkoxyamine was synthesized *via* the 1,2 addition of MAMA-SG1 onto styrene according to the work reported by Dufils *et al.*<sup>30</sup> (Scheme 9). A solution of the alkoxyamine MAMA-SG1 (1 eq) and styrene (1 eq) in *tert*-butanol was heated at 100°C for 7h. The synthetic details and purification steps are reported in the experimental part (Chapter 5). The final product labelled as MAMA-SG1-styrene presents a phenyl group corresponding to the olefin substituent.



Scheme 9: Synthetic methodology for second generation alkoxyamine based on styrene

To verify the proton structure of the purified alkoxyamine and the presence of diastereoisomers, several NMR techniques were employed. First, <sup>1</sup>H NMR was performed on the MAMA-SG1-styrene in deuterated chloroform (CDCl<sub>3</sub>). The attribution of the signals was made thanks to the predictions of the ChemDraw Ultra software and the previous work of Dufils *et al.*<sup>30</sup> On the <sup>1</sup>H NMR spectrum (Figure 14), the signals from 7.14 to 7.33 ppm are easily attributable to the phenyl protons (a), (b), and (c) from the styrene and the CH<sub>3</sub> protons (h), (i), (j), (k) have their chemical shifts between 0.72 and 1.36 ppm. In the work of Dufils *et al.*, two diastereoisomers were obtained in a ratio 54:46 with different chemical shifts.

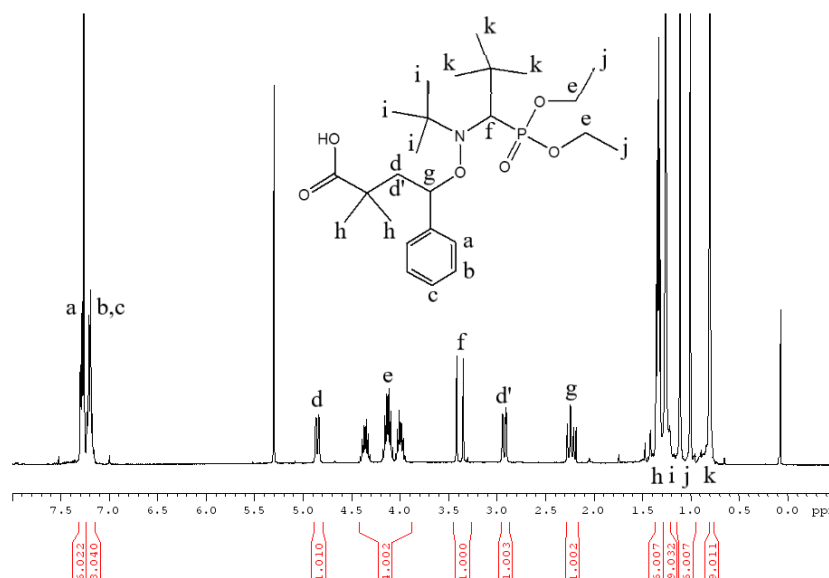


Figure 14: <sup>1</sup>H NMR spectrum of the second generation alkoxyamine MAMA-SG1-styrene (400 MHz, CDCl<sub>3</sub>)

### Chapter 3: Rod-coil block copolymers with filmogenic properties based on low band-gap conjugated polymers

Since the attribution of the  $^1\text{H}$  NMR spectrum was hard to complete, a two-dimensional spectroscopy known as correlated spectroscopy (COSY) was employed to determine which signals are coupled to each other (Figure 15).<sup>45</sup> This technique is based on the homonuclear correlation of the chemical shifts *via* J coupling.<sup>46</sup> On a typical spectrum, correlations are visible when there is spin-spin coupling between protons: diagonal and cross peaks are obtained. Since the diagonal peaks correspond to the 1D spectrum, only the cross peaks are interesting as they indicate couplings between two multiplets up to three bonds away. By tracing the cross-peaks and crossing the  $^1\text{H}$  NMR results, the protons (d) and (d') were correlated with the proton (g). Hence, the proton (g) was attributed to the signal centered at 2.22 ppm and the protons (d) and (d') to the doublets centered at 4.84 and 2.91 ppm, respectively. The protons (e) and (f) were attributed to the multiplet from 3.88 to 4.42 ppm and the doublet centered at 3.36 ppm, respectively. The calculated integrals fit the attribution and the assignment corresponds to the one of the minor diastereoisomer obtained by Dufils *et al.*

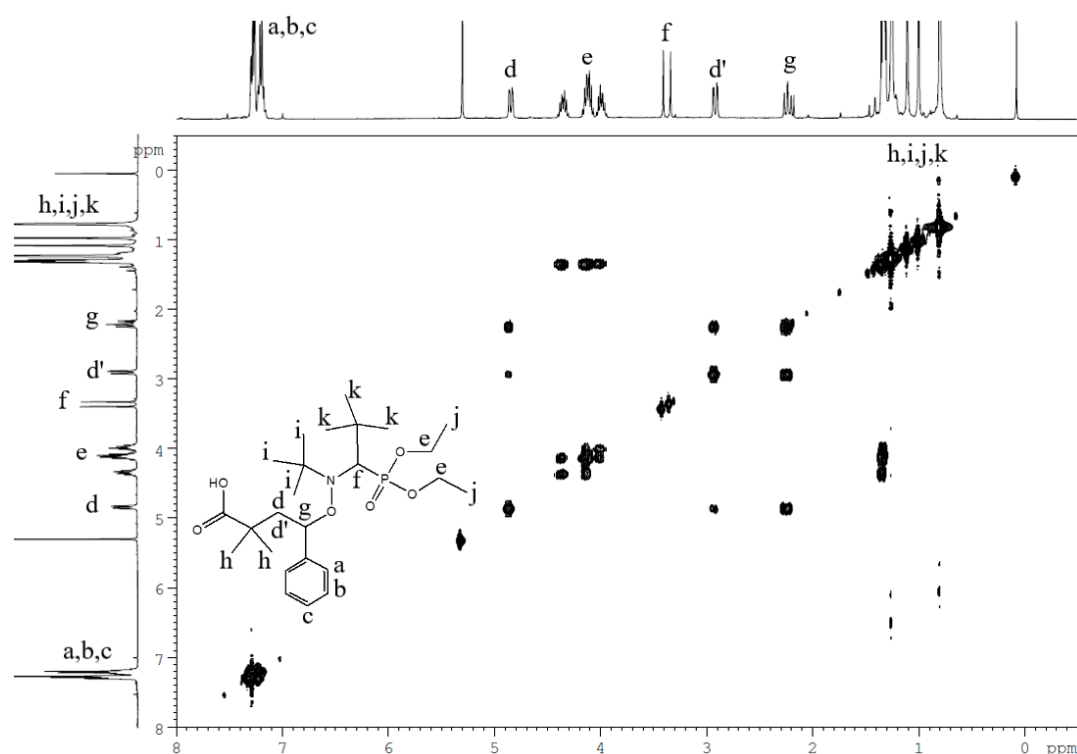


Figure 15: NMR COSY spectrum of the second generation alkoxyamine MAMA-SG1-styrene (400 MHz,  $\text{CDCl}_3$ )

Such attribution implies that only one diastereoisomer was synthesized instead of two diastereoisomers in the work of Dufils *et al.* This result was confirmed by using the  $^{31}\text{P}$  NMR (Figure 16) with and without  $^1\text{H}$  coupling. In the decoupled  $^{31}\text{P}$  NMR spectrum (Figure 16b), only one signal is observable at 24.91 ppm. Since carbons 2 and 3 are asymmetric (labelled



### Chapter 3: Rod-coil block copolymers with filmogenic properties based on low band-gap conjugated polymers

with \*), four diastereoisomers are possible. It means four different molecules can be produced, including two with different phosphorus due to the asymmetric carbon 2. Such result would be verified if two different signals were observed on the decoupled  $^{31}\text{P}$  NMR spectrum. Yet, only one signal is noticeable on the spectrum meaning only one molecule was synthesized. This result is in accordance with the attribution of the  $^1\text{H}$  NMR spectrum. Moreover, the  $^1\text{H}$  coupled  $^{31}\text{P}$  NMR spectrum (Figure 16a) shows a doublet of quintuplet centered at 24.91 ppm corresponding to the signal observed in the decoupled  $^{31}\text{P}$  NMR spectrum (Figure 16b). Such a multiplet is explained by the coupling of the phosphorus with the four equivalent protons on the carbon 1 and with the proton on carbon 2. Hence, coupling constants have been calculated:  $^1J_{\text{PH}}$  is around 27 Hz and  $^3J_{\text{PH}}$  is equal to 7.4 Hz.<sup>47</sup>

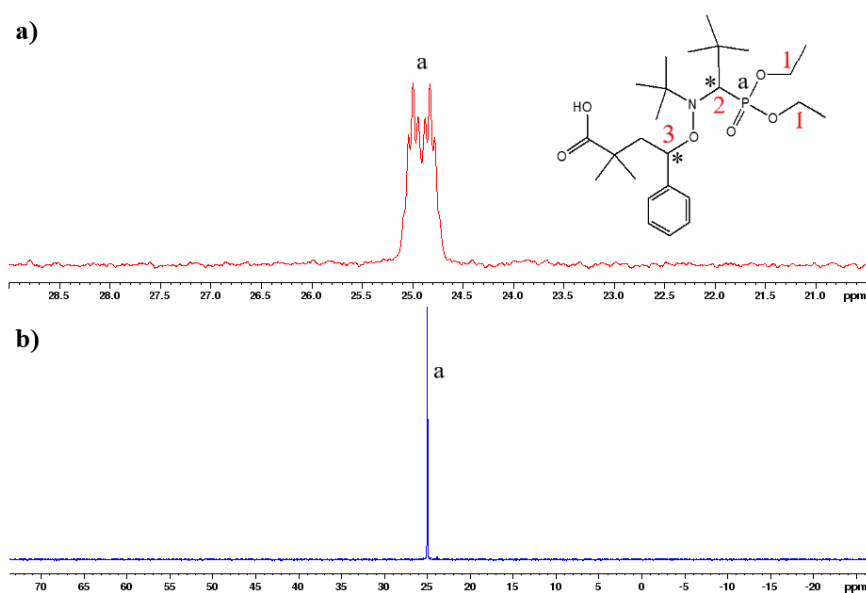
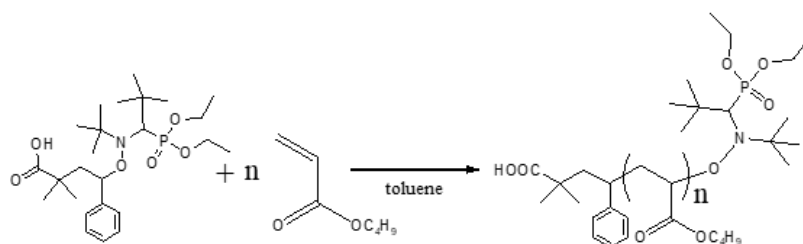


Figure 16:  $^{31}\text{P}$  NMR spectra of the second generation alkoxyamine MAMA-SG1-styrene (400 MHz,  $\text{CDCl}_3$ ) with **a)** with  $^1\text{H}$  coupling and **b)** without  $^1\text{H}$  coupling

#### b. Synthesis of the coil homopolymer

The *n*-butyl acrylate (*n*BA) monomer was polymerized *via* nitroxide-mediated polymerization (NMP) using the second generation alkoxyamine MAMA-SG1-styrene to synthesize a phenyl end-functionalized polymer (Scheme 10). The synthetic details are reported in the experimental part (Chapter 5).



Scheme 10: Synthetic methodology for phenyl end-functionalized coil homopolymer

The NMP was performed under inert atmosphere in dry toluene at 120°C and the polymerization kinetics were followed by  $^1\text{H}$  NMR by withdrawing samples at predefined times. After calculation of the conversion  $p$  by comparing integral of one of monomer peaks and integral of one of the polymer peak (detailed in Chapter 5), semi-logarithmic kinetic of  $\ln((1-p)^{-1})$  versus time was plotted (Figure 17). The controlled behavior of the polymerization is not clearly verified as no strict linear evolution of  $\ln((1-p)^{-1})$  versus time can be observed. The reaction was stopped after reaching a conversion of 55% in order to have short coil chains contrary to the long coil chains obtained *via* the macroinitiator method.

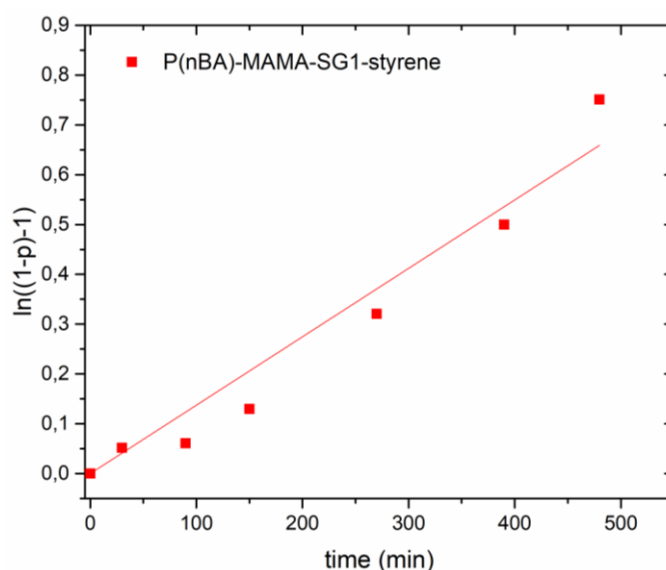


Figure 17: Semi-logarithmic kinetic plots of  $\ln((1-p)^{-1})$ , where  $p$  represents the overall monomer conversion, versus time for *n*-butyl acrylate (*n*BA) polymerizations *via* NMP with the MAMA-SG1-styrene initiator

The coil homopolymer labelled as P(*n*BA)-MAMA-SG1-styrene was purified by simple evaporation of monomer and solvent, dissolved in a good solvent and dried. In Figure 18, the  $^1\text{H}$  NMR spectrum of the polymer, performed in  $\text{C}_2\text{D}_2\text{Cl}_4$ , shows a large peak at 4.08 ppm corresponding to the two aliphatic protons (d) in  $\alpha$  position of the ester of *n*-butyl acrylate. Other peaks centered at 2.32 ppm and 0.97 ppm belong to protons (f) and (g) of poly(*n*-butyl

Chapter 3: Rod-coil block copolymers with filmogenic properties based on low band-gap conjugated polymers

acrylate). The protons of the phenyl group (a), (b), and (c) have their signals between 7.1 and 7.35 ppm. Finally, the signal at 3.27 ppm belongs to the proton (e) on the SG1 chain end. Thanks to the integral of the protons of the phenyl group (b) ( $I_b$ ) or thanks to the integral of the proton (e) of the SG1 chain end ( $I_e$ ), the degree of polymerization  $DP_n$  can be calculated following this equation:

$$DP_n = \frac{I_{d/2}}{I_{b/2}} = \frac{I_{d/2}}{I_{e/1}} = 55 = I_f \quad (7)$$

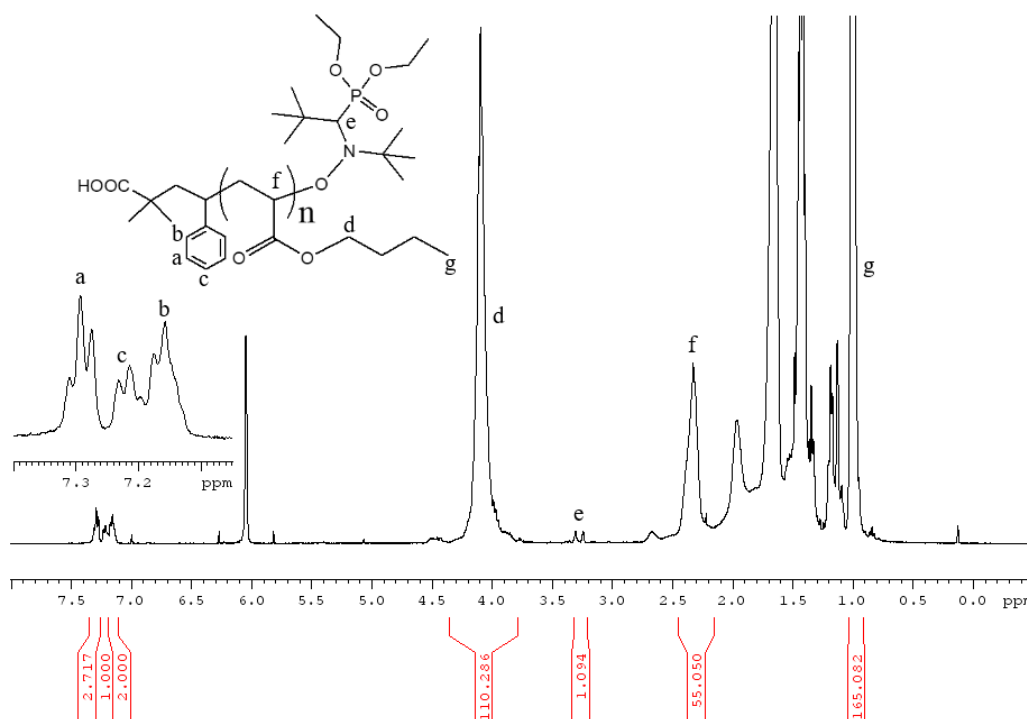


Figure 18:  $^1H$  NMR spectrum of the coil homopolymer  $P(nBA)_{55}$ -MAMA-SG1-styrene (400 MHz,  $C_2D_2Cl_4$ )

The coil homopolymer was characterized by size-exclusion chromatography (SEC) in THF equipped with a RI detector (Figure 19). A dispersity of  $\sim 1.15$  was calculated from conventional calibration using polystyrene standards which is one of the features of living polymerization like NMP.<sup>21,48</sup> The SEC results are reported in Table 4. The  $DP_n$  calculated from the  $^1H$  NMR was chosen for the rest of the study as the  $DP_n$  extracted from the SEC results is less correct due to the polystyrene calibration.

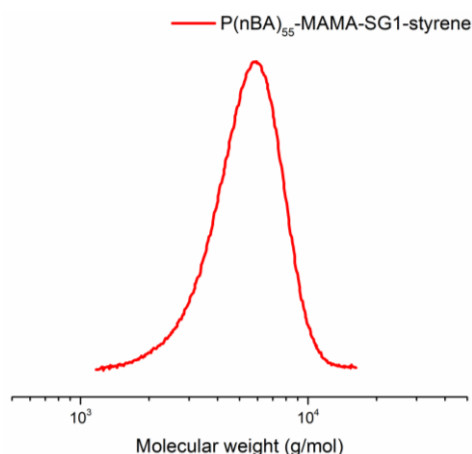


Figure 19: SEC-THF chromatogram of the coil homopolymer P(nBA)<sub>55</sub>-MAMA-SG1-styrene (RI detector)

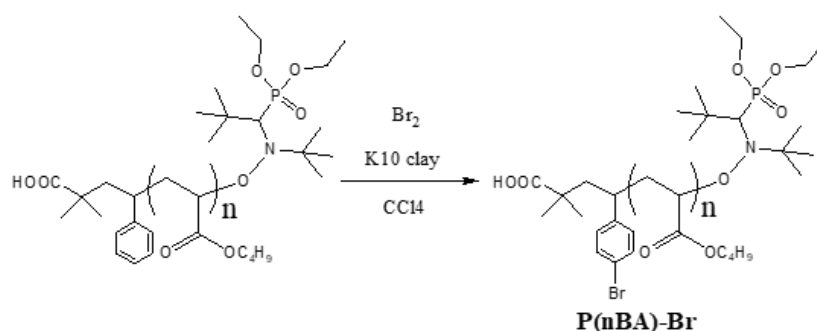
Table 4: Macromolecular characteristics of the coil homopolymer

<i>Polymer</i>	<i>Mn<sup>a</sup></i>	<i>Mw<sup>a</sup></i>	<i>Đ<sup>a</sup></i>	<i>Mn<sup>b</sup></i>	<i>DPn<sup>b</sup></i>
P(nBA) <sub>55</sub> -MAMA-SG1-styrene	4860	5600	1.15	7050	55

<sup>a</sup> measured by SEC with a RI detector; <sup>b</sup> based on <sup>1</sup>H NMR

### c. Functionalization of the coil homopolymer

The phenyl end-functionalized coil homopolymer was brominated to install a bromine function at the chain end in presence of K10-montmorillonite (Scheme 11). The functionalization reaction was conducted according to previous work reported by Ouhib<sup>49</sup> and by Venkatachalapathy *et al.*<sup>50</sup> A solution of P(nBA) (1 eq) in CCl<sub>4</sub> was mixed with the clay and bromine (1 eq) was added dropwise prior to stirring at room temperature for 6h. The synthetic details are reported in the experimental part (Chapter 5).



Scheme 11: Synthetic methodology for bromine end-functionalized coil homopolymer

The bromination was expected to occur with regioselectivity on the aromatic ring (para-substitution) as a heterogeneous catalyst (*i.e.* clay mineral also called K10-montmorillonite) was employed. Actually, such catalysts are well-known for their high catalytic activity, versatility, and selectivity.<sup>51,52</sup> After 6h of reaction, the brominated polymer was purified by filtration and washings with diethyl ether. The brominated coil homopolymer labelled as P(*n*BA)<sub>55</sub>-MAMA-SG1-styrene-Br was dried and obtained with good yield (86%).

The <sup>1</sup>H NMR was performed in C<sub>2</sub>D<sub>2</sub>Cl<sub>4</sub> to confirm the bromination on the aromatic ring. In Figure 20, the spectrum shows a large peak at 4.08 ppm corresponding to the two aliphatic protons (d) in  $\alpha$  position of the ester function of *n*-butyl acrylate. Other peaks centered at 2.33 ppm and 0.97 ppm belong to the protons (f) and (g) of *n*-butyl acrylate. Considering the aromatic protons, the attribution was slightly more complex. Actually, the final material is a mixture of brominated and non-brominated polymer chains. The protons of the non-brominated phenyl group (a) and (c) have their signals centered at 7.30 and 7.23 ppm, respectively. The protons of the brominated phenyl group (a') have their signals centered at 7.54 ppm: a deshielding of the protons occurs as the bromine atom (an electronegative atom) is installed on the phenyl group. Finally, the signal centered at 7.16 ppm belongs to protons of both the brominated and non-brominated phenyl group (b) and (b').

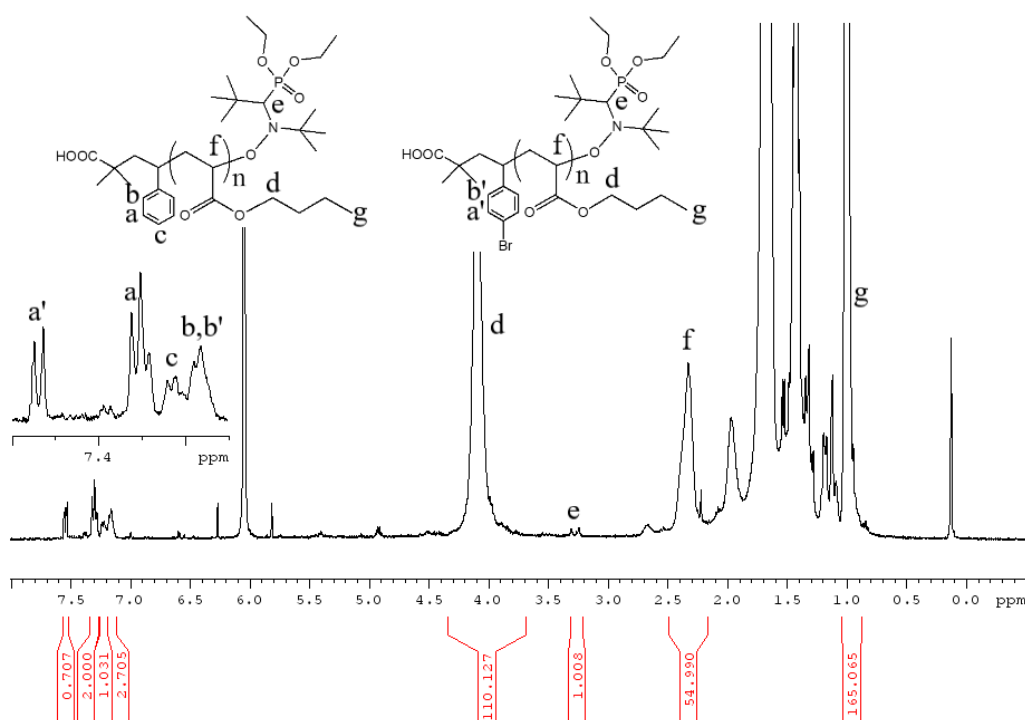


Figure 20: <sup>1</sup>H NMR spectrum of the bromine end-functionalized coil homopolymer P(*n*BA)<sub>55</sub>-MAMA-SG1-styrene-Br (400 MHz, C<sub>2</sub>D<sub>2</sub>Cl<sub>4</sub>)

### Chapter 3: Rod-coil block copolymers with filmogenic properties based on low band-gap conjugated polymers

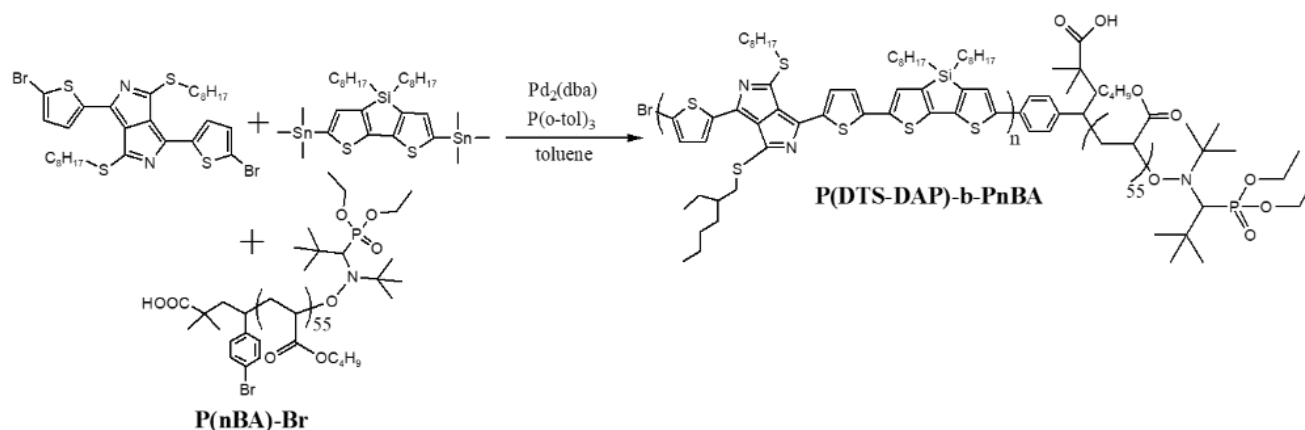
The functionalization yield was calculated by comparing the integral of the protons (a') with the integral of the protons (a) following this equation:

$$\text{bromination yield} = \frac{I_{a'}}{I_a + I_{a'}} \times 100 = 26 \quad (8)$$

In the end, 26% of the polymer chains were successfully brominated. Despite repeating this post-polymerization step, the functionalization yield was not increased. Moreover, since the brominated and non-brominated polymer chains have the same solubility, no purification could be performed to separate the two different homopolymers. However, we decided to use the unpurified polymer in the next step synthesis.

#### d. Synthesis of the rod-coil block copolymer

The dibrominated DAP and the distannylated DTS monomers were polymerized *via* a Stille cross-coupling polycondensation, using a Pd<sup>0</sup> catalyst (Pd<sub>2</sub>(dba)<sub>3</sub>), the tri(*o*-tolyl)phosphine ligand (P(*o*-tol)<sub>3</sub>), and the bromine end-functionalized coil homopolymer P(*n*BA)<sub>55</sub>-MAMA-SG1-styrene-Br as a macro end-capper (monofunctional) to synthesize a rod-coil block copolymer (Scheme 12).



Scheme 12: Synthetic methodology for rod-coil block copolymer *via* the macro end-capper copolymerization method

The brominated styrene end-functionalized coil homopolymer was selected as a macro end-capper due to its Stille polymerizable bromophenyl group. The stoichiometry of the

### Chapter 3: Rod-coil block copolymers with filmogenic properties based on low band-gap conjugated polymers

reagents was not maintained due to the low bromination yield of the coil block (*i.e.* 26%) (Table 5), according to the Carothers equation introduced in Chapter 2:

$$N_A = N_B + N_{B'} \quad \rightarrow \quad 2N_{DTS} = 2N_{DAP} + N_{EG} \quad (9)$$

In which  $N_A$ ,  $N_B$ ,  $N_{B'}$  represent the mole number of stannate functions and bromide groups pertaining to the DAP monomer and to the end-capping agent respectively.  $N_{DTS}$ ,  $N_{DAP}$  and  $N_{EG}$ , define the mole number of DTS and DAP monomers and 4-bromostyrene end-groups (EG), respectively.

Due to the low bromination yield of the coil block, the total number of aryl bromides (*i.e.* 1.9) is not equal to the total number of aryl stannanes (*i.e.* 2). Hence, the macro end-capping is not totally promoted. The synthetic details are reported in the experimental part (Chapter 5). The Stille polycondensation was performed under inert atmosphere in dry toluene and followed by the precipitation of the polymer in ethanol. After filtration, the polymer was purified by Soxhlet extraction in ethanol to remove impurities such as metallic byproducts, catalysts, ligands and unreacted monomers. This extraction *via* ethanol was also performed to remove the non-brominated and the unreacted brominated coil polymers. As the ethanol fraction was colorless, we assumed it did not contain the block copolymer. Two other Soxhlet extractions were performed in THF and in chloroform in order to isolate the rod-coil block copolymer. As the chloroform fraction was totally empty and the filtrate was colorless, we assumed the rod-coil block copolymer was in the THF fraction. Moreover, since the P(*n*BA) coil block is supposed to enhance the solubility of the rod block, the rod-coil block copolymer should be completely soluble in THF regardless of the rod block size. The final yield, calculated from the THF fraction, was around 30%.

$^1\text{H}$  NMR was performed to verify the proton structure of the final material in the THF fraction. In Figure 21, the spectrum, obtained at 60°C to enhance the solubility of the rod polymer chains in tetrachloroethane ( $\text{C}_2\text{D}_2\text{Cl}_4$ ), shows a multiplet between 7.10 and 8.18 ppm assigned to the thiophene protons (a), (b), and (c). The signal at 4.10 ppm corresponds to the two aliphatic protons (e) in the  $\alpha$  position of the ester function of *n*-butyl acrylate in the coil block. Finally, the signal centered at 3.65 ppm belongs to the four aliphatic protons (d) in  $\alpha$  position of sulfur atoms on the alkyl chains of the rod block. Integrals of the protons (a), (b), (c), (d) and (e) were compared to estimate a number average degree of polymerization ( $\text{DP}_n$ ) of

### Chapter 3: Rod-coil block copolymers with filmogenic properties based on low band-gap conjugated polymers

the rod block. The integral of the two protons (e) is equal to 110 while the integral of the six protons (a), (b), and (c) is equal to 172 and the integral of the four protons (d) is equal to 115. Hence, the rod block is two times smaller than the coil block suggesting the  $DP_n$  of the rod block is equal to 29.

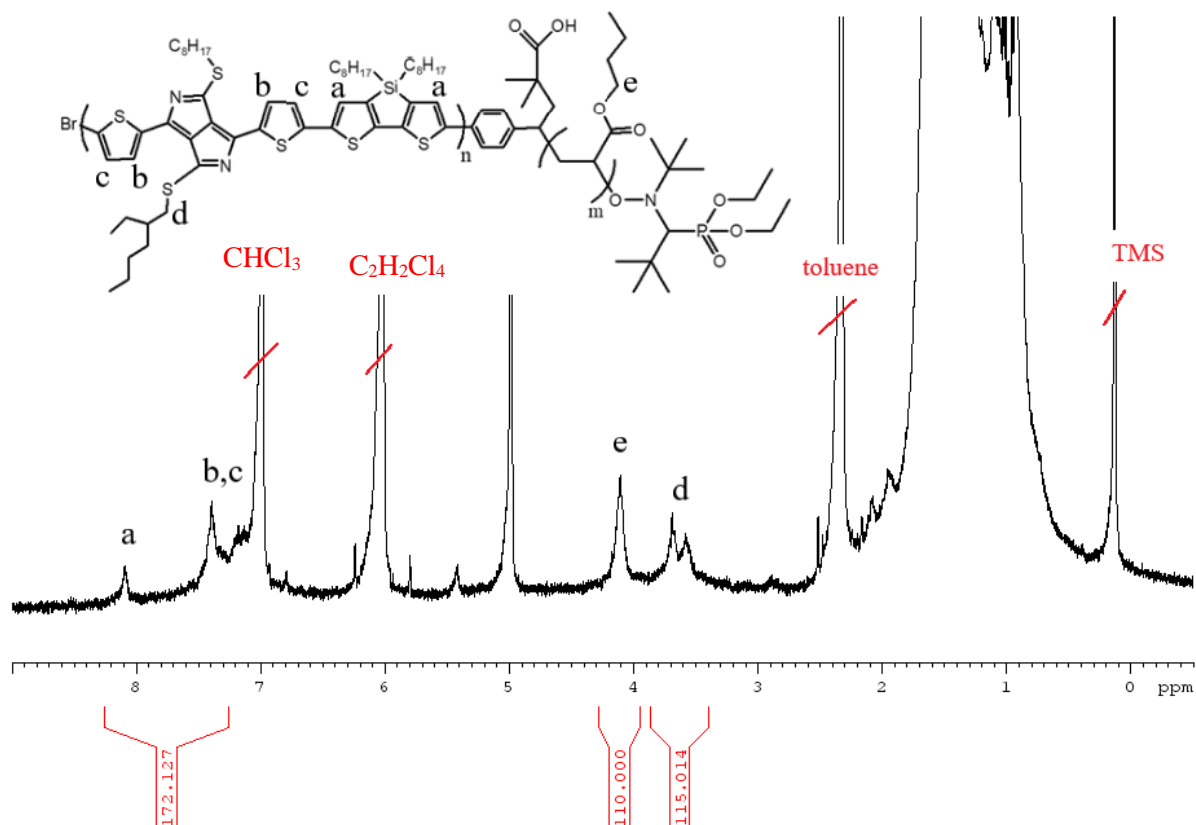


Figure 21:  $^1\text{H}$  NMR spectrum of the rod-coil block copolymer  $\text{P}(\text{DTS-DAP})_{29}\text{-}b\text{-P}(\text{nBA})_{55}$  (400 MHz,  $\text{C}_2\text{D}_2\text{Cl}_4$ )

DOSY NMR was performed in the same solvent as  $^1\text{H}$  NMR in order to assess the effective formation of the  $\text{P}(\text{DTS-DAP})\text{-}b\text{-P}(\text{nBA})$  block copolymers by the macro end-capper copolymerization method. In Figure 22, the DOSY NMR spectrum of the rod-coil block copolymer  $\text{P}(\text{DTS-DAP})_{29}\text{-}b\text{-P}(\text{nBA})_{55}$  shows a zoomed view of the DOSY experiment with the related  $^1\text{H}$  spectrum projected on the top and the diffusion coefficients on the vertical axis. On the DOSY map, the signals corresponding to  $\text{P}(\text{DTS-DAP})$  and  $\text{P}(\text{nBA})$  blocks seem to be aligned around  $10^{-10} \text{ m}^2\cdot\text{s}^{-1}$  but the vertical axis presents a wide diffusion coefficient. This result cannot confirm the formation of a block copolymer but rather indicates the presence of a blend between homopolymers and block copolymers.



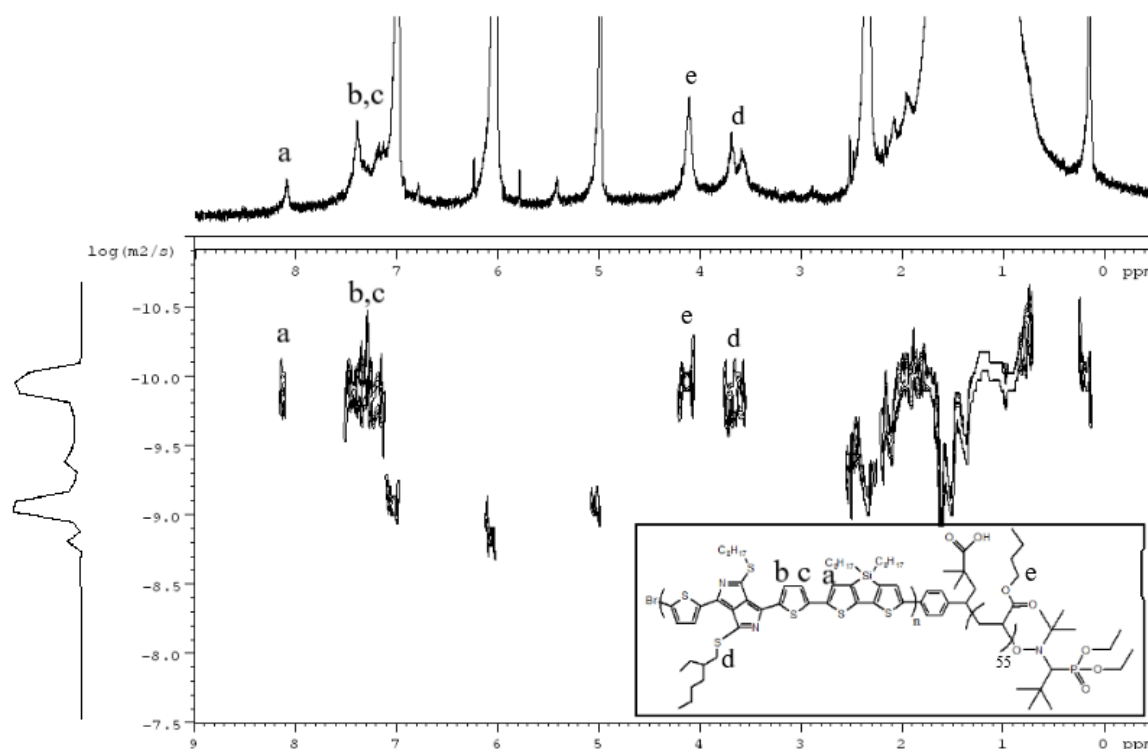


Figure 22: NMR DOSY spectrum of the rod-coil block copolymer P(DTS-DAP)<sub>29</sub>-*b*-P(*n*BA)<sub>55</sub> (400 MHz, C<sub>2</sub>D<sub>2</sub>Cl<sub>4</sub>)

The rod-coil block copolymer was characterized by SEC in THF equipped with a UV-Visible detector set at  $\lambda = 700$  nm. The SEC chromatogram was compared to the one of the coil homopolymer obtained with a RI detector (Figure 23). A shoulder towards higher molar mass is apparent, suggesting the presence of the desired material. However, the peak towards lower molar mass on the block copolymer SEC chromatogram have the same molar mass as the coil homopolymer in RI detector. Yet, the coil homopolymer cannot be analyzed *via* UV-Visible detector as it does not absorb in the UV-Visible region. Hence, the peak towards lower molar mass obtained with the UV-Visible detector does not correspond to the coil homopolymer alone. We hypothesized that this peak stands for the rod alternating copolymer alone that was not end-capped with the macro end-capper coil homopolymer and the shoulder towards higher molar mass is correlated to the block copolymer. Indeed, this result could correspond to the DOSY NMR where the signal at 3.65 ppm, corresponding to the four aliphatic protons (d) in the  $\alpha$  position of the sulfur atoms on the alkyl chains of the rod block, presents two spots on the diffusion pattern. The spot with the lowest diffusion coefficient is aligned with the spot corresponding to the aliphatic protons (e) in  $\alpha$  position of the ester function of *n*-butyl acrylate (signal at 4.1 ppm) and must correspond to the block copolymer. The spot with the highest diffusion coefficient is not aligned with P(*n*BA) diffusion spot and must rely on smaller

### Chapter 3: Rod-coil block copolymers with filmogenic properties based on low band-gap conjugated polymers

homopolymer chains. Hence, the final material is a mixture of rod alternating copolymer and rod-coil block copolymer. As reported in Chapter 1, it is a challenge to separate homopolymers from block copolymers. Yet, in this case, the difference of solubility between the rod alternating copolymer and the block copolymer could be sufficient to perform a second Soxhlet extraction in ethanol to separate them. Unfortunately, due to lack of time, we could not try to purify the block copolymer.

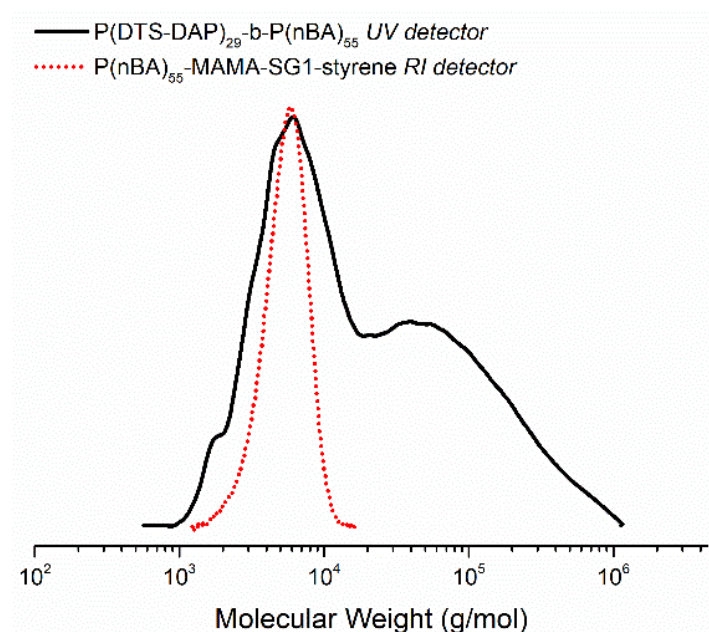


Figure 23: SEC-THF chromatograms of the coil homopolymer P(nBA)-MAMA-SG1-styrene (RI detector) and the rod-coil block copolymer P(DTS-DAP)<sub>29</sub>-b-P(nBA)<sub>55</sub> (UV-Visible detector set at 700 nm)

The amount of the rod block/homopolymer was calculated from <sup>1</sup>H NMR and reported in Table 5. 29 units of DTS-DAP were polymerized for 55 units of nBA. For simplicity, we called this sample P(DTS-DAP)<sub>29</sub>-b-P(nBA)<sub>55</sub> even though it is a mixture. Here, the coil block is smaller than the ones attached to the rod blocks *via* the first synthetic strategy. The molar mass of the shoulder towards high molar mass was calculated from the SEC results and is consistent with the molar masses calculated *via* <sup>1</sup>H NMR.

Table 5: Macromolecular characteristics of the rod-coil block copolymer

Polymer	$r^a$	$N_{DTS}^b$	$N_{DAP}^b$	$N_{EG}^b$	$Mn_{rod}^c$ ( $g.mol^{-1}$ )	$DPn_{rod}^c$	$Mn_{coil}^c$ ( $g.mol^{-1}$ )	$DPn_{coil}^c$	$Mp_{shoulder}^e$ ( $g.mol^{-1}$ )
P(DTS-DAP) <sub>29-b-</sub> P( <i>n</i> BA) <sub>55</sub>	1.04	1	0.94	0.02	28300	29	7050	55	34050

<sup>a</sup> feed ratio calculated according to Carothers equations; <sup>b</sup> molar fraction; <sup>c</sup> based on the <sup>1</sup>H NMR <sup>d</sup> measured by SEC with a RI detector; <sup>e</sup> measured by SEC with a UV-Visible detector at 700 nm

This second synthetic method led to smaller coil block than in the first synthetic method. However, even if the size of the two blocks are more homogeneous, this synthetic strategy is less efficient than in the first one as the bromination step did not lead to satisfactory yields. Moreover, this method includes more synthesis steps than the macroinitiator method and is therefore more time consuming than the other one.

#### 4) Optical, thermal, and structural properties

##### a. Optical properties

Optical properties of the materials described in this chapter were studied by Visible-NIR spectrophotometry.

First, the Visible-NIR absorption spectra of the rod alternating copolymers (described in II.1)a.) were measured in chloroform. In Figure 24, the three spectra present the same shape with two characteristic absorption peaks, which is a feature commonly observed for alternating donor-acceptor copolymers.<sup>53</sup> The three spectra show an absorption band between 400 and 560 nm corresponding to a  $\pi$ - $\pi^*$  transition along the polymer backbone with  $\lambda_{max}$  around 475 nm. In the literature, it is well-known that alternating monomers with different electronic levels in the polymer produces a transition assigned to an intramolecular charge transfer (ICT) between the donor and the acceptor monomers.<sup>54</sup> This phenomenon is observed on the three spectra where a second absorption band appears between 560 and 1100 nm. The strength of the acceptor dictates the range of the ICT band: the stronger the acceptor is, the higher the maximum wavelength is.<sup>55,56</sup> The bathochromic phenomenon (also called red shift) is also influenced by

### Chapter 3: Rod-coil block copolymers with filmogenic properties based on low band-gap conjugated polymers

rigidity<sup>57</sup>, conjugation length<sup>58</sup>, and aggregation<sup>59</sup> also called  $\pi$ -stacking where the aromatic rings interact with each other.<sup>60</sup> All these parameters are closely related and can be influenced by several other criteria such as the employment of a  $\pi$ -linker or the planarization of the polymer backbone. In Figure 24, the maximum of the ICT band is located around 845 nm for the three polymers. Finally, there is a shoulder around 930 nm that can be attributed to aggregates of the conjugated polymer *via*  $\pi$ -stacking. This result will be confirmed later by the observation of thin film spectra.

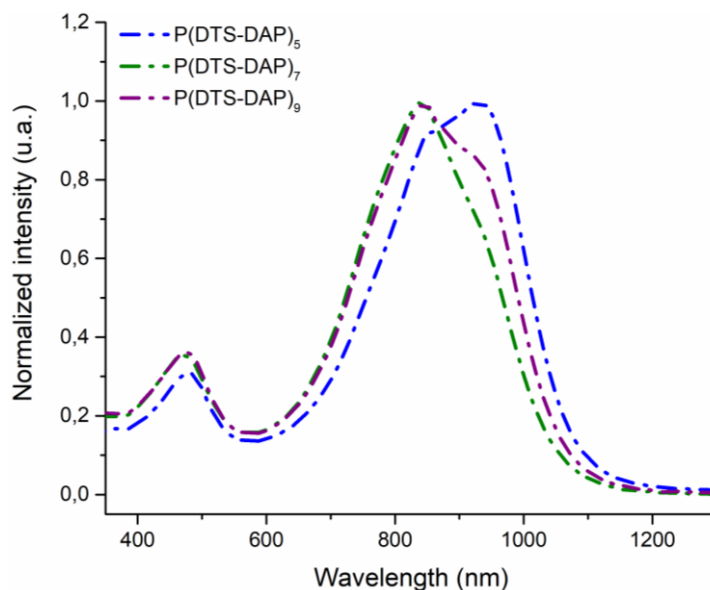


Figure 24: Visible-NIR absorption spectra of the rod copolymers in  $\text{CHCl}_3$

Then, the Visible-NIR absorption spectra of the rod-coil block copolymers (described in II.1).c. and II.3).d.) were measured in chloroform. The spectra, presented in Figure 25, have been normalized considering the maximum absorption of the  $\pi$ - $\pi^*$  transition band of each material with  $\lambda_{\text{max}}$  between 470 and 482 nm. Concerning the ICT bands around 800 nm, they present different maximum absorptions varying in position (wavelength) and intensity (absorbance). The  $\lambda_{\text{max}}$  of the ICT band of each block copolymers are reported in Table 6.

Since the coil block does not absorb in the 350-1300 nm spectral range, the absorption spectra seen in Figure 25 largely reflect the conjugated rod blocks in the block copolymers.<sup>61</sup> A tendency is observed: the rod-coil block copolymers with moderate coil block lengths (*i.e.*  $\text{P(DTS-DAP)}_{29}\text{-}b\text{-P(nBA)}_{55}$  and  $\text{P(DTS-DAP)}_5\text{-}b\text{-P(nBA)}_{110}$ ) show pretty much the same optical behavior than the rod copolymer. By superimposing the absorption spectra (normalized with the  $\pi$ - $\pi$  transition) of the rod copolymer  $\text{P(DTS-DAP)}_7$  and those of the two rod-coil block copolymers, we could observe that the ICT transition band of all samples have a similar

position, despite normalization. On the contrary, the block copolymers containing longer coil chains (*i.e.* P(DTS-DAP)<sub>9</sub>-*b*-P(nBA)<sub>450</sub> and P(DTS-DAP)<sub>7</sub>-*b*-P(nBA)<sub>520</sub>) present a strong hypsochromic shift of around 60 nm. Moreover, the intensity of the ICT absorbance decreased by a factor of 2.5 in comparison with the rod copolymer. The vanishing of the intensity of the ICT band occurs with the decrease of the rod block ratio. This result suggests that interchain interactions among the rod block are reduced by incorporating the coil block.<sup>62</sup>

Besides, we can clearly see, by the observation of all the samples, that the transition around 930 nm, attributed to the  $\pi$ -stacking, decreases in intensity when the size of the P(nBA) coil block increases. This result can be explained by the fact that the steric hindrance induced by the increase of the coil block disrupts the planarity of the rod block and as a consequence hinders to a certain extent the  $\pi$ -stacking.<sup>63</sup>

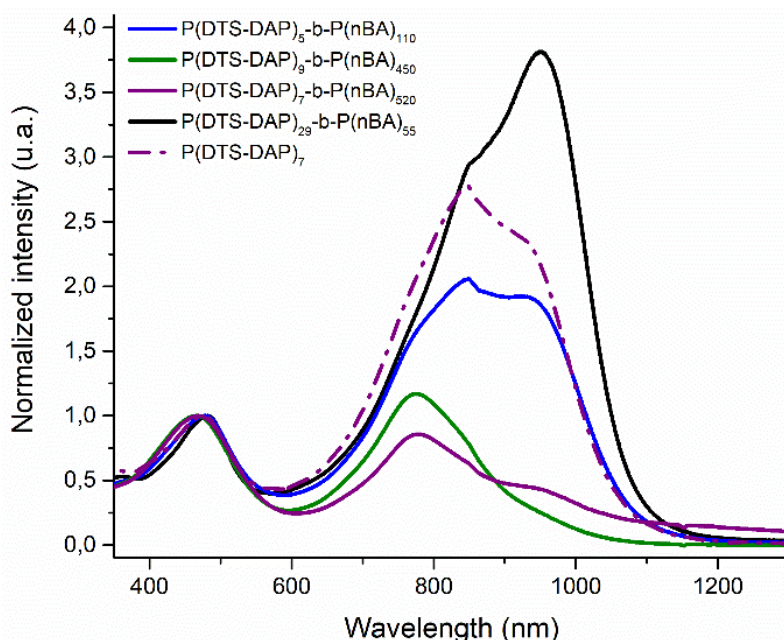


Figure 25: Visible-NIR absorption spectra of the rod-coil block copolymers in CHCl<sub>3</sub>

Molar extinction coefficients  $\epsilon$  of the rod-coil block copolymers and one rod copolymer were calculated by using Beer-Lambert's law in the concentration range from 0.009 mM to 0.05 mM. Molar extinction coefficients  $\epsilon$  of the rod copolymer P(DTS-DAP)<sub>9</sub> was calculated from the molar concentration  $C_n$  obtained from the following equation:

$$C_n = \frac{C_m}{M_0} \quad (10)$$

### Chapter 3: Rod-coil block copolymers with filmogenic properties based on low band-gap conjugated polymers

where  $C_m$  corresponds to the mass concentration and  $M_0$  to the molar mass of the DTS-DAP repetitive unit of the rod copolymer. The maxima molar extinction coefficients  $\epsilon$  are reported in Table 6.

For the determination of molar extinction coefficients of block copolymers, only the block having a Visible-NIR absorption (*i.e.* playing the role of the “chromophore”) contributes to the final absorption.<sup>64</sup> Hence,  $\epsilon$  of the rod-coil block copolymers were calculated from the molar concentration  $C_n$  obtained from the following equation:

$$C_n = \frac{C_{m P(DTS-DAP)}}{M_0} = \frac{w_{P(DTS-DAP)} \times C_{m copo}}{M_0} \quad (11)$$

where  $M_0$  corresponds to the molar mass of the DTS-DAP repetitive unit of the rod copolymers and  $C_{m P(DTS-DAP)}$  to the mass concentration of the rod copolymers calculated by multiplying the mass fraction  $w_{P(DTS-DAP)}$  (calculated from the molar fractions obtained *via*  $^1\text{H}$  NMR and reported in Table 6) by the mass concentration of the block copolymers  $C_{m copo}$ .

Superimpositions of the molar extinction coefficients  $\epsilon$  of the rod copolymer and rod-coil block copolymers are presented in Figure 26. The difference of the contributions of ICT and  $\pi$ - $\pi^*$  transition are easily observable. The highest  $\epsilon$  for the ICT band correspond to the block copolymer  $P(DTS-DAP)_5$ -*b*- $P(nBA)_{110}$  and the maxima  $\epsilon_{ICT}$  of the other block copolymers decrease when the coil block length increases. This result confirms the hypothesis formulated previously: the incorporation of coil blocks disrupts the ICT and the interchain  $\pi$ -stacking. Important effects of chromophore size and spatial confinement of chromophores on the electronic structure are observed. For the block copolymers containing longer coil chains, there may be both reduced chromophore size and three-dimensional spatial confinement as the rod chromophores are dispersed in the coil-like matrix.<sup>61</sup>

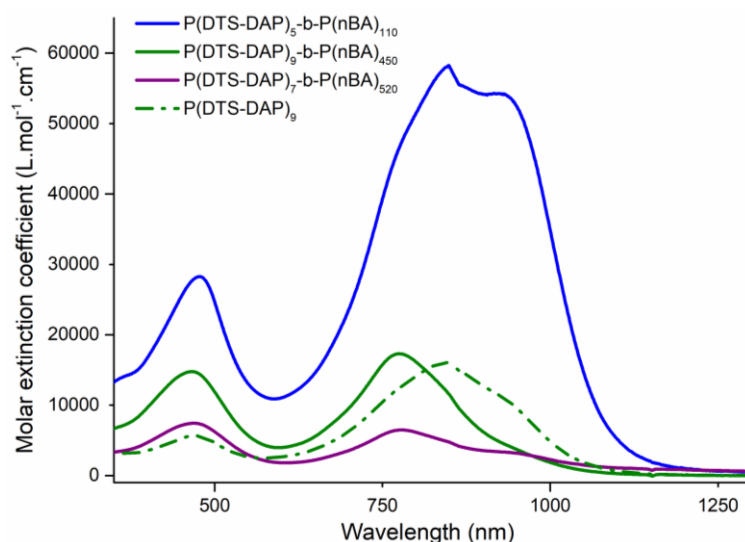


Figure 26: Superimpositions of the Visible-NIR absorption spectra of the rod copolymers and the corresponding rod-coil block copolymers in  $\text{CHCl}_3$

The maxima molar extinction coefficients  $\epsilon$  are reported in Table 6 and vary between  $0.74$  and  $2.82 \cdot 10^4 \text{ L.mol}^{-1} \cdot \text{cm}^{-1}$  for the  $\pi\text{-}\pi^*$  transition bands and between  $0.65$  and  $5.82 \cdot 10^4 \text{ L.mol}^{-1} \cdot \text{cm}^{-1}$  for the ICT bands.

Table 6: Optical characteristics of the rod copolymers and the rod-coil block copolymers

	$WP_{(DTS-DAP)}$	$\lambda_{max\ ICT}$ (nm)	$\lambda_{max\ \pi\text{-}\pi^*}$ (nm)	$\epsilon_{max\ ICT} \cdot 10^4$ ( $\text{L.mol}^{-1} \cdot \text{cm}^{-1}$ )	$\epsilon_{max\ \pi\text{-}\pi^*} \cdot 10^4$ ( $\text{L.mol}^{-1} \cdot \text{cm}^{-1}$ )
$P(DTS-DAP)_9$	1	845	471	1.60	0.56
$P(DTS-DAP)_5\text{-}b\text{-}P(nBA)_{110}$	0.26	849	478	5.82	2.82
$P(DTS-DAP)_9\text{-}b\text{-}P(nBA)_{450}$	0.13	775	466	1.73	1.47
$P(DTS-DAP)_7\text{-}b\text{-}P(nBA)_{520}$	0.09	778	469	0.65	0.74

Then, the Visible-NIR absorption spectra of the rod copolymer  $P(DTS-DAP)_5$  and the rod-coil block copolymer  $P(DTS-DAP)_7\text{-}b\text{-}P(nBA)_{520}$  were measured in thin films. The two different materials were dissolved in chlorobenzene (10 g/L) and the solutions were deposited on glass coverslips by drop-casting. The absorption spectra in solution and in film of the two materials are presented in Figure 27. Concerning the rod copolymer  $P(DTS-DAP)_5$ , the absorption spectrum in film presents a bathochromic shift of the shoulder centered at 950 nm. The intensity of the ICT band is decreased in solid state, compared to the solution spectrum. In addition, the ICT band is larger in thin film. Concerning the rod-coil block copolymer  $P(DTS-$

DAP)<sub>7</sub>-*b*-P(nBA)<sub>520</sub>, the absorption spectrum in film does not present a bathochromic shift, but the intensity of the shoulder of the  $\pi$ -stacking band centered at 950 nm is increased. However, the maxima absorption of the ICT and the  $\pi$ - $\pi^*$  transition bands, located at 775 and 470 nm, respectively, do not show intensity variation compared to the absorption spectra in solution. Hence, the contributions of ICT and  $\pi$ - $\pi^*$  transition are similar in film or in solution for the rod-coil block copolymer but not for the rod copolymer. The difference of contributions of each band and the bathochromic shift observed for the rod copolymer are explained by the redistribution of  $\pi$ -electrons in the conjugated backbone due to the close proximity to each other<sup>58</sup> and the augmentation of the planarity and the degree of crystallinity in solid state.<sup>63</sup> This specific feature is sometimes avoided by thermal annealing of the thin films<sup>59</sup> but this chromic phenomenon could also be seen as an advantage as the absorption area of the polymer is extended leading to enhanced photocurrent and photoconversion efficiency in photovoltaic devices. Besides, the  $\pi$ -stacking improves the charge carrier mobility enhancing the efficiency of organic thin film transistors.

The rod-coil block copolymer does not show an important red shift between the absorption spectra in solution and in solid state as the material presents less aggregation phenomenon due to the incorporation of the coil block. The block copolymer can be easily processed in thin films thanks to the *n*-butyl acrylate.

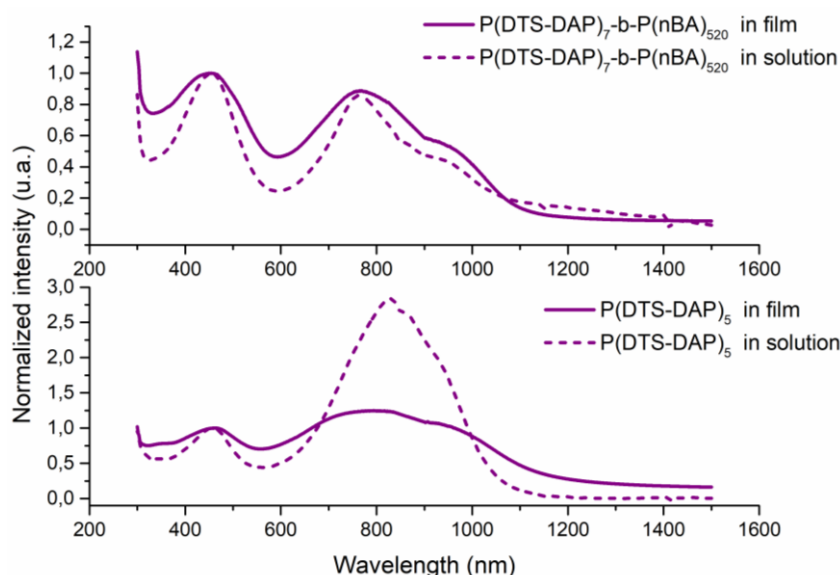


Figure 27: Visible-NIR absorption spectra of the rod-coil block copolymer P(DTS-DAP)<sub>7</sub>-*b*-P(nBA)<sub>520</sub> and the rod copolymer P(DTS-DAP)<sub>5</sub> in CHCl<sub>3</sub> solutions and in thin films



In the end, optical bandgaps were estimated from the low energy band edge in the optical spectra (Figure 24, Figure 25, Figure 27) following the equation presented in Chapter 1:

$$E_g = \frac{1240}{\lambda_{onset}} \quad (12)$$

The optical bandgaps  $E_g^{opt}$  in solution and in thin film are reported in Table 7. For the rod copolymer  $P(DTS-DAP)_5$ , the average  $E_g^{opt}$  is 1.17 eV and for the block copolymers  $P(DTS-DAP)_{7-b-P(nBA)_{520}}$ , the average  $E_g^{opt}$  is around 1.23 eV. This result is due to the higher amount of  $\pi$ -stacking in the rod polymer. In film, the optical bandgap of the rod copolymer is slightly decreased at 1.00 eV and the one of the block copolymer is 1.10 eV. Again, this difference is logically attributed to the coil block hindering the formation of  $\pi$ -stacking.

Table 7: Optical characteristics of the rod copolymers and the rod-coil block copolymers

	$\lambda_{onset} (nm)$ <i>in solution</i>	$E_g^{opt} (eV)$ <i>in solution</i>	$\lambda_{onset} (nm)$ <i>in thin film</i>	$E_g^{opt} (eV)$ <i>in thin film</i>
$P(DTS-DAP)_5$	1080	1.148	1230	1.00
$P(DTS-DAP)_9$	1045	1.186	-	-
$P(DTS-DAP)_7$	1055	1.175	-	-
$P(DTS-DAP)_5-b-P(nBA)_{110}$	1070	1.158	-	-
$P(DTS-DAP)_9-b-P(nBA)_{450}$	938	1.321	-	-
$P(DTS-DAP)_{7-b-P(nBA)_{520}}$	952	1.302	1130	1.10
$P(DTS-DAP)_{29-b-P(nBA)_{55}}$	1075	1.153	-	-

#### b. Thermal properties

The thermal stability of two rod alternating copolymers and their corresponding block copolymers was investigated by thermogravimetric analysis (TGA) at a heating rate of 10°C/min under nitrogen. The weight loss curves of the materials are presented in Figure 28. The rod copolymer present two steps of thermal degradation between 250-350°C and 400-500°C. The first degradation represents a mass loss of about 20% and corresponds to the decomposition of the alkyl side chains on the DTS unit.<sup>65,66</sup> The second process of degradation represents a mass loss of about 30% and can be attributed to the decomposition of the polymer main chain. Concerning the block copolymer, its weight loss curve displays a single step decomposition around 410°C and corresponds to a mass loss of about 95%. This single degradation step is attributed to the high mass content of  $P(nBA)$  in the block copolymers. Both rod copolymer and block copolymer have an acceptable thermal stability explained by the

presence of the aromatic ring dithieno[3,2-*b*:2',3'-*d*]silole rich in silicon in the polymer backbones.

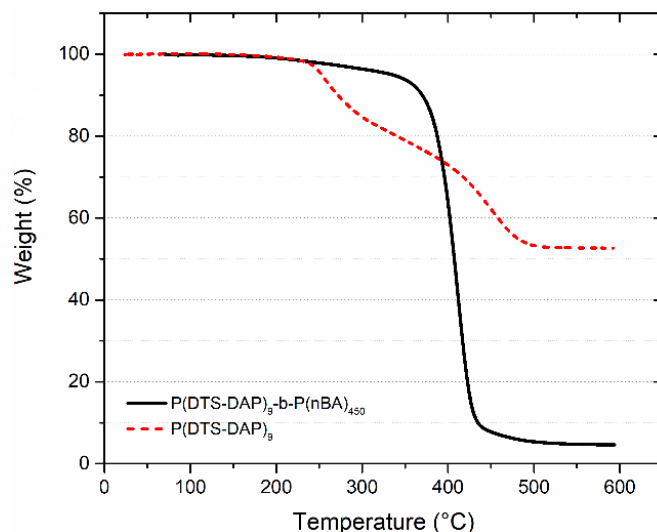


Figure 28: TGA thermograms of the rod copolymer P(DTS-DAP)<sub>9</sub> and the rod-coil block copolymer P(DTS-DAP)<sub>9</sub>-b-P(nBA)<sub>450</sub>

The transition temperatures of one neat rod alternating copolymer P(DTS-DAP)<sub>9</sub> and the four neat block copolymers P(DTS-DAP)<sub>5</sub>-b-P(nBA)<sub>110</sub>, P(DTS-DAP)<sub>9</sub>-b-P(nBA)<sub>450</sub>, P(DTS-DAP)<sub>7</sub>-b-P(nBA)<sub>520</sub>, and P(DTS-DAP)<sub>29</sub>-b-P(nBA)<sub>55</sub> were analyzed by differential scanning calorimetry (DSC).

For the rod alternating copolymer P(DTS-DAP)<sub>9</sub>, the DSC curves of the first and second heatings are given in Figure 29a and are not exactly similar. During the first heating, no glass transition (T<sub>g</sub>) can be seen while during the second heating, the T<sub>g</sub> is visible and centered at -47°C. This second-order transition is defined by IUPAC as “the process in which a polymer melt changes on cooling to a polymer glass or a polymer glass changes on heating to a polymer melt”.<sup>67,68</sup> However, this phenomenon, which is not considered as a thermodynamic transition, is still subject to ongoing scientific investigation. Regarding the rod alternating copolymer, the amorphous parts could correspond to the long alkyl chains providing better solubility and less rigidity to the polymer backbone. Hence, the glass transition observed is due to the presence of alkyl chains on both the DTS and the DAP monomers. Moreover, the first scan leads to two transitions at 56°C and 71°C with dissimilar intensities. The sharpness of the endotherm at 71°C could be the evidence of a melting peak. The second scan presents the same two transitions slightly shifted at 56°C and 68°C. The second transition centered at 68°C lost the major part of its intensity compared to the first scan. A small exothermic peak is observed at 18°C upon the

### Chapter 3: Rod-coil block copolymers with filmogenic properties based on low band-gap conjugated polymers

2<sup>nd</sup> heating scan. This feature is attributed to the cold crystallization process in which the material undergoes some crystallization while heating at temperatures slightly above the glass transition temperature due to sufficient mobility to arrange itself into ordered structure.<sup>67</sup> This phenomenon is observed if crystallization was not completed before sample vitrification, *i.e.* the crystallization does not occur during the cooling cycle as no stable nuclei was formed.<sup>69</sup> In this chapter, no characteristic peak could be observed upon cooling for the rod alternating copolymer P(DTS-DAP)<sub>9</sub> (Figure 29b) and all the other materials. The absence of crystallization peaks can also be explained by a low crystallinity due to insufficient flatness which prevents the stacking of polymer chains at long distance to form crystalline domains. Hence, the cooling processes will not be depicted for the other materials in this chapter.

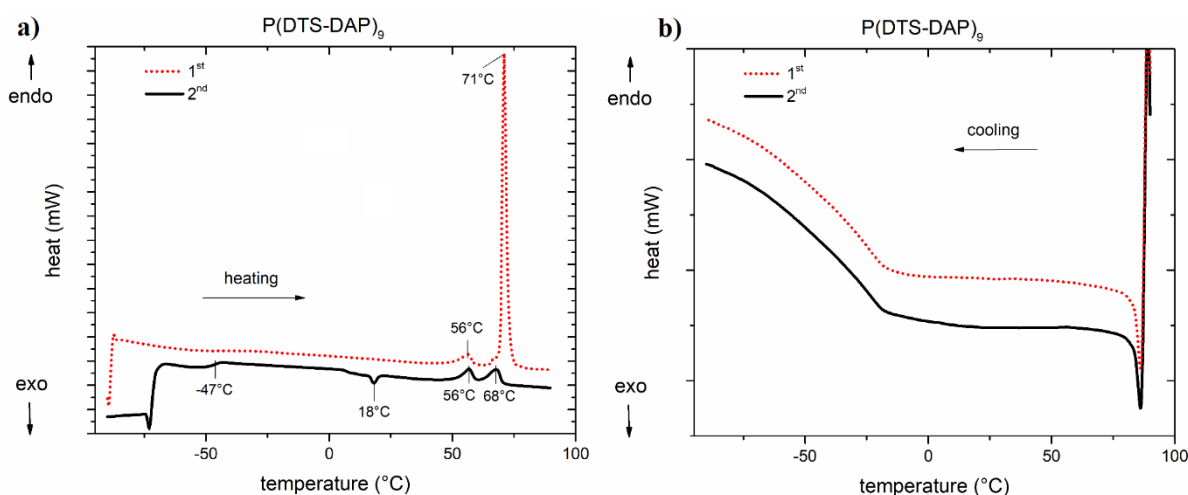


Figure 29: **a)** First and second heating and **b)** first and second cooling DSC thermograms of the rod copolymer P(DTS-DAP)<sub>9</sub> obtained with a scanning rate of 20°C.min<sup>-1</sup>

For the block copolymer P(DTS-DAP)<sub>5</sub>-*b*-P(nBA)<sub>110</sub>, four heating scans were performed and are depicted in Figure 30. The second order glass transition is visible on all the scans and is centered at -43 °C. The amorphous part of the material responsible for the glass transition corresponds to the coil block providing an important mobility to the polymer backbone. The glass transition temperature of homopolymers based on *n*-butyl acrylate is well reported in the literature and is between -45 and -55 °C.<sup>70</sup> Normally, for block copolymers, two distinct glass transitions should be observed to exhibit the immiscibility of the corresponding blocks.<sup>71</sup> Here, only one Tg is observable probably because of the high content of P(*n*BA) compared to the rod block and the similar values of their Tg. No clear endotherm or exotherm were observed suggesting the absence of crystallization phenomenon probably hindered by the length of the coil chains.

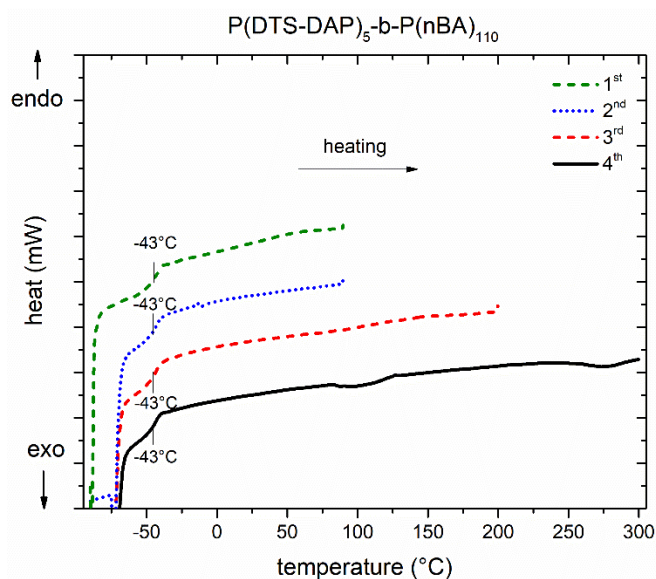


Figure 30: First, second, third, and fourth heating DSC thermograms of the block copolymer P(DTS-DAP)<sub>5</sub>-b-P(nBA)<sub>110</sub> obtained with a scanning rate of 20°C.min<sup>-1</sup>

For the block copolymer P(DTS-DAP)<sub>9</sub>-b-P(nBA)<sub>450</sub>, two heating scans were performed and are depicted in Figure 31. The glass transition is visible on all the scans and is centered at -55 °C corresponding to the glass transition temperature of the coil block. However, the transitions present endothermic peaks at the T<sub>g</sub> region revealing the enthalpy relaxation phenomenon which is the enthalpy change observed near the glass transition when a sample is heated at a rate different from that at which it was cooled down, according to IUPAC.<sup>67</sup> The enthalpy relaxation phenomenon can also be observed after aging the sample in the glassy state below the glass transition temperature. This excess of enthalpy exposes that polymer glasses are in a non-equilibrium thermodynamic state and the position and magnitude of this endothermic peak depends upon the thermal history and the structural characteristic of the polymer glasses.<sup>72</sup> These observations on the DSC thermograms are in accordance with the DSC program employed to analyze the block copolymer P(DTS-DAP)<sub>9</sub>-b-P(nBA)<sub>450</sub> as the sample was aged for 30 min at -90°C prior to heating it.

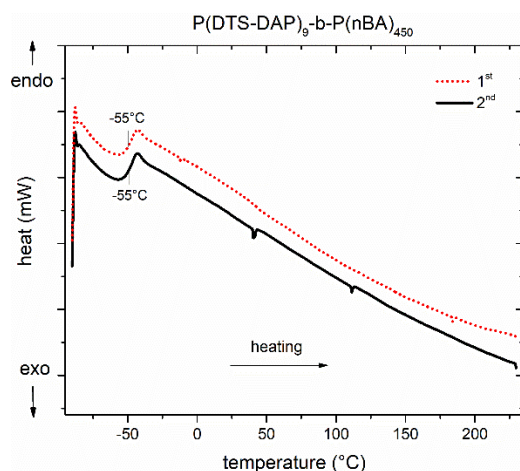


Figure 31: First and second heating DSC thermograms of the block copolymer P(DTS-DAP)<sub>9</sub>-b-P(nBA)<sub>450</sub> obtained with a scanning rate of 20°C.min<sup>-1</sup>

For the block copolymer P(DTS-DAP)<sub>7</sub>-b-P(nBA)<sub>520</sub>, four heating scans were performed and are depicted in Figure 32. The glass transition is visible on all the scans and is located between -50 and -52°C. Same observations were made as for the block copolymer P(DTS-DAP)<sub>9</sub>-b-P(nBA)<sub>450</sub>: enthalpy relaxation phenomena are visible on all the heating scans. These results are consistent with the DSC program employed to analyze the block copolymer as the sample was aged 30 min at -90°C and the heating and cooling scans were not performed at the same rate (20°C.min<sup>-1</sup> and 1°C.min<sup>-1</sup>, respectively).

For both block copolymers P(DTS-DAP)<sub>9</sub>-b-P(nBA)<sub>450</sub> and P(DTS-DAP)<sub>7</sub>-b-P(nBA)<sub>520</sub>, no crystallization phenomenon was observed suggesting that the length of the coil chains hinders it, which is in accordance with the absorbance spectra of these materials.

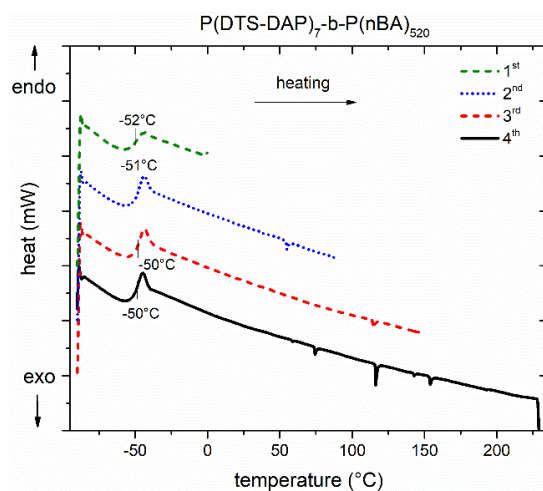


Figure 32: First, second, third, and fourth heating DSC thermograms of the block copolymer P(DTS-DAP)<sub>7</sub>-b-P(nBA)<sub>520</sub> obtained with a scanning rate of 20°C.min<sup>-1</sup>

For the block copolymer  $P(\text{DTS-DAP})_{29}\text{-}b\text{-}P(\text{nBA})_{55}$ , two heating/cooling scans were performed and showed two endothermic peaks around  $-27$  and  $70^\circ\text{C}$ . The sharpness of the second peak at  $70^\circ\text{C}$  indicates the possibility of a melting peak.

In order to determine if the melting temperatures correspond to the ones of the rod alternating copolymer  $P(\text{DTS-DAP})$  and the block copolymer or if they are related to liquid crystalline phase transitions, four heating scans were performed at different heating rates like in the work of Abdelsamie *et al.*<sup>73</sup> In their study, decreasing the rate led to notable decreases in the observable endothermic transition which indicates a phase transition with a small activation barrier. This type of transition is characteristic of liquid crystalline phase transition with the evolution from a more ordered to a less ordered state. The four heating scans performed on the block copolymer are depicted in Figure 33. No glass transition is observed on all the scans, but two transitions with dissimilar intensities and shapes are visible upon heating at different scans. The first scan displays two endotherms: one large centered at  $-27^\circ\text{C}$  and the other sharp at  $70^\circ\text{C}$ . By decreasing the heating rate from  $20^\circ\text{C}\cdot\text{min}^{-1}$  to  $1^\circ\text{C}\cdot\text{min}^{-1}$ , the two endothermic peaks decreased notably from  $-27^\circ\text{C}$  to  $-38^\circ\text{C}$  for the first one, and from  $70^\circ\text{C}$  to  $51.5^\circ\text{C}$  for the second one. Hence, the two endotherms do not correspond to melting temperatures but are related to liquid crystalline phase transitions.

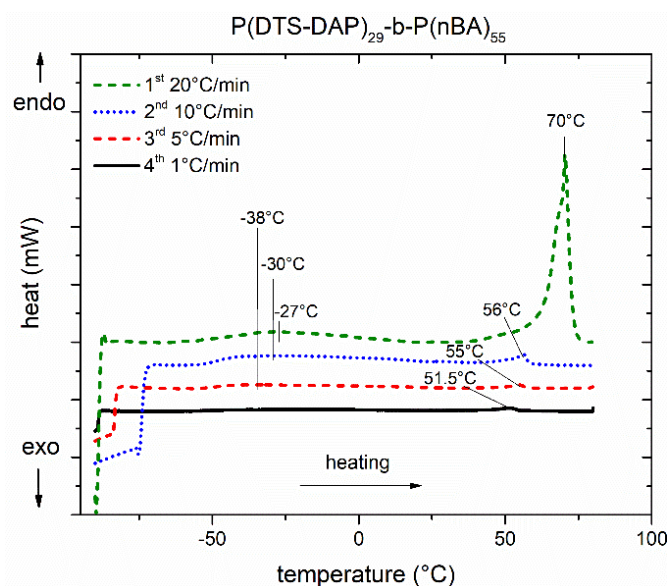


Figure 33: First, second, third, and fourth heating DSC thermograms of the block copolymer  $P(\text{DTS-DAP})_{29}\text{-}b\text{-}P(\text{nBA})_{55}$  obtained with different scanning rates

It is worth reminding that a liquid crystal is a substance that is able to flow like liquids and displays special symmetry properties inherited from crystalline solids.<sup>74</sup> Between three-

### Chapter 3: Rod-coil block copolymers with filmogenic properties based on low band-gap conjugated polymers

dimensionally ordered crystals and disordered fluids<sup>75</sup>, polymer with liquid-crystalline structures can be characterized by different mesophases such as the nematic phase and the smectic phases A and C.<sup>76</sup> Upon heating, various transitions are observed from the crystalline phase to isotropic liquid as depicted in Figure 34. In the smectic phase, the molecules are ordered along one direction in well-defined layers oriented specifically. In the nematic phase, the rod-shaped molecules self-align to have long-range directional order. Finally, all order is lost forming an isotropic liquid.

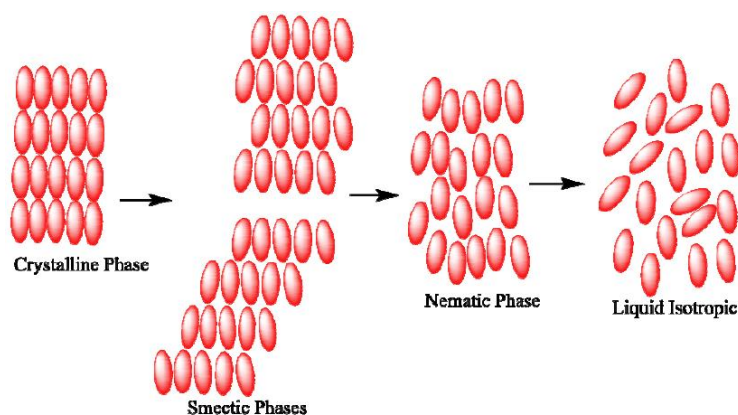


Figure 34: Phase transition between crystals, smectic, nematic, and isotropic liquid phases as function of temperature.

Hence, the endotherms around  $-27$  and  $70^{\circ}\text{C}$  observed on the DSC thermograms of the block copolymer  $\text{P}(\text{DTS-DAP})_{29}\text{-}b\text{-P}(\text{nBA})_{55}$  could be attributed to the smectic phase and the isotropic phase transitions, respectively.

As previously shown in Figure 29, the DSC thermograms of the rod alternating copolymer  $\text{P}(\text{DTS-DAP})_9$  exhibited two endothermic peaks. We hypothesized that the rod alternating copolymer presents liquid crystalline transitions as well. In the literature, it is reported that long side chains can induce liquid crystallinity in rod polymers as they have their own crystallization and melt behavior.<sup>5</sup> The two endotherms around  $56$  and  $71^{\circ}\text{C}$  could correspond to the nematic phase and the isotropic phase transitions, respectively.

Since  $\text{P}(\text{DTS-DAP})_{29}\text{-}b\text{-P}(\text{nBA})_{55}$  is a mixture of block copolymer and alternating copolymer, the liquid crystalline phases could be observable due to the presence of the rod alternating copolymer, the molecular group responsible for the liquid crystalline behavior also called the mesogenic group. For the other block copolymers, they have long coil blocks that could hinder the liquid crystalline features: no endothermic peak is observed on their DSC thermograms.

However, liquid crystalline behavior could be more evidenced by using polarized optical microscopy (POM) as they exhibit a unique texture under microscopy.<sup>77</sup> Such images present contrasting areas corresponding to domains where liquid crystals are oriented toward different directions. Unfortunately, due to lack of time, no POM could have been performed to confirm the presence of liquid crystalline polymers.

c. Structural properties

Since the several DSC experiments were not sufficient to determine the liquid crystallinity of the materials, a detailed structural analysis of the rod alternating copolymers P(DTS-DAP)<sub>9</sub> and two block copolymers (P(DTS-DAP)<sub>29</sub>-*b*-P(nBA)<sub>55</sub> and P(DTS-DAP)<sub>9</sub>-*b*-P(nBA)<sub>520</sub>) was performed by means of grazing incidence wide-angle X-ray scattering (GIWAXS) in order to gain structural information of the different phases like in the work of Peng *et al.*<sup>78</sup> and Li *et al.*<sup>79</sup> The materials of interest were deposited as thin films by wire-bar coating onto preheated silicon substrates at different temperatures: room temperature, 35°C, 60°C, and 85°C. These specific temperatures were chosen according to the DSC thermograms displaying thermal transitions around -30°C, 55°C, and 70°C. The wire-bare coating is a simple deposition method where the thickness is controlled by the diameter of the wire and this technique displays several advantages such as excellent control of solidification rate and control of deposition temperature and speed.<sup>80</sup> However, the final thin films, presented in Figure 35, did not present homogeneous depositions. In order to have an ideal total scattering intensity for GIWAXS measurement, the thin films must present a thickness of at least 100 nm. Hence, the film thicknesses were measured on different areas with a profilometer to verify this requirement. All the thin films presented a thickness of at least 100 nm at the side and center areas of the samples. However, the thicknesses were not homogeneous. By a simple comparison of the color and aspect of the thin films, we can observe that thin films from the rod alternating copolymer P(DTS-DAP)<sub>9</sub> and from the rod-coil block copolymer P(DTS-DAP)<sub>29</sub>-*b*-P(nBA)<sub>55</sub> with a moderate coil length look similar. Regarding the thin film from P(DTS-DAP)<sub>9</sub>-*b*-P(nBA)<sub>520</sub>, the color and aspect are very different. This can be due to the high coil content that is an advantage to process thin films.



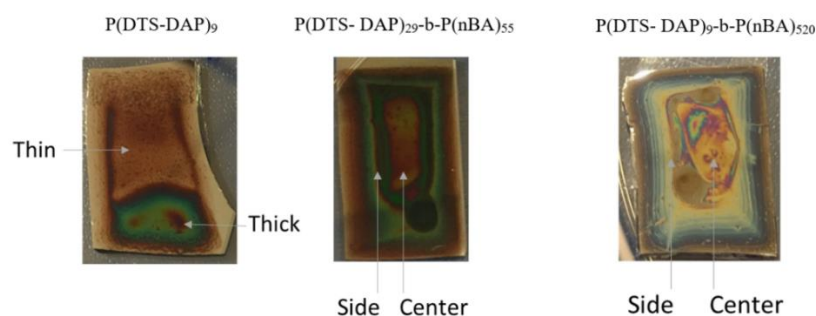


Figure 35: Pictures of thin films of the rod copolymer  $P(\text{DTS-DAP})_9$  and the rod-coil block copolymers  $P(\text{DTS- DAP})_{29-b}\text{-P}(\text{nBA})_{55}$  and  $P(\text{DTS- DAP})_9\text{-}b\text{-P}(\text{nBA})_{520}$

The geometry of a GIWAXS experiment is presented in Figure 36a in which an incident X-ray beam grazes the sample under a very small angle. On the GIWAXS patterns and corresponding 2D profiles, peaks and reflections can be observed indicating periodicities in the film microstructure which may arise from crystallinity or self-assembly processes.<sup>81</sup> The GIWAXS measurements provide information on both in-plane ( $q_{xy}$ , direction parallel to substrate) and out-of-plane ( $q_z$ , direction perpendicular to the substrate) structures of the thin films (Figure 36b). Indeed, high intensity of lamellar peaks in the out-of-plane orientation indicates an edge-on orientation wherein the side-chains interact with substrate interface and the  $\pi$ -stacking direction parallel to the substrate (Figure 36c). On the contrary, high intensity of lamellar peaks in the in-plane orientation indicates a face-on orientation wherein the aromatic rings stacked along the film with  $\pi$ -stacking direction perpendicular to the substrate (Figure 36d).<sup>82</sup> Hence, GIWAXS enables probing of the molecular-scale packing of the components and the intensity along scattering rings can be used to quantify the orientation distribution of the material.<sup>83,84</sup>

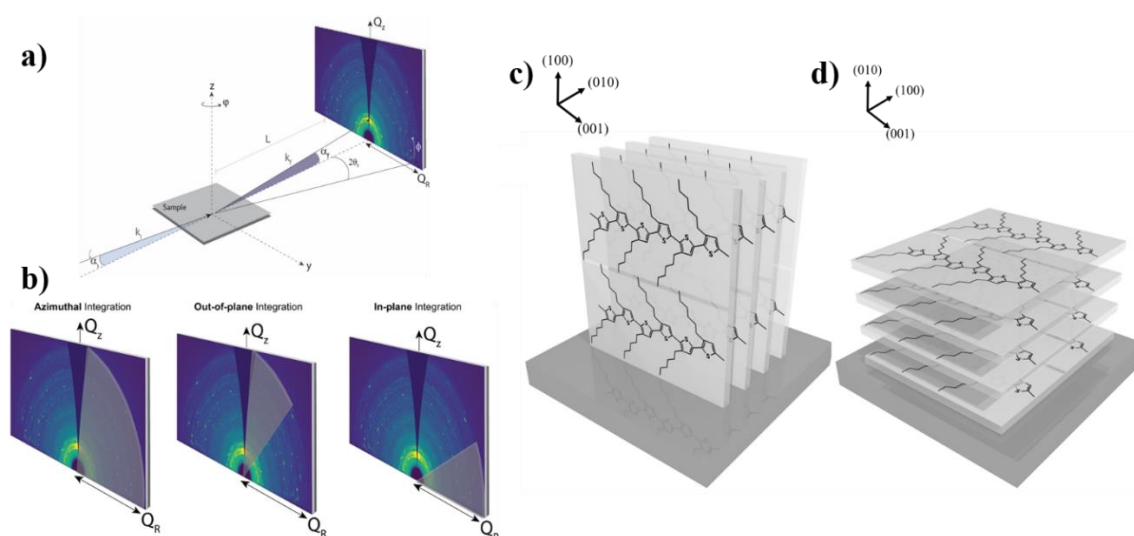


Figure 36: **a)** GIWAXS geometry; **b)** Integration planes; Schematic **c)** edge-on and **d)** face-on P3HT orientations. Adapted from Johnston *et al.*<sup>83</sup>

### Chapter 3: Rod-coil block copolymers with filmogenic properties based on low band-gap conjugated polymers

In Figure 37, the GIWAXS 2D profiles of the rod alternating copolymer P(DTS-DAP)<sub>9</sub> films exhibited a (100) peak on both in-plane and out-of plane directions at  $q_0 = 3.8 \text{ nm}^{-1}$ . However, the out-of-plane profiles presented four other peaks. The (200) and (300) peaks were observed at  $q$ -values of  $2q_0 = 7.6 \text{ nm}^{-1}$  and  $3q_0 = 11.3 \text{ nm}^{-1}$ , respectively. These peaks are the result of lamellar stacking and a characteristic distance  $d$  can be calculated from the following Bragg's law:

$$d = \frac{2\pi}{q} \quad (13)$$

In the rod alternating copolymer P(DTS-DAP)<sub>9</sub> films, the characteristic distance  $d$  is 1.65 nm and correspond to the distance between two chains. Both in-plane and out-of-plane profiles also presented a peak at  $q = 17.3 \text{ nm}^{-1}$  which was attributed to the  $\pi$ -stacking of the aromatic rings and corresponds to a characteristic distance  $d$  of 3.63 Å. Other peaks were visible in the out-of-plane at  $q = 14 \text{ nm}^{-1}$ , which corresponds to a characteristic distance  $d$  equal to 4.48 Å, and in the in-plane at  $q = 12.6 \text{ nm}^{-1}$  corresponding to a characteristic distance  $d$  of 4.98 Å. By comparing the intensities of the peaks on the 2D profiles, the results at room temperature, 35°C, 60°C, and 85°C were very similar. However, the peaks were more intense in the out-of-plane direction which may indicate an edge-on orientation.

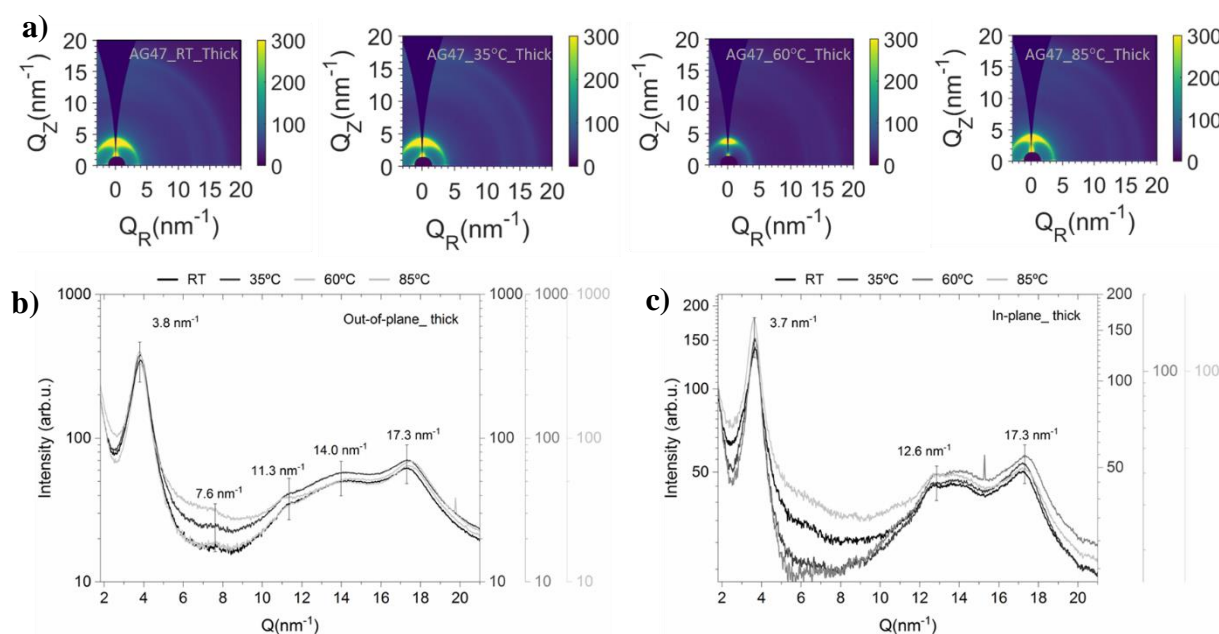


Figure 37: **a)** GIWAXS patterns of the rod copolymer P(DTS-DAP)<sub>9</sub> thin films coated from chlorobenzene solution at different temperatures and their corresponding 2D GIWAXS profiles reduced from the **b)** out-of-plane and **c)** in-plane directions

Regarding the overall results, the rod copolymer is semi-crystalline, which is consistent with Visible-NIR spectrophotometry and DSC measurements. However, the thin films coated at 85°C should not display all the peaks contrary to the results obtained at room temperature as the melting point of the material is presumably around 70°C. It is possible that the coating process at 85°C is not high enough to hinder the crystallization of the material. Rather a thermal annealing should be performed during GIWAXS experiments.

In Figure 38, the GIWAXS 2D profiles of P(DTS-DAP)<sub>29</sub>-*b*-P(nBA)<sub>55</sub> films exhibited the same features as the rod copolymer P(DTS-DAP)<sub>9</sub> films. A sharp (100) peak on both in-plane and out-of-plane directions was visible at  $q_0 = 3.8 \text{ nm}^{-1}$ . Four other peaks were observed on the out-of-plane directions. The (200) and (300) peaks were spotted at  $q$ -values of  $2q_0 = 7.6 \text{ nm}^{-1}$  and  $3q_0 = 11.3 \text{ nm}^{-1}$ , respectively. These peaks are due to lamellar stacking with a characteristic distance  $d$  of 1.65 nm. The same well-defined peak at  $q \sim 17.3 \text{ nm}^{-1}$  was observed on both in-plane and out-of-plane directions and was attributed to the  $\pi$ -stacking with a distance of 3.63 Å. Like with the rod copolymer, peaks were visible in the out-of-plane at  $q = 14 \text{ nm}^{-1}$ , which corresponds to a characteristic distance  $d$  equal to 4.48 Å, and in the in-plane at  $q = 12.5 \text{ nm}^{-1}$  corresponding to a characteristic distance  $d$  of 5.02 Å. The intensities of the peaks on the 2D profiles were different depending on the casting temperature: the crystallinity seems to be higher at moderate temperatures (room temperature and 35°C) than at higher temperatures (60°C and 85°C). However, the peaks were more intense in the out-of-plane direction which may indicate an edge-on orientation.

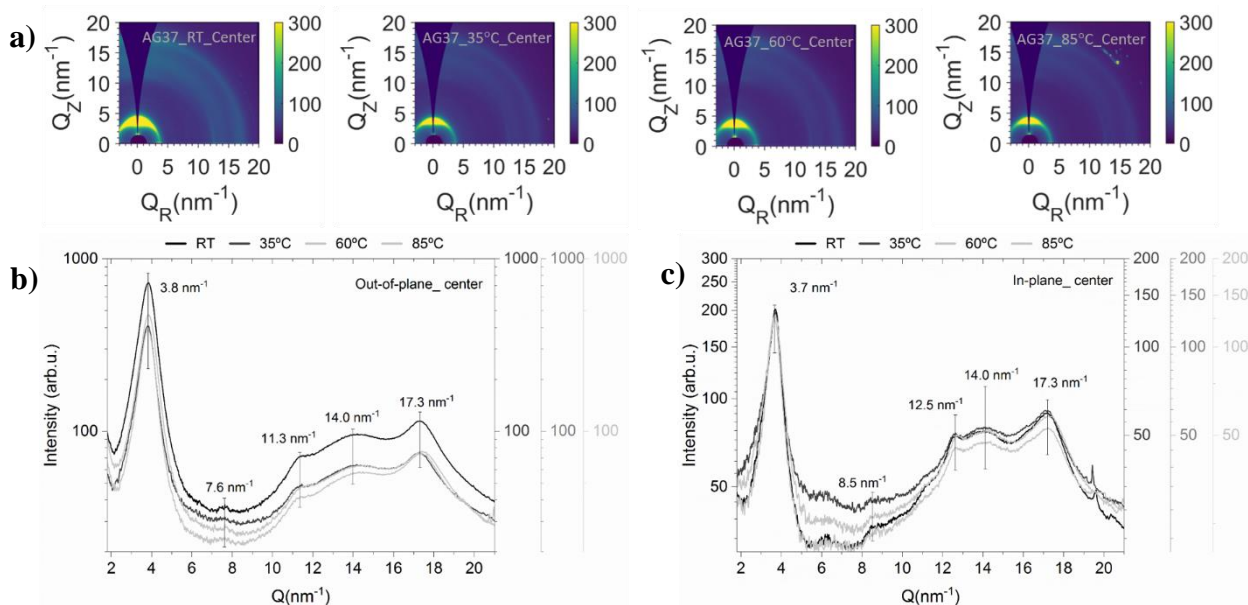


Figure 38: **a)** GIWAXS patterns of the rod-coil block copolymer P(DTS-DAP)<sub>29</sub>-*b*-P(nBA)<sub>55</sub> thin films coated from chlorobenzene solution at different temperatures and their corresponding 2D GIWAXS profiles reduced from the **b)** out-of-plane and **c)** in-plane directions

The crystallinity of the block copolymer is in accordance with the observation made with Visible-NIR spectrophotometry and DSC measurements. Yet, like the rod copolymer, the thin films of block copolymer coated at 85°C should not display all the peaks contrary to the results obtained at room temperature as the melting point of the material is presumably around 70°C.

Temperature-dependent GIWAXS measurements could be performed to improve the GIWAXS patterns and to enhance the difference between the different casting temperatures. Unfortunately, due to lack of time, such experiments could have not been performed.

In Figure 39, GIWAXS patterns of the block copolymer P(DTS-DAP)<sub>9</sub>-*b*-P(nBA)<sub>520</sub> films did not exhibit a (100) peak but displayed two weak and diffuse in-plane and out-of-plane reflections at  $q \sim 5 \text{ nm}^{-1}$  and  $q \sim 14 \text{ nm}^{-1}$ . The peaks displayed the same intensities regardless of orientation. The four orders previously observed for the other block copolymer were not detected for this sample and no specific orientation was observed. No  $\pi$ -stacking peak was observed at  $q = 17.3 \text{ nm}^{-1}$ . These results confirm the amorphous nature of the P(DTS-DAP)<sub>9</sub>-*b*-P(nBA)<sub>520</sub>, observed by DSC experiments and Visible-NIR spectrophotometry, which could be due to the presence of long coil block chains.

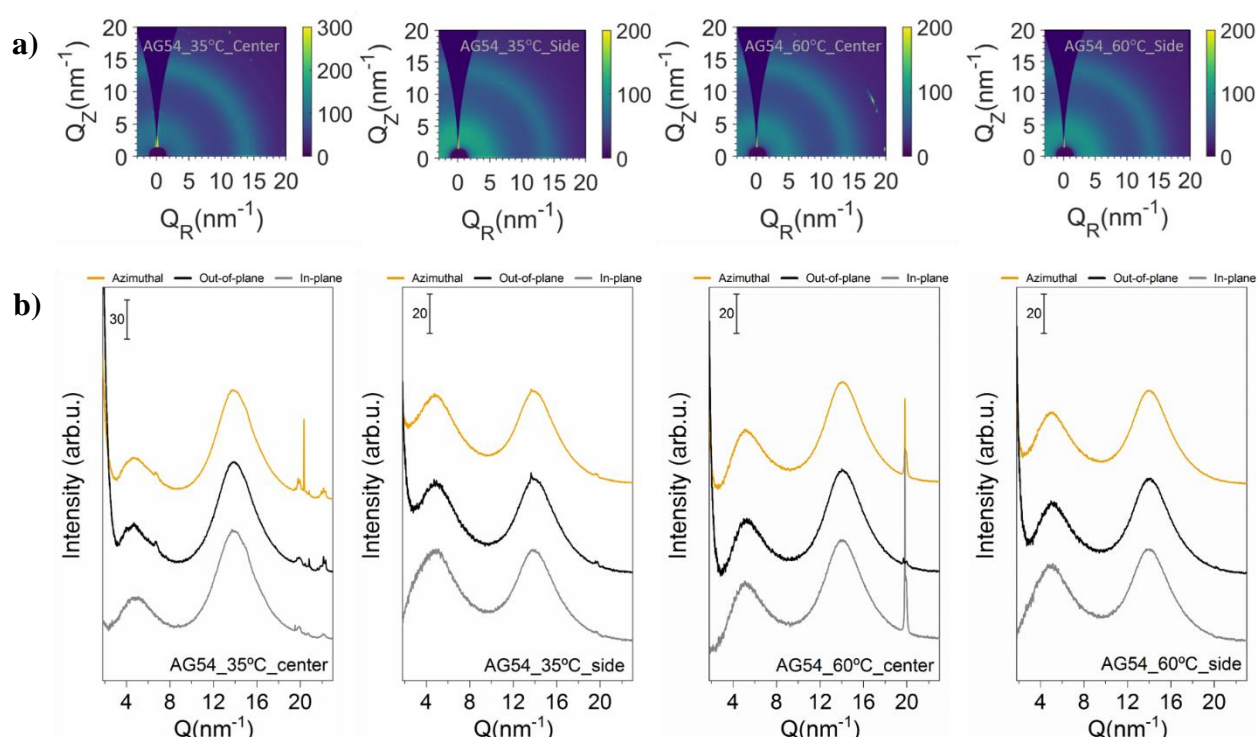


Figure 39: **a)** GIWAXS patterns of the rod-coil block copolymer P(DTS-DAP)<sub>9</sub>-*b*-P(nBA)<sub>520</sub> thin films coated from chlorobenzene solution at different temperatures and **b)** their corresponding 2D GIWAXS profiles reduced from the out-of-plane, the in-plane, and the azimuthal directions

### III. Conclusion

In this chapter, we employed two synthetic methods to yield rod-coil block copolymers based on an IR-absorbing rod block and a filmogenic coil block to improve the overall solubility of the material. Such macromolecules were obtained *via* the macroinitiator method and the macro end-capper copolymerization method. However, one synthetic strategy is more efficient than the other: the macroinitiator technique. Indeed, this technique presents the main advantage to access the synthesis and the characterization of a well-defined end-functionalized low band-gap polymer prior to produce block copolymer. Moreover, the polymerization of the coil block was controlled thanks to the use of a nitroxide macroinitiator *via* NMP. Yet, this method shows a drawback: the impossibility to reach short coil blocks due to the large excess of monomers introduced in the mixture. Therefore, another synthetic strategy was employed, the macro end-capper copolymerization method, to produce smaller coil block in block copolymers. This technique led to more homogeneous size of the rod and the coil blocks but a residual rod copolymer is observed as a secondary product that could not be removed from the block copolymer. Moreover, this synthetic pathway is less efficient than the macroinitiator method as it contains more synthesis steps. Besides, the bromination step did not lead to satisfactory yields.

Visible-NIR spectrophotometry was employed to study the optical properties of the materials obtained in this chapter. It was found that the introduction of a coil block with filmogenic properties enhanced the solubility of the block copolymers by reducing the formation of aggregates and decreasing the  $\pi$ -stacking. Molar extinction coefficients of the rod-coil block copolymers and their corresponding rod copolymers were calculated. The highest molar extinction coefficient for the intramolecular charge transfer band correspond to the block copolymer with the shortest coil block P(DTS-DAP)<sub>5</sub>-*b*-P(nBA)<sub>110</sub>. For the other block copolymers, it was found that the molar extinction coefficients of the ICT band decreased when the coil block length increased. Solid-state properties of one block copolymer and one rod copolymer films were studied as well. The rod-coil block copolymer presented less aggregation phenomenon due to the incorporation of a filmogenic coil block. The thermal stability of some materials was assessed by thermogravimetric analysis and their thermal transitions were studied by differential scanning calorimetry. It appeared that the block copolymer P(DTS-DAP)<sub>29</sub>-*b*-P(nBA)<sub>55</sub> and the rod copolymer P(DTS-DAP)<sub>9</sub> presented liquid crystalline transitions possibly due to the presence of long side chains on the rod block having their own crystallization and

### Chapter 3: Rod-coil block copolymers with filmogenic properties based on low band-gap conjugated polymers

melt behavior. However, this hypothesis must be confirmed by the observation of the thin films on a polarized optical microscope. In addition, a detailed structural analysis was performed on the two materials by means of GIWAXS experiments. The block copolymer and the rod copolymer presented a periodicity more pronounced in the out-of-plane direction. This result suggests that the materials adopt a lamellar structure with an edge-on orientation: the  $\pi$ -stacking direction is parallel to the substrate.

## IV. References

- (1) Gebeyehu, D.; Brabec, C. J.; Padinger, F.; Fromherz, T.; Hummelen, J. C.; Badt, D.; Schindler, H.; Sariciftci, N. S. The Interplay of Efficiency and Morphology in Photovoltaic Devices Based on Interpenetrating Networks of Conjugated Polymers with Fullerenes. *Synthetic Metals* **2001**, *9*.
- (2) Beek, W. J. E.; Slooff, L. H.; Wienk, M. M.; Kroon, J. M.; Janssen, R. A. J. Hybrid Solar Cells Using a Zinc Oxide Precursor and a Conjugated Polymer. *Adv. Funct. Mater.* **2005**, *15* (10), 1703–1707. <https://doi.org/10.1002/adfm.200500201>.
- (3) Brochon, C.; Mognier, S.-J.; Cloutet, E.; Hadziioannou, G. Design of  $\Pi$ -Conjugated Graft and Block Copolymers: A Tool Box for Nanostructured Materials in Optoelectronic Devices. *MRS Proceedings* **2012**, *1448*. <https://doi.org/10.1557/opl.2012.1442>.
- (4) Brochon, C.; Hadziioannou, G. Controlled Radical Polymerizations as Versatile Synthetic Routes for Conjugated Rod-Coil Block Copolymers and Their Use as Active Polymer Semiconducting Materials in Flexible Organic Electronic Devices and Systems. In *Controlled/Living Radical Polymerization: Progress in ATRP*; Matyjaszewski, K., Ed.; ACS Symposium Series; American Chemical Society: Washington DC, 2009; Vol. 1023, pp 243–256. <https://doi.org/10.1021/bk-2009-1023.ch017>.
- (5) van der Veen, M. H.; de Boer, B.; Stalmach, U.; van de Wetering, K. I.; Hadziioannou, G. Donor–Acceptor Diblock Copolymers Based on PPV and C<sub>60</sub>: Synthesis, Thermal Properties, and Morphology. *Macromolecules* **2004**, *37* (10), 3673–3684. <https://doi.org/10.1021/ma035643o>.
- (6) Welterlich, I.; Tieke, B. Dithioketopyrrolopyrrole (DTPP)-Based Conjugated Polymers Prepared upon Thionation with Lawesson’s Reagent. *Polym. Chem.* **2013**, *4* (13), 3755. <https://doi.org/10.1039/c3py00396e>.
- (7) Khelifi, W.; Awada, H.; Brymora, K.; Blanc, S.; Hirsch, L.; Castet, F.; Bousquet, A.; Lartigau-Dagron, C. Halochromic Switch from the 1st to 2nd Near-Infrared Window of Diazapentalene–Dithienosilole Copolymers. *Macromolecules* **2019**. <https://doi.org/10.1021/acs.macromol.9b00675>.
- (8) Iqbal, A.; Jost, M.; Kirchmayr, R.; Pfenninger, J.; Rochat, A.; Wallquist, O. The Synthesis and Properties of 1,4-Diketo-Pyrrolo[3,4-C]Pyrroles. *Bull. Soc. Chim. Belges* **2010**, *97* (8–9), 615–644. <https://doi.org/10.1002/bscb.19880970804>.
- (9) Rochat, A. C.; Cassar, L.; Iqbal, A. Preparation of Pyrrolo[3,4-c]Pyrroles. 4,579,949, May 11, 1983.
- (10) Chandran, D.; Lee, K.-S. Diketopyrrolopyrrole: A Versatile Building Block for Organic Photovoltaic Materials. *Macromol. Res.* **2013**, *21* (3), 272–283. <https://doi.org/10.1007/s13233-013-1141-3>.
- (11) Qian, G.; Qi, J.; Davey, J. A.; Wright, J. S.; Wang, Z. Y. Family of Diazapentalene Chromophores and Narrow-Band-Gap Polymers: Synthesis, Halochromism, Halofluorism, and Visible–Near Infrared Photodetectivity. *Chem. Mater.* **2012**, *24* (12), 2364–2372. <https://doi.org/10.1021/cm300938s>.
- (12) Stas, S.; Sergeev, S.; Geerts, Y. Synthesis of Diketopyrrolopyrrole (DPP) Derivatives Comprising Bithiophene Moieties. *Tetrahedron* **2010**, *66* (10), 1837–1845. <https://doi.org/10.1016/j.tet.2010.01.027>.
- (13) Jesberger, M.; Davis, T. P.; Barner, L. Applications of Lawesson’s Reagent in Organic and Organometallic Syntheses. *Synthesis* **2003**, *13*, 1929–1958. <https://doi.org/10.1055/s-2003-41447>.
- (14) Kim, J. S.; Fei, Z.; James, D. T.; Heeney, M.; Kim, J.-S. A Comparison between Dithienosilole and Dithienogermole Donor–Acceptor Type Co-Polymers for Organic

- Bulk Heterojunction Photovoltaic Devices. *J. Mater. Chem.* **2012**, *22* (19), 9975. <https://doi.org/10.1039/c2jm30256j>.
- (15) Kularatne, R. S.; Magurudeniya, H. D.; Sista, P.; Biewer, M. C.; Stefan, M. C. Donor–Acceptor Semiconducting Polymers for Organic Solar Cells. *J. Polym. Sci. A Polym. Chem.* **2013**, *51* (4), 743–768. <https://doi.org/10.1002/pola.26425>.
- (16) Huang, J.-H.; Teng, C.-M.; Hsiao, Y.-S.; Yen, F.-W.; Chen, P.; Chang, F.-C.; Chu, C.-W. Nanoscale Correlation between Exciton Dissociation and Carrier Transport in Silole-Containing Cyclopentadithiophene-Based Bulk Heterojunction Films. *J. Phys. Chem. C* **2011**, *115* (5), 2398–2405. <https://doi.org/10.1021/jp1090894>.
- (17) Braunecker, W. A.; Matyjaszewski, K. Controlled/Living Radical Polymerization: Features, Developments, and Perspectives. *Prog. Polym. Sci.* **2007**, *54*.
- (18) Ravve, A. *Principles of Polymer Chemistry*; Springer New York: New York, NY, 2012. <https://doi.org/10.1007/978-1-4614-2212-9>.
- (19) Blas, H. Polymérisation radicalaire contrôlée par le nitroxyde SG1 à la surface de particules de silice mésoporeuse, UPMC - Université Pierre et Marie Curie, Paris 6, 2009.
- (20) Braun, D.; Cherdron, H.; Rehahn, M.; Ritter, H.; Voit, B. *Polymer Synthesis: Theory and Practice*; Springer Berlin Heidelberg: Berlin, Heidelberg, 2013. <https://doi.org/10.1007/978-3-642-28980-4>.
- (21) Gigmès, D.; Moad, G.; Bagryanskaya, E.; Blinco, J.; Marić, M.; Delaittre, G.; Junkers, T.; Guillaneuf, Y.; Harth, E.; Rizzardo, E.; Marque, S. R. A.; Bottle, S.; Fairfull-Smith, K.; Simpson, E.; Komba, T.; Lalevéé, J.; Barner-Kowollik, C.; Nicolas, J.; Guégain, E.; Rayeroux, D.; Bonzi, G.; Maria, S.; Billon, L.; Save, M.; Cunningham, M. F.; Lessard, B.; Lessard, B. *Nitroxide Mediated Polymerization: From Fundamentals to Applications in Materials Science*; Royal Society of Chemistry: Cambridge, 2015. <https://doi.org/10.1039/9781782622635-FP001>.
- (22) Grimaldi, S.; Lemoigne, F.; Finet, J.-P.; Tordo, P.; Nicol, P.; Plechot, M. Polymerization in the Presence of a Beta-Substituted Nitroxide Radical. WO 1996024620A1, August 15, 1996.
- (23) Grimaldi, S.; Finet, J.-P.; Le Moigne, F.; Zeghdaoui, A.; Tordo, P.; Benoit, D.; Fontanille, M.; Gnanou, Y. Acyclic  $\beta$ -Phosphonylated Nitroxides: A New Series of Counter-Radicals for “Living”/Controlled Free Radical Polymerization. *Macromolecules* **2000**, *33* (4), 1141–1147. <https://doi.org/10.1021/ma9913414>.
- (24) Guerret, O.; Bertin, D.; Gigmès, D.; Marque, S.; Tordo, P.; Chauvin, F.; Dufils, P.-E.; Couturier, J.-L. Alkoxyamines Originating from Beta-Phosphorated Nitroxides and Use Thereof in Radical Polymerization, August 10, 2010.
- (25) Zhang, Y.; Chung, I. S.; Huang, J.; Matyjaszewski, K.; Pakula, T. Structure and Properties of Poly(Butyl Acrylate-Block-Sulfone-Block-Butyl Acrylate) Triblock Copolymers Prepared by ATRP. *Macromol. Chem. Phys.* **2005**, *206* (1), 33–42. <https://doi.org/10.1002/macp.200400199>.
- (26) Gaynor, S. G.; Matyjaszewski, K. Step-Growth Polymers as Macroinitiators for “Living” Radical Polymerization: Synthesis of ABA Block Copolymers. *Macromolecules* **1997**, *30* (14), 4241–4243. <https://doi.org/10.1021/ma970358o>.
- (27) Mennicken, M.; Nagelsdiek, R.; Keul, H.; Höcker, H. A Novel Macroinitiator for the Synthesis of Triblock Copolymers via Atom Transfer Radical Polymerization: Polystyrene-Block-Poly(Bisphenol A Carbonate)-Block-Polystyrene and Poly(Methyl Methacrylate)-Block-Poly(Bisphenol A Carbonate)-Block-Poly(Methyl Methacrylate). *Macromol. Chem. Phys.* **2004**, *205* (2), 143–153. <https://doi.org/10.1002/macp.200300059>.
- (28) Van De Wetering, K.; Brochon, C.; Ngov, C.; Hadziioannou, G. Design and Synthesis of a Low Band Gap Conjugated Macroinitiator: Toward Rod–Coil Donor–Acceptor Block



- Copolymers. *Macromolecules* **2006**, *39* (13), 4289–4297. <https://doi.org/10.1021/ma060497i>.
- (29) Gignes, D.; Dufils, P.-E.; Glé, D.; Bertin, D.; Lefay, C.; Guillaneuf, Y. Intermolecular Radical 1,2-Addition of the BlocBuilder MA Alkoxyamine onto Activated Olefins: A Versatile Tool for the Synthesis of Complex Macromolecular Architecture. *Polym. Chem.* **2011**, *2* (8), 1624. <https://doi.org/10.1039/c1py00057h>.
- (30) Dufils, P.-E.; Chagneux, N.; Gignes, D.; Trimaille, T.; Marque, S. R. A.; Bertin, D.; Tordo, P. Intermolecular Radical Addition of Alkoxyamines onto Olefins: An Easy Access to Advanced Macromolecular Architectures Precursors. *Polymer* **2007**, *48* (18), 5219–5225. <https://doi.org/10.1016/j.polymer.2007.06.050>.
- (31) Hawker, C. J.; Bosman, A. W.; Harth, E. New Polymer Synthesis by Nitroxide Mediated Living Radical Polymerizations. *Chem. Rev.* **2001**, *101* (12), 3661–3688. <https://doi.org/10.1021/cr990119u>.
- (32) Nicolas, J.; Guillaneuf, Y. Living Radical Polymerization: Nitroxide-Mediated Polymerization. In *Encyclopedia of Polymeric Nanomaterials*; Kobayashi, S., Müllen, K., Eds.; Springer Berlin Heidelberg: Berlin, Heidelberg, 2014; pp 1–16. [https://doi.org/10.1007/978-3-642-36199-9\\_191-1](https://doi.org/10.1007/978-3-642-36199-9_191-1).
- (33) Barrau, S.; Heiser, T.; Richard, F.; Brochon, C.; Ngov, C.; van de Wetering, K.; Hadziioannou, G.; Anokhin, D. V.; Ivanov, D. A. Self-Assembling of Novel Fullerene-Grafted Donor–Acceptor Rod–Coil Block Copolymers. *Macromolecules* **2008**, *41* (7), 2701–2710. <https://doi.org/10.1021/ma7022099>.
- (34) Lessard, B.; Tervo, C.; Marić, M. High-Molecular-Weight Poly( *Tert* -Butyl Acrylate) by Nitroxide-Mediated Polymerization: Effect of Chain Transfer to Solvent. *Macromolecular Reaction Engineering* **2009**, *3* (5–6), 245–256. <https://doi.org/10.1002/mren.200900014>.
- (35) Bian, K.; Cunningham, M. F. Nitroxide-Mediated Living Radical Polymerization of 2-Hydroxyethyl Acrylate and the Synthesis of Amphiphilic Block Copolymers. *Macromolecules* **2005**, *38* (3), 695–701. <https://doi.org/10.1021/ma0485383>.
- (36) Guégain, E.; Delplace, V.; Trimaille, T.; Gignes, D.; Siri, D.; Marque, S. R. A.; Guillaneuf, Y.; Nicolas, J. On the Structure–Control Relationship of Amide-Functionalized SG1-Based Alkoxyamines for Nitroxide-Mediated Polymerization and Conjugation. *Polymer Chemistry* **2015**, *6* (31), 5693–5704. <https://doi.org/10.1039/C5PY00283D>.
- (37) Nabifar, A. Investigations of Kinetic Aspects in Nitroxide-Mediated Radical Polymerization of Styrene, University of Waterloo, 2007.
- (38) Chevalier, C. Polymérisation radicalaire contrôlée par les nitroxydes: applicabilité et développements nouveaux, Université Bordeaux I, 2003.
- (39) Bertin, D.; Gignes, D.; Marque, S. R. A.; Tordo, P. Kinetic Subtleties of Nitroxide Mediated Polymerization. *Chem. Soc. Rev.* **2011**, *40* (5), 2189. <https://doi.org/10.1039/c0cs00110d>.
- (40) Johnson, C. S. Diffusion Ordered Nuclear Magnetic Resonance Spectroscopy: Principles and Applications. *Progress in Nuclear Magnetic Resonance Spectroscopy* **1999**, *34* (3–4), 203–256. [https://doi.org/10.1016/S0079-6565\(99\)00003-5](https://doi.org/10.1016/S0079-6565(99)00003-5).
- (41) Jiménez-Martínez, T. S.; Romero-Manig, S.; Esturau-Escofet, N.; Briseño-Terán, M. DOSY Experiments to Monitor Block Copolymer Polymerization. 4.
- (42) Etchenausia, L.; Khoukh, A.; Deniau, E. RAFT/MADOX Emulsion Copolymerization of Vinyl Acetate and N-Vinylcaprolactam: Towards Waterborne Physically Crosslinked Thermoresponsive Particles. *Polym. Chem.* **2017**, *8* (14), 2244–2256. <https://doi.org/10.1039/C7PY00221A>.
- (43) Cherifi, N.; Khoukh, A.; Benaboura, A.; Billon, L. Diffusion-Ordered Spectroscopy NMR DOSY: An All-in-One Tool to Simultaneously Follow Side Reactions, Livingness and

- Molar Masses of Polymethylmethacrylate by Nitroxide Mediated Polymerization. *Polym. Chem.* **2016**, 7 (33), 5249–5257. <https://doi.org/10.1039/C6PY00927A>.
- (44) Bakkour, Y.; Darcos, V.; Li, S.; Coudane, J. Diffusion Ordered Spectroscopy (DOSY) as a Powerful Tool for Amphiphilic Block Copolymer Characterization and for Critical Micelle Concentration (CMC) Determination. *Polym. Chem.* **2012**, 3 (8), 2006. <https://doi.org/10.1039/c2py20054f>.
- (45) Bovey, F. A.; Jelinski, L.; Mirau, P. A. *Nuclear Magnetic Resonance Spectroscopy*, 2nd ed.; Academic Press: San Diego, 1988.
- (46) Hatada, K.; Kitayama, T. Two-Dimensional NMR Spectroscopy. In *NMR spectroscopy of polymers*; Springer, Berlin, Heidelberg, 2004.
- (47) Kühl, O. *Phosphorus-31 NMR Spectroscopy: A Concise Introduction for the Synthetic Organic and Organometallic Chemist*; Springer: Berlin Heidelberg, 2008.
- (48) Ma, J.; Peng, J.; Zhai, M. Radiation-Grafted Membranes for Applications in Renewable Energy Technology. In *Radiation Technology for Advanced Materials*; Elsevier, 2019; pp 207–247. <https://doi.org/10.1016/B978-0-12-814017-8.00007-X>.
- (49) Ouhib, F. Elaboration de matériaux dérivés du polythiophène. Application aux cellules photovoltaïques organiques., Université de Pau et des Pays de l'Adour, 2008.
- (50) Venkatachalapathy, C.; Pitchumani, K. Selectivity in Bromination of Alkylbenzenes in the Presence of Montmorillonite Clay. *Tetrahedron* **1997**, 53 (7), 2581–2584. [https://doi.org/10.1016/S0040-4020\(96\)01147-7](https://doi.org/10.1016/S0040-4020(96)01147-7).
- (51) Thirumamagal, B. T. S.; Narayanasamy, S.; Venkatesan, R. Regiospecific Chlorination of Xylenes Using K-10 Montmorillonite Clay. *Synthetic Communications* **2008**, 38 (16), 2820–2825. <https://doi.org/10.1080/00397910801979338>.
- (52) Kumar, B. S.; Dhakshinamoorthy, A.; Pitchumani, K. K10 Montmorillonite Clays as Environmentally Benign Catalysts for Organic Reactions. *Catal. Sci. Technol.* **2014**, 4 (8), 2378–2396. <https://doi.org/10.1039/C4CY00112E>.
- (53) Chochos, C. L.; Drakopoulou, S.; Katsouras, A.; Squeo, B. M.; Sprau, C.; Colsmann, A.; Gregoriou, V. G.; Cando, A.-P.; Allard, S.; Scherf, U.; Gasparini, N.; Kazerouni, N.; Ameri, T.; Brabec, C. J.; Avgeropoulos, A. Beyond Donor-Acceptor (D-A) Approach: Structure-Optoelectronic Properties-Organic Photovoltaic Performance Correlation in New D-A<sub>1</sub>-D-A<sub>2</sub> Low-Bandgap Conjugated Polymers. *Macromolecular Rapid Communications* **2017**, 38 (7), 1600720. <https://doi.org/10.1002/marc.201600720>.
- (54) Roquet, S.; Cravino, A.; Leriche, P.; Alévêque, O.; Frère, P.; Roncali, J. Triphenylamine–Thienylenevinylene Hybrid Systems with Internal Charge Transfer as Donor Materials for Heterojunction Solar Cells. *J. Am. Chem. Soc.* **2006**, 128 (10), 3459–3466. <https://doi.org/10.1021/ja058178e>.
- (55) Bureš, F. Fundamental Aspects of Property Tuning in Push–Pull Molecules. *RSC Adv.* **2014**, 4 (102), 58826–58851. <https://doi.org/10.1039/C4RA11264D>.
- (56) Kathiravan, A.; Panneerselvam, M.; Sundaravel, K.; Pavithra, N.; Srinivasan, V.; Anandan, S.; Jaccob, M. Unravelling the Effect of Anchoring Groups on the Ground and Excited State Properties of Pyrene Using Computational and Spectroscopic Methods. *Phys. Chem. Chem. Phys.* **2016**, 18 (19), 13332–13345. <https://doi.org/10.1039/C6CP00571C>.
- (57) Bu, L.; Qu, Y.; Yan, D.; Geng, Y.; Wang, F. Synthesis and Characterization of Coil–Rod–Coil Triblock Copolymers Comprising Fluorene-Based Mesogenic Monodisperse Conjugated Rod and Poly(Ethylene Oxide) Coil. *Macromolecules* **2009**, 42 (5), 1580–1588. <https://doi.org/10.1021/ma802601c>.
- (58) Seo, D.; Park, J.; Shin, T. J.; Yoo, P. J.; Park, J.; Kwak, K. Bathochromic Shift in Absorption Spectra of Conjugated Polymer Nanoparticles with Displacement along

- Backbones. *Macromol. Res.* **2015**, *23* (6), 574–577. <https://doi.org/10.1007/s13233-015-3078-1>.
- (59) Fujita, H.; Michinobu, T.; Tokita, M.; Ueda, M.; Higashihara, T. Synthesis and Postfunctionalization of Rod–Coil Diblock and Coil–Rod–Coil Triblock Copolymers Composed of Poly(3-Hexylthiophene) and Poly(4-(4'-N,N-Dihexylaminophenylethynyl)Styrene) Segments. *Macromolecules* **2012**, *45* (24), 9643–9656. <https://doi.org/10.1021/ma301692b>.
- (60) Hayes, W.; Greenland, B. W. Donor–Acceptor  $\pi$ – $\pi$  Stacking Interactions: From Small Molecule Complexes to Healable Supramolecular Polymer Networks. In *Supramolecular Polymer Networks and Gels*; Seiffert, S., Ed.; Advances in Polymer Science; Springer International Publishing: Cham, 2015; Vol. 268, pp 143–166. [https://doi.org/10.1007/978-3-319-15404-6\\_4](https://doi.org/10.1007/978-3-319-15404-6_4).
- (61) Osaheni, J. A.; Jenekhe, S. A. Electroactive and Photoactive Rod-Coil Copolymers: Design, Synthesis, and Supramolecular Regulation of Photophysical Properties. *J. Am. Chem. Soc.* **1995**, *117* (28), 7389–7398. <https://doi.org/10.1021/ja00133a012>.
- (62) Fang, Y.-K.; Liu, C.-L.; Li, C.; Lin, C.-J.; Mezzenga, R.; Chen, W.-C. Synthesis, Morphology, and Properties of Poly(3-Hexylthiophene)-Block-Poly(Vinylphenyl Oxadiazole) Donor-Acceptor Rod-Coil Block Copolymers and Their Memory Device Applications. *Adv. Funct. Mater.* **2010**, *20* (18), 3012–3024. <https://doi.org/10.1002/adfm.201000879>.
- (63) Strover, L. T.; McCulloch, B.; Ho, V.; Segalman, R.; Malmström, J.; McGillivray, D. J.; Sejdic, J. T. Tuning the Optoelectronic Properties of P3EHT Block Copolymers by Surface Modification. *International Journal of Nanotechnology* **2017**, *14* (1/2/3/4/5/6), 540. <https://doi.org/10.1504/IJNT.2017.082481>.
- (64) Beaujuge, P. M.; Amb, C. M.; Reynolds, J. R. Spectral Engineering in  $\pi$ -Conjugated Polymers with Intramolecular Donor–Acceptor Interactions. *Acc. Chem. Res.* **2010**, *43* (11), 1396–1407. <https://doi.org/10.1021/ar100043u>.
- (65) Medlej, H.; Awada, H.; Abbas, M.; Wantz, G.; Bousquet, A.; Grelet, E.; Hariri, K.; Hamieh, T.; Hiorns, R. C.; Dagron-Lartigau, C. Effect of Spacer Insertion in a Commonly Used Dithienosilole/Benzothiadiazole-Based Low Band Gap Copolymer for Polymer Solar Cells. *European Polymer Journal* **2013**, *49* (12), 4176–4188. <https://doi.org/10.1016/j.eurpolymj.2013.09.025>.
- (66) Li, M.; Qin, Y.; Dai, W.; Luo, X. Tuning the Performance of the Non-Fullerene Organic Solar Cells by the Polarizability. *RSC Adv.* **2018**, *8* (7), 3809–3815. <https://doi.org/10.1039/C7RA11297A>.
- (67) Slomkowski, S.; Fellows, C. M.; Hiorns, R. C.; Jones, R. G.; Kubisa, P.; Luscombe, C. K.; Nakano, T.; Russell, G. T.; dos Santos, C. G.; Scholz, C.; Stingelin, N.; Walter, M. G. List of Keywords for Polymer Science (IUPAC Technical Report). *Pure and Applied Chemistry* **2019**, *91* (6), 997–1027. <https://doi.org/10.1515/pac-2018-0917>.
- (68) Meille, S. V.; Allegra, G.; Geil, P. H.; He, J.; Hess, M.; Jin, J.-I.; Kratochvíl, P.; Mormann, W.; Stepto, R. Definitions of Terms Relating to Crystalline Polymers (IUPAC Recommendations 2011). *Pure and Applied Chemistry* **2011**, *83* (10), 1831–1871. <https://doi.org/10.1351/PAC-REC-10-11-13>.
- (69) Klonos, P. A. Crystallization, Glass Transition, and Molecular Dynamics in PDMS of Low Molecular Weights: A Calorimetric and Dielectric Study. *Polymer* **2018**, *159*, 169–180. <https://doi.org/10.1016/j.polymer.2018.11.028>.
- (70) Aldrich. *Thermal Transitions of Homopolymers: Glass Transition and Melting Point*; p 2.
- (71) Gao, L.-C.; Pan, Q.-W.; Yi, Y.; Fan, X.-H.; Chen, X.-F.; Zhou, Q.-F. Copolymers of 2,5-Bis[(4-Methoxyphenyl) Oxycarbonyl]Styrene Withn-Butyl Acrylate: Design, Synthesis,

- and Characterization. *Journal of Polymer Science Part A: Polymer Chemistry* **2005**, *43* (23), 5935–5943. <https://doi.org/10.1002/pola.21110>.
- (72) Tsitsilianis, C.; Papaioannou, P. Physical Aging in Block Copolymers by Thermal Analysis. *International Journal of Polymer Analysis and Characterization* **1995**, *1* (1), 63–73. <https://doi.org/10.1080/10236669508009707>.
- (73) Abdelsamie, M.; Treat, N. D.; Zhao, K.; McDowell, C.; Burgers, M. A.; Li, R.; Smilgies, D.-M.; Stingelin, N.; Bazan, G. C.; Amassian, A. Toward Additive-Free Small-Molecule Organic Solar Cells: Roles of the Donor Crystallization Pathway and Dynamics. *Advanced Materials* **2015**, *27* (45), 7285–7292. <https://doi.org/10.1002/adma.201503395>.
- (74) Widom, M.; D. Mahan, G. Liquid Crystal. *Encyclopaedia Britannica*; 2019; p 8.
- (75) Wendorff, J. H.; Finkelmann, H.; Ringsdorf, H. Structure and Morphology of Liquid-Crystalline Polymers. *J. polym. sci., C Polym. symp.* **2007**, *63* (1), 245–261. <https://doi.org/10.1002/polc.5070630121>.
- (76) Singh, S. Phase Transitions in Liquid Crystals. *Physics Reports* **2000**, 163.
- (77) Raja, P. M. V.; Barron, A. R. The Analysis of Liquid Crystal Phases Using Polarized Optical Microscopy; 2020; p 4.
- (78) Peng, Z.; Ye, L.; Ade, H. Understanding, Quantifying, and Controlling the Molecular Ordering of Semi-Conducting Polymers: From Novices to Experts and Amorphous to Perfect Crystals. *Soft Condensed Matter* **2020**, 37.
- (79) Li, M.; Balawi, A. H.; Leenaers, P. J.; Ning, L.; Heintges, G. H. L.; Marszalek, T.; Pisula, W.; Wienk, M. M.; Meskers, S. C. J.; Yi, Y.; Laquai, F.; Janssen, R. A. J. Impact of Polymorphism on the Optoelectronic Properties of a Low-Bandgap Semiconducting Polymer. *Nature Communications* **2019**, *10* (1). <https://doi.org/10.1038/s41467-019-10519-z>.
- (80) Murphy, C. E.; Yang, L.; Ray, S.; Yu, L.; Knox, S.; Stingelin, N. Wire-Bar Coating of Semiconducting Polythiophene/Insulating Polyethylene Blend Thin Films for Organic Transistors. *Journal of Applied Physics* **2011**, *110* (9), 093523. <https://doi.org/10.1063/1.3660779>.
- (81) Lin, Y.-H.; Yager, K. G.; Stewart, B.; Verduzco, R. Lamellar and Liquid Crystal Ordering in Solvent-Annealed All-Conjugated Block Copolymers. *Soft Matter* **2014**, *10* (21), 3817–3825. <https://doi.org/10.1039/C3SM53090F>.
- (82) Li, F.; Yager, K. G.; Dawson, N. M.; Jiang, Y.-B.; Malloy, K. J.; Qin, Y. Stable and Controllable Polymer/Fullerene Composite Nanofibers through Cooperative Noncovalent Interactions for Organic Photovoltaics. *Chem. Mater.* **2014**, *26* (12), 3747–3756. <https://doi.org/10.1021/cm501251n>.
- (83) Johnston, D. E.; Yager, K. G.; Hlaing, H.; Lu, X.; Ocko, B. M.; Black, C. T. Nanostructured Surfaces Frustrate Polymer Semiconductor Molecular Orientation. *ACS Nano* **2014**, *8* (1), 243–249. <https://doi.org/10.1021/nn4060539>.
- (84) Allen, J. E.; Ray, B.; Khan, M. R.; Yager, K. G.; Alam, M. A.; Black, C. T. Self-Assembly of Single Dielectric Nanoparticle Layers and Integration in Polymer-Based Solar Cells. *Appl. Phys. Lett.* **2012**, *101* (6), 063105. <https://doi.org/10.1063/1.4744928>.

### Chapter 3: Rod-coil block copolymers with filmogenic properties based on low band-gap conjugated polymers

# Chapter 4

## Table of Contents

I.	Introduction.....	198
II.	Results and discussion .....	200
1)	Synthesis of rod-coil block copolymers <i>via</i> the macroinitiator method.....	200
a.	Synthesis of the rod alternating copolymers .....	200
b.	Synthesis of the macroinitiators .....	205
c.	Synthesis of the rod-coil block copolymers .....	208
2)	Synthesis of rod-coil block copolymers <i>via</i> the macro end-capper copolymerization method.....	215
a.	Synthesis of the statistical coil copolymer .....	215
b.	Functionalization of the statistical coil copolymer .....	218
3)	Optical and photothermal properties .....	221
a.	Optical properties .....	221
b.	Photothermal properties .....	226
4)	Study of the nano-objects in water .....	230
III.	Conclusion .....	236
IV.	References.....	237

## I. Introduction

In the work described in this chapter, the main goal was to extend the possible applications of IR-absorbing polymers, by designing an amphiphilic rod-coil diblock copolymer able to self-assemble in water. It is well-known that in the last thirty years the field of organic electronics has experienced tremendous growth, notably for the development of OLEDs, OFETs, and OPVs. Now, research also tend to focus on the application of organic electronic materials in the field of bioelectronics.<sup>1,2</sup> Among the scientific progress in that field, the development of biosensors such as glucose monitors for diabetics, pacemakers/defibrillators, cochlear implants, and biomedical instruments must be cited as major advances.<sup>3</sup> In addition to health monitoring, bioelectronic devices can be applied to medical therapy such as photo/thermo therapy or surgical actuation mechanisms.<sup>4</sup> Yet, medical therapy includes also the field of cancer treatment that has seen the development of tremendous emerging therapies such as photodynamic therapy based on the use of a photosensitizer<sup>5-7</sup> or photothermal therapy based on the nonradiative conversion of light energy into heat<sup>8-10</sup> to trigger the death of cancer cells. In this chapter, we aimed at synthesizing photothermal nano-objects of an amphiphilic diblock copolymer containing a photothermal hydrophobic block (P(DTS-DAP)) and a biocompatible hydrophilic block made of di(ethylene glycol) ethyl ether acrylate (eDEGA) and oligo(ethylene glycol) methyl ether acrylate (mOEGA) units (P(eDEGA-*co*-mOEGA)).

Such materials can be obtained by various synthetic routes described in Chapter 1, and in this work, we decided to focus on two strategies already employed in Chapter 3: the macroinitiator method and the macro end-capper copolymerization method. The main difference in this chapter is the nature of the coil block: a random copolymer based on the di(ethylene glycol) ethyl ether acrylate (eDEGA) monomer and the oligo(ethylene glycol) methyl ether acrylate (mOEGA) macromonomer in a composition of 90% and 10%, respectively. At first, we chose a thermoresponsive polymer due to its ability to easily control the self-assembling behavior of the final copolymer *via* a simple variation of the temperature and its high potential for *in vitro* and *in vivo* applications.<sup>11</sup> Indeed, such polymers present biocompatibility thanks to their polyethylene glycol (PEG) parts and a versatile and controllable lower critical solubility temperature (LCST) behavior when mixing short and long oligo ethylene glycol (OEG) side chains (2 and 9 repetitive units, respectively).<sup>12</sup> Combining this



#### Chapter 4: Rod-coil block copolymers with water compatibility

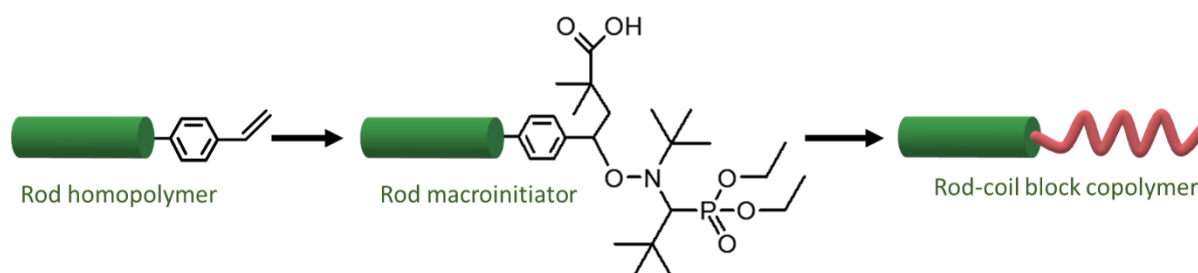
hydrophilic block to a hydrophobic conjugated block covalently linked led to an amphiphilic copolymer with promising properties for bioelectronic devices and optoelectronic materials.<sup>13</sup>

Then, the optical properties of the different materials obtained in this chapter were studied. We also studied the photothermal properties of one low band-gap homopolymer and two rod-coil block copolymers in different solvents and under different parameters. Outstanding photothermal performances of the different materials were found. Finally, a study of the nano-objects formed by the diblock copolymer in water was conducted using dynamic light scattering (DLS) in order to determine the structure of such amphiphilic materials.

## II. Results and discussion

### 1) Synthesis of rod-coil block copolymers *via* the macroinitiator method

In this first synthetic strategy, a low band-gap polymer was end-functionalized with a reactive end-capper, which was then modified into a nitroxide initiator. Finally, the macroinitiator was employed to initiate the polymerization of a coil block (Scheme 1). This synthetic strategy is similar to the one described in Chapter 3, but the nature of the coil block is different.



Scheme 1: Synthetic methodology for rod-coil block copolymer *via* the macroinitiator method

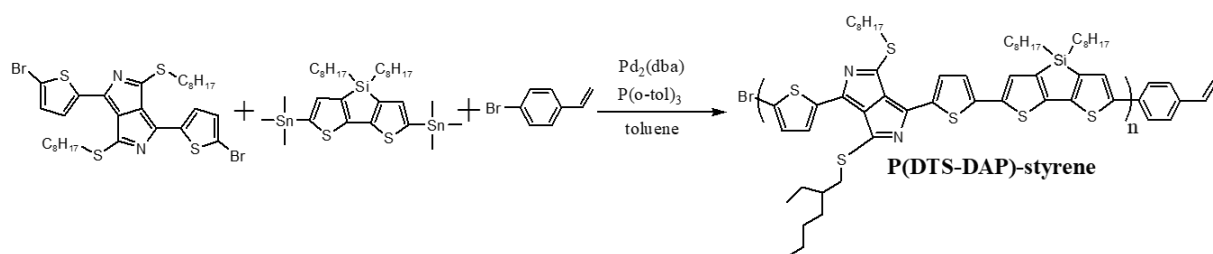
#### a. Synthesis of the rod alternating copolymers

The dibrominated 2,5-diazapentalene (DAP) (synthetic details reported in Chapters 3 and 5) and the distannylated 4,4'-bis(2-ethyl-hexyl)-5,5-bis(trimethyltin)-dithieno[3,2-b:2',3'-d]silole (DTS) monomers were polymerized *via* a Stille cross-coupling polycondensation in the same conditions as described in Chapter 3. The 4-bromostyrene was employed as an end-capper (monofunctional) to obtain a styrenic end-functionalized polymer (Scheme 2). 4-bromostyrene was selected as an appropriate end-capper due to its Stille polymerizable bromophenyl group and the presence of the styrene unit allowing unambiguous characterization of the resulting end-functional material. Most importantly, this styrene unit allows radical polymerization. The stoichiometry of the reagents was maintained according to the Carothers equation introduced in Chapter 2:

$$N_A = N_B + N_{B'} \quad \rightarrow \quad 2N_{DTS} = 2N_{DAP} + N_{EG} \quad (1)$$

In which  $N_A$ ,  $N_B$ ,  $N_{B'}$  represent the mole number of stannate functions and bromide groups pertaining to the DAP monomer and to the end-capping agent respectively.  $N_{DTS}$ ,  $N_{DAP}$  and  $N_{EG}$ , define the mole number of DTS and DAP monomers and 4-bromostyrene end-groups (EG), respectively. By following this stoichiometry, the total number of aryl bromides is equal to the total number of aryl stannanes and the formation of chains bearing 4-bromostyrene is

promoted. The Stille polycondensation was performed under inert atmosphere in dry toluene and followed by the precipitation of the polymer in cold ethanol. The synthetic details are reported in the experimental part (Chapter 5). The polymer was purified by Soxhlet extraction in ethanol to remove impurities such as metallic byproducts, catalysts, ligands and unreacted monomers. Two other Soxhlet extractions were performed in THF and  $\text{CHCl}_3$ . For a question of quantity, two end-functional polymers were obtained by repeating the same monomer feed ratio (initial end-copper molar equivalent  $N_{\text{EG}} = 0.08$ , Table 1) and were isolated in THF fractions. The final polymers were obtained with good yields (75% and 76%, respectively) and were labelled as P(DTS-DAP)-S. Yields were calculated as the ratio of the THF fraction weight on the theoretical polymer weight. For all the alternating copolymers, the THF fraction was the major fraction (average yield: 75%) and the  $\text{CHCl}_3$  fraction was considered as the minor fraction. It is also possible that the ethanol fraction contains small chains (*i.e.* oligomers). Hence, the chloroform fraction was not employed and not analyzed for the rest of the study. Indeed, the solubilization of this last fraction was difficult and some characterization techniques were not possible such as SEC in THF. In addition, the material must be soluble in toluene for the following synthetic steps. Therefore, all the following syntheses and analyses have been performed on the THF fraction which obviously led to a lack of information about the full polymer sample.



Scheme 2: Synthetic methodology for styrenic end-functionalized rod alternating copolymer

$^1\text{H}$  NMR was performed to verify the proton structure of the polymers and to calculate the ratio between the repetitive units and the end-group ( $n_{\text{DTS-DAP}}/n_{\text{EG}}$ , Table 1). In Figure 1, the  $^1\text{H}$  NMR spectrum, obtained at  $80^\circ\text{C}$  to enhance the solubility of the polymer chains, shows two areas assigned to the thiophene groups: the first zone between 7.80 and 8.46 ppm belongs to the aromatic protons (a) and the second zone between 7.38 and 7.70 ppm is related to the aromatic protons (b) and (c). The multiplet centered at 3.68 ppm corresponds to the two aliphatic protons (d) in  $\alpha$  position of sulfur atoms on the alkyl chains. The CH,  $\text{CH}_2$ , and  $\text{CH}_3$  protons of the alkyl chains have their chemical shifts between 0.67 and 2.03 ppm. The peaks at

6.56, 5.61 and 5.10 ppm coincide with the styrenic protons (e), (f) and (g), respectively. The integral of the proton (g) was compared to the integrals of the proton (d) in order to estimate the  $n_{\text{DTSDAP}}/n_{\text{EG}}$  ratio in the final polymers. In Figure 1, the integral of the protons (d) ( $I_d$ ) is equal to 28 and the integral of the proton (g) ( $I_g$ ) is equal to 1. Hence, the  $n_{\text{DTSDAP}}/n_{\text{EG}}$  ratio was calculated from the following equation:

$$n_{\text{DTSDAP}}/n_{\text{EG}} = \frac{I_d/4}{I_g} \quad (2)$$

The  $n_{\text{DTSDAP}}/n_{\text{EG}}$  ratio was found to be equal to 7 and was reported in Table 1, entry 3. The same calculation was applied to the other alternating copolymer and the corresponding ratio was reported in Table 1, entry 2.

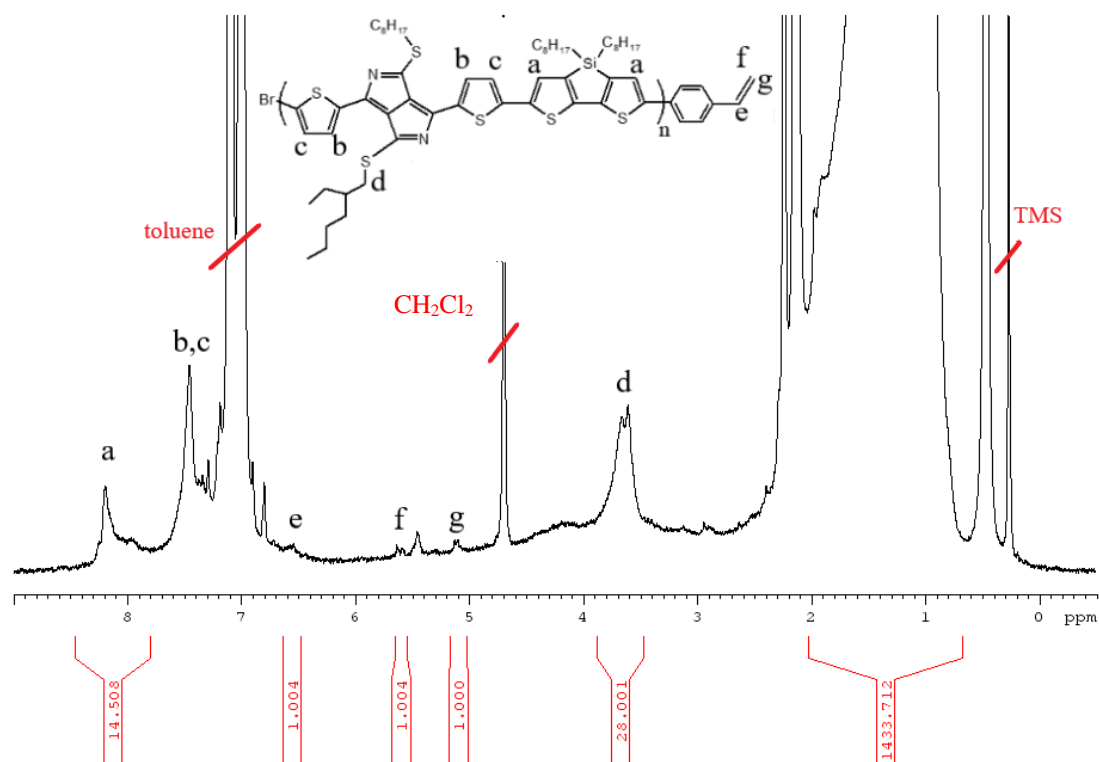


Figure 1:  $^1\text{H}$  NMR spectrum of the styrenic end-functionalized  $\text{P}(\text{DTS-DAP})_7\text{-S}$  alternating copolymer (400 MHz, toluene- $d_8$ )

The  $n_{\text{DTSDAP}}/n_{\text{EG}}$  ratio in the final alternating copolymers were also calculated from Carothers equation below and reported in Table 1:

$$\overline{DP}_n = \frac{1+r}{1+r-2rp} \quad (3)$$

In which  $r$  is the ratio of monomer groups, and  $p$  is the conversion. It should be noted that in this equation,  $\text{DP}_n$  counts the number of DTS + DAP units, so it is twice the number of repeat

units  $n$  used in the calculation of the number average molar mass  $M_n$ . Therefore,  $M_n$  can be calculated as follows:

$$\bar{M}_n = M_0 \frac{\overline{DP}_n}{2} = \frac{M_0}{2} \frac{1+r}{1+r-2rp} \quad (4)$$

Where  $M_0$  is the molar mass of the repeat unit. When monofunctional reagent (as the end-capping agent) is introduced, the monomer group ratio is defined by the following equation:

$$r = \frac{N_A}{N_B+2N_{B'}} = \frac{2N_{DTS}}{2N_{DAP}+2N_{EG}} = \frac{N_{DTS}}{N_{DAP}+N_{EG}} \quad (5)$$

Where the factor 2 relative to  $N_{B'}$  enters in the equation because the end-capper reagent has the same effect on the degree of polymerization than a difunctional monomer therefore is two times more effective.

The ratios obtained *via*  $^1\text{H}$  NMR were found to be slightly different compared to the theory. For the polymer analyzed in Figure 1, the  $n_{\text{DTS}/\text{DAP}}/n_{\text{EG}}$  ratio was estimated to be 7. Thanks to the Carothers equation, the theoretical  $\text{DP}_n$  of the same polymer was calculated to be 50 (at 100% conversion), corresponding to 25 DTS-DAP repetitive units. Since bromostyrene has been included in the stoichiometry, styrene units should be at both end-chains for a 100% conversion. Therefore, for this polymer, the theoretical  $n_{\text{DTS}/\text{DAP}}/n_{\text{EG}}$  ratio is around 12 (Table 1). The difference between the theory and the experiment may be due to conversion, since a theoretical conversion of 98.4% leads to a repetitive unit (DTS-DAP) to styrene ratio of 7. The molar masses  $M_n$  were calculated from the theory and compared to the molar masses  $M_n$  directly calculated from the ratio  $n_{\text{DTS}/\text{DAP}}/n_{\text{EG}}$  obtained *via*  $^1\text{H}$  NMR with the hypothesis that each chain bore one end-capper. For the alternating copolymer P(DTS-DAP)<sub>7</sub>-S (entry 3, Table 1), the molar mass  $M_n$ , calculated from  $^1\text{H}$  NMR, and with the hypothesis that only one styrene is present on the chain, is equal to 7000 g.mol<sup>-1</sup>. Theoretically, a molar mass of 24000 g.mol<sup>-1</sup> can be reached at 100% of conversion. For all the alternating copolymers, the experimental molar masses deviated from the theoretical ones due to several parameters: the incomplete conversion, the approximation that each chain is monofunctionalized for conversion below 100%, and finally the fact that only the THF fraction was analyzed while the CHCl<sub>3</sub> fraction contains the highest molar masses. As it was previously detailed in Chapter 1, high molar masses are difficult to reach in step-growth polycondensation as the conversion increases exponentially with the  $\text{DP}_n$  and full conversions are rarely achieved.

Table 1: Macromolecular characteristics of the synthesized polymers

Polymer	$r^a$	$N_{DTS}^b$	$N_{DAP}^b$	$N_{EG}^b$	$n_{DTS DAP}$ $/n_{EG}^c$	$n_{DTS DAP}$ $/n_{EG}^d$	$M_n$ th <sup>c</sup> (g.mol <sup>-1</sup> )	$M_n^d$ (g.mol <sup>-1</sup> )	$p$
P(DTS-DAP)	1	0.5	0.5	0	$\infty$	-	$\infty$		
P(DTS-DAP) <sub>10</sub> -S	0.96	1	0.96	0.08	12	10	24000	10000	0.994
P(DTS-DAP) <sub>7</sub> -S	0.96	1	0.96	0.08	12	7	24000	7000	0.984

<sup>a</sup> feed ratio calculated according to Carothers equations, <sup>b</sup> molar fraction; <sup>c</sup> calculated from Carothers equations and based on the hypothesis that 100% of conversion is reached; <sup>d</sup> based on <sup>1</sup>H NMR; <sup>e</sup> measured by SEC with a UV-Visible detector at 700 nm

The two end-functional alternating copolymers were characterized by size-exclusion chromatography (SEC) in THF equipped with a UV-Visible detector set a  $\lambda = 700$  nm (Figure 2). Reasonable dispersity values around 1.4 and  $M_n$  and  $M_w$  from 3600 to 5400 g.mol<sup>-1</sup> were calculated from conventional calibration using polystyrene standards. As depicted in Figure 2, both alternating copolymers display the same molar masses due to an incomplete solubility of the polymer chains in THF at room temperature. Indeed, the filter used prior to injection is slightly colored and the longest chains may have been retained.

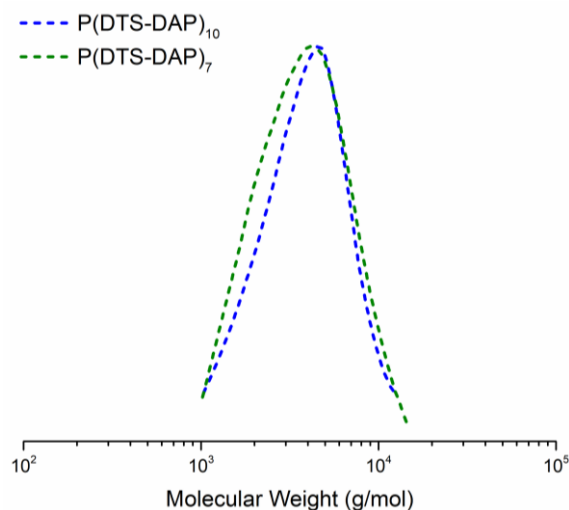
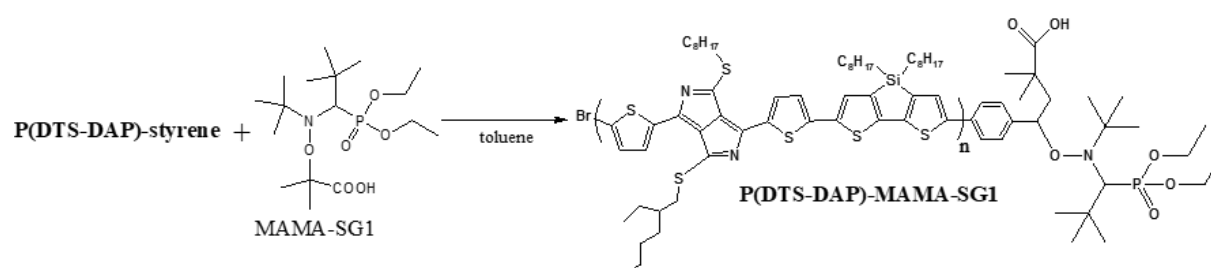


Figure 2: SEC-THF chromatograms of the two styrenic end-functionalized P(DTS-DAP)-S alternating copolymers (UV-Visible detector set at 700 nm)

## b. Synthesis of the macroinitiators



Scheme 3: Synthetic methodology for nitroxide end-functionalized rod alternating copolymer: a macroinitiator

The two styrenic end-functionalized rod alternating copolymers were transformed into macroinitiators by converting the styrenic end-groups into alkoxyamine initiating groups (Scheme 3). As already described in Chapter 3, macroinitiators can be synthesized *via* the 1,2 addition of MAMA-SG1 onto styrenic end groups. Hence, the alkoxyamine MAMA-SG1 was added in slight excess (2.5 eq compared to the polymer chains) to a solution of styrenic end-functionalized polymer P(DTS-DAP)-S and the mixture was heated at 100°C, like the dissociation temperature of the MAMA-SG1. The synthetic details are reported in the experimental part (Chapter 5). After purification of the macroinitiators by precipitation in cold ethanol, two nitroxide end-functionalized polymers were obtained with yields comprised between 60 and 62% and labelled as P(DTS-DAP)-MAMA-SG1. Lower yields were obtained, compared to the yields of the polymerization, maybe due to the change of macromolecule solubility. In fact, the macroinitiators present a higher solubility, probably due to the presence of the MAMA-SG1 at the chain ends. Hence, during the precipitation, it is possible that some chains have been solubilized in ethanol and lost, explaining the reduced yields.

<sup>1</sup>H NMR was performed to verify the proton structure of the macroinitiators. In Figure 3, the <sup>1</sup>H NMR spectrum of one of the macroinitiator, obtained at 80°C to enhance the solubility of the polymer chains, shows two areas assigned to the thiophene groups: the first zone between 8.1 and 8.27 ppm belongs to the aromatic protons (a) and the second zone between 7.38 and 7.56 ppm is related to the aromatic protons (b) and (c). The multiplet centered at 3.62 ppm corresponds to the two aliphatic protons (d) in  $\alpha$  position of sulfur atoms on the alkyl chains. The multiplet centered at 3.25 ppm belongs to four aliphatic protons (h) on the phosphonic ester chain ends. The integral of the proton (h) was compared to the integral of the protons (d) centered at 3.63 ppm in order to estimate the  $n_{\text{DTS-DAP}}/n_{\text{EG}}$  ratio in the final polymers. The ratios  $n_{\text{DTS-DAP}}/n_{\text{MAMA}}$  of the macroinitiators were found to be similar to the ratios  $n_{\text{DTS-DAP}}/n_{\text{EG}}$  of the alternating copolymers, meaning that all styrene units have been converted into MAMA-SG1

units. Nevertheless, the superimposition of the  $^1\text{H}$  NMR spectra of the styrenic end-functionalized polymer  $\text{P}(\text{DTS-DAP})_5\text{-S}$  and the macroinitiator  $\text{P}(\text{DTS-DAP})_5\text{-MAMA-SG1}$  in Figure 3 shows that the signals at 6.56, 5.61 and 5.10 ppm pertaining to the parent styrene end-functionalized polymer have not completely disappeared. From this result, we calculated the conversion of styrenic protons into MAMA-SG1 alkoxyamines according to this equation:

$$\text{functionalization yield} = \frac{I_{h/4}}{I_f/1 + I_{h/4}} \times 100 = 77 \quad (6)$$

Here, it should be emphasized that the integration of the signals at 6.56, 5.61 and 5.10 ppm was difficult to take because of the weak intensity compared to the baseline, and may be overestimated. Therefore, we can conclude that at least 77% of the chains are now functionalized with MAMA-SG1 alkoxyamines.

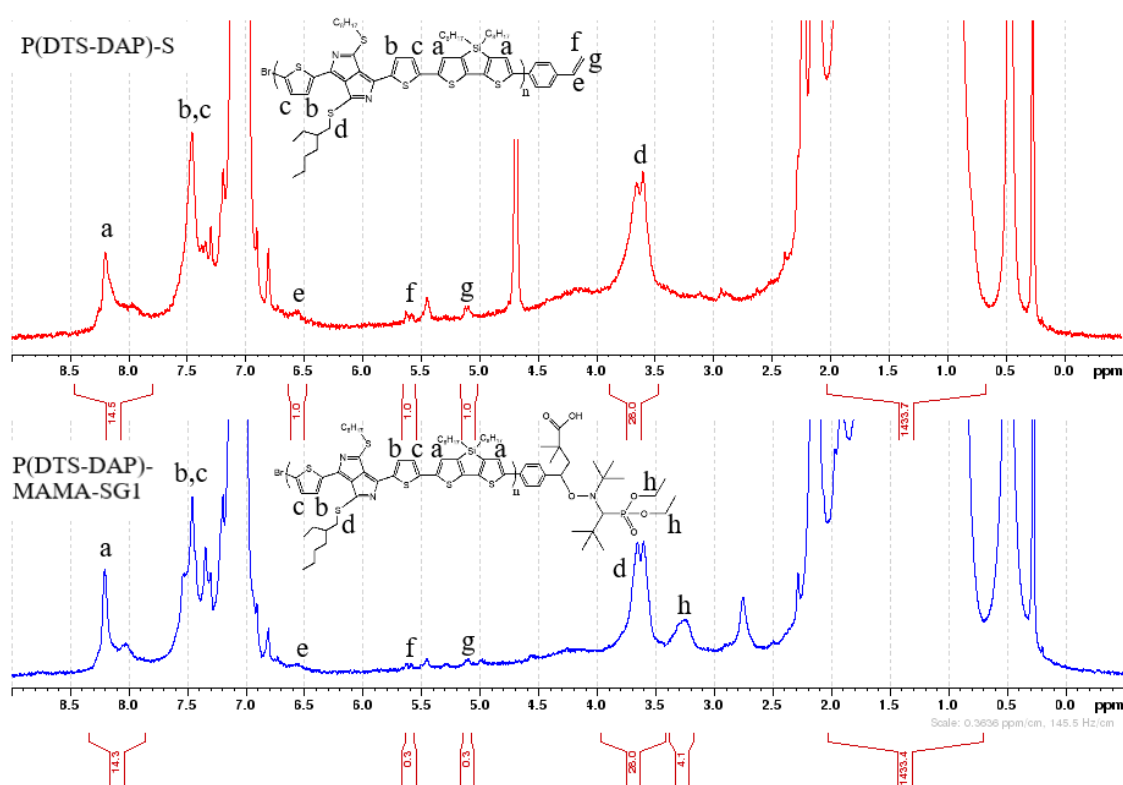


Figure 3: Superimposition of  $^1\text{H}$  NMR spectra of the styrenic end-functionalized  $\text{P}(\text{DTS-DAP})_7\text{-S}$  alternating copolymer and the nitroxide end-functionalized  $\text{P}(\text{DTS-DAP})_7\text{-MAMA-SG1}$  macroinitiator (400 MHz, toluene- $d_8$ )



The two macroinitiators were characterized by size-exclusion chromatography (SEC) in THF equipped with a UV-Visible detector set at  $\lambda = 700$  nm (Figure 4). Dispersity values between 1.6 and 2.25 and  $M_n$  and  $M_w$  from 6600 to 15500  $\text{g}\cdot\text{mol}^{-1}$  were calculated from conventional calibration using polystyrene standards and were reported in Table 2. Generally, molar masses and dispersities of macroinitiators are higher than the ones found for the rod alternating copolymers (also reported in Table 2). We explained it by the enhancement of the solubility of polymer chains thanks to the presence of the MAMA-SG1 alkoxyamines at the chain ends that allows the solvation of the complete sample in THF. Molar masses obtained by SEC deviate from the ones obtained *via*  $^1\text{H}$  NMR due to the polystyrene calibration.

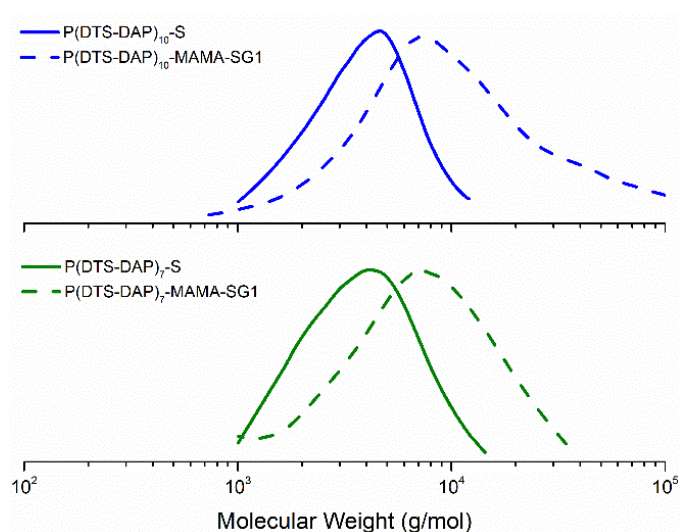


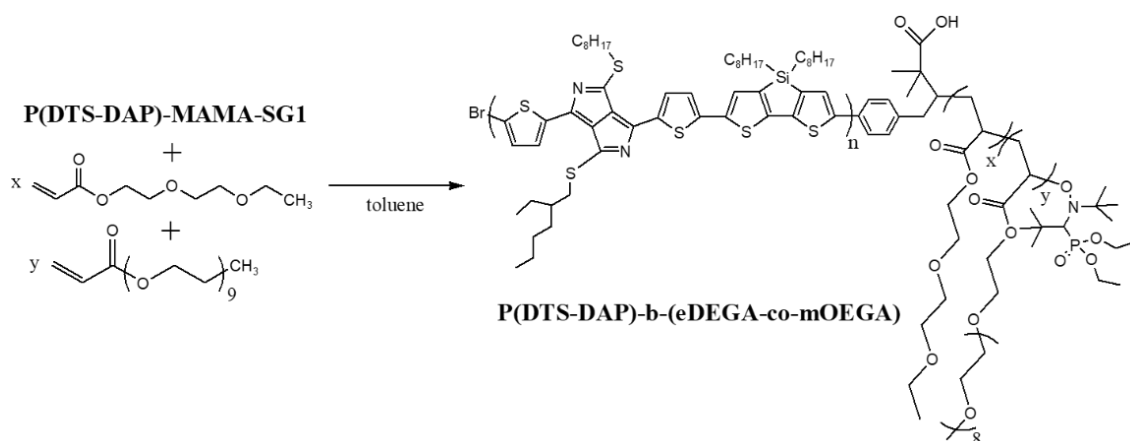
Figure 4: Superimposition of the SEC-THF chromatograms of the styrenic end-functionalized P(DTS-DAP)-S alternating copolymers and the nitroxide end-functionalized P(DTS-DAP)-MAMA-SG1 macroinitiators (UV-Visible detector set at 700 nm)

Table 2: Macromolecular characteristics of the macroinitiators

Polymer	$M_n^a$	$M_n^b$	$M_w^b$	$\mathcal{D}^b$
P(DTS-DAP) <sub>10</sub> -S	10000	3600	5100	1.4
P(DTS-DAP) <sub>7</sub> -S	7000	3700	5400	1.4
P(DTS-DAP) <sub>10</sub> -MAMA-SG1	10400	6900	15500	2.25
P(DTS-DAP) <sub>7</sub> -MAMA-SG1	7400	6600	10500	1.6

<sup>a</sup> based on the  $^1\text{H}$  NMR and with the hypothesis that each chain bore 2 end-capper; <sup>b</sup> measured by SEC with a UV-Visible detector at 700 nm

## c. Synthesis of the rod-coil block copolymers

Scheme 4: Synthetic methodology for rod-coil block copolymer *via* the macroinitiator method

The two nitroxide end-functionalized macroinitiators were employed to initiate the random copolymerization of the di(ethylene glycol) ethyl ether acrylate (eDEGA) monomer and the oligo(ethylene glycol) methyl ether acrylate (mOEGA) macromonomer in a composition of 90% and 10% respectively, *via* nitroxide-mediated polymerization (NMP) (Scheme 4). This ratio was chosen according to the work of Mawele Loudy *et al.* where they employed this specific composition for 2-(2-methoxyethoxy)ethyl methacrylate (MEO<sub>2</sub>MA) and oligo(ethylene glycol) methacrylate (OEGMA) monomers in order to obtain thermoresponsive polymers.<sup>12,14,15</sup> The use of a controlled radical polymerization is an asset in the synthesis of block copolymers as it makes it more efficient with greater degree of control compared to free-radical polymerizations (FRP).<sup>16,17</sup>

For the first batch, a mixture of eDEGA and mOEGA monomers was added in large excess (5200 eq compared to the macroinitiator) to a solution of the nitroxide end-functionalized macroinitiator P(DTS-DAP)<sub>10</sub>-MAMA-SG1 in toluene. Since NMP is usually carried out above 110°C, high boiling point solvents are preferred. Here, toluene was the solvent of choice because of its high boiling point (110°C) and it does not contain any chlorine atoms (in comparison with chlorobenzene based solvents), which can lead to transfer in radical polymerization.<sup>18–20</sup> However, for the first batch (*i.e.* 5200 eq of monomer), the solubility of the P(DTS-DAP)<sub>10</sub>-MAMA-SG1 was poor and a large amount of toluene was needed to achieve an acceptable sample (19 mg in 1.8 mL). Since the volume was important, and in order to keep a suitable concentration of monomer for the polymerization ( $C_{mOEGA} = 0.8 \text{ mol.L}^{-1}$  and  $C_{eDEGA}$

$= 3 \text{ mol.L}^{-1}$ ), a substantial amount of monomer had to be inserted (around 5200 eq compared to the macroinitiator chains). As seen in Chapter 3, a polymerization temperature of  $130^\circ\text{C}$  improves the initiation rate. Hence, the polymerization was performed at this temperature. The polymerization kinetics of the first batch were followed by  $^1\text{H}$  NMR by withdrawing samples at predefined times. After calculation of the conversion  $p$  by using integral of one of monomer peaks and integral of one of the polymer peak (detailed in Chapter 5), semi-logarithmic kinetic of  $\ln((1-p)^{-1})$  versus time were plotted in Figure 5 (blue squares). The kinetic plot does not show a strict linear evolution throughout the reaction, thus it is impossible to conclude clearly on the controlled behavior of the polymerization (*i.e.* the concentration of active propagating species is constant throughout the polymerization balancing the rates of activation and deactivation).<sup>21</sup> Three other copolymerizations were run with two different macroinitiators (P(DTS-DAP)<sub>10</sub>-MAMA-SG1 and P(DTS-DAP)<sub>7</sub>-MAMA-SG1) in the same experimental conditions by varying the polymerization time to reduce the coil block length.

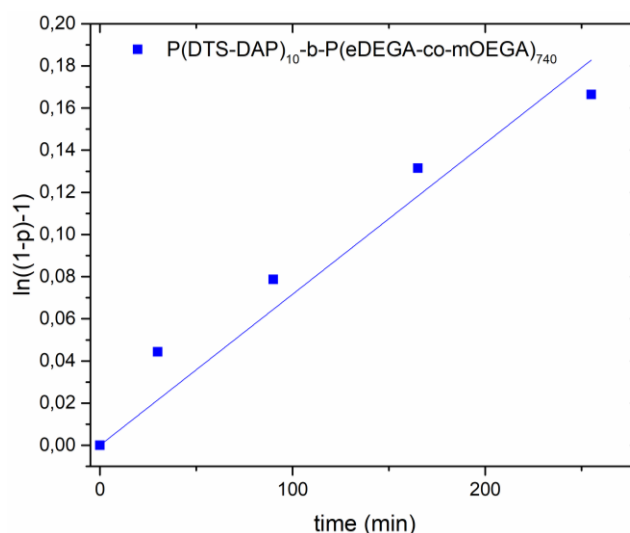


Figure 5: Semi-logarithmic kinetic plot of  $\ln((1-p)^{-1})$ , where  $p$  represents the overall monomer conversion, versus time for eDEGA and mOEGA copolymerizations via NMP with macroinitiator P(DTS-DAP)<sub>10</sub>-MAMA-SG1

The block copolymers were purified by dialysis to remove the free monomers. The mixtures were diluted with THF and dialyzed against deionized water using a regenerated cellulose (RC) membrane (weight cutoff: 2.0 kDa). The final conversions obtained are 21% (after 250 min of polymerization), 13% (after 60 min), 10% (after 30 min), and 8% (after 15 min) leading to four block copolymers bearing different lengths of the hydrophilic P(eDEGA-co-mOEGA) block (see Table 3).

$^1\text{H}$  NMR was performed to verify the proton structure of the purified block copolymers. In Figure 6, the  $^1\text{H}$  NMR spectrum of one of the block copolymer in tetrachloroethane ( $\text{C}_2\text{D}_2\text{Cl}_4$ ) shows one area assigned to the thiophene protons (a), (b), and (c) of the rod block between 6.98 and 8.15 ppm. The large peak at 4.23 ppm corresponds to the two aliphatic protons (e) in  $\alpha$  position of the ester function of acrylates in the coil block. Other peak centered at 2.36 ppm belongs to the protons (h) of acrylates in the coil block. The integral of the protons (a), (b), and (c) was calibrated at 42 protons and was compared to the integral of the protons (e) to estimate a number average degree of polymerization ( $\text{DP}_n$ ) of the coil block. For the fourth polymerization, the integral of the two protons (e) is equal to 86 while the integral of the six protons (a), (b), and (c) is equal to 42. Hence, the  $\text{DP}_n$  of the coil block is equal to 43. The  $\text{DP}_n$  of the other block copolymers were estimated with the same calculation and are reported in Table 3.

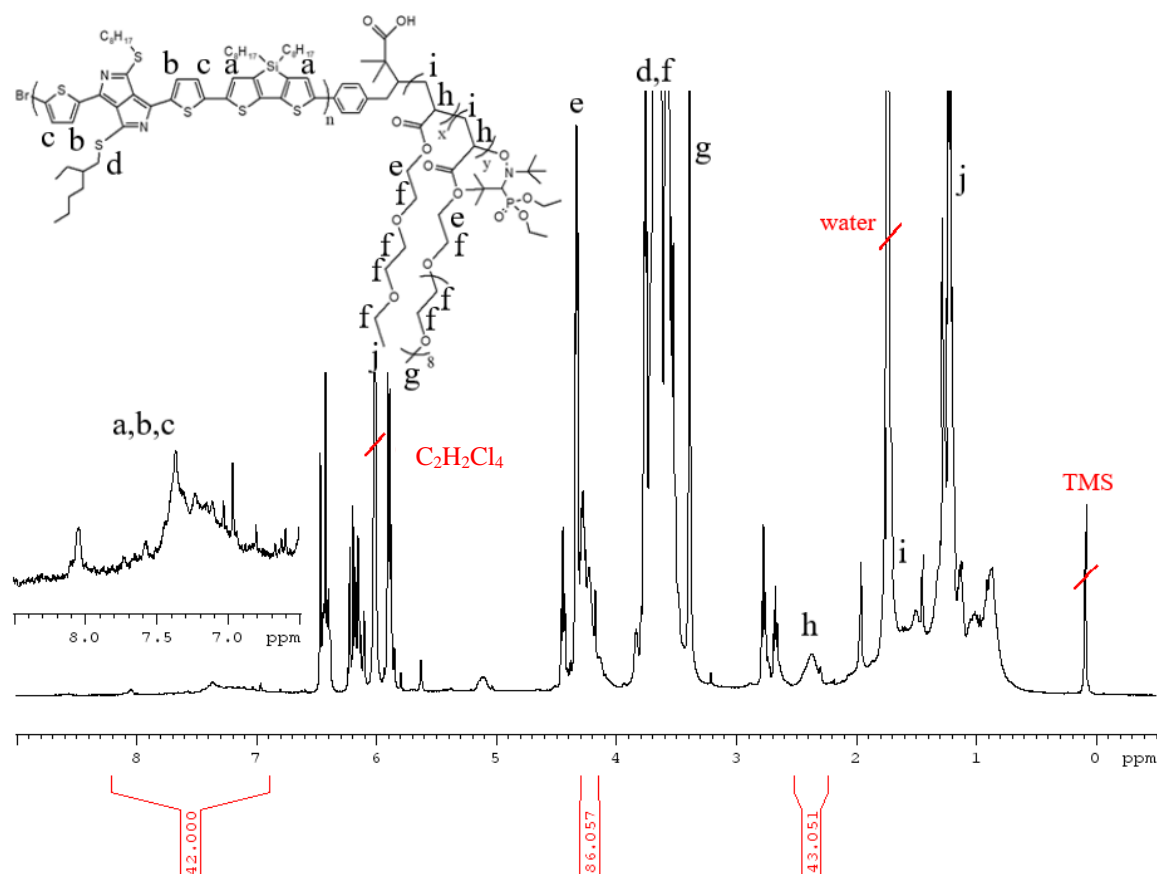


Figure 6:  $^1\text{H}$  NMR spectrum of the rod-coil block copolymer  $\text{P}(\text{DTS-DAP})_7\text{-}b\text{-P}(\text{eDEGA-co-mOEGA})_{43}$  (400 MHz,  $\text{C}_2\text{D}_2\text{Cl}_4$ )

DOSY NMR was performed in the same solvent as  $^1\text{H}$  NMR in order to assess the effective formation of the P(DTS-DAP)-*b*-P(eDEGA-*co*-mOEGA) block copolymers by NMP. In Figure 7, the DOSY NMR spectrum of the rod-coil block copolymer P(DTS-DAP)<sub>7</sub>-*b*-P(eDEGA-*co*-mOEGA)<sub>43</sub> shows a zoomed view of the DOSY experiment with the related  $^1\text{H}$  NMR spectrum projected on the top. The  $^1\text{H}$  NMR spectrum has already been explained above (Figure 6). On the DOSY map, the signals corresponding to P(DTS-DAP) and P(eDEGA-*co*-mOEGA) blocks seem to be aligned but the vertical axis presents a wide diffusion coefficient with a double population at -10.5 and -10.15  $\text{m}^2/\text{s}$ . This result cannot confirm the formation of a pure block copolymer but rather suggests the presence of a mixture of residual macroinitiator (peak at -10.15  $\text{m}^2/\text{s}$ ) and block copolymer (peak at -10.5  $\text{m}^2/\text{s}$ ). In this specific sample, there is also a peak at -9.5  $\text{m}^2/\text{s}$  which is related to residual monomer. Another purification step has been performed to remove it.

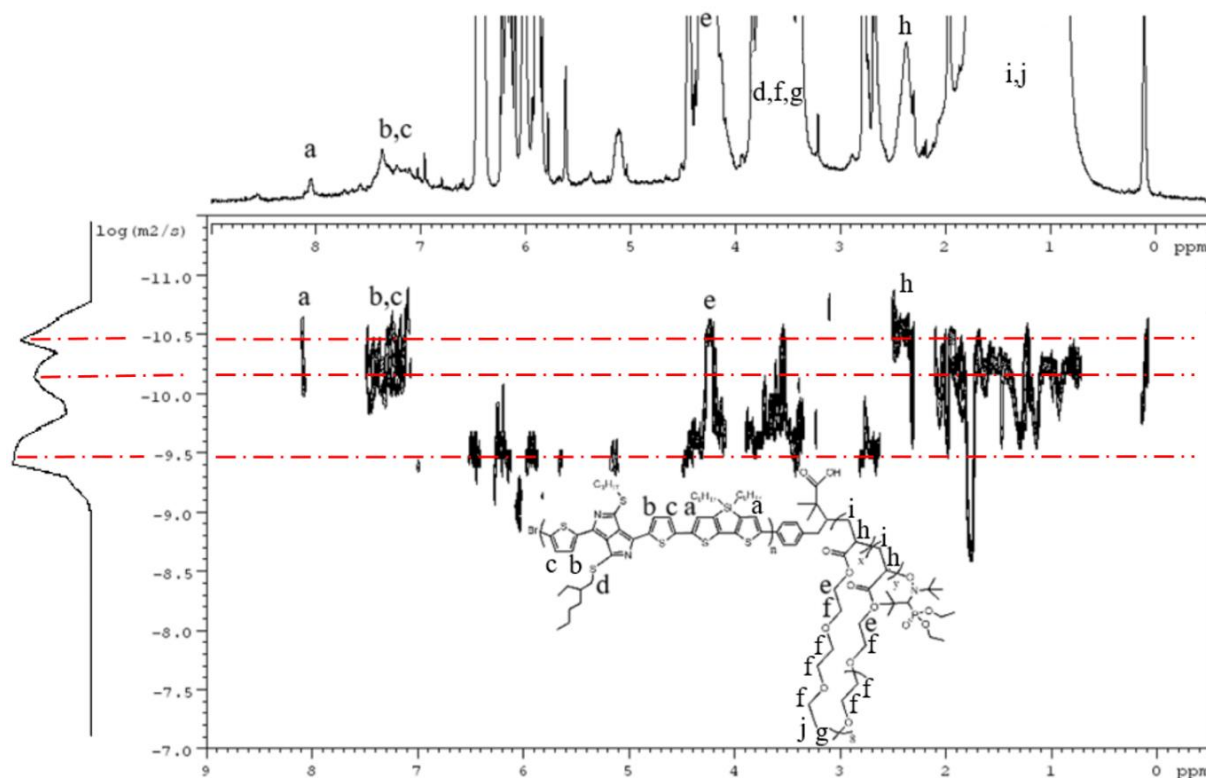


Figure 7: NMR DOSY spectrum of the rod-coil block copolymer P(DTS-DAP)<sub>7</sub>-*b*-P(eDEGA-*co*-mOEGA)<sub>43</sub> (400 MHz,  $\text{C}_2\text{D}_2\text{Cl}_4$ )

The four rod-coil block copolymers were characterized by size-exclusion chromatography (SEC) in THF equipped with a UV-Visible detector set at  $\lambda = 700$  nm (Figure 8). Dispersity values between 2.2 and 3.2 and  $M_n$  and  $M_w$  from 7000 to 25000  $\text{g}\cdot\text{mol}^{-1}$  were

calculated from conventional calibration using polystyrene standards and are reported in Table 3.

On the obtained chromatograms, we can observe a bimodal distribution. This result is consistent with the presence of another population shown by DOSY NMR. The superimposition of the SEC traces of the styrenic end-functionalized P(DTS-DAP)<sub>10</sub>-S alternating copolymer, the nitroxide end-functionalized P(DTS-DAP)<sub>10</sub>-MAMA-SG1 macroinitiator, and the rod-coil block copolymer P(DTS-DAP)<sub>10</sub>-*b*-P(eDEGA-*co*-mOEGA)<sub>740</sub> in Figure 9 confirms that the peak at lower molar masses corresponds to residual P(DTS-DAP) macroinitiator.

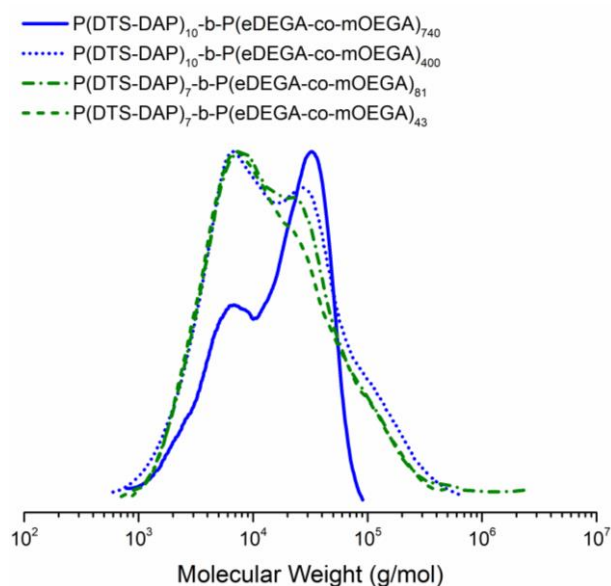


Figure 8: SEC-THF chromatograms of the four rod-coil block copolymers P(DTS-DAP)-*b*-P(eDEGA-*co*-mOEGA) (UV-visible detector set at 700 nm)

In Figure 9, the shift observed in the SEC chromatogram of the block copolymer towards, higher molar mass compared to that of the macroinitiator, proves the chain extension of P(DTS-DAP) by the P(eDEGA-*co*-mOEGA) coil block. However, at low molar masses, the SEC chromatogram of the block copolymer exhibits a shoulder at the same abscissa as the residual peak of the macroinitiator. This result means that the final material is composed of a mixture of residual unreacted macroinitiators and block copolymers. The same observations were made for the rod-coil block copolymers P(DTS-DAP)<sub>10</sub>-*b*-P(eDEGA-*co*-mOEGA)<sub>400</sub>, P(DTS-DAP)<sub>7</sub>-*b*-P(eDEGA-*co*-mOEGA)<sub>81</sub>, and P(DTS-DAP)<sub>7</sub>-*b*-P(eDEGA-*co*-mOEGA)<sub>43</sub>. Yet, the shoulders are more intense for these three block copolymers. This result may be related to slow initiation since the polymerization time and conversion were smaller in these cases.

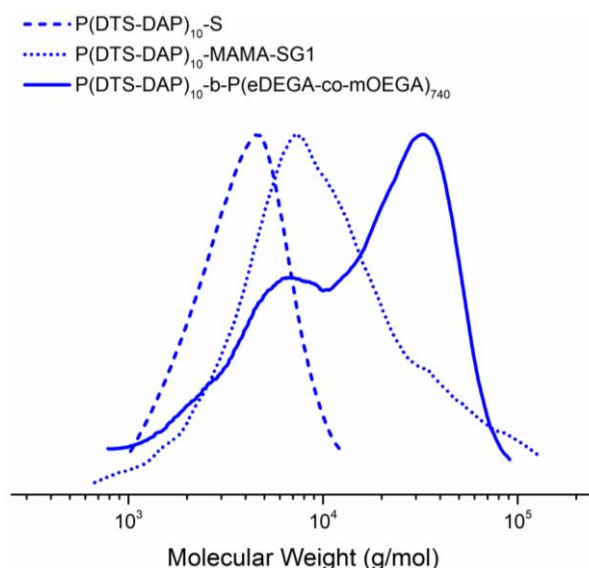


Figure 9: SEC-THF chromatograms of the styrenic end-functionalized  $P(\text{DTS-DAP})_{10}$  alternating copolymer, the  $P(\text{DTS-DAP})_{10}$ -MAMA-SG1 macroinitiator, and the rod-coil block copolymer  $P(\text{DTS-DAP})_{10}$ -*b*- $P(\text{eDEGA-co-mOEGA})_{740}$  (UV-visible detector set at 700 nm)

It was expected to observe an increase of the molar masses with the length of the coil blocks. Yet, the  $M_n$  and  $M_w$  of the block copolymers were almost identical although the coil block lengths, calculated from  $^1\text{H}$  NMR, were different. This phenomenon is called the abnormal co-elution effect and can occur when ultrahigh molar mass and/or comb/branched polymers are analyzed by SEC.<sup>22</sup> For this type of macromolecules, the SEC separation is often disturbed leading to a late elution at high elution volume and an overlaying with lower molar mass polymers and smaller molecules.<sup>23</sup> Our block copolymers, which contain pendant polyethylene oxide chains, present a comb topology. This abnormal exclusion behavior observed may be explained by a partial entanglement for large macromolecules and limited diffusion of large chains in and out of the SEC pores. In the literature, it is reported that this phenomenon is influenced by the type of SEC column and the flow rate.<sup>24</sup> Hence, one solution to tackle this problem could be the analysis of the block copolymers through high-temperature asymmetrical flow field-flow fractionation (HT-AF4) due to the absence of an obstructing porous stationary phase.

As reported in Chapter 1, it is a challenge to separate alternating copolymers from block copolymers. We could have tried a purification *via* Soxhlet extraction in a proper solvent, like in Chapter 3, in which the  $P(\text{DTS-DAP})$  is insoluble but the block copolymer is soluble. Unfortunately, due to lack of time, we have not been able to purify the block copolymers.

Table 3: Macromolecular characteristics of the rod-coil block copolymers

<i>Copolymer</i>	$Mn_{rod}^a$ ( $g.mol^{-1}$ )	$DPn_{rod}^a$	$Mn_{coil}^a$ ( $g.mol^{-1}$ )	$DPn_{coil}^a$	$Mn^b$ ( $g.mol^{-1}$ )	$Mw^b$ ( $g.mol^{-1}$ )	$\mathcal{D}^b$
P(DTS-DAP) <sub>10-b-</sub> P(eDEGA-co-mOEGA) <sub>740</sub>	10000	10	160000	740	8700	19200	2.2
P(DTS-DAP) <sub>10-b-</sub> P(eDEGA-co-mOEGA) <sub>400</sub>	10000	10	87000	400	7800	25000	3.2
P(DTS-DAP) <sub>7-b-</sub> P(eDEGA-co-mOEGA) <sub>81</sub>	7000	7	17600	81	8000	22300	2.7
P(DTS-DAP) <sub>7-b-</sub> P(eDEGA-co-mOEGA) <sub>43</sub>	7000	7	9350	43	7000	20800	2.9

<sup>a</sup> based on <sup>1</sup>H NMR; <sup>b</sup> measured by SEC with a UV-Visible detector at 700 nm,  $M_n$  and  $M_w$  were calculated from conventional calibration using polystyrene standards.

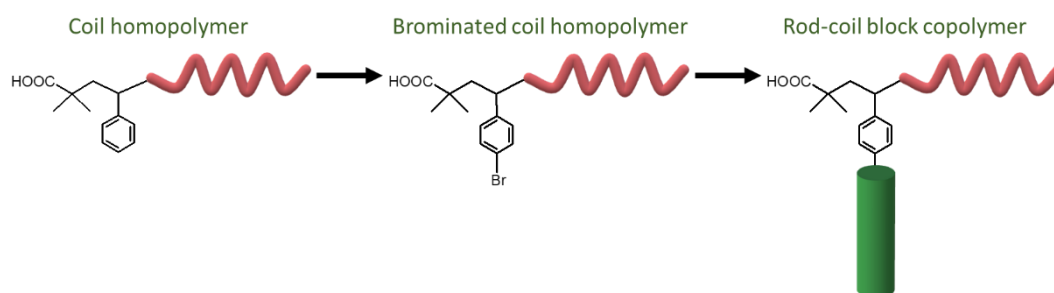
In this first part, four rod-coil block copolymers were synthesized *via* the macroinitiator method and are detailed in Table 3. The advantage of this methodology is the synthesis and characterization of a well-defined end-functionalized low band-gap polymer prior to produce block copolymer. The use of a nitroxide macroinitiator is advantageous to perform the polymerization of the second block *via* NMP. The installation of such nitroxide at the chain end of a low band-gap polymer was possible thanks to the intermolecular radical 1,2 addition which avoid numerous synthetic steps. Different sizes of coil block could be reached, even short, despite the introduction of monomers in large excess. The use of such high equivalent number of monomers was dictated by the relatively poor solubility of the macroinitiator in toluene.

The main limitation of this methodology is the difficulty to purify the rod alternating copolymer that has not initiated the polymerization of the eDEGA and mOEGA monomers.



## 2) Synthesis of rod-coil block copolymers *via* the macro end-capper copolymerization method

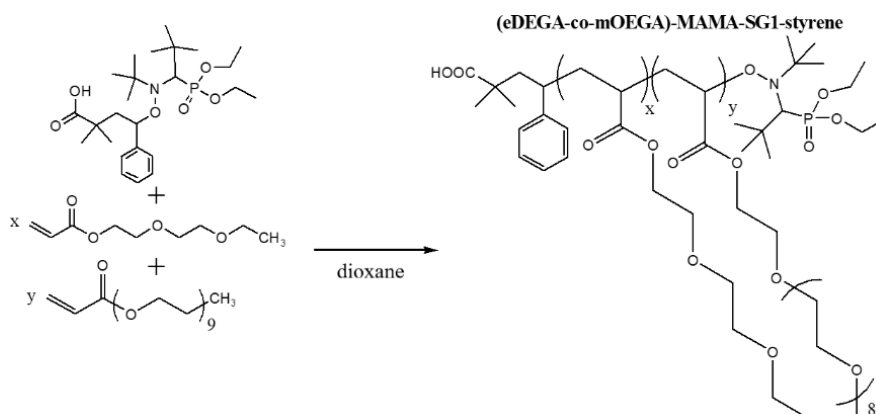
In this second synthetic strategy, a statistical coil copolymer of P(eDEGA-*co*-mOEGA) was synthesized with a specific initiator molecule. The copolymer was then modified at its chain end by a bromination reaction. Finally, the brominated coil copolymer was employed as a macro end-capper in the polycondensation of the low band-gap rod block. This synthetic strategy is similar to the one described in Chapter 3, but the nature of the coil block is different.



Scheme 5: Synthetic methodology for rod-coil block copolymer *via* the macro end-capper copolymerization method

### a. Synthesis of the statistical coil copolymer

The di(ethylene glycol) ethyl ether acrylate (eDEGA) monomer and the oligo(ethylene glycol) methyl ether acrylate (mOEGA) macromonomer were randomly copolymerized *via* nitroxide-mediated polymerization (NMP) using the second generation alkoxyamine MAMA-SG1-styrene, previously synthesized and detailed in Chapter 3 (Scheme 6). The synthetic details are reported in the experimental part (Chapter 5). The same copolymer composition as in the section I. 1) c. was targeted with 90% mol of eDEGA and 10% mol of mOEGA.



Scheme 6: Synthetic methodology nitroxide MAMA-SG1-styrene end-functionalized coil copolymer

NMP was performed under inert atmosphere in dioxane at 115°C and the polymerization kinetics were followed by  $^1\text{H}$  NMR by withdrawing samples at predefined times. After calculation of the conversion  $p$  by comparing integral of one of the monomer peak to integral of one of the polymer peak (detailed in Chapter 5), semi-logarithmic kinetic of  $\ln((1-p)^{-1})$  versus time was plotted in Figure 10. The controlled behavior of the polymerization was not clearly verified as no strict linear evolution of  $\ln((1-p)^{-1})$  versus time could be observed. The reaction was stopped after reaching a conversion of 30% in order to have shorter coil chains compared to coil chains obtained with the MAMA-SG1 initiator (27% of conversion,  $\text{DP}_n = 73$ ).

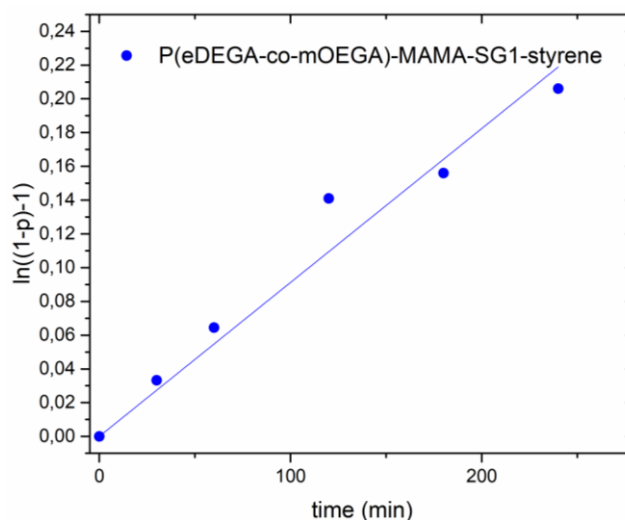


Figure 10: Semi-logarithmic kinetic plots of  $\ln((1-p)^{-1})$ , where  $p$  represents the overall monomers conversion, versus time for eDEGA and mOEGA copolymerizations via NMP

The statistical coil copolymer labelled as P(eDEGA-co-mOEGA)-MAMA-SG1 was purified by dialysis to remove free monomers. The mixture was diluted with ethanol and dialyzed against deionized water using a regenerated cellulose (RC) membrane (weight cutoff: 2.0 kDa).

The final material was analyzed by  $^1\text{H}$  NMR in  $\text{C}_2\text{D}_2\text{Cl}_4$  and the corresponding spectrum is depicted in Figure 11. A large peak at 4.25 ppm is observed, corresponding to the two aliphatic protons (a) in  $\alpha$  position of the ester function of acrylates. The other peak centered at 2.40 ppm belongs to the protons (d) of acrylates. The signals centered at 3.41 ppm and 1.24 ppm correspond to the protons (c) of the  $-\text{CH}_3$  on the mOEGA monomer and to the protons (f) of the  $-\text{CH}_3$  on the eDEGA monomer, respectively. The protons of the phenyl group (g), (h), and (i) have their signals between 7.0 and 7.4 ppm. Finally, the signal at 3.26 ppm belongs to the proton (j) on the SG1 chain end. Thanks to the integral of the protons of the phenyl group

(g) ( $I_g$ ) or thanks to the integral of the proton (j) of the SG1 chain end ( $I_j$ ), the degree of polymerization  $DP_n$  can be calculated following this equation:

$$DP_n = \frac{I_{a/2}}{I_{g/2}} = \frac{I_{a/2}}{I_{j/1}} = 50 = I_d \quad (7)$$

The final composition of the statistical copolymer can also be deduced from the  $^1H$  NMR spectrum. The fraction of mOEGA can be estimated by comparing the integral of the protons (c) and (a) ( $I_c$  and  $I_a$ ) following this equation:

$$f_{mOEGA} = \frac{I_{c/3}}{I_{a/2}} = 0.20 \quad (8)$$

The fraction of eDEGA in the copolymer can be deduced from this result by this equation:

$$f_{eDEGA} = 1 - f_{mOEGA} = 0.80 \quad (9)$$

Hence, experimental molar fractions estimated from the  $^1H$  NMR spectrum are in agreement with the feed ratio.

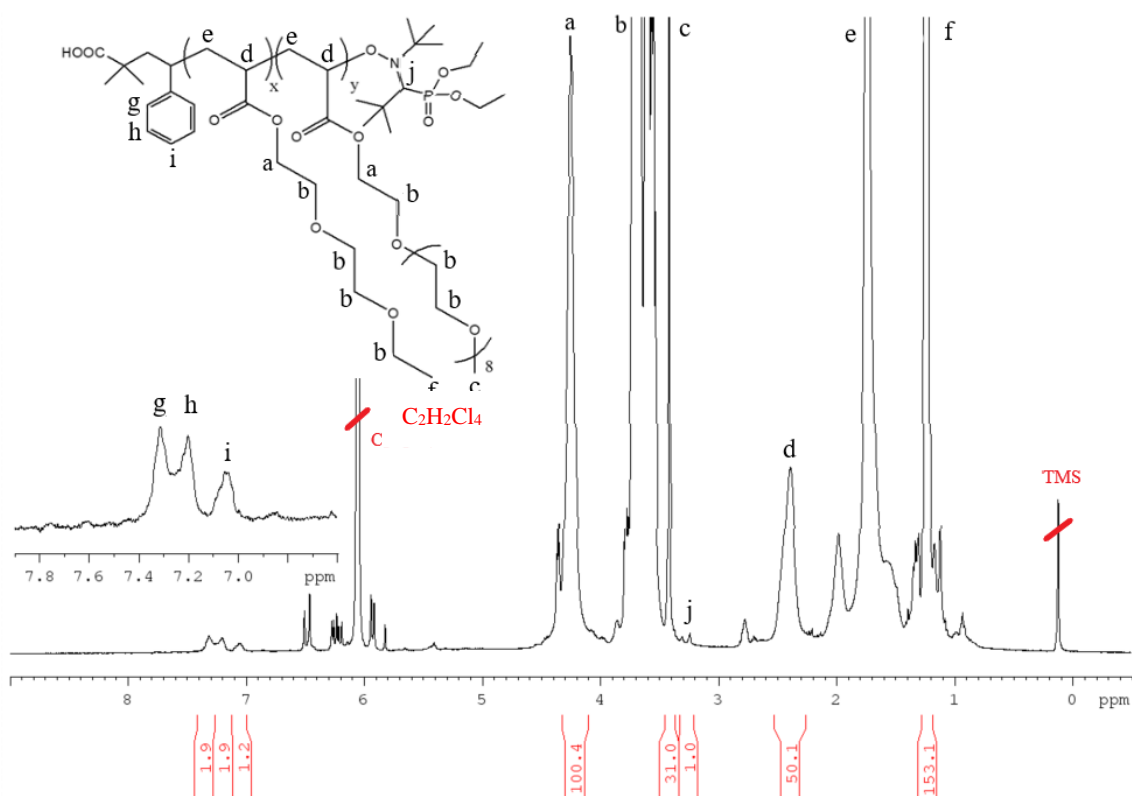


Figure 11:  $^1H$  NMR spectrum of the coil copolymer  $P(eDEGA-co-mOEGA)_{50}$ -MAMA-SG1-styrene (400 MHz,  $C_2D_2Cl_4$ )

The statistical coil copolymer was characterized by size-exclusion chromatography (SEC) in THF equipped with a RI detector (Figure 12). A dispersity of  $\sim 1.25$  was calculated (against calibration using polystyrene standards) indicating good control of the polymerization which is expected when using NMP.<sup>25,26</sup> The SEC results are reported in Table 4. The  $DP_n$  calculated from the  $^1H$  NMR was chosen for the rest of the study as the  $DP_n$  extracted from the SEC results is less accurate due to the polystyrene calibration.

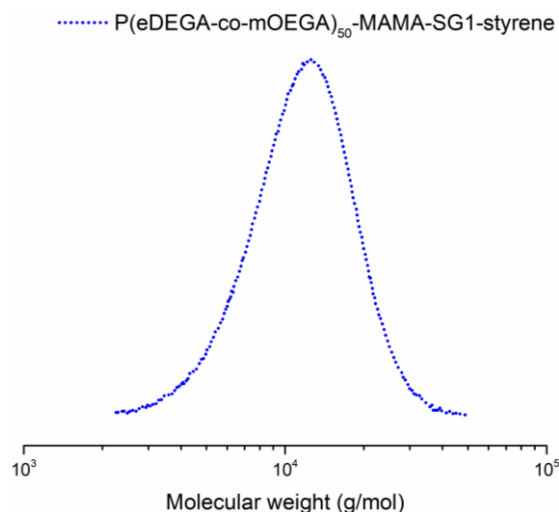


Figure 12: SEC-THF chromatogram of the coil copolymer P(eDEGA-co-mOEGA)<sub>50</sub>-MAMA-SG1-styrene (RI detector)

Table 4: Macromolecular characteristics of the coil copolymer

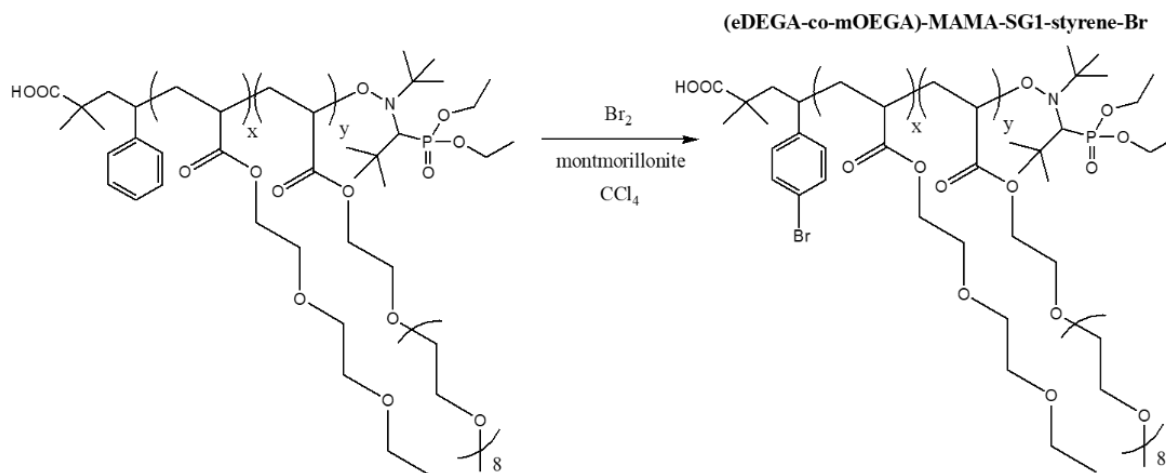
Polymer	$Mn^a$	$Mw^a$	$\bar{D}^a$	$Mn^b$	$DPn^b$
P(eDEGA-co-mOEGA) <sub>50</sub> - MAMA-SG1-styrene	9950	12500	1.25	10900	50

<sup>a</sup> measured by SEC with a RI detector, values were calculated from conventional calibration using polystyrene standards.; <sup>b</sup> based on  $^1H$  NMR

#### b. Functionalization of the statistical coil copolymer

The phenyl end-functionalized coil copolymer was brominated in order to functionalize the copolymer with a bromine function at the chain end in presence of K10-montmorillonite (Scheme 7). The functionalization reaction was conducted according to previous work reported by Ouhib<sup>27</sup> and Venkatachalapathy *et al.*<sup>28</sup> and in the same conditions as in Chapter 3. A solution of P(eDEGA-co-mOEGA) (1 eq) in  $CCl_4$  was mixed with the clay and bromine (1 eq)

was added dropwise prior to stirring at room temperature for an overnight reaction. The synthetic details are reported in the experimental part (Chapter 5).



Scheme 7: Synthetic methodology for bromine end-functionalized coil copolymer

The bromination was expected to occur with regioselectivity on the aromatic ring (para-substitution) as a heterogeneous catalyst (*i.e.* clay mineral also called K10-montmorillonite) was employed. Actually, such catalysts are well-known for their high catalytic activity, versatility, and selectivity.<sup>29,30</sup> After an overnight reaction, the brominated polymer was purified by filtration and washing with diethyl ether and chloroform. The brominated coil copolymer labelled as P(eDEGA-*co*-mOEGA)<sub>50</sub>-MAMA-SG1-styrene-Br was dried and obtained with good yield (63%).

The <sup>1</sup>H NMR was performed in C<sub>2</sub>D<sub>2</sub>Cl<sub>4</sub> to confirm the bromination on the aromatic ring. In Figure 13, the spectrum shows a large peak at 4.27 ppm corresponding to the two aliphatic protons (a) in  $\alpha$  position of the ester function of acrylates. Another peak centered at 2.42 ppm belongs to the protons (d) of acrylates. Considering the aromatic protons, the attribution was slightly more complex. Actually, the final material is a mixture of brominated and non-brominated polymer chains. The proton of the non-brominated phenyl group (i) has its signal centered at 7.06 ppm. The protons of the brominated phenyl group (g') and (h') and the protons of the non-brominated phenyl group (g) and (h) have their signals centered at 7.34 ppm.

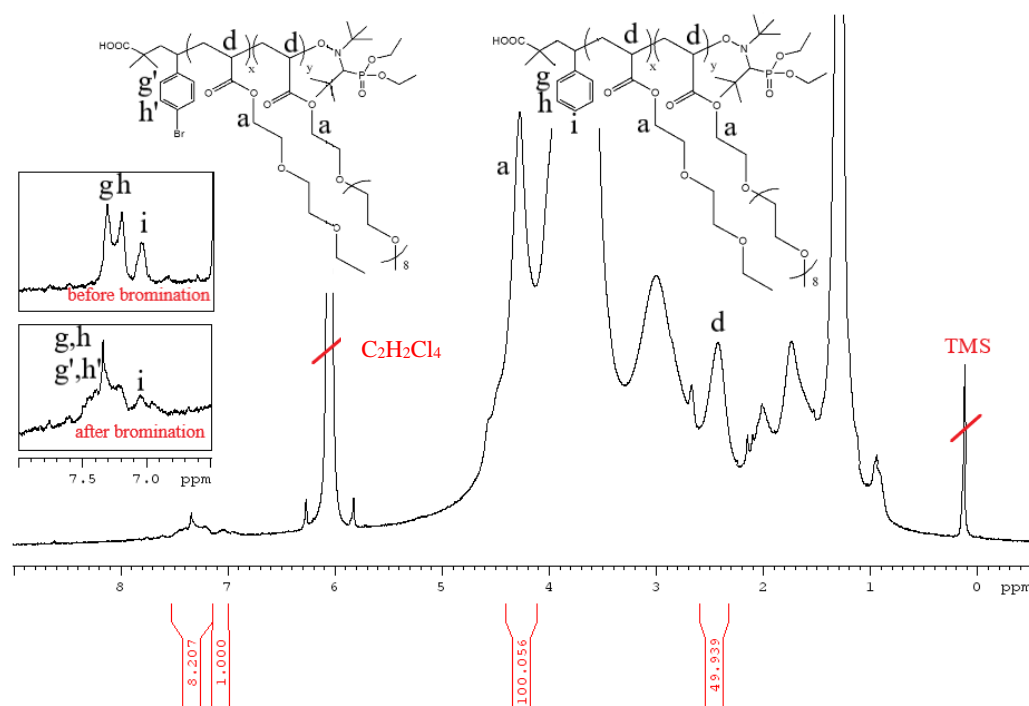


Figure 13:  $^1\text{H}$  NMR spectrum of the bromine end-functionalized coil copolymer P(eDEGA-co-mOEGA)<sub>50</sub>-MAMA-SG1-styrene-Br (400 MHz,  $\text{C}_2\text{D}_2\text{Cl}_4$ ) (inset “before bromination” is taken from the spectrum present in Figure 11)

No clear deshielding of the protons ( $g'$ ) and ( $h'$ ) was observed, however, the functionalization yield was calculated thanks to the integral of the protons ( $g'$ ), ( $h'$ ), ( $g$ ), and ( $h$ ) ( $I_{7.34 \text{ ppm}}$ ) following this equation:

$$\text{bromination yield} = \frac{\frac{I_{7.34 \text{ ppm}} - 4}{4}}{1 + \frac{I_{7.34 \text{ ppm}} - 4}{4}} \times 100 = 51 \quad (10)$$

In the end, 51% of the polymer chains were successfully brominated. Despite repeating this post-polymerization step, the functionalization yield was not increased. Since the brominated and non-brominated polymer chains have the same solubility, no purification could be performed to separate the two different copolymers. Moreover, we already obtained rod-coil block copolymer with short coil blocks *via* the macroinitiator method thus, we decided to not perform the next step synthesis (*i.e.* the macro end-capping copolymerization).

### 3) Optical and photothermal properties

#### a. Optical properties

Optical properties of the materials described in this chapter were studied by UV-Visible spectrophotometry. First, the UV-Visible absorption spectra of the rod alternating copolymers (described in II.1)a.) were measured in chloroform. In Figure 14a, both absorption spectra present the same shape with two characteristic absorption peaks, which is a feature commonly observed for alternating donor-acceptor copolymers.<sup>31</sup> Both spectra show an absorption band between 400 and 560 corresponding to a  $\pi$ - $\pi^*$  transition along the polymer backbone with  $\lambda_{\text{max}}$  around 480 nm. As already detailed in Chapter 3, the presence of alternating monomers with different electronic levels in the polymer leads to the production of a transition assigned to an intramolecular charge transfer (ICT) between the donor and the acceptor monomers.<sup>32</sup> This phenomenon is observed on both spectra where a second absorption band appears at 875 nm and 865 nm for the P(DTS-DAP)<sub>10</sub>-S and the P(DTS-DAP)<sub>7</sub>-S, respectively. Unfortunately, the samples have not been analyzed by Visible-NIR spectrophotometry, thus the absorption spectra are not complete. Hence, the maximum of the ICT band could have not been determined for the two rod copolymers. Moreover, no red shift could be observed to conclude on the possible aggregation phenomenon. Nevertheless, the number-average degree of polymerizations of the rod copolymers are comparable to those of the rod copolymers obtained in Chapter 3. Therefore, the absorption spectra of the copolymers should be similar to those of the copolymer obtained in Chapter 3 (Figure 14b).

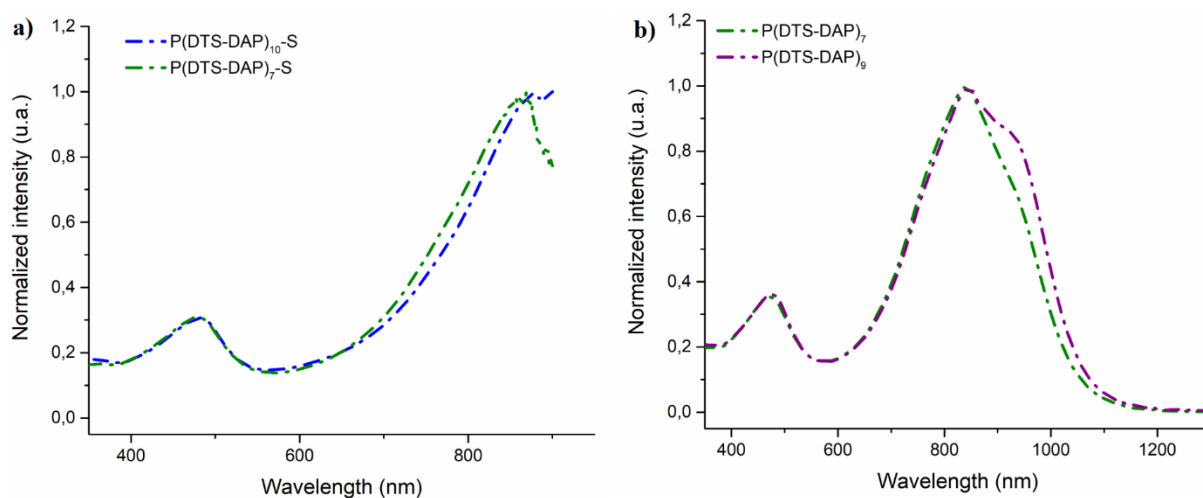


Figure 14: **a)** UV-Visible absorption spectra of the rod copolymers in CHCl<sub>3</sub> and **b)** Visible-NIR absorption spectra of the rod copolymers obtained in Chapter 3 in CHCl<sub>3</sub>

Then, the Visible-NIR absorption spectra of the rod-coil block copolymers (described in II.1)c.) were measured in chloroform, since both blocks are well soluble in this solvent. The spectra, presented in Figure 15, have been normalized considering the maximum absorption of the  $\pi-\pi^*$  transition band of each material.

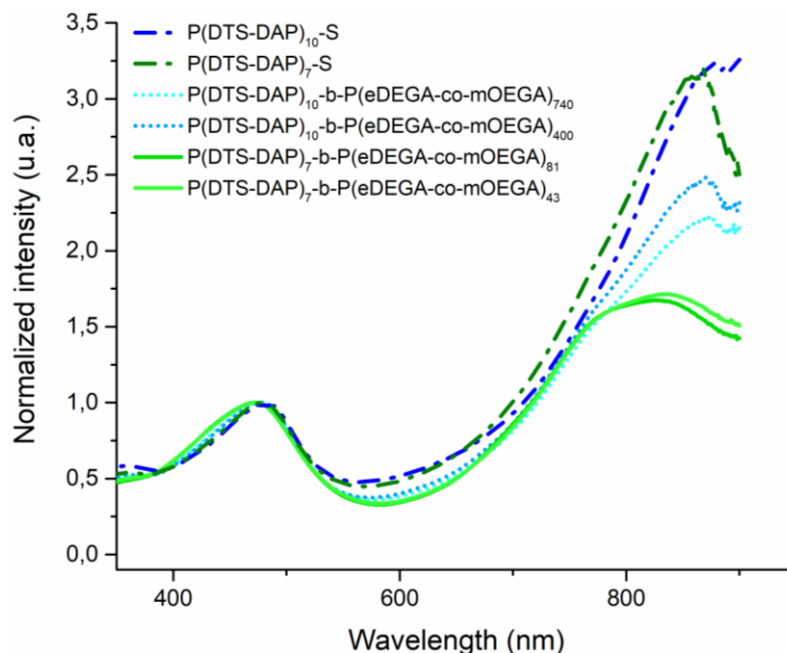


Figure 15: UV-Visible absorption spectra of the rod-coil block copolymers and their corresponding rod copolymers in  $\text{CHCl}_3$

Since the coil block does not absorb in the 350-1300 nm spectral range, the absorption spectra seen in Figure 15 largely reflect the conjugated rod block in the block copolymers.<sup>33</sup> Concerning the ICT bands of the block copolymers, they present different maximum absorption wavelength but, since the spectra are not complete, no shoulder could be observed. The  $\text{P(DTS-DAP)}_{10}\text{-}b\text{-P(eDEGA-co-mOEGA)}_{740}$  and the  $\text{P(DTS-DAP)}_{10}\text{-}b\text{-P(eDEGA-co-mOEGA)}_{400}$ , synthesized from the same rod copolymer  $\text{P(DTS-DAP)}_{10}\text{-S}$ , display similar absorption spectra. The same observation was made for the other block copolymers, the  $\text{P(DTS-DAP)}_{7}\text{-}b\text{-P(eDEGA-co-mOEGA)}_{81}$  and the  $\text{P(DTS-DAP)}_{7}\text{-}b\text{-P(eDEGA-co-mOEGA)}_{43}$ , synthesized from the same rod copolymer  $\text{P(DTS-DAP)}_{7}\text{-S}$ , where the absorption spectra are similar. Even though the absorption spectra are not complete, the ICT bands of each material display different intensities. By comparison with the parent rod copolymers, the intramolecular charge transfer bands seem to be less intense in block copolymers due to the introduction of a coil block. This result suggests that the intramolecular charge transfer between the rod and the coil blocks is



relatively weak and the interchain interactions among the rod block are reduced by incorporating the coil block.<sup>34,35</sup>

Two block copolymers were analyzed by Visible-NIR spectrophotometry in chloroform and in deionized water. Molar extinction coefficients  $\epsilon$  were calculated using Beer-Lambert's law in the concentration range from 0.004 mM to 0.019 mM. The determination of the molar extinction coefficients  $\epsilon$  was based on the block presenting a Visible-NIR absorption (*i.e.* playing the role of the “chromophore”).<sup>36</sup> The coefficients were calculated from the molar concentration  $C_n$  obtained from the following equation:

$$C_n = \frac{C_{mP(DTS-DAP)}}{M_0} = \frac{w_{P(DTS-DAP)} \times C_{m copo}}{M_0} \quad (11)$$

where  $M_0$  corresponds to the molar mass of the repetitive unit DTS-DAP of the rod copolymers and  $C_{mP(DTS-DAP)}$  to the mass concentration of the rod copolymers calculated by multiplying the mass fraction  $w_{P(DTS-DAP)}$  (obtained *via*  $^1\text{H}$  NMR and reported in Table 5) by the mass concentration of the block copolymers  $C_{m copo}$ . The corresponding spectra are shown in Figure 16. The maxima molar extinction coefficients  $\epsilon$  are reported in and vary between  $1.31$  and  $1.11 \cdot 10^4 \text{ L} \cdot \text{mol}^{-1} \cdot \text{cm}^{-1}$  for the  $\pi\text{-}\pi^*$  transition bands and between  $1.04$  and  $3.65 \cdot 10^4 \text{ L} \cdot \text{mol}^{-1} \cdot \text{cm}^{-1}$  for the ICT bands.

In chloroform, the spectra of the rod-coil block copolymers present three absorption bands with maxima at 470 nm, 845 nm, and 950 nm attributed to  $\pi\text{-}\pi$  transition, ICT, and  $\pi$ -stacking, respectively. Accordingly, the spectrum of the corresponding rod copolymer presents two absorption bands with maxima at 470 nm, 845 nm, and 940 nm attributed to  $\pi\text{-}\pi$  transition, ICT, and  $\pi$ -stacking, respectively. For the three materials, the  $\pi\text{-}\pi$  transition and ICT bands are similar. Nevertheless, the  $\pi$ -stacking bands of the rod-coil block copolymers and the corresponding rod copolymer are different with maximum absorptions varying in position (wavelength) and intensity (molar extinction coefficient). Indeed, the  $\lambda_{\text{max}}$  of the  $\pi$ -stacking bands of the block copolymers are red shifted of about 10 nm compared to the rod copolymer. Hence, the  $\pi$ -stacking phenomenon is less important for the rod copolymer than the rod-coil block copolymer. In addition, the molar extinction coefficients of the  $\pi$ -stacking bands for block copolymers are higher than that of the rod copolymer. The same observation was made for the molar extinction coefficient of the  $\pi\text{-}\pi^*$  transition bands.

In water, the spectrum calculated on the molar extinction coefficients for the rod copolymer was not done since it was not soluble in water. However, for the block copolymers,

the spectra in water were different from those in chloroform. They present three absorption bands with maxima at 495 nm, 830 nm, and around 975 nm attributed to  $\pi$ - $\pi$  transition, ICT, and  $\pi$ -stacking, respectively. Both block copolymers showed similar absorption profiles with similar band intensities. However, the  $\lambda_{\max}$  of the  $\pi$ -stacking band of the block copolymer P(DTS-DAP)<sub>10</sub>-b-P(eDEGA-co-mOEGA)<sub>400</sub> is red shifted by about 20 nm compared to the block copolymer P(DTS-DAP)<sub>10</sub>-b-P(eDEGA-co-mOEGA)<sub>740</sub>. This result could be explained by the mass fraction of chromophore which is higher for the P(DTS-DAP)<sub>10</sub>-b-P(eDEGA-co-mOEGA)<sub>400</sub>.

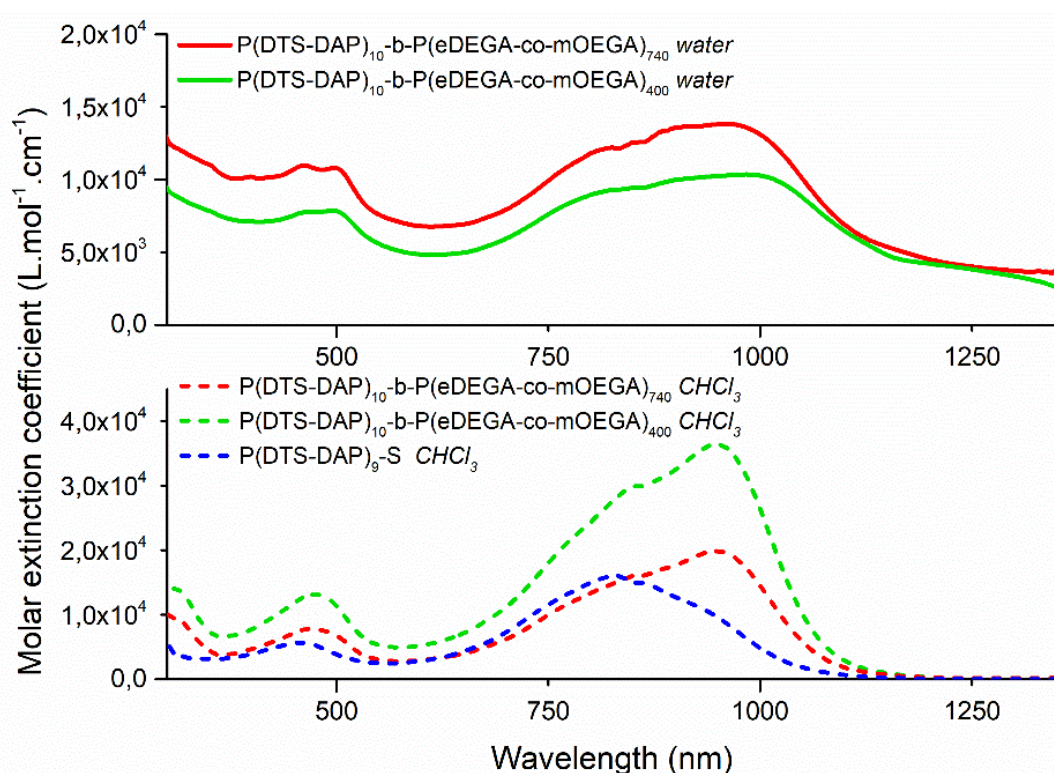


Figure 16: Superimpositions of the Visible-NIR absorption spectra of the rod-coil block copolymers in water and in  $\text{CHCl}_3$  and their corresponding rod copolymer in  $\text{CHCl}_3$

Thus, the absorption spectra are not identical in both solvents. This result suggests that the ground-state electronic structures of the block copolymers are affected by the solvent.<sup>37</sup> In order to better understand the influence of the solvent on the absorption of the block copolymers, we superimposed the absorption spectra of each material in water and in chloroform in Figure 17. The first noticeable thing is the diminution of the ICT and the  $\pi$ -stacking bands intensities in water compared to those in chloroform. As a consequence, in water, the intensities of the ICT and the  $\pi$ - $\pi^*$  transition bands are quite similar, whereas, in

chloroform, the contribution of ICT is three times more important than the contribution of  $\pi$ - $\pi^*$  transitions. This result is characteristic of supramolecular organization<sup>38,39</sup> and could be explained by different conformations of the block copolymer in the different solvents. Chloroform is a good solvent for both blocks of the copolymer but water is a selective solvent for the coil block. Hence, it is expected that the block copolymer forms unimers in chloroform and self-assembles into objects like micelles in water.

Thus, in water, the amphiphilic nature of the block copolymer (the rod block is hydrophobic and the coil block is hydrophilic) must induce self-assembly with nano-object presenting a rod core and a coil shell. Hence, in water, the ICT and  $\pi$ -stacking bands are reduced which could be explained by the H-type aggregation of rod blocks, not to the change in the effective conjugation length upon aggregation.<sup>40,41</sup> In addition, we still have to determine if the coil shell could have an impact on the light intensity effectively absorbed by the core, by some interactions with light. On the contrary, in chloroform both blocks are soluble and the copolymer spectrum presents a profile similar to the one of the rod parent.

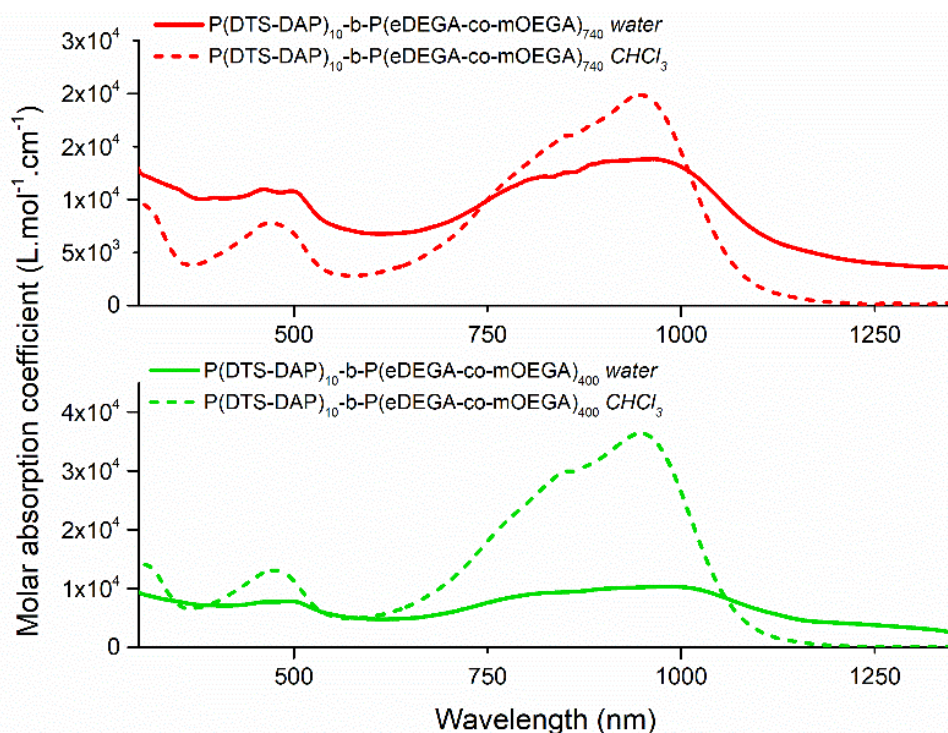


Figure 17: Superimpositions of the Visible-NIR absorption spectra of the rod-coil block copolymers in different solvents

Table 5: Optical characteristics of the rod-coil block copolymers in different solvents

	$WP(DTS-DAP)$	$\lambda_{max\ ICT}$ (nm)	$\lambda_{max\ \pi\rightarrow\pi}^*$ (nm)	$\epsilon_{max\ ICT} \cdot 10^4$ ( $L \cdot mol^{-1} \cdot cm^{-1}$ )	$\epsilon_{max\ \pi\rightarrow\pi}^* \cdot 10^4$ ( $L \cdot mol^{-1} \cdot cm^{-1}$ )	
in water	$P(DTS-DAP)_{10-b-}$ $P(eDEGA-co-mOEGA)_{740}$	0.06	830	495	1.21	1.07
	$P(DTS-DAP)_{10-b-}$ $P(eDEGA-co-mOEGA)_{400}$	0.10	830	495	0.92	0.78
in $CHCl_3$	$P(DTS-DAP)_{10-b-}$ $P(eDEGA-co-mOEGA)_{740}$	0.06	845	468	1.60	0.77
	$P(DTS-DAP)_{10-b-}$ $P(eDEGA-co-mOEGA)_{400}$	0.10	845	475	2.95	1.31
	$P(DTS-DAP)_{9-S}$	1	845	471	1.60	0.56

## b. Photothermal properties

The photothermal performances of one rod copolymer and two block copolymers were studied in different solvents. First, several solutions of the rod copolymer  $P(DTS-DAP)_{10}$  at different concentrations (from  $C = 0.1$  to  $1$  g/L) in toluene were irradiated with a NIR-I laser ( $\lambda_{IR} = 808$  nm) with a power density fixed at  $0.70$   $W \cdot cm^{-2}$  for 15 minutes. Toluene was chosen because its boiling point is high ( $110^\circ C$ ) and it will not suffer significant volume variation upon heating. As shown in Figure 18, the temperature of the solutions rapidly increased in contrast to pure toluene that showed insignificant changes under the same irradiation conditions. A high-temperature increase of average  $30^\circ C$  has been detected for all the solutions within 15 min. The difference between the initial and the final temperatures of the solutions is not significantly influenced by tuning the rod copolymer concentration in this range of concentrations. For instance, the temperature of the solution at  $C = 0.1$  g/L increased by  $28^\circ C$  while the temperature of the solution at  $C = 1$  g/L increased by  $32^\circ C$ .

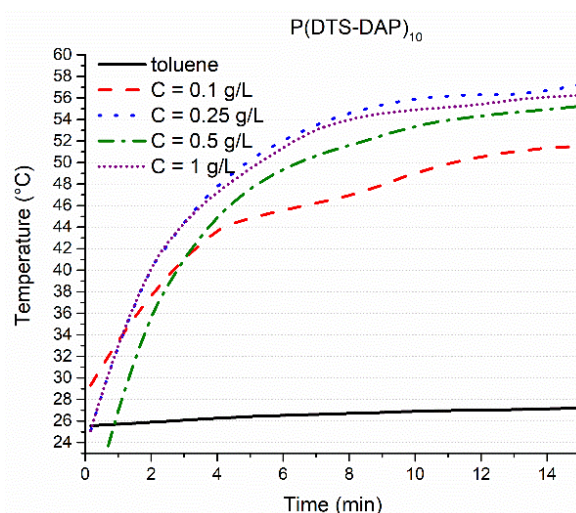


Figure 18: Temperature elevation of toluene and rod copolymer toluene solutions with different concentrations as a function of irradiation time

Multiple cycles of laser irradiation were conducted to investigate the photothermal stability and reversibility of the rod copolymer P(DTS-DAP)<sub>10</sub>. After four heating/cooling cycles, the changes in temperature were consistent as depicted in Figure 19. From these experiments, we concluded the conjugated P(DTS-DAP)<sub>10</sub> has stable and reversible photothermal properties with good photothermal conversion.

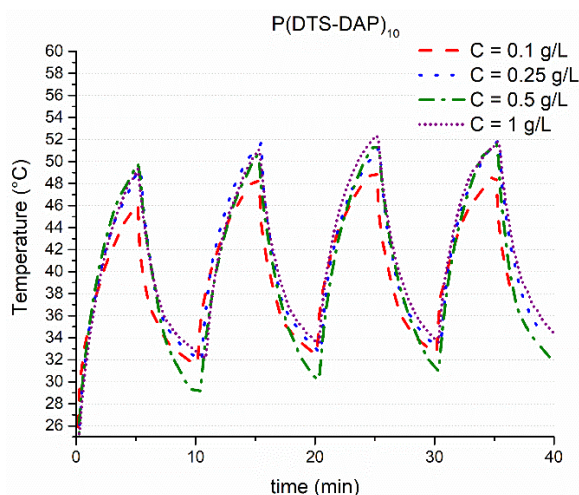


Figure 19: Temperature variations of rod copolymer toluene solutions with different concentrations over 4 cycles of heating and natural cooling

Since the rod copolymer P(DTS-DAP)<sub>10</sub> showed photothermal properties in this organic solvent (toluene), we tested the same experiments on the two block copolymers P(DTS-DAP)<sub>10</sub>-*b*-P(eDEGA-*co*-mOEGA)<sub>740</sub> and P(DTS-DAP)<sub>10</sub>-*b*-P(eDEGA-*co*-mOEGA)<sub>400</sub> at different concentrations (from C = 0.116 to 2 g/L) in chloroform (boiling point at 62°C). This organic solvent has a lower boiling point than toluene but is a much better solvent for the coil block. As shown in Figure 20, an obvious concentration-dependent temperature increase was observed for both block copolymers within 15 min whereas pure chloroform presented a slight increase of the temperature (*i.e.* 3.7°C). For the P(DTS-DAP)<sub>10</sub>-*b*-P(eDEGA-*co*-mOEGA)<sub>740</sub>, the temperature of the solution at C = 0.15 g/L increased by 10.3°C while the temperature of the solution at C = 2g/L increased by 22.1°C. For the other block copolymer P(DTS-DAP)<sub>10</sub>-*b*-P(eDEGA-*co*-mOEGA)<sub>400</sub>, the temperature of the solution at C = 0.116 g/L increased by 16.4°C while the temperature of the solution at C = 1 g/L increased by 24.6°C. This result is explained by the different chromophore mass fractions  $w_{\text{P(DTS-DAP)}}$  in each block copolymer. For the P(DTS-DAP)<sub>10</sub>-*b*-P(eDEGA-*co*-mOEGA)<sub>740</sub>,  $w_{\text{P(DTS-DAP)}}$  is equal to 0.06 while for the P(DTS-DAP)<sub>10</sub>-*b*-P(eDEGA-*co*-mOEGA)<sub>400</sub>,  $w_{\text{P(DTS-DAP)}}$  is equal to 0.10. Since the chromophore P(DTS-DAP) is responsible for the photothermal properties, it is expected to obtain better

photothermal performances for the block copolymer containing the highest chromophore content (*i.e.* the shortest coil block).

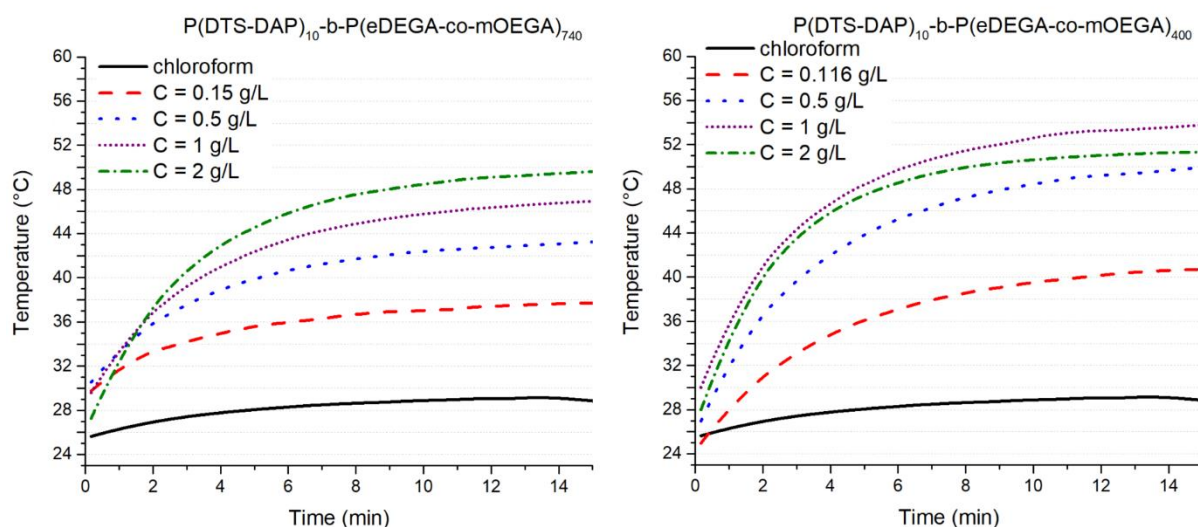


Figure 20: Temperature elevation of chloroform and rod-coil block copolymers chloroform solutions with different concentrations as a function of irradiation time

Multiple cycles of laser irradiation were conducted to investigate the photothermal stability and reversibility of the block copolymers. After four heating/cooling cycles, the changes in temperature were consistent, as depicted in Figure 21. These experiments confirmed that the block copolymer presenting the highest chromophore P(DTS-DAP) content (*i.e.* the shortest coil block) displays better photothermal performance than the other block copolymer. Moreover, we concluded both block copolymers have stable and reversible photothermal properties with good photothermal conversion.

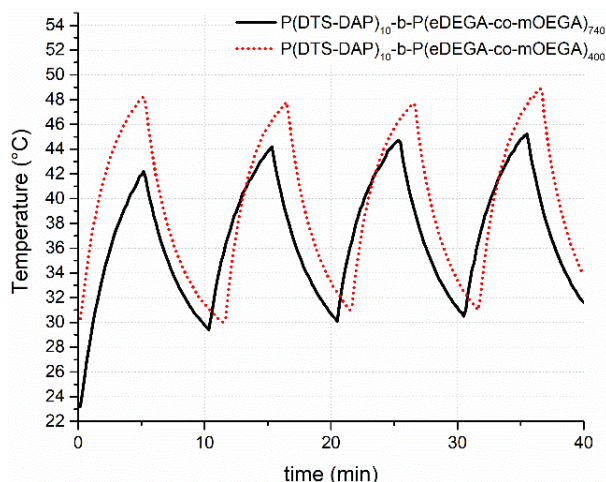


Figure 21: Temperature variations of rod-coil block copolymers chloroform solutions (2 g/L) over 4 cycles of heating and natural cooling

Since the final target is to operate these materials as photothermal agent *in vivo*, we decided to investigate the photothermal properties of the two block copolymers  $P(\text{DTS-DAP})_{10}\text{-}b\text{-}P(\text{eDEGA-co-mOEGA})_{740}$  and  $P(\text{DTS-DAP})_{10}\text{-}b\text{-}P(\text{eDEGA-co-mOEGA})_{400}$  in deionized water, in addition to the experiments conducted in chloroform. Two solutions of both block copolymers at different concentrations (from  $C = 0.116$  to  $2$  g/L) in deionized water were irradiated with a NIR-I laser ( $\lambda_{\text{IR}} = 808$  nm) with a power density fixed at  $0.70$   $\text{W}\cdot\text{cm}^{-2}$  for 15 minutes. As depicted in Figure 22, an obvious concentration-dependent temperature increase was observed for both block copolymers whereas pure water presented a slight increase of the temperature (*i.e.*  $3.9^\circ\text{C}$ ). For the  $P(\text{DTS-DAP})_{10}\text{-}b\text{-}P(\text{eDEGA-co-mOEGA})_{740}$ , the temperature of the solution at  $C = 0.116$  g/L increased by  $6^\circ\text{C}$  while the temperature of the solution at  $C = 2$  g/L increased by  $18.5^\circ\text{C}$ . For the other block copolymer  $P(\text{DTS-DAP})_{10}\text{-}b\text{-}P(\text{eDEGA-co-mOEGA})_{400}$ , the temperature of the solution at  $C = 0.183$  g/L increased by  $7.5^\circ\text{C}$  while the temperature of the solution at  $C = 2$  g/L increased by  $17^\circ\text{C}$ . In water, the block copolymers displayed similar photothermal performances. However, photothermal performances are better in chloroform. This difference may be attributed to the lower absorption at 800 nm of the copolymer in water than in chloroform as demonstrated in Figure 17.

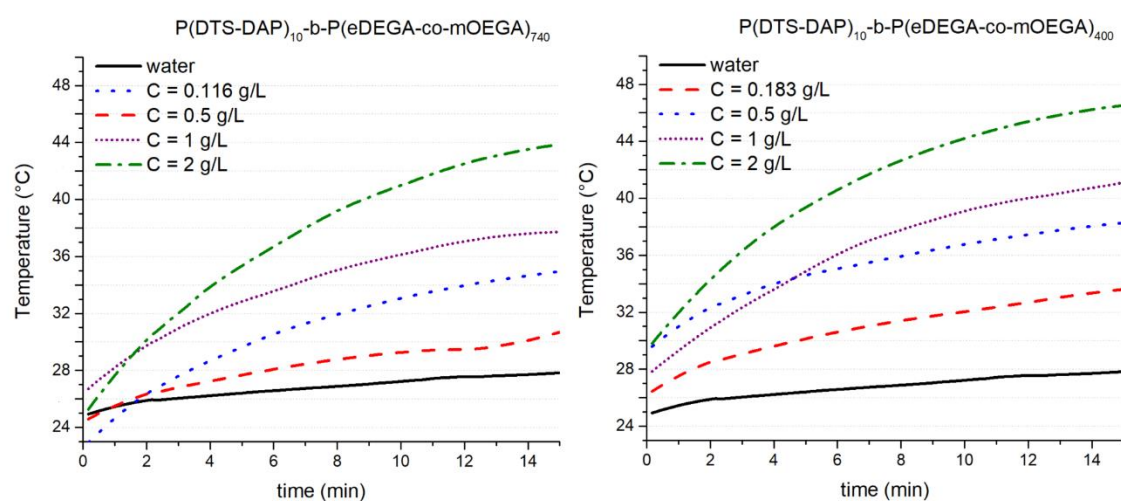


Figure 22: Temperature elevation of water and rod-coil block copolymers aqueous solutions with different concentrations as a function of irradiation time

Multiple cycles of laser irradiation were conducted to investigate the photothermal stability and reversibility of the block copolymers in water. After four heating/cooling cycles, the changes in temperature were consistent, as depicted in Figure 23. These experiments confirmed that the block copolymers display similar photothermal performances. Moreover, we

concluded both block copolymers have stable and reversible photothermal properties with good photothermal conversion.

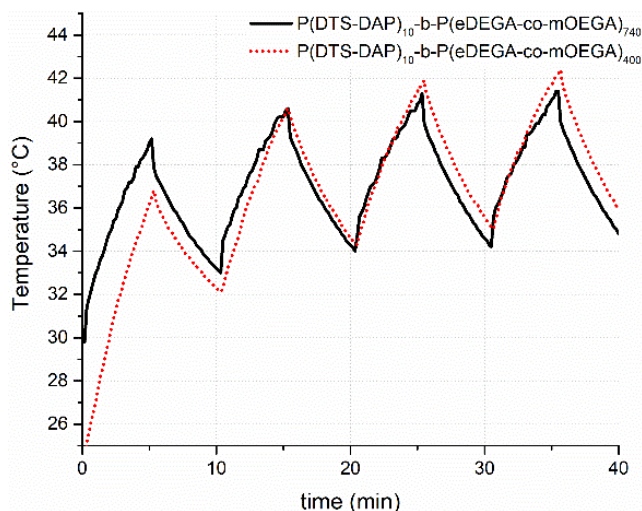


Figure 23: Temperature variations of rod-coil block copolymers aqueous solutions (2 g/L) over 4 cycles of heating and natural cooling

#### 4) Study of the nano-objects in water

The amphiphilic block copolymers, bearing a hydrophilic P(eDEGA-co-mOEGA) block and a hydrophobic P(DTS-DAP) block, should be able to self-assemble in water within aggregates exhibiting various morphologies (such as spheres, cylinders, vesicles).<sup>42-44</sup> We expected that in water the non-polar hydrophobic rod segments self-assembled, in order to avoid contact with water, by forming a core domain stabilized by a shell formed by the hydrophilic block (here the P(eDEGA-co-mOEGA)). The morphology of the object formed by amphiphilic block copolymers in water is based on the hydrophilic/hydrophobic volume ratio. It was formulated by Discher *et al.* that aggregate morphology can be predicted based on the volume fraction of the hydrophobic block, which is related to the molar mass of the hydrophobic block.<sup>45</sup> Hence, spheres are expected when the ratio of the molar mass of the hydrophobic segment on the molar mass of the hydrophilic segments is below 50/50. Above this ratio, the aggregates tend to form cylinders until a ratio of 75/25 where the aggregates take a vesicular morphology.<sup>45</sup>

Considering the hydrophobic/hydrophilic ratio of the studied block copolymers, with much longer hydrophilic moieties, we could expect a spherical morphology of the aggregates formed in water.<sup>46</sup> However, interactions between the conjugated hydrophobic moieties could occur by  $\pi$ -stacking, hence a cylindrical morphology could also be obtained.



An aggregate formed in aqueous solution can be characterized by several structural parameters:

- The hydrodynamic radius  $R_h$ , corresponding to the radius of a sphere exhibiting the same diffusion coefficient;
- The radius of gyration  $R_g$ , corresponding to the radius of a sphere exhibiting the same gravity center;
- The core radius  $R_c$  occupied by the hydrophobic blocks;
- The aggregation number  $N_{agg}$ , corresponding to the number of polymer chains constituting the aggregate.

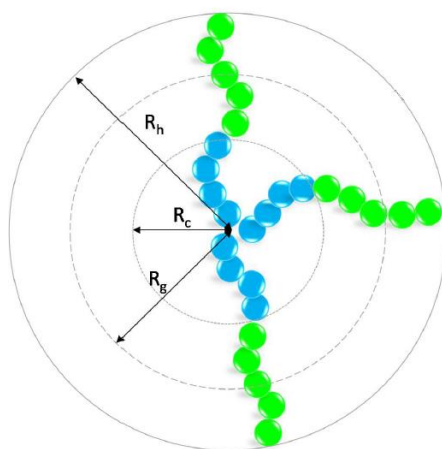


Figure 24: Schematic representation of AB diblock copolymer micelles based on 3 macromolecules (number of aggregation  $N_{agg} = 3$ ) in a selective solvent of the A block (in green). Adapted from Lespes<sup>42</sup>

Through experimentation, these parameters are accessible using several characterization techniques, mainly scattering methods and microscopy, in order to determine the morphology of the aggregates formed in solution.<sup>47,48</sup> The  $R_g$  and  $N_{agg}$  are measured by static light scattering (SLS), while  $R_c$  can be determined from small-angle X-ray scattering (SAXS) or small-angle neutron scattering (SANS) measurements and by transmission electron microscopy (TEM, CryoTEM). The  $R_h$  can be measured by dynamic light scattering (DLS).

In our laboratory, two techniques are available: SLS and DLS. First, we investigated the self-assembling behavior of the block copolymer  $P(\text{DTS-DAP})_{10-b}\text{-P}(\text{eDEGA-co-mOEGA})_{740}$  dispersed directly in water at a concentration  $C = 1$  g/L by means of dynamic light scattering (DLS). By conducting a preliminary study at different concentrations, it was determined that the concentration  $C = 1$  g/L was the ideal concentration to perform the DLS experiments. The DLS measurements were carried out at an angle of  $173^\circ$  on a Nano-ZS Model ZEN3600

Zetasizer (Malvern, UK). A 4.0 mW He–Ne laser was used, operating at a wavelength of 633 nm. We measured the properties of the aggregates formed before and after filtration using a 0.45  $\mu\text{m}$  PTFE filter. The results are presented in Figure 25 (upper part: before filtration; lower part: after filtration) and are divided in three type of graphs: the percentage of the scattered intensity as a function of the size (Figure 25a and 25d), the corresponding volume percentage of the scatterers as function of the size (Figure 25b and 25e), and the autocorrelation function (Figure 25c and 25f). In order to understand the results below, the three graphs must be analyzed all together.

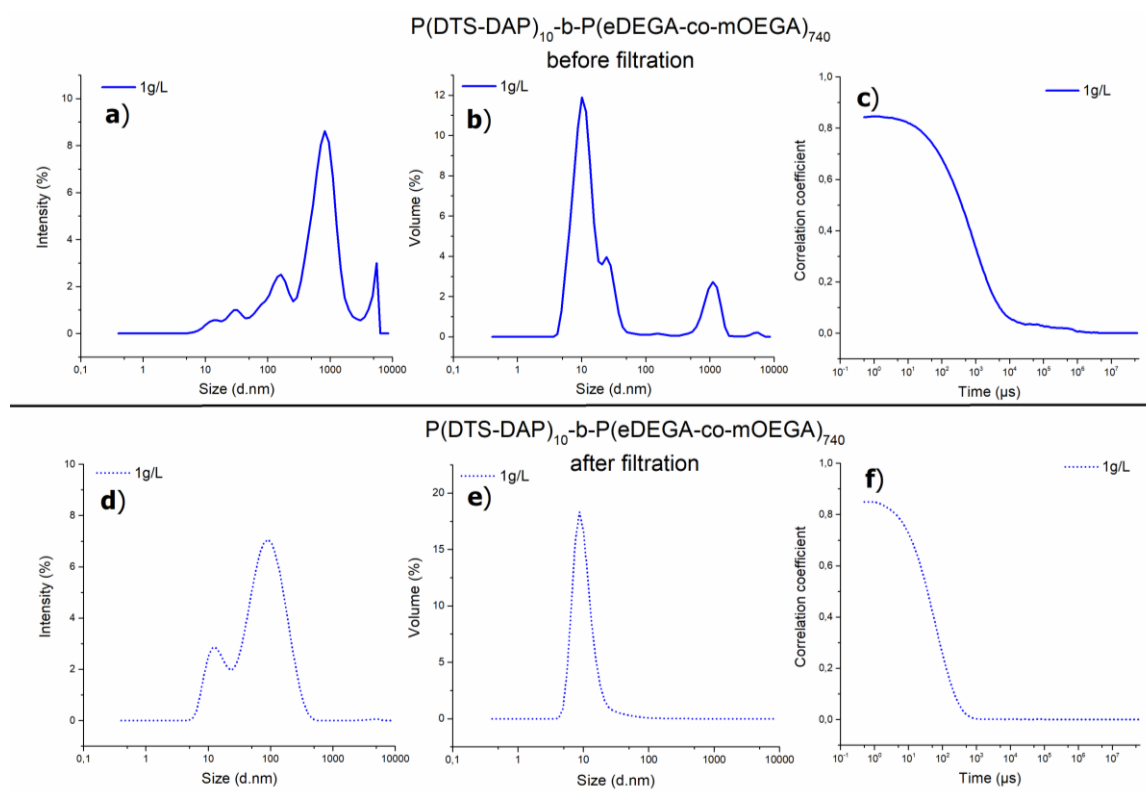


Figure 25: Dynamic light scattering results obtained from the aqueous solution of the block copolymer  $\text{P}(\text{DTS-DAP})_{10}\text{-}b\text{-P}(\text{eDEGA-co-mOEGA})_{740}$  dispersed directly in water at 1 g/L. **a)** and **d)** represent the intensity-size distributions; **b)** and **e)** the volume-size distributions; and **c)** and **f)** the autocorrelation functions. Upper part shows the results obtained before filtration (**a**, **b**, **c**) and lower part after filtration on a 0.45  $\mu\text{m}$  filter (**d**, **e**, **f**)

First of all, we can see that before filtration the autocorrelation function (Figure 25c) measured by DLS is not well-defined (shoulder at high time values) and leads to several size distributions (Figures 25a and 25b) indicating the presence of multiple populations of scatterers, probably due to the presence of non-soluble objects. These multiple populations could also be due to the presence of residual macroinitiator, which is not soluble in water (see Section II. 1) c)). Therefore, the solution was filtered and analyzed by DLS. After filtration, we observe that the autocorrelation function looks more accurate (Figure 25f) and leads to less size distributions

(Figures 25d and 25e). Two populations can then be observed when looking at the intensity size-distributions (Figure 25d) one at 14 nm and another at 105 nm. It must be realized that light scattering is sensitive to  $z$ -average sizes that is to large particles. Thus, although the population of larger particles is overwhelming in terms of scattered light intensity (Figure 25d), their volume fraction is negligible compared to the smaller aggregates (Figure 25e). Moreover, the autocorrelation function after filtration is well-defined (intercept closer to 1, no shoulder).

We hypothesized that the direct dispersion of the block copolymer in water could lead to aggregation of the particles, due to hydrophobic interactions between the particles, which cannot be solubilized in water. Hence, another preparation method was considered in order to optimize the dispersion of the aggregates. The block copolymer P(DTS-DAP)<sub>10</sub>-*b*-P(eDEGA-*co*-mOEGA)<sub>740</sub> was first solubilized in a minimum of THF and the water was introduced dropwise to the solution under vigorous stirring. Then, the THF was removed by evaporation. The self-assembling behavior of a solution prepared at  $C = 1$  g/L was then investigated by means of DLS, again before and after filtration on a 0.45  $\mu\text{m}$  PFTE filter.

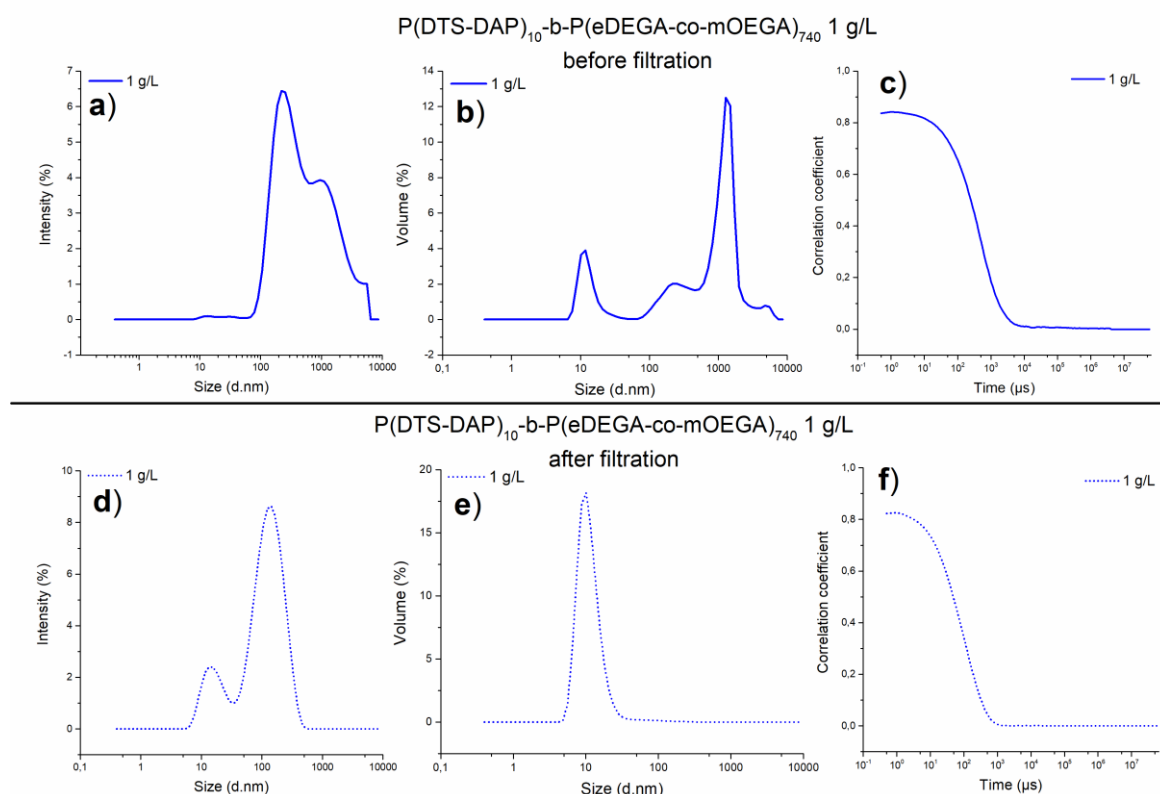


Figure 26: Dynamic light scattering results obtained from the aqueous solution of the block copolymer P(DTS-DAP)<sub>10</sub>-*b*-P(eDEGA-*co*-mOEGA)<sub>740</sub> dispersed undirectly in water at 1 g/L. **a)** and **d)** represent the intensity-size distributions; **b)** and **e)** the volume-size distributions; and **c)** and **f)** the autocorrelation functions. Upper part shows the results obtained before filtration (**a**, **b**, **c**) and lower part after filtration on a 0.45  $\mu\text{m}$  filter (**d**, **e**, **f**)

Before filtration, the autocorrelation function presented in Figure 26c is better than in the previous case (Figure 25c): there is no shoulder at high time values. Nevertheless, we can see several size distributions before filtration (Figures 26a and 26b) indicating the presence of multiple populations of scatterers, probably due to the presence of non-soluble objects. These multiple populations could also be due to the presence of residual macroinitiator which is not soluble in water (see Section II. 1) c)). Therefore, the solution was filtered and analyzed by DLS. After filtration, the results are close to those obtained with the first preparation method: we observe less size distributions (Figures 26d and 26e). Two populations can then be observed when looking at the intensity size-distributions (Figure 26d) one at 17 nm and another at 146 nm. However, the volume fraction of these large aggregates is negligible compared to the population observed 17 nm. (Figure 26e).

By comparing the different preparation methods, the results obtained look similar. In both methods, the direct dissolution in water or the use of THF as a co-solvent, a population around 15 nm was found which indicates the presence of micelles formed by self-assembly of the block copolymer  $P(\text{DTS-DAP})_{10}\text{-}b\text{-}P(\text{eDEGA-co-mOEGA})_{740}$ .

In addition, the concentrations of each solution before and after filtration prepared *via* both preparation methods were measured by NIR-Visible spectrophotometry. The results are presented in Table 6. We can clearly see that more solid content is lost after filtration using the first preparation method (*i.e.* direct dissolution) compared to the use of THF as a co-solvent. Hence, this last preparation method looks more promising. Nevertheless, the mass loss is still important (even though there is 30% of rod homopolymer in the sample) and some more preparation work is needed to lower it.

Table 6: Concentrations of the copolymer solutions studied by DLS

<i>Preparation method</i>	<i>Concentration before filtration (g.L<sup>-1</sup>)<sup>a</sup></i>	<i>Concentration after filtration (g.L<sup>-1</sup>)<sup>a</sup></i>	<i>%loss</i>
<i>Direct dissolution of copolymer</i>	1	0.046	95
<i>Co-solvent method</i>	1	0.2	80

<sup>a</sup> measured by NIR-Visible spectrophotometry

We can conclude that the study of the self-assembling behavior of the amphiphilic block copolymer  $P(\text{DTS-DAP})_{10}\text{-}b\text{-}P(\text{eDEGA-co-mOEGA})_{740}$  dispersed in water gives promising

results. The copolymer seems to form micelle-like aggregates in water, exhibiting a hydrophobic core of P(DTS-DAP) and a hydrophilic shell of P(eDEGA-*co*-mOEGA). However, we faced the difficulty to prepare homogeneous dispersed particles in water, probably due to the high hydrophobicity of the hydrophobic conjugated P(DTS-DAP) block leading to some interparticles aggregation, but also due to the presence of residual hydrophobic macroinitiator. Thus, a deeper characterization should be performed such as:

- i. Studying other ways of preparation. The co-solvent method appears to be the most promising, thus we could consider to prepare a solution of the copolymer in THF that will be added dropwise into water or also added in one time;
- ii. Studying the aqueous dispersion also by SLS in order to determine  $R_g$  and  $N_{agg}$ ;
- iii. Performing TEM or CryoTEM in order to determine the morphology of the aggregates formed;
- iv. Trying to purify the copolymer from the residual macroinitiator.

### III. Conclusion

In this chapter, we employed two synthetic methods to yield amphiphilic rod-coil block copolymers with photothermal properties that could self-assemble into micelle-like aggregates in water. Such macromolecules were successfully obtained using the macroinitiator method. The main advantage of this technique is the synthesis and characterization of a well-defined end-functionalized low band-gap polymer prior to producing block copolymer. Another advantage of this methodology is the use of a nitroxide macroinitiator to control the polymerization of the coil block *via* NMP. However, this technique presents a drawback: the difficulty of purification of the residual macroinitiator that has not initiated the polymerization of the coil block. Therefore, we employed the macro end-capper copolymerization method, as in Chapter 3, to produce block copolymer with less purification steps. Unfortunately, this synthetic methodology was unsuccessful: the bromination yield of the coil block, prior to use it in the macro end-capper copolymerization, was too low. Hence, we did not perform this second synthetic method.

UV-Visible and Visible-NIR spectrophotometries were employed to study the optical properties of the materials obtained in this chapter. It was found that the block copolymer did not present the same optical spectra depending on the solvent used due to their amphiphilic properties: the ICT absorption band was shifted toward lower wavelengths while the two absorption bands ( $\pi$ - $\pi$  transition and  $\pi$ -stacking) were red-shifted in water. Moreover, the contribution of each band was quite similar in water whereas the contribution of the ICT band was more important than the contribution of  $\pi$ - $\pi^*$  transition band in chloroform. Hence, the block copolymer presents different conformations in the different solvents.

We studied the photothermal properties of the materials under different parameters and in different solvents to study their influence. Interesting photothermal performances were measured for the rod copolymer and the block copolymers in organic solvents and in water. The materials were found to have stable and reversible photothermal properties with good photothermal conversions. Finally, the nano-objects in water were studied by DLS and we showed that the block copolymers self-assemble in water within micelle-like aggregates formed by a hydrophobic core of P(DTS-DAP) and a hydrophilic shell of P(eDEGA-*co*-mOEGA). We also showed that the preparation method is very important for the formation of soluble particles but a deeper study need to be conducted by using more techniques (SLS, TEM, CryoTEM) in order to characterize the morphology of the obtained objects.

## IV. References

- (1) Rivnay, J.; Owens, R. M.; Malliaras, G. G. The Rise of Organic Bioelectronics. *Chem. Mater.* **2014**, *26* (1), 679–685. <https://doi.org/10.1021/cm4022003>.
- (2) Pacheco-Moreno, C. M.; Schreck, M.; Scaccabarozzi, A. D.; Bourgun, P.; Wantz, G.; Stevens, M. M.; Dautel, O. J.; Stingelin, N. The Importance of Materials Design to Make Ions Flow: Toward Novel Materials Platforms for Bioelectronics Applications. *Advanced Materials* **2017**, *29* (4), 1604446. <https://doi.org/10.1002/adma.201604446>.
- (3) Ohayon, D.; Inal, S. Organic Bioelectronics: From Functional Materials to Next-Generation Devices and Power Sources. *Adv. Mater.* **2020**, 2001439. <https://doi.org/10.1002/adma.202001439>.
- (4) Wu, H.; Gao, W.; Yin, Z. Materials, Devices and Systems of Soft Bioelectronics for Precision Therapy. *Adv. Healthcare Mater.* **2017**, *6* (10), 1700017. <https://doi.org/10.1002/adhm.201700017>.
- (5) Allison, R. R.; Bagnato, V. S.; Sibata, C. H. Future of Oncologic Photodynamic Therapy. *Future Oncology* **2010**, *6* (6), 929–940. <https://doi.org/10.2217/fon.10.51>.
- (6) Deng, K.; Li, C.; Huang, S.; Xing, B.; Jin, D.; Zeng, Q.; Hou, Z.; Lin, J. Recent Progress in Near Infrared Light Triggered Photodynamic Therapy. *Small* **2017**, *13* (44), 1702299. <https://doi.org/10.1002/sml.201702299>.
- (7) Kwiatkowski, S.; Knap, B.; Przystupski, D.; Saczko, J.; Kędzierska, E.; Knap-Czop, K.; Kotlińska, J.; Michel, O.; Kotowski, K.; Kulbacka, J. Photodynamic Therapy – Mechanisms, Photosensitizers and Combinations. *Biomedicine & Pharmacotherapy* **2018**, *106*, 1098–1107. <https://doi.org/10.1016/j.biopha.2018.07.049>.
- (8) Liu, Y.; Bhattarai, P.; Dai, Z.; Chen, X. Photothermal Therapy and Photoacoustic Imaging via Nanotheranostics in Fighting Cancer. *Chem. Soc. Rev.* **2019**, *48* (7), 2053–2108. <https://doi.org/10.1039/C8CS00618K>.
- (9) Jaque, D.; Martínez Maestro, L.; del Rosal, B.; Haro-Gonzalez, P.; Benayas, A.; Plaza, J. L.; Martín Rodríguez, E.; García Solé, J. Nanoparticles for Photothermal Therapies. *Nanoscale* **2014**, *6* (16), 9494–9530. <https://doi.org/10.1039/C4NR00708E>.
- (10) Sheng, W.; He, S.; Seare, W. J.; Almutairi, A. Review of the Progress toward Achieving Heat Confinement—the Holy Grail of Photothermal Therapy. *J. Biomed. Opt.* **2017**, *22* (8), 080901. <https://doi.org/10.1117/1.JBO.22.8.080901>.
- (11) Vancoillie, G.; Frank, D.; Hoogenboom, R. Thermoresponsive Poly(Oligo Ethylene Glycol Acrylates). *Progress in Polymer Science* **2014**, *39* (6), 1074–1095. <https://doi.org/10.1016/j.progpolymsci.2014.02.005>.
- (12) Lutz, J.-F. Polymerization of Oligo(Ethylene Glycol) (Meth)Acrylates: Toward New Generations of Smart Biocompatible Materials. *J. Polym. Sci. A Polym. Chem.* **2008**, *46* (11), 3459–3470. <https://doi.org/10.1002/pola.22706>.
- (13) Lu, S.; Fan, Q.-L.; Chua, S.-J.; Huang, W. Synthesis of Conjugated–Ionic Block Copolymers by Controlled Radical Polymerization. *Macromolecules* **2003**, *36* (2), 304–310. <https://doi.org/10.1021/ma020408b>.
- (14) Mawele Loudy, C.; Allouche, J.; Bousquet, A.; Courrèges, C.; Martinez, H.; Billon, L. Core@Corona Functional Nanoparticle-Driven Rod–Coil Diblock Copolymer Self-Assembly. *Langmuir* **2019**, *35* (51), 16925–16934. <https://doi.org/10.1021/acs.langmuir.9b02744>.
- (15) Lutz, J.-F.; Weichenhan, K.; Akdemir, Ö.; Hoth, A. About the Phase Transitions in Aqueous Solutions of Thermoresponsive Copolymers and Hydrogels Based on 2-(2-Methoxyethoxy)Ethyl Methacrylate and Oligo(Ethylene Glycol) Methacrylate. *Macromolecules* **2007**, *40* (7), 2503–2508. <https://doi.org/10.1021/ma062925q>.

- (16) Hawker, C. J.; Bosman, A. W.; Harth, E. New Polymer Synthesis by Nitroxide Mediated Living Radical Polymerizations. *Chem. Rev.* **2001**, *101* (12), 3661–3688. <https://doi.org/10.1021/cr990119u>.
- (17) Nicolas, J.; Guillaneuf, Y. Living Radical Polymerization: Nitroxide-Mediated Polymerization. In *Encyclopedia of Polymeric Nanomaterials*; Kobayashi, S., Müllen, K., Eds.; Springer Berlin Heidelberg: Berlin, Heidelberg, 2014; pp 1–16. [https://doi.org/10.1007/978-3-642-36199-9\\_191-1](https://doi.org/10.1007/978-3-642-36199-9_191-1).
- (18) Lessard, B.; Tervo, C.; Marić, M. High-Molecular-Weight Poly( *Tert* -Butyl Acrylate) by Nitroxide-Mediated Polymerization: Effect of Chain Transfer to Solvent. *Macromolecular Reaction Engineering* **2009**, *3* (5–6), 245–256. <https://doi.org/10.1002/mren.200900014>.
- (19) Bian, K.; Cunningham, M. F. Nitroxide-Mediated Living Radical Polymerization of 2-Hydroxyethyl Acrylate and the Synthesis of Amphiphilic Block Copolymers. *Macromolecules* **2005**, *38* (3), 695–701. <https://doi.org/10.1021/ma0485383>.
- (20) Guégain, E.; Delplace, V.; Trimaille, T.; Gignes, D.; Siri, D.; Marque, S. R. A.; Guillaneuf, Y.; Nicolas, J. On the Structure–Control Relationship of Amide-Functionalized SG1-Based Alkoxyamines for Nitroxide-Mediated Polymerization and Conjugation. *Polymer Chemistry* **2015**, *6* (31), 5693–5704. <https://doi.org/10.1039/C5PY00283D>.
- (21) Nabifar, A. Investigations of Kinetic Aspects in Nitroxide-Mediated Radical Polymerization of Styrene, University of Waterloo, 2007.
- (22) Otte, T.; Pasch, H.; Macko, T.; Brüll, R.; Stadler, F. J.; Kaschta, J.; Becker, F.; Buback, M. Characterization of Branched Ultrahigh Molar Mass Polymers by Asymmetrical Flow Field-Flow Fractionation and Size Exclusion Chromatography. *Journal of Chromatography A* **2011**, *1218* (27), 4257–4267. <https://doi.org/10.1016/j.chroma.2010.12.072>.
- (23) Otte, T.; Klein, T.; Brüll, R.; Macko, T.; Pasch, H. Study of the Abnormal Late Co-Elution Phenomenon of Low Density Polyethylene in Size Exclusion Chromatography Using High Temperature Size Exclusion Chromatography and High Temperature Asymmetrical Flow Field-Flow Fractionation. *Journal of Chromatography A* **2011**, *1218* (27), 4240–4248. <https://doi.org/10.1016/j.chroma.2011.01.009>.
- (24) Podzimek, S. Importance of MultiAngle Light Scattering in Polyolefin Characterization. *Macromol. Symp.* **2013**, *11*.
- (25) Ma, J.; Peng, J.; Zhai, M. Radiation-Grafted Membranes for Applications in Renewable Energy Technology. In *Radiation Technology for Advanced Materials*; Elsevier, 2019; pp 207–247. <https://doi.org/10.1016/B978-0-12-814017-8.00007-X>.
- (26) Gignes, D.; Moad, G.; Bagryanskaya, E.; Blinco, J.; Marić, M.; Delaittre, G.; Junkers, T.; Guillaneuf, Y.; Harth, E.; Rizzardo, E.; Marque, S. R. A.; Bottle, S.; Fairfull-Smith, K.; Simpson, E.; Komba, T.; Lalevéé, J.; Barner-Kowollik, C.; Nicolas, J.; Guégain, E.; Rayeroux, D.; Bonzi, G.; Maria, S.; Billon, L.; Save, M.; Cunningham, M. F.; Lessard, B.; Lessard, B. *Nitroxide Mediated Polymerization: From Fundamentals to Applications in Materials Science*; Royal Society of Chemistry: Cambridge, 2015. <https://doi.org/10.1039/9781782622635-FP001>.
- (27) Ouhib, F. Elaboration de matériaux dérivés du polythiophène. Application aux cellules photovoltaïques organiques., Université de Pau et des Pays de l'Adour, 2008.
- (28) Venkatachalapathy, C.; Pitchumani, K. Selectivity in Bromination of Alkylbenzenes in the Presence of Montmorillonite Clay. *Tetrahedron* **1997**, *53* (7), 2581–2584. [https://doi.org/10.1016/S0040-4020\(96\)01147-7](https://doi.org/10.1016/S0040-4020(96)01147-7).
- (29) Thirumamagal, B. T. S.; Narayanasamy, S.; Venkatesan, R. Regiospecific Chlorination of Xylenes Using K-10 Montmorillonite Clay. *Synthetic Communications* **2008**, *38* (16), 2820–2825. <https://doi.org/10.1080/00397910801979338>.



- (30) Kumar, B. S.; Dhakshinamoorthy, A.; Pitchumani, K. K10 Montmorillonite Clays as Environmentally Benign Catalysts for Organic Reactions. *Catal. Sci. Technol.* **2014**, *4* (8), 2378–2396. <https://doi.org/10.1039/C4CY00112E>.
- (31) Chochos, C. L.; Drakopoulou, S.; Katsouras, A.; Squeo, B. M.; Sprau, C.; Colsmann, A.; Gregoriou, V. G.; Cando, A.-P.; Allard, S.; Scherf, U.; Gasparini, N.; Kazerouni, N.; Ameri, T.; Brabec, C. J.; Avgeropoulos, A. Beyond Donor-Acceptor (D-A) Approach: Structure-Optoelectronic Properties-Organic Photovoltaic Performance Correlation in New D-A<sub>1</sub>-D-A<sub>2</sub> Low-Bandgap Conjugated Polymers. *Macromolecular Rapid Communications* **2017**, *38* (7), 1600720. <https://doi.org/10.1002/marc.201600720>.
- (32) Roquet, S.; Cravino, A.; Leriche, P.; Alévêque, O.; Frère, P.; Roncali, J. Triphenylamine–Thienylenevinylene Hybrid Systems with Internal Charge Transfer as Donor Materials for Heterojunction Solar Cells. *J. Am. Chem. Soc.* **2006**, *128* (10), 3459–3466. <https://doi.org/10.1021/ja058178e>.
- (33) Osaheni, J. A.; Jenekhe, S. A. Electroactive and Photoactive Rod-Coil Copolymers: Design, Synthesis, and Supramolecular Regulation of Photophysical Properties. *J. Am. Chem. Soc.* **1995**, *117* (28), 7389–7398. <https://doi.org/10.1021/ja00133a012>.
- (34) Fang, Y.-K.; Liu, C.-L.; Li, C.; Lin, C.-J.; Mezzenga, R.; Chen, W.-C. Synthesis, Morphology, and Properties of Poly(3-Hexylthiophene)-Block-Poly(Vinylphenyl Oxadiazole) Donor-Acceptor Rod-Coil Block Copolymers and Their Memory Device Applications. *Adv. Funct. Mater.* **2010**, *20* (18), 3012–3024. <https://doi.org/10.1002/adfm.201000879>.
- (35) Strover, L. T.; McCulloch, B.; Ho, V.; Segalman, R.; Malmström, J.; McGillivray, D. J.; Sejdic, J. T. Tuning the Optoelectronic Properties of P3EHT Block Copolymers by Surface Modification. *International Journal of Nanotechnology* **2017**, *14* (1/2/3/4/5/6), 540. <https://doi.org/10.1504/IJNT.2017.082481>.
- (36) Beaujuge, P. M.; Amb, C. M.; Reynolds, J. R. Spectral Engineering in  $\pi$ -Conjugated Polymers with Intramolecular Donor–Acceptor Interactions. *Acc. Chem. Res.* **2010**, *43* (11), 1396–1407. <https://doi.org/10.1021/ar100043u>.
- (37) Zhu, Y.; Gibbons, K. M.; Kulkarni, A. P.; Jenekhe, S. A. Polyfluorenes Containing Dibenzo[*a,c*]Phenazine Segments: Synthesis and Efficient Blue Electroluminescence from Intramolecular Charge Transfer States. *Macromolecules* **2007**, *40* (4), 804–813. <https://doi.org/10.1021/ma062445z>.
- (38) de Cuendias, A.; Ibarboure, E.; Lecommandoux, S.; Cloutet, E.; Cramail, H. Synthesis and Self-Assembly in Water of Coil-Rod-Coil Amphiphilic Block Copolymers with Central  $\pi$ -Conjugated Sequence. *Journal of Polymer Science Part A: Polymer Chemistry* **2008**, *46* (13), 4602–4616. <https://doi.org/10.1002/pola.22793>.
- (39) Jenekhe, S. A.; Chen, X. L. Supramolecular Photophysics of Self-Assembled Block Copolymers Containing Luminescent Conjugated Polymers. *J. Phys. Chem. B* **2000**, *104* (27), 6332–6335. <https://doi.org/10.1021/jp000896u>.
- (40) Mori, T.; Watanabe, T.; Minagawa, K.; Tanaka, M. Self-Assembly of Oligo(p-Phenylenevinylene)-Block-Poly(Ethylene Oxide) in Polar Media and Solubilization of an Oligo(p-Phenylenevinylene) Homooligomer inside the Assembly. *J. Polym. Sci. A Polym. Chem.* **2005**, *43* (8), 1569–1578. <https://doi.org/10.1002/pola.20631>.
- (41) Chen, S. H.; Su, A. C.; Han, S. R.; Chen, S. A.; Lee, Y. Z. Molecular Aggregation and Luminescence Properties of Bulk Poly(2,5-Di-*n*-Octyloxy-1,4-Phenylenevinylene). *Macromolecules* **2004**, *37* (1), 181–186. <https://doi.org/10.1021/ma035230n>.
- (42) Lespes, A. Synthèse et Caractérisation de Copolymères Diblocs Amphiphiles Thermo-CO<sub>2</sub>- Stimulables, Université de Pau et des Pays de l'Adour et Université de Sherbrooke, 2015.

- (43) Riess, G. Micellization of Block Copolymers. *Progress in Polymer Science* **2003**, 28 (7), 1107–1170. [https://doi.org/10.1016/S0079-6700\(03\)00015-7](https://doi.org/10.1016/S0079-6700(03)00015-7).
- (44) Mai, Y.; Eisenberg, A. Self-Assembly of Block Copolymers. *Chem. Soc. Rev.* **2012**, 41 (18), 5969. <https://doi.org/10.1039/c2cs35115c>.
- (45) Discher, D. E. Polymer Vesicles. *Science* **2002**, 297 (5583), 967–973. <https://doi.org/10.1126/science.1074972>.
- (46) Ferretti, A. M.; Zappia, S.; Scavia, G.; Giovanella, U.; Villafiorita-Monteleone, F.; Destri, S. Surfactant-Free Miniemulsion Approach for Low Band Gap Rod-Coil Block Copolymer Water-Processable Nanoparticle Fabrication: Film Preparation and Morphological Characterization. *Polymer* **2019**, 174, 61–69. <https://doi.org/10.1016/j.polymer.2019.04.055>.
- (47) Patterson, J. P.; Robin, M. P.; Chassenieux, C.; Colombani, O.; O'Reilly, R. K. The Analysis of Solution Self-Assembled Polymeric Nanomaterials. *Chem. Soc. Rev.* **2014**, 43 (8), 2412–2425. <https://doi.org/10.1039/C3CS60454C>.
- (48) Rodriguezhernandez, J.; Checot, F.; Gnanou, Y.; Lecommandoux, S. Toward 'Smart' Nano-Objects by Self-Assembly of Block Copolymers in Solution. *Progress in Polymer Science* **2005**, 30 (7), 691–724. <https://doi.org/10.1016/j.progpolymsci.2005.04.002>.

## General conclusions and outlook

The main goal of this work, which was the chemical design and synthesis of novel materials based on low band-gap polymers absorbing in the near infrared region, was successfully performed. We aimed at incorporating low band-gap polymers into rod-coil block copolymers to broaden their applications from optoelectronic devices to biological applications. Indeed, rod-coil block copolymers exhibit better solubility useful for improving the processing of active layers of solar cells and present self-assembly properties which are particularly interesting for applications in the biomedical field.

In Chapter 1, we presented organic near-infrared materials and their applications, the chemistry design approaches to tune the bandgaps of conjugated polymers, and polycondensation. The essential key to the success of our mission mainly concerned the choice of synthetic strategy to end-functionalize low band-gap polymers in order to broaden the range of their possible applications. This choice was based on the results of the literature review. The grafting methodology, used to anchor low band-gap polymers on surfaces, was also selected according to this literature report. After an attentive study of the synthetic strategies available to synthesize block copolymers involving a low band-gap block, we chose two synthetic routes to employ in this manuscript: the macroinitiator and the macro end-capper copolymerization methods. Therefore, we were able to synthesize novel materials based on low band-gap polymers absorbing the desired wavelength range (650-1000 nm).

Chapter 2 focused on the study of the end-functionalization of a low band-gap polymer and the influence of the stoichiometry of the end-capping molecule on the chain lengths. Triethoxysilane and catechol terminated macromolecules were successfully obtained and grafted onto ZnO nanospheres. The surface morphology of such hybrid materials was anchoring agent dependent. Indeed, cross-linked aggregates of nanoparticles were obtained with silane functionalized polymers while well-dispersed core-shell particles were synthesized with catechol functionalized polymers. The photoluminescence of these patchy particles was studied and showed an electron transfer from polymer to zinc oxide. Finally, hybrid materials were introduced in the active layer of inverted solar cells and photovoltaic performance was found to be really weak. In order to understand these poor efficiencies, it could be interesting to study the photoluminescence properties of the thin films and to measure the charge mobilities of the material.

In Chapter 3, we described the synthesis of rod-coil block copolymers based on an IR-absorbing block and a filmogenic coil block *via* two synthetic methods: the macroinitiator and the macro end-capper copolymerization methods. It appeared that the macroinitiator technique was more efficient than the other one and presented a major advantage: access to the synthesis and characterization of a well-defined end-functionalized low band-gap polymer prior to use it as a macroinitiator in the synthesis of the coil block. However, this method was not efficient to reach short coil blocks and the use of the macro end-capper copolymerization method led us to more homogeneous sizes of the rod and the coil blocks. Yet, this technique produced a mixture of block copolymer and low band-gap polymer. The spectrophotometric study of the materials in solution showed that the introduction of a filmogenic block enhanced the overall solubility of the block copolymer by reducing the  $\pi$ -stacking phenomenon. Same observations were made in solid state. Through DSC experiments, it was found that the rod alternating copolymer and a block copolymer with short coil chains presented liquid crystalline behavior. A detailed structural analysis was conducted by means of GIWAXS and these two materials showed lamellar structure with an edge-on orientation. In order to confirm the liquid crystalline behavior of these materials, it could be interesting to observe their corresponding thin films under a polarized optical microscope. Finally, it could be interesting to use these materials as filmogenic additive in the elaboration of organic infrared photodetectors.

Chapter 4 was directed towards the synthesis of rod-coil block copolymers based on an IR-absorbing hydrophobic block and a hydrophilic biocompatible block *via* the macroinitiator method. This efficient technique led to the creation of short coil blocks, yet it showed a drawback: the difficult purification of the macroinitiator that has not initiated the polymerization of the coil block. The spectrophotometric study of the materials in solution in different solvents showed that the ground-state electronic structures of the block copolymers were affected by the solvent. This result suggested that the block copolymer formed different conformations depending on the choice of the solvent due to its amphiphilic nature. Through DLS experiments, it was found that the block copolymer formed micelles in aqueous solutions. Photothermal properties of the block copolymers were assessed under different parameters and in different solvents and interesting photothermal performances were measured. In the future, it could be interesting to study the impact of the coil shell on the light intensity absorbed by the core, and thus on photothermal properties of the material. In order to determine the exact morphology of the self-assembled the block copolymers, more

investigations are needed especially *via* static light scattering and transmission electron microscopy.

In this PhD work, novel materials as block copolymers based on low band-gap block absorbing in near infrared were obtained. This research work showed the potential of these low band-gap polymers concerning their synthesis, grafting onto inorganic surfaces, and use in rod-coil block copolymers and opened broad prospects for the future. Yet, synthetic efforts must be made in order to better control the polymerization of the coil block in the macroinitiator method and to reduce the amount of residual homopolymer in the final product to avoid a last purification step. It could be interesting to replace the MAMA-SG1 initiator by the TIPNO initiator (2,2,5-trimethyl-4-phenyl-3-azahexane-3-nitroxide) at the chain ends of the rod alternating copolymer in order to improve the polymerization of the coil block. In addition, the monomer of the coil block could be changed to vary the different possible applications.

## Conclusions générales et perspectives

Le but principal de ce travail, qui a consisté en la conception chimique et la synthèse de nouveaux matériaux à base de polymères à faible bande interdite absorbant dans la région du proche infrarouge, a été atteint avec succès. Nous visions à intégrer des polymères à faible bande interdite dans des copolymères à blocs rigide-flexible pour étendre leurs applications allant des dispositifs optoélectroniques aux applications biologiques. En effet, les copolymères à blocs rigide-flexible présentent une meilleure solubilité utile pour améliorer la mise en œuvre des couches actives des cellules solaire et démontrent des propriétés d'auto-assemblage particulièrement intéressantes pour des applications dans le domaine biomédical.

Dans le Chapitre 1, nous avons présenté quelques généralités sur les matériaux organiques absorbant dans l'infrarouge et leurs applications, sur les différentes approches chimiques pour modifier la bande interdite des polymères conjugués et sur la polycondensation. La clé essentielle du succès de notre mission est le choix d'une stratégie de synthèse pour fonctionnaliser les polymères à faible bande interdite en bout de chaînes afin d'étendre la gamme de leurs applications. Ce choix s'est appuyé sur les résultats de la littérature. La méthodologie de greffage, utilisée pour greffer des polymères à faible bande interdite sur des surfaces, a aussi été sélectionnée selon la littérature. Après une étude attentive des stratégies de synthèse accessibles pour obtenir des copolymères à blocs incluant un bloc à faible bande interdite, nous avons choisi deux voies de synthèses à employer dans ce manuscrit : les méthodes du macroamorceur et de copolymérisation avec une macro molécule fonctionnalisante. Dès lors, nous avons été capables de synthétiser de nouveaux matériaux à base de polymères à faible bande interdite absorbant dans la gamme de longueurs d'onde souhaitée (650-1000 nm).

Le Chapitre 2 s'est concentré sur l'étude de la fonctionnalisation en bout de chaînes d'un polymère à faible bande interdite et l'influence de la stœchiométrie de la molécule fonctionnalisante sur la longueur des chaînes. Des macromolécules terminées par un triéthoxysilane ou un catéchol ont été obtenues avec succès et greffées sur des nanosphères de ZnO. La morphologie de la surface de ces matériaux hybrides était dépendante de l'agent de greffage. En effet, des agrégats de nanoparticules réticulées ont été obtenus avec les polymères fonctionnalisés par le silane tandis que des particules cœur-écorce bien dispersées ont été synthétisées avec les polymères fonctionnalisés par le catéchol. La photoluminescence de ces particules éparses a été étudiée et a montré un transfert d'électrons du polymère vers

l'oxyde de zinc. Enfin, les matériaux hybrides ont été introduits dans la couche active de cellules solaires inversées et de faibles performances photovoltaïques ont été mesurées. Afin de comprendre ces rendements bas, il serait intéressant d'étudier les propriétés de photoluminescence des films minces et de mesurer les mobilités de charge du matériau.

Dans le Chapitre 3, nous avons décrit la synthèse de copolymères à blocs dit rigide-flexible composés d'un bloc absorbant dans l'infrarouge et d'un bloc flexible et filmogène *via* deux méthodes de synthèse : les méthodes du macroamorceur et de copolymérisation avec une macro molécule fonctionnalisante. Il est apparu que la technique du macroamorceur était plus efficace que l'autre technique et qu'elle présentait un avantage majeur : l'accès à la synthèse et la caractérisation d'un polymère à faible bande interdite bien défini et fonctionnalisé en bout de chaînes avant de l'utiliser comme macroamorceur dans la polymérisation du bloc flexible. Cependant, cette méthode n'a pas été efficace pour atteindre des blocs flexibles courts et l'utilisation de la copolymérisation avec une macro molécule fonctionnalisante a mené à des tailles homogènes des blocs rigides et flexibles. Malgré cela, cette technique a produit un mélange de copolymère à blocs et de polymère à faible bande interdite. L'étude de la spectrophotométrie des matériaux en solution a montré que l'introduction d'un bloc filmogène améliore la solubilité générale du copolymère à blocs en réduisant le phénomène de  $\pi$ -stacking. Les mêmes observations ont été faites à l'état solide. Au travers d'expériences DSC, il a été trouvé que le copolymère rigide alterné et le copolymère à blocs ayant des chaînes courtes de bloc flexible présentaient un comportement liquide cristallin. Une analyse structurale détaillée a été menée grâce au GIWAXS et ces deux matériaux ont montré une structure lamellaire avec une orientation edge-on. Afin de confirmer le caractère liquide cristallin de ces matériaux, il serait intéressant d'observer leurs films en couches minces sous un microscope optique polarisé. Enfin, il serait intéressant d'utiliser ces matériaux en tant qu'additif filmogène dans la conception de photodétecteur infrarouge.

Le Chapitre 4 s'est concentré sur la synthèse de copolymères à blocs amphiphiles dit rigide-flexible composés d'un bloc hydrophobe absorbant dans l'infrarouge et d'un bloc hydrophile biocompatible *via* la méthode du macroamorceur. Cette technique efficace a mené à l'obtention de blocs flexibles courts bien qu'elle ait montré un inconvénient : la purification complexe du macroamorceur n'ayant pas amorcé la polymérisation du bloc flexible. L'étude spectrophotométrique des matériaux en solution dans différents solvants a montré que les structures électroniques des copolymères à blocs à l'état fondamental étaient affectées par le solvant. Ce résultat suggère que le copolymère à blocs forme différentes conformations selon

le choix du solvant à cause de sa nature amphiphile. Au travers d'expériences DLS, il a été trouvé que le copolymère à blocs forme des micelles en solutions aqueuses. Les propriétés photothermiques des copolymères à blocs ont été évaluées sous différents paramètres et dans différents solvants et d'intéressantes performances ont été mesurées. Dans le futur, il serait intéressant d'étudier l'impact de la couronne flexible sur l'intensité de la lumière effectivement absorbée par le cœur, et donc sur les propriétés photothermiques du matériau. Afin de déterminer la morphologie exacte des copolymères à blocs auto-assemblés, des études approfondies sont nécessaires notamment *via* diffusion statique de la lumière et microscopie électronique à transmission.

Dans ce manuscrit, il apparait que de nouveaux matériaux à base de polymères à faible bande interdite sont accessibles. Ce travail de recherche a montré le potentiel de ces polymères à faible bande interdite concernant leur synthèse, leur greffage sur des surfaces inorganiques et sur leur utilisation dans des copolymères à blocs rigide-flexible et a ouvert de larges perspectives d'avenir. Cependant, des efforts de synthèse doivent être faits afin de mieux contrôler la polymérisation radicalaire dans la méthode du macroamorceur et de réduire la quantité d'homopolymère résiduel pour éviter une étape terminale de purification. Il serait intéressant de remplacer l'amorceur MAMA-SG1 par l'amorceur TIPNO (2,2,5-triméthyl-4-phényl-3-azahexane-3-nitroxyde) en bout de chaînes du copolymère rigide alterné afin d'améliorer la polymérisation du bloc flexible. De plus, le monomère du bloc flexible pourrait être changé pour varier les différentes applications possibles.



# Chapter 5: Experimental Part

## 1. Materials

All reactions were performed under nitrogen using flame-dried glassware and conventional Schlenk tube techniques. Syringes used to transfer reagents or solvents were purged with nitrogen prior use. Chemicals and reagents were used as received from Aldrich (France), ABCR (Germany), and TCI Europe (Belgium) and stored in the glove box. Solvents (Aldrich, France) were used as received. 4,4'-bis(2-ethylhexyl)-5,5'-bis(trimethyltin)-dithieno[3,2-b:2',3'-d]silole was purchased from 1-Material and used without further purification. MAMA-SG1 (Bloc Builder ®) was kindly provided by Arkema (France).

## 2. Instrumentation

$^1\text{H}$ ,  $^{31}\text{P}$ , *DOSY* and *COSY* Nuclear Magnetic Resonance (NMR) spectra were recorded using a Bruker 400 MHz instrument in deuterated solvents at different temperatures (25°C, 60°C, and 80°C).

*Size Exclusion Chromatography (SEC)* was performed using a bank of 4 columns (Shodex KF801, 802.5, 804 and 806) each 300 mm x 8 mm at 30 °C with THF eluent at a flow rate of 1.0 ml.min<sup>-1</sup> controlled by a Malvern pump (Viskotech, VE1122) and connected to Malvern VE3580 refractive index (RI) and Malvern VE3210 UV-Visible detectors. Conventional calibration was performed against polystyrene standards.

*UV-visible absorption* spectra were recorded at room temperature on a Shimadzu UV-2450PC spectrophotometer in steps of 1 nm in the range 300 – 900 nm using a 1 cm quartz optical cell (Helma).

*Visible-NIR absorption* spectra were recorded at room temperature on a double beam Cary 5000 spectrophotometer in steps of 1 nm in the range 300 – 1600 nm using a 1 cm quartz optical cell (Helma).

*Thermal gravimetric analysis (TGA)* was performed on a TA-Q50, TA Instruments under nitrogen with a weighing precision of  $\pm 0.01\%$ , a sensitivity of 0.1  $\mu\text{g}$ , isothermal temperature accuracy of  $\pm 1^\circ\text{C}$ , isothermal temperature precision of  $\pm 0.1^\circ\text{C}$  and a controlled heating rate at 10°C/min. Aluminium pan were used. The typical sample weight was  $\approx 3$  mg and the typical procedure included a heating ramp of 10°C/min up to 600°C.

*Differential scanning calorimetry (DSC)* was performed with a Mettler Toledo DSC 3+. Heating and cooling runs at various speed were carried out under a constant flow of nitrogen. Prior to these measurements, some samples were drop-casted at room temperature and 85°C from chlorobenzene solutions (10 g/L). Thermograms were analyzed with the STARe System Software.

*Emission Spectroscopy (Photoluminescence)*: Corrected steady-state emission and excitation spectra were recorded at 2 nm resolution using a photon counting Edinburgh FLS920 fluorescence spectrometer with a xenon lamp. Concentrations in CHCl<sub>3</sub> were adjusted to an absorbance around 0.1 at 670 nm (excitation wavelength) in a 1 cm quartz fluorescence cell (Hellma).

*Electron Microscopy (TEM)* images were obtained with a TEM 1400 JEOL at 120 kV, HR TEM images were obtained with a JEOL JEM 2200FS FEG HR 200 kV.

*Wire-bar coating* K101 Control Coater System was used to deposit thin films of chlorobenzene solutions (~ 30 µL) containing materials of interest (10 g/L) onto ~ 1cm x 2cm silicon substrates previously cleaned with deionized water, acetone, and isopropanol and treated 10 min with ozone. The depositions were made onto preheated silicon substrates at different temperatures: room temperature, 35°C, 60°C, and 85°C.

*Profilometer* was employed to measure the thickness of the films on a Dektak XT Bruker Profilometer with 64-bit parallel processing, true HD color camera and single-arch design.

*Grazing incidence wide-angle X-ray scattering (GIWAXS)* experiments were conducted at the beamline at ALBA Synchrotron Radiation Facility (Spain). Samples were illuminated for 5 s with an X-ray beam of 12.4 keV at incidence angles between 0.5° and 1°. Scattering patterns were acquired using a Rayonix® LX255-HS detector.

*Photothermal performances* were assessed by irradiating solutions with different concentrations using a NIR-I laser ( $\lambda_{\text{IR}} = 808 \text{ nm}$ ) with a power density of 0.70 W.cm<sup>-2</sup>. The solution temperature was measured with a probe at 10 s intervals for a total of 15min.

Dynamic Light Scattering (DLS) experiments were carried out at an angle of  $173^\circ$  on a Nano-ZS Model ZEN3600 Zetasizer (Malvern, UK). A 4.0 mW He–Ne laser was used, operating at a wavelength of 633 nm.

### 3. Chapter 2: Experimental Part

#### a. Synthesis of 4,7-dibromo-2,1,3-benzothiadiazole monomer (BT)

The synthesis was performed following a procedure reported in the literature by DaSilveira Neto *et al.*<sup>1</sup> and Medlej *et al.*<sup>2</sup>

<sup>1</sup>H NMR BT ( $\delta$  ppm, CDCl<sub>3</sub>): 7.67 (s, 2H)

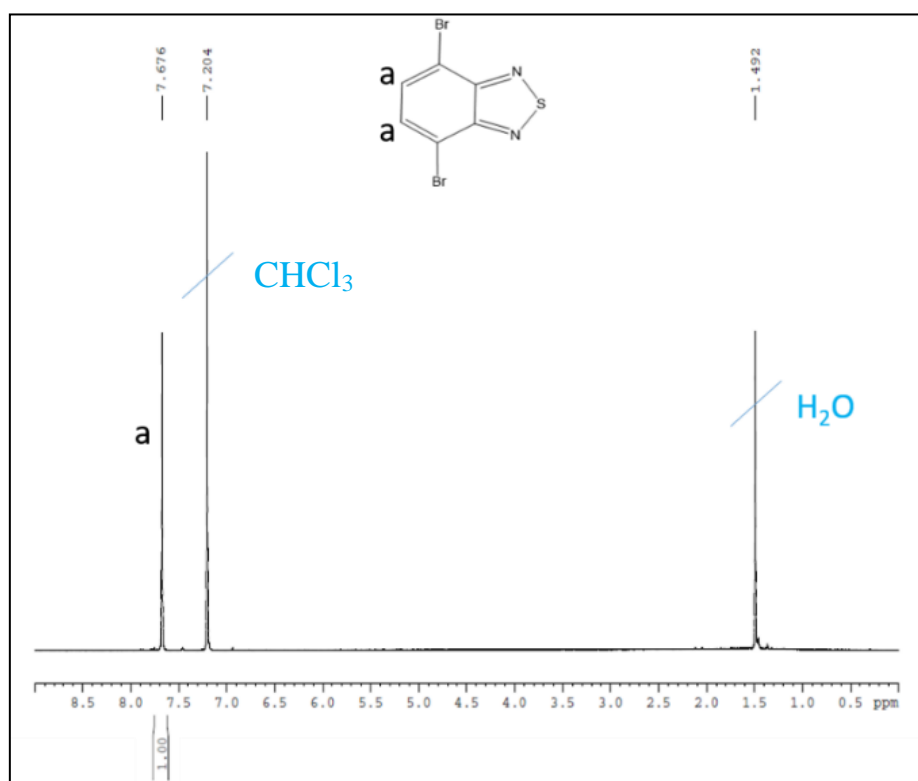
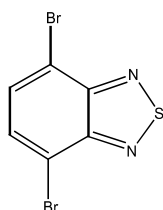
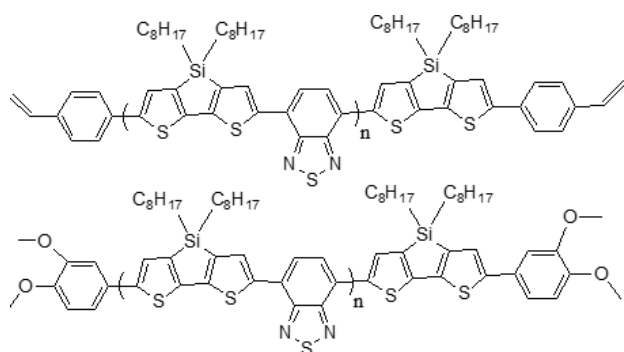


Figure 1: <sup>1</sup>H NMR spectrum of 4,7-dibromo-2,1,3-benzothiadiazole (400 MHz, CDCl<sub>3</sub>)

<sup>1</sup> B.A. DaSilveira Neto, A.S. Lopes, M. Wüst, V.E.U. Costa, G. Ebeling, J. Dupont, Reductive sulfur extrusion reaction of 2,1,3-benzothiadiazole compounds: a new methodology using NaBH<sub>4</sub>/CoCl<sub>2</sub>.6H<sub>2</sub>O<sub>(cat)</sub> as the reducing system, Tetrahedron Letters. 46 (2005) <https://doi.org/10.1016/j.tetlet.2005.08.017>

<sup>2</sup> H. Medlej, H. Awada, M. Abbas, G. Wantz, A. Bousquet, E. Grelet, K. Hariri, T. Hamieh, R.C. Hiorns, C. Dagron-Lartigau, Effect of spacer insertion in a commonly used dithienosilole/benzothiadiazole-based low band gap copolymer for polymer solar cells, European Polymer Journal. 49 (2013) <https://doi.org/10.1016/j.eurpolymj.2013.09.025>

## b. General Synthesis of End-Functional Conjugated Polymer P(DTS-BT)-End-cap



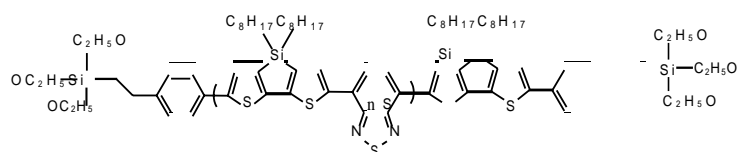
4,4'-bis(2-ethylhexyl)-5,5'-bis(trimethylsilyl)-dithieno[3,2-b:2',3'-d]silole monomer DTS (1 eq.), 4,7-dibromo-2,1,3-benzothiadiazole monomer BT (0.96 eq.), end-capping unit either 4-bromostyrene or 4-bromoveratrole (0.08 eq.),

tris(dibenzylideneacetone)dipalladium(0) (Pd<sub>2</sub>dba) (0.02 eq.), and tri(o-tolyl)phosphine (P(o-tol)<sub>3</sub>) (0.1 eq.) were accurately weighed into a 10 mm Biotage microwave vial equipped with a PTFE magnetic stirrer. The reaction vial was brought into a nitrogen-filled glovebox and dry chlorobenzene (2.0 ml) was added. Afterwards, the vial was securely sealed with a septum and removed from the glovebox. The vial was placed into an oil bath and stirred for 6 hours at 140 °C. After cooling, the polymer was precipitated in methanol (200 ml), filtered in a Soxhlet thimble, washed by Soxhlet extraction using ethanol and recovered with chloroform. The polymer was dried under *vacuum* to afford a dark blue solid, with a yield of 66%.

<sup>1</sup>H NMR P(DTS-BT)-BrS (δ ppm, CDCl<sub>3</sub>): 8.26-7.76 (m, 28H), 6.73 (q, 1H), 5.78 (d, 1H), 5.26 (d, 1H), 1.46-0.7 (m, 238H)

<sup>1</sup>H NMR P(DTS-BT)-BrV (δ ppm, CDCl<sub>3</sub>): 8.26-7.76 (m, 28H), 4.0-3.8 (m, 6H), 1.46-0.7 (m, 238H)

## c. General Synthesis of triethoxysilane-terminated P(DTS-BT)-Si

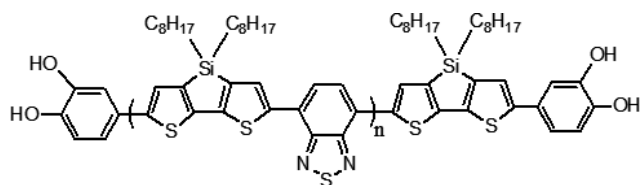


In flame-dried 50 ml flask, 40 mg of P(DTS-BT)-BrS (2 eq.) was mixed with 2.6 mg of H<sub>2</sub>PtCl<sub>6</sub>

(catalyst, 1 eq) and 15 ml of CHCl<sub>3</sub>. The solution mixture was degassed for 15 min to avoid oxygen. Under stirring, 0.2 ml (0.170 g, 200 eq.) of triethoxysilane was added drop wise. The mixture was stirred for 30 min at room temperature before the temperature was raised to 55 °C for 5h. Finally, the polymer was precipitated in dry ethanol, filtered under nitrogen and stored in the glove box to avoid hydrolysis/condensation of the polymer end-chain. Yield = 88 %.

<sup>1</sup>H NMR (ppm, CDCl<sub>3</sub>): 8.26-7.26 (m, 4H), 3.86 (s, 6H), 2.67 (t, 1H), 1.46-0.7 (m, 249H)

d. General Synthesis of the catechol-terminated P(DTS-BT)-Cat



In a flame-dried 250 ml flask, 100 mg of P(DTS-BT)-BrV (1 eq.) was mixed with 75 ml of dried  $\text{CHCl}_3$ . The flask was placed into an ethanol/nitrogen bath at  $-40\text{ }^\circ\text{C}$  during 15 min to allow a good

solubilization. Under stirring, 0.2 ml (0.313 g, 50 eq.) of boron tribromide was added drop wise. The mixture was allowed to go back to room temperature and stirred for 24h at room temperature. Then, the flask was placed into an ice bath at  $0\text{ }^\circ\text{C}$  and 12.5 ml of distilled water were added to the mixture. The mixture was stirred for 12h at room temperature under vigorous stirring. The solution was concentrated under reduced pressure and the polymer was precipitated in MeOH (400 ml), filtered and stored in the glove-box to avoid hydrolysis/condensation of the polymer end-chain. Yield = 80 %.

e. ZnO NPs synthesis

The ZnO nanoparticles synthesis method was adapted from Seow *et al.*<sup>3</sup> Briefly, zinc acetate dihydrate (0.87g, 3.35 mmol) was first dissolved in methanol (31.25 ml) while a methanolic potassium hydroxide solution was prepared by dissolving potassium hydroxide (0.37 g, 6.59 mmol) in 16.25 ml of methanol. This potassium hydroxide solution was added dropwise under vigorous stirring into the zinc acetate solution, pre-heated to  $60\text{ }^\circ\text{C}$ . After 1.5h, the NPs started to precipitate leading to a turbid solution, which was maintained as such for 2 more hours. The heater and stirrer were then removed and the solution was allowed to stand at room temperature for another 2h. The ZnO nanoparticles settled at the bottom; the supernatant was removed and the precipitate was collected by centrifugation at 9000 rpm with methanol for 20 min. and washed 3 times with methanol. The precipitate was then dispersed in 12.5 ml of methanol and 2.5 ml of chloroform.

<sup>3</sup>Z.L.S. Seow, A.S.W. Wong, V. Thavasi, R. Jose, S. Ramakrishna, G.W. Ho, Controlled synthesis and application of ZnO nanoparticles, nanorods and nanospheres in dye-sensitized solar cells, *Nanotechnology*. 20 (2009) 045604. <https://doi.org/10.1088/0957-4484/20/4/045604>.

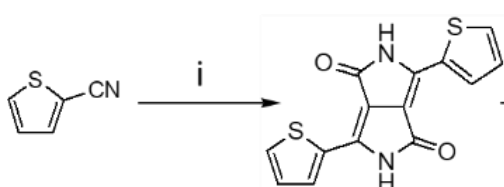
f. General procedure for grafting P(DTS-BT) onto ZnO NPs

ZnO NPs were dispersed in  $\text{CHCl}_3$  ( $2 \text{ mg.ml}^{-1}$ , 12 ml) by ultrasonication for 1h. 2 ml solution of polymer P(DTS-BT) terminated with triethoxysilane or catechol ( $17.7 \text{ mg.ml}^{-1}$ ) in  $\text{CHCl}_3$  was added to the mixture. From the ZnO NPs specific surface area (SSA), we calculated that P(DTS-BT) was introduced at  $1 \text{ chain/nm}^2$  of ZnO surface in order to not saturate the surface. The reaction then proceeded at  $60 \text{ }^\circ\text{C}$  for 10h under inert atmosphere. The medium was cooled to room temperature and ZnO@P(DTS-BT) was purified by centrifugation (10,000 rpm, 10 min,  $15 \text{ }^\circ\text{C}$ ) with removal of the supernatant containing excess of ungrafted polymer chains. The purification was repeated several times until the UV-visible spectra of the  $\text{CHCl}_3$  supernatant became featureless (no P(DTS-BT) absorption around 670 nm). The precipitated particles were collected, dried and stored under nitrogen. A change in the color of the ZnO NPs was clearly observable from white to blue after grafting of P(DTS-BT) (dry state).

#### 4. Chapter 3: Experimental Part

a. Synthesis of 2,5-diazapentalene monomer (DAP)

i. Synthesis of 3,6-dithiophene-2-yl-2,5-dihydropyrrolo[3,4-*c*]pyrrole-1,4-dione monomer (DPP)

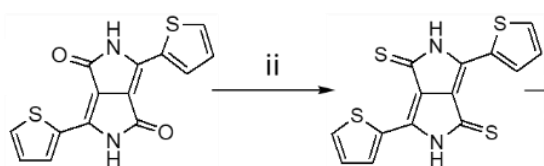


In a double neck round bottom flask with a magnetic stirring bar, sodium (3.5 g, 0.15 mol) was added to 60 ml of *t*-amyl alcohol with a small amount of iron(III) chloride anhydrous (50 mg, 0.3 mmol). The

mixture was stirred under inert atmosphere ( $\text{N}_2$ ) for 1 h at  $110 \text{ }^\circ\text{C}$ , until complete sodium dissolution. The mixture was then cooled to  $80 \text{ }^\circ\text{C}$  and 2-thiophene-carbonitrile (9.5 g, 0.87 mol) was added in one shot; then a solution of di-isopropylsuccinate (7.092 g, 0.35 mol) in *t*-amyl alcohol was added drop-wise using a 100 ml dropping funnel. When the addition was completed, the reaction was left at  $85 \text{ }^\circ\text{C}$  for 5 h. The brown-red mixture was cooled at room temperature and filtered on a Buchner funnel. The brown-red solid filtrate was washed several times with warm deionized water and methanol. The final product (8.9 g, 85% yield) was dried under vacuum until complete solvent removal.

$^1\text{H NMR}$  (ppm,  $d_6$ -DMSO): 11.24 (s, 2H), 8.21 (d,  $J = 4.0 \text{ Hz}$ , 2H), 7.96 (d,  $J = 4.0 \text{ Hz}$ , 2H), 7.31 (dd,  $J_1 = 4.0 \text{ Hz}$ ,  $J_2 = 4.0 \text{ Hz}$ , 2H)

ii. Synthesis of 3,6-di(thiophen-2-yl)-2,5-dihydropyrrolo[3,4-*c*]pyrrole-1,4-dithione (DTPP)

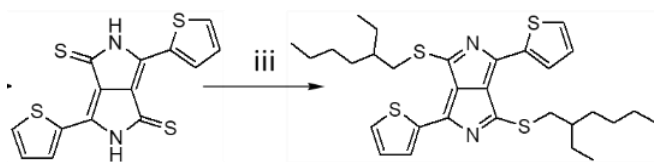


In a one necked round bottom flask with a magnetic stirring bar, DPP (3.00 g, 10.0 mmol), previously synthesized and Lawesson's reagent (8.10 g, 20.0 mmol) were added to 100 ml of dry

chlorobenzene. The mixture was bubbled with nitrogen for 15 min at room temperature and then stirred at 135°C for 8 hours. The color of the solution turned red to dark green in 6 hours' time. The solution mixture was precipitated in 400 ml methanol and filtered. The precipitate was washed with methanol and Soxhlet extraction was done using ethanol to remove any phosphate by-products. The desired thiolactam intermediate was obtained as a dark green solid and stored under dark and nitrogen (3.1 g, 93% yield).

<sup>1</sup>H NMR (ppm, *d*<sub>6</sub>-DMSO): 12.82 (s, 2H), 9.00 (dd, *J* = 3.9 Hz, 1.2 Hz, 2H), 8.06 (dd, *J* = 4.9 Hz, 1.1 Hz, 2H), 7.39 (dd, *J* = 5.0 Hz, 3.9 Hz, 2H)

iii. Synthesis of 1,4-bis((2-ethylhexyl)thio)-3,6-di(thiophen-2-yl)pyrrolo[3,4-*c*]pyrrole



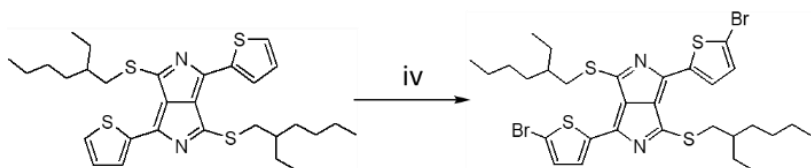
In a one neck roud bottom flask, the mixture of DTPP (2 g, 6.02 mmol), previously synthesized, 2-ethylhexyl bromide (13 mmol), anhydrous

powdered K<sub>2</sub>CO<sub>3</sub> (2.8 g, 20 mmol), and acetone (75 ml) was purged with nitrogen for 15 minutes. The reaction was then stirred at reflux overnight. The reaction solvent was removed by vacuum and the crude compound was extracted with chloroform. The solvent was concentrated and the product was purified by Flash Chromatography (silica gel, cyclohexane-dichloromethane, 1:1, v/v). A dark green flaky solid was obtained (2.1 g, 63% yield).

<sup>1</sup>H-NMR (ppm, CDCl<sub>3</sub>): 8.12 (d, *J* = 3.9 Hz, 2H), 7.64 (d, *J* = 5.0 Hz, 2H), 7.33-7.24 (m, 2H), 3.65-6.45 (m, 4H), 1.96-1.74 (m, 2H), 1.66-1.25 (m, 16H), 1.11-0.81 (m, 12H)



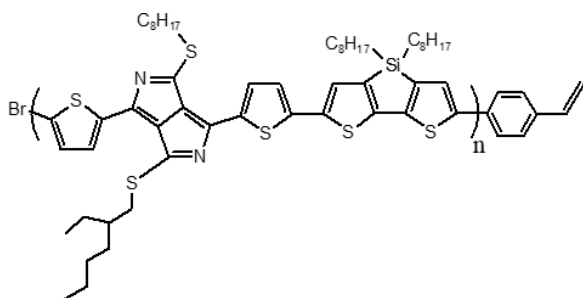
iv. Synthesis of 1,4-bis(5-bromothiophen-2-yl)-3,6-bis((2-ethylhexyl)thio)pyrrolo [3,4-*c*]pyrrole (DAP)



The previous compound (1.5 g, 2.69 mmol) was dissolved in dry chloroform in a round bottom flask and flushed with nitrogen for 15 minutes. NBS (1.07 g, 6 mmol) was added portion at a time and the solution was stirred at room temperature in the dark for 3 hours. The chloroform was removed and the crude product was precipitated in methanol and filtered to give a dark green solid (1.05 g, 54% yield).

$^1\text{H NMR}$  (ppm,  $\text{CDCl}_3$ ): 7.82 (d,  $J = 4.1$  Hz, 2H), 7.23 (d,  $J = 4.1$  Hz, 2H), 3.60-3.41 (m, 4H), 1.89-1.73 (m, 2H), 1.61-1.27 (m, 16H), 1.06-0.87 (m, 12H)

b. General synthesis of styrene end-functional conjugated polymer P(DTS-DAP)-styrene

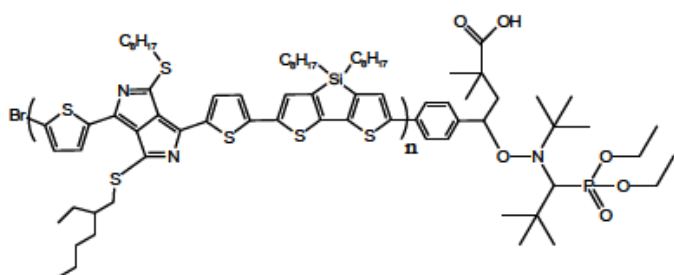


4,4'-bis(2-ethylhexyl)-5,5'-bis(trimethyltin)-dithieno[3,2-*b*:2',3'-*d*]silole monomer DTS (83 mg, 1 eq), 1,4-bis(5-bromothiophen-2-yl)-3,6-bis((2-ethylhexyl)thio)pyrrolo[3,4-*c*]pyrrole monomer DAP (76.5 mg, 0.96 eq), end-capping unit 4-bromostyrene (0.08 eq),

$\text{Pd}_2\text{dba}$  (2.04 mg, 0.02 eq), and  $\text{P}(o\text{-tol})_3$  (3.39 mg, 0.1 eq) were accurately weighed into a 10 ml Biotage microwave vial equipped with a PTFE magnetic stirrer. The reaction vial was taken into a nitrogen-filled glovebox and dry toluene (3.0 ml) was added, the vial was securely sealed with a septum and removed from the glovebox. The vial was placed into an oil bath and stirred for 20 minutes at 125 °C. After cooling, the polymer was precipitated in ethanol (200 ml), filtered in a Soxhlet thimble, washed by Soxhlet extractions using ethanol, THF, and chloroform. The THF fraction was dried under vacuum to afford 94 mg (yield 92%) of a dark green solid.

$^1\text{H NMR}$  (ppm,  $\text{CDCl}_3$ ): 8.40-7.39 (m, 30H), 6.56 (q, 1H), 5.60 (d, 1H), 5.11 (d, 1H), 3.93-3.26 (m, 20H), 2.04-0.67 (m, 340H)

c. General synthesis of macroinitiator P(DTS-DAP)-MAMA-SG1

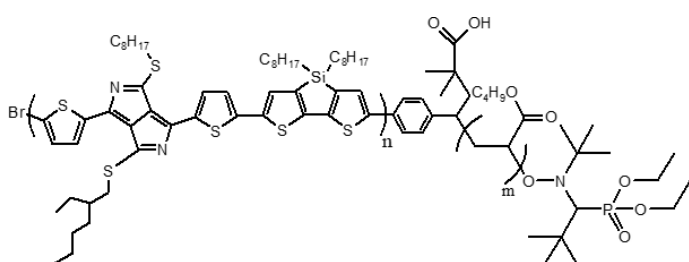


In a flame-dried 25 ml round bottom flask, 100 mg of P(DTS-DAP)-styrene (1 eq) was dissolved into 5 ml of dry toluene. The mixture was stirred and sonicated during 30 min prior to add a solution of 25 mg of

BlocBuilder<sup>®</sup> MAMA-SG1 (2.5 eq) dissolved in 5 ml of dry toluene. The full mixture was sonicated 10 min and degased 20 min under nitrogen to remove oxygen. The flask was placed into an oil bath and stirred for 5 h at 100°C. After cooling, the macroinitiator was precipitated in cold ethanol (200 ml), filtered and washed by ethanol. The final product was dried under vacuum to afford 61 mg (yield 61%) of a dark brown solid.

<sup>1</sup>H NMR (ppm, CDCl<sub>3</sub>): 8.33-7.37 (m, 30H), 6.56 (q, 1H), 5.60 (d, 1H), 5.11 (d, 1H), 3.73-3.48 (m, 20H), 3.35-3.15 (m, 4H), 2.04-0.67 (m, 340H)

d. General synthesis of block copolymer P(DTS-DAP)-*b*-P(*n*BA)



In a one-neck 25 ml round-bottom flask, 9.3 mg of macroinitiator P(DTS-DAP)-MAMA-SG1 (1 eq) was dissolved into 1.9 ml of dry toluene. The mixture was sonicated 1h and stirred overnight to dissolve

completely the macroinitiator. 1.85 ml of monomer *n*-butyl acrylate (*n*BA ; 6600 eq) was added dropwise into the flask. The mixture was degased 20 min under nitrogen into an ice/water bath to avoid monomer evaporation. The flask was placed into an oil bath previously heated at 130°C and the mixture was stirred for different times depending on the size block targeted. Samples were withdrawn at predefined times for determination of the conversion through <sup>1</sup>H NMR analysis. To end the polymerization, the flask was placed into an ice/water bath and the mixture was poured into a glass Petri dish. After complete evaporation of monomers and solvent, the block copolymer was dissolved into a minimum amount of CHCl<sub>3</sub> and transferred in a small glass vial. The final product was dried under vacuum to afford 113 mg (yield 80%) of a dark green sticky putty.

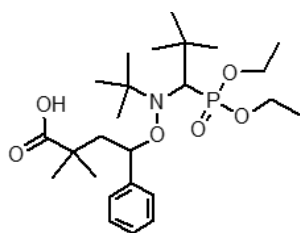
<sup>1</sup>H NMR (ppm, CDCl<sub>3</sub>): 8.25-6.69 (m, 30H), 4.22-3.86 (m, 220H), 3.84-3.30 (m, 20H), 2.49-2.19 (m, 110H)

The conversion  $p$  was calculated from the following equation:

$$p = \frac{I_{4.0-4.5 \text{ ppm}} - 2 \times I_{5.8 \text{ ppm}}}{I_{4.0-4.50 \text{ ppm}}} \times 100$$

with the integral between 4.0 and 4.5 ppm  $I_{4.0-4.5 \text{ ppm}}$  corresponding to one monomer peak and one polymer peak and the integral at 5.8 ppm  $I_{5.8 \text{ ppm}}$  corresponding to one monomer peak.

e. General intermolecular radical addition (IRA) of MAMA-SG1 onto styrene



The monoadduct was prepared according to previous work reported by Dufils *et al.*<sup>4</sup> A solution of the alkoxyamine MAMA-SG1 (3g, 7.86 mmol, 1M) and styrene (7.86 mmol, 1M) in *tert*-butanol was introduced in a round-bottom flask, deoxygenated by nitrogen bubbling and heated at 100°C for 7h under stirring. The reaction mixture was then concentrated under reduced pressure and

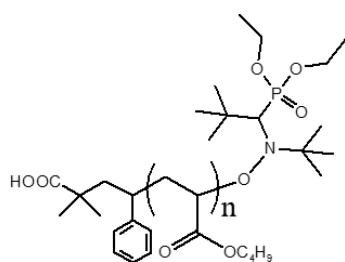
precipitated in pentane. To enhance the precipitation, the solution was stored in the fridge during one week. The solid was separated from the liquid by centrifugation at 7,500 rpm during 30 min at 0°C. The solid was dried to obtain a white sticky powder.

<sup>1</sup>H NMR (ppm, CDCl<sub>3</sub>): 7.31-7.14 (m, 5H), 4.88-4.79 (dd, 1H), 4.42-3.88 (m, 4H), 3.36 (d, 1H), 2.91 (dd, 1H), 2.28-2.16 (q, 1H), 1.32 (m, 6H), 1.24 (s, 9H), 1.05 (d, 6H), 0.78 (s, 9H)

<sup>31</sup>P NMR with <sup>1</sup>H coupling (ppm, CDCl<sub>3</sub>): 24.9 (m, <sup>1</sup>J<sub>PH</sub> = 27 Hz, <sup>3</sup>J<sub>PH</sub> = 7.4 Hz, 1P)

<sup>31</sup>P NMR without <sup>1</sup>H coupling (ppm, CDCl<sub>3</sub>): 24.9 (s, 1P)

f. General nitroxide-mediated polymerization of homopolymer P(*n*BA)



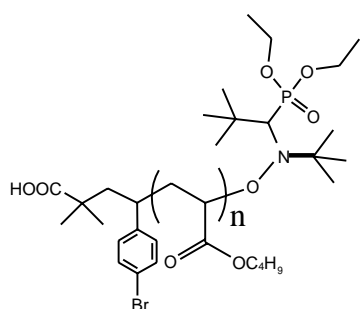
In a one-neck 10 ml round-bottom flask, 55 mg of alkoxyamine MAMA-SG1-styrene (1 eq) was dissolved in 1.8 ml of dry toluene. 1.218 ml of monomer *n*-butyl acrylate (*n*BA; 75 eq) was added dropwise into the flask. The mixture was degassed 20 min under nitrogen into an ice/water bath to avoid monomer evaporation. The flask was placed into an oil bath previously

heated at 117°C and the mixture was stirred during 8h. Samples were withdrawn at predefined times for determination of the conversion through <sup>1</sup>H NMR analysis. To end the

<sup>4</sup> P. Dufils, N. Chagneux, D. Gignes, T. Trimaille, S.R.A. Marque, D. Bertin, P. Tordo, Intermolecular radical addition of alkoxyamines onto olefins: an easy access to advanced macromolecular architectures precursors, *Polymer*. 48 (2007) <https://doi.org/10.1016/j.polymer.2007.06.050>

polymerization, the flask was placed into an ice/water bath and the mixture was poured into a glass Petri dish. After complete evaporation of monomers and solvent, the homopolymer was dissolved into a minimum amount of  $\text{CHCl}_3$  and transferred in a small glass vial. The final product was dried under vacuum to afford 275 mg (yield 82%) of a transparent sticky putty.  $^1\text{H NMR}$  (ppm,  $\text{CDCl}_3$ ): 7.34-7.11 (m, 5H), 4.07 (m, 110H), 3.26 (d, 1H), 2.30 (m, 55H), 0.97 (t, 165H)

g. General bromination of homopolymer P(*n*BA)

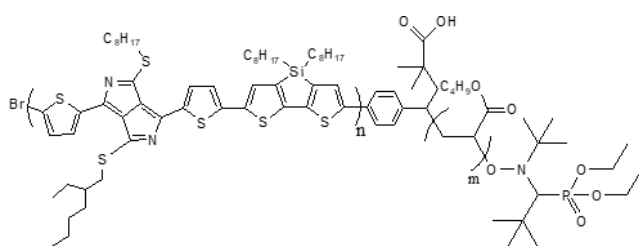


In a one-neck 10 ml round-bottom flask, 275 mg of P(*n*BA) (1 eq) was dissolved in 2 ml of dry  $\text{CCl}_4$  270 mg of K10-montmorillonite clay was added into the flask and the mixture was vigorously stirred while 0.5 ml of bromine in  $\text{CCl}_4$  (1 eq) was added dropwise for 10 min. The mixture was stirred at room temperature for an additional 6 h. The clay was then filtrated

from the mixture and washed with diethyl ether. The washings were evaporated with the mother liquor to leave a residue. The final product was dried under vacuum to afford 232 mg (yield 86%) of a slight brownish sticky putty.

$^1\text{H NMR}$  (ppm,  $\text{CDCl}_3$ ): 7.54 (d, 0.7H), 7.30 (m, 2H), 7.23 (m, 1H), 7.16 (m, 2.7H), 4.34-3.89 (m, 110H), 3.26 (d, 1H), 2.33 (m, 55H), 0.96 (t, 165H)

h. General Stille coupling polycondensation of block copolymer P(DTS-DAP)-*b*-P(*n*BA)



4,4'-bis(2-ethylhexyl)-5,5'-bis(trimethyltin)-dithieno[3,2-*b*:2',3'-*d*]silole monomer DTS (51.4 mg, 1 eq), 1,4-bis(5-bromothiophen-2-yl)-3,6-bis((2-ethylhexyl)thio)pyrrolo[3,4-

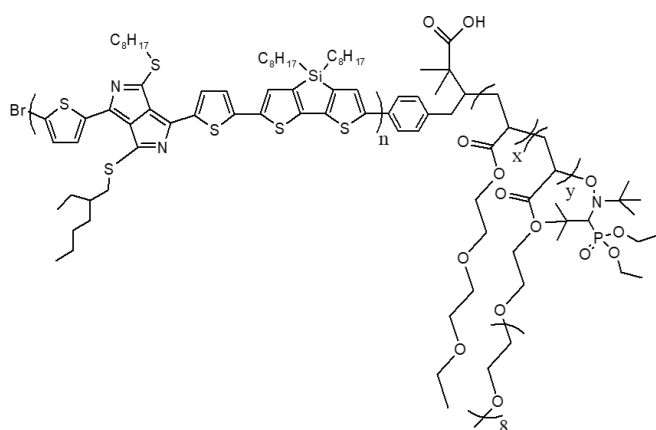
c]pyrrole monomer DAP (46.4 mg, 0.94 eq), brominated homopolymer P(*n*BA)-Br (28.5 mg, 0.062 eq),  $\text{Pd}_2\text{dba}$  (1.23 mg, 0.02 eq), and  $\text{P}(o\text{-tol})_3$  (2.04 mg, 0.1 eq) were accurately weighed into a 10 ml Biotage microwave vial equipped with a PTFE magnetic stirrer. The reaction vial was taken into a nitrogen-filled glovebox and dry toluene (3.0 ml) was added, the vial was securely sealed with a septum and removed from the glovebox. The vial was placed into an oil

bath and stirred for 20 minutes at 125 °C. After cooling, the polymer was precipitated in ethanol (200 ml), filtered in a Soxhlet thimble, washed by Soxhlet extraction using ethanol, THF, and chloroform. The THF fraction was dried under vacuum to afford 87.6 mg (yield 97%) of a dark green solid.

$^1\text{H NMR}$  (ppm,  $\text{CDCl}_3$ ): 8.25-7.25 (m, 172H), 4.11 (m, 110H), 3.86-3.40 (m, 115H)

## 5. Chapter 4: Experimental Part

### a. General synthesis of block copolymer P(DTS-DAP)-*b*-P(eDEGA-*co*-mOEGA)



In a one-neck round bottom flask, 19 mg of macroinitiator P(DTS-DAP)<sub>10</sub>-MAMA-SG1 (1eq) was dissolved into 1.8 ml of dry toluene. The mixture was sonicated 1h and stirred overnight to dissolve completely the macroinitiator. 2.43 ml of di(ethylene glycol) ethyl ether acrylate monomer (eDEGA, 4700

eq) and 0.64 ml of oligo(ethylene glycol) ethyl ether acrylate macromonomer (mOEGA, 500 eq) were added dropwise into the flask. The mixture was degassed 20 min under nitrogen into an ice/water bath to avoid monomer evaporation. The flask was placed into an oil bath previously heated at 130°C and the mixture was stirred for different times depending on the size block targeted. Samples were withdrawn at predefined times for determination of the conversion through  $^1\text{H NMR}$  analysis. To end the polymerization, the flask was placed into an ice/water bath and the mixture was diluted with THF and dialyzed with deionized water using a regenerated cellulose (RC) membrane (weight cutoff: 2.0 kDa). The polymer was passed into a freeze-drier during 3 days to remove water traces. After complete evaporation of water traces, the block copolymer was dissolved into a minimum amount of ethanol and transferred in a small glass vial. The final product was dried under vacuum to afford 69 mg (yield 70%) of a dark green sticky dough.

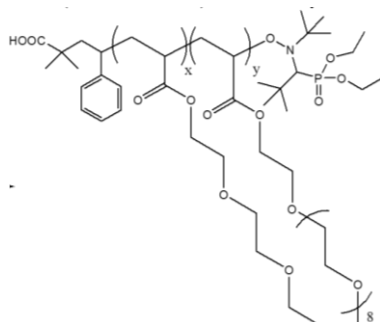
$^1\text{H NMR}$  (ppm,  $\text{CDCl}_3$ ): 8.20-6.88 (m, 42H), 4.23 (m, 86H), 2.38 (m, 43H)

The conversion  $p$  was calculated from the following equation:

$$p = \frac{I_{4.0-4.5 \text{ ppm}} - 2 \times I_{5.85 \text{ ppm}}}{I_{4.0-4.50 \text{ ppm}}} \times 100$$

with the integral between 4.0 and 4.5 ppm  $I_{4.0-4.5 \text{ ppm}}$  corresponding to one monomer peak and one polymer peak and the integral at 5.85 ppm  $I_{5.85 \text{ ppm}}$  corresponding to one monomer peak.

b. General nitroxide-mediated polymerization of homopolymer P(eDEGA-co-mOEGA)



In a one-neck round bottom flask, 46 mg of alkoxyamine MAMA-SG1-styrene (1 eq) was dissolved in 0.98 ml of dioxane. 2.57 ml of di(ethylene glycol) ethyl ether acrylate monomer (eDEGA, 147 eq) and 0.68 ml of oligo(ethylene glycol) ethyl ether acrylate macromonomer (mOEGA, 16 eq) were added dropwise into the flask. The mixture was degassed 20 min under nitrogen into an ice/water bath to avoid monomer evaporation. The flask was placed into an oil bath previously heated at 115°C and the mixture was stirred during 4h. Samples were withdrawn at predefined times for determination of the conversion through  $^1\text{H}$  NMR analysis. To end the polymerization, the flask was placed into an ice/water bath and the mixture was diluted with THF and dialyzed with deionized water using a regenerated cellulose (RC) membrane (weight cutoff: 2.0 kDa). The polymer was passed into a freeze-drier during 3 days to remove water traces. After complete evaporation of water traces, the polymer was dissolved into a minimum amount of ethanol and transferred in a small glass vial. The final product was dried under vacuum to afford 50 mg (yield 72%) of a transparent sticky dough.

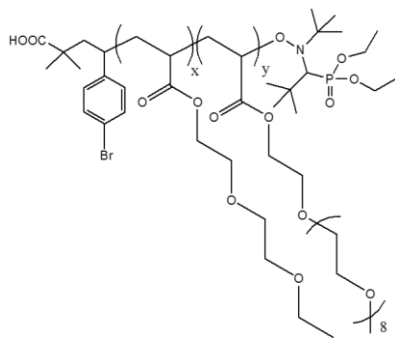
$^1\text{H}$  NMR (ppm,  $\text{CDCl}_3$ ): 7.41-6.99 (m, 5H), 4.21 (m, 100H), 3.41 (s, 31H), 3.26 (d, 1H), 2.39 (m, 50H), 1.24 (t, 153H)

The conversion  $p$  was calculated from the following equation:

$$p = \frac{I_{4.0-4.5 \text{ ppm}} - 2 \times I_{5.8 \text{ ppm}}}{I_{4.0-4.50 \text{ ppm}}} \times 100$$

with the integral between 4.0 and 4.5 ppm  $I_{4.0-4.5 \text{ ppm}}$  corresponding to one monomer peak and one polymer peak and the integral at 5.8 ppm  $I_{5.8 \text{ ppm}}$  corresponding to one monomer peak.

c. General bromination of homopolymer P(eDEGA-co-mOEGA)



In a one-neck round bottom flask, 270 mg of P(eDEGA-co-mOEGA) (1 eq) was dissolved in 2 ml of dry  $\text{CCl}_4$ . 270 mg of K10-montmorillonite clay was added into the flask and the mixture was vigorously stirred while 2 ml of bromine in  $\text{CCl}_4$  (1 eq) was added dropwise for 10 min. The mixture was stirred at room temperature for an additional 6 h. The clay was then filtrated from the mixture and washed with diethyl

ether. The washings were evaporated with the mother liquor to leave a residue. The final product was dried under vacuum to afford 230 mg (yield 86%) of a slight brownish sticky dough.

$^1\text{H NMR}$  (ppm,  $\text{CDCl}_3$ ): 7.55-6.99 (m, 8.6H), 4.26 (m, 100H), 2.48 (m, 50H)

## List of publications

1. **Adèle Gapin**, Hisham Idriss, Sylvie Blanc, Laurent Billon, Marie-Hélène Delville, Antoine Bousquet, Christine Lartigau-Dagron, Low band-gap polymer brushes: Influence of the end-group on the morphology of core-shell nanoparticles, *Reactive and Functional Polymers*, **2020**, 155, 104700, <https://doi.org/10.1016/j.reactfunctpolym.2020.104700>

2. Hisham Idriss, **Adèle Gapin**, Wissem Khelifi, Sylvie Blanc, Iyad Karamé, Sylvain Chambon, Lionel Hirsch, Antoine Bousquet, Christine Lartigau-Dagron, Complementary absorption versus morphology in all-conjugated block copolymer solar cells, *Macromolecules*, **2020**, 53, 9043, <https://doi.org/10.1021/acs.macromol.0c01680>



## Abstract

Nowadays, organic materials absorbing in the near infrared region have found fertile ground in a variety of applications and have significantly contributed in improving optoelectronic devices, bioimaging, biosensing, and biomedical therapies. The development of low band-gap polymers draw particular attention since their reduced bandgaps determine interesting optical and electronic properties. The end-functionalization of these conjugated polymers paves the way to the development of hybrid materials which could improve the performances of optoelectronic devices. Furthermore, rod-coil block copolymers incorporating low band-gap polymers are reachable and could provide broader light absorption, better solubility, as well as self-assembly properties. In this context, the objective of our work was to develop innovative materials based on low band-gap polymers absorbing in the spectral range 650-1000 nm in order to obtain active materials in the near infrared region. We synthesized a new hybrid material by grafting a low band-gap polymer onto ZnO nanospheres *via* the grafting onto technique. We designed and prepared rod-coil block copolymers involving a low band-gap block *via* two synthetic method. The first copolymer was based on the use of a coil block with filmogenic properties which we plan to employ as additive in the elaboration of organic infrared photodetectors. The second copolymer was based on the use of a hydrophilic biocompatible coil block in order to obtain water soluble nano-objects with photothermal properties.

## Résumé

De nos jours, les matériaux organiques absorbant dans la région du proche infrarouge ont trouvé un terrain fertile dans une variété d'applications et ont contribué de manière significative à l'amélioration des dispositifs optoélectroniques, de la bioimagerie, de la biodétection et des thérapies biomédicales. Le développement de polymères à faible bande interdite retient particulièrement l'attention car leurs bandes interdites réduites conduisent à des propriétés optiques et électroniques intéressantes. La fonctionnalisation de ces polymères conjugués en bout de chaînes ouvre la voie au développement de matériaux hybrides susceptibles d'améliorer les performances des dispositifs optoélectroniques. En outre, les copolymères à blocs rigide-flexible intégrant des polymères à faible bande interdite sont désormais accessibles et pourraient fournir une plus large absorption de la lumière, une meilleure solubilité, ainsi que des propriétés d'auto-assemblage. Dans ce contexte, l'objectif de nos travaux a été de développer des matériaux innovants à base de polymères à faible bande interdite absorbant dans le domaine spectral 650-1000 nm afin d'obtenir des matériaux actifs dans la région proche infrarouge. Nous avons synthétisé un nouveau matériau hybride en greffant un polymère à faible bande interdite sur des nanosphères de ZnO *via* la technique de *grafting onto*. Nous avons conçu et préparé des copolymères à blocs rigide-flexible intégrant un bloc à faible bande interdite *via* deux méthodes de synthèse. Le premier copolymère est composé d'un bloc flexible aux propriétés filmogènes que nous prévoyons d'utiliser comme additif dans l'élaboration de photodétecteurs infrarouges organiques. Le second copolymère présente un bloc flexible biocompatible et hydrophile afin d'obtenir des nano-objets hydrosolubles aux propriétés photothermiques.

École doctorale :  
Sciences Exactes et leurs Applications (ED211)

Laboratoire :  
Institut des Sciences Analytiques et de Physico-Chimie pour l'Environnement et les  
Matériaux (IPREM)